A Numerical Investigation of Roughness Facilitated Turbulent Rayleigh-Bénard Convection

A thesis submitted in
partial fulfilment of the requirements
for the degree of

Doctor of Philosophy

in

Mechanical Engineering

by

Mukesh Sharma

under the guidance of

Dr. Arnab Kumar De

Department of Mechanical Engineering
Indian Institute of Technology Guwahati
Guwahati - 781039
Assam, India.

November 2023

Dedicated to my parents.

CERTIFICATE

This is to certify that the work presented in this thesis entitled "**A Numerical Investigation of Roughness Facilitated Turbulent Rayleigh-Bénard Convection**" is carried out by **Mukesh Sharma** for the award of Doctor of Philosophy in the Department of Mechanical Engineering, Indian Institute of Technology Guwahati. The thesis embodies the result of original work and studies carried out by the student himself under my supervision and has not been submitted elsewhere for a degree.

Dr. Arnab Kumar De,
Associate Professor,
Department of Mechanical Engineering,
Indian Institute of Technology Guwahati
Guwahati, Assam, Pin - 781039, India.

Date: 4 November, 2023
Place: Guwahati

ACKNOWLEDGEMENT

First of all, I would like to express my gratitude to the almighty for his continuous grace and mercy in my life. The work presented in the thesis would not have been possible without the continuous support, guidance, and motivation of my thesis supervisor, Dr. Arnab Kumar De. It is under his training and guidance I have learned invaluable skills that helped me mature as a researcher. His continuous discussions and suggestions have helped me shape my research ideas. I express my sincere gratitude to my doctoral committee members, Prof. Amaresh Dalal, Prof. Ujjwal K. Saha, and Prof. Santabrata Das, for their valuable insights during the research. My special thanks to Prof. Amaresh Dalal for allowing us to use his high-performance computational server. My research would not have been possible if it was not for the 'Param-Ishan' supercomputing facility at the institute.

During my stay at IIT Guwahati, I came across several friends who made this journey pleasant and memorable. I acknowledge all the love and company that I have received from them during different stages of my Ph.D. I thank Antarik Saikia, Nitesh Kumar, Debojit Paul, Akash Rana, Vivek Kushwaha, Dharmanshu Dave, Naren M., Debojyoti Nath, Mukesh Kumar, Raman Kumar, Deepak Kumar, Angan Sarkar, Sumit Kumar Das, and many other friends whose memories are engraved on my heart. My special thanks to Krishan Chand and Vishnu Venugopal for showing great enthusiasm in discussing several aspects of turbulent thermal convection. I am thankful to my CFD lab mates, who were always there to support me in all possible ways.

No words can express my gratitude to my parents and family members, who have always stood by me through thick and thin. They are my pillars of strength. I am indebted to their continuous support, encouragement, and blessings, which have kept me going throughout this journey and beyond. I will always be grateful for all the sacrifices made by my parents to transform my dream into reality.

Mukesh Sharma

ABSTRACT

Rayleigh-Bénard convection (RBC) is an ideal model used to study thermal convection, where a layer of fluid confined between two horizontal plates is heated from below and cooled from the top. With the purpose of facilitating a better representation of thermal convection processes in nature, the conventional RBC setup is modified to take into account surface asperities in direct numerical simulations (DNS). Taking a cue from nature, we have employed multi-scale irregular roughness on the isothermal plates, where no bias towards any particular length scale of roughness elements is present. The presence of rough surfaces adds to turbulence in the system with the emission of extra thermal plumes, which augments the heat transfer rate. The rough surfaces consist of triangular elements in 2D, while conical ones are incorporated in 3D.

Using DNS in 2D with air as working fluid, we have explored the efficacy of the irregular surfaces containing triangular elements for a very high $10^8 \leq Ra \leq 10^{11}$ range in sustaining the enhanced heat transfer scaling exponent. It is observed that the varied response of the roughness elements at different Ra allows retention of the enhanced heat transfer scaling ($\gamma = 0.41$) throughout the explored Ra range. The plume emission process is triggered by the taller roughness elements at a lower Ra, while smaller elements contribute significantly at a higher Ra. The activation of small-scale roughness elements is seen to play a pivotal role in sustaining an augmented heat transport at higher Ra. Detailed analysis of the near-wall dynamics unveils the complex role of the roughness elements and the associated throat, valley, and tip regions in influencing dominant flow structures and heat transport mechanism. The extent of transformation of vertical profiles of mean temperature passing through different valley regions from flat linear into steeper ones with increasing Ra bears close connection with the effectiveness of the given throat region in the higher Ra regime.

Incorporating the effect of Pr in the 2D roughness framework for $10^7 \leq Ra \leq 5 \times 10^9$ and $0.1 \leq Pr \leq 100$, a monotonic increasing behavior of *Nu* as a function of Pr is observed. The

result is in contrast to the near invariant behavior shown by *Nu* with Pr in smooth cells. In case of the 3D roughness setup with $Ra = 10^8$ and $1 \leq Pr \leq 50$, Pr is not seen to influence the global heat transport, though Nusselt number is observed to be around 50% higher compared to its smooth counterpart. The projection of the strength of angular rotation of fluid flow, calculated about the geometric center of the cell, onto the chosen directions reveals that roughness elements alter the preferred orientation of large-scale circulation (LSC). For $Pr \leq 10$, the large-scale rotational tendency is found to be highest in a Cartesian horizontal direction. The result is in contrast to the observation made for the smooth cubic cell, where the large-scale flow has a strong inclination to reside in one of the two diagonal planes. Quantitatively, the roughened cells are observed to have a higher volume fraction of plumes along with the associated thermal dissipation rate in comparison to the smooth case. Amplified fluctuations in both bulk and near-wall regions also corroborate increased turbulent intensity for the roughened cells.

CONTENTS

ABBREVIATIONS

BiCGSTAB	Bi-Conjugate Gradient Stabilized
BL	Boundary layer
BO59	Bolgiano scaling
DIIBM	Diffuse interface immersed boundary method
DNS	Direct Numerical Simulation
K41	Kolmogorov scaling
LSC	Large Scale Circulation
MPI	Message passing interface
MSI	Modified strongly implicit method
PDF	Probability density function
RBC	Rayleigh-Bénard Convection
rms	Root mean square
SIP	Strongly implicit procedure
TBL	Thermal boundary layer
TKE	Turbulent kinetic energy

SYMBOLS

g	Acceleration due to gravity (m/s^2)
H	Height of box (m)
h	Amplitude of a roughness element
L	Length of box (m)
Nu	Nusselt number
N_x, N_y, N_z	Grid resolution in x, y, z directions, respectively
p	Pressure (N/m^2)
Pr	Prandtl number
Ra	Rayleigh number
Re	Reynolds number
T_C	Temperature of cold surface $(^\circ C)$
T_H	Temperature of hot surface $(^\circ C)$
u, v, w	Cartesian components of the velocity vector
v_{plc}	Mean vertical velocity of cold plumes
v_{plh}	Mean vertical velocity of hot plumes
V_{bg}	Volume fraction of background
V_{pl}	Volume fraction of plumes
V^r	Reference velocity

GREEK SYMOBLS

α	Thermal diffusivity (m^2/s)
β	Isobaric thermal expansion coefficient
Γ	Aspect ratio of the rectangular box
ΔT	Temperature difference between hot and cold surfaces $(^\circ C)$
ϵ_θ	Non-dimensional thermal dissipation rate
$\epsilon_{\theta_{pl}}$	Net non-dimensional thermal dissipation rate contribution from plumes
$\epsilon_{\theta_{bg}}$	Net non-dimensional thermal dissipation rate contribution from background
ϵ_u	Non-dimensional viscous dissipation rate
η	Kolmogorov length scale
η_τ	Kolmogorov time scale
θ	Non-dimensional temperature
θ_{plc}	Mean temperature of cold plumes
θ_{plh}	Mean temperature of hot plumes
λ	Widhth of a roughness element
μ	Dynamic viscosity $(N/m^2 s)$
ν	Kinematic viscosity of fluid (m^2/s)
ρ	Density of fluid (kg/m^3)
σ_θ	Root mean square of temperature
σ_θ^2	Variance of temperature
σ_v	Root mean square of vertical velocity
σ_v^2	Variance of vertical velocity

LIST OF FIGURES

LIST OF TABLES

1 INTRODUCTION

1.1 Rayleigh-Bénard convection

Natural convection is ubiquitous in nature and finds application in various engineering and industrial applications [1–3]. It occurs in the Earth's outer core, atmosphere, and oceans, inside the Sun, and in other stellar bodies. Figure 1.1 schematically shows the application of natural convection in Earth's mantle, circulation of sea and land breezes, and boiling of water. Convective motion inside the Earth's mantle is responsible for tectonic drift and volcanic activities. The heated mantle close to the Earth's hot core rises to the top, while the cooler mantle near the lithosphere sinks, and thus, a convection current is created in the Earth's Mantle. The same principle also governs the development of sea and land breezes. During the day, the sea is surrounded by a hotter land, leading to a convection current where the cool air from the sea replaces the hot rising air of the land surface. This phenomenon is called the "sea breeze". In the nighttime, the land surface cools down quickly in comparison to the sea. It results in a cool breeze flowing from land towards the sea, which is defined as the "land breeze". The heating of water is another classic example where the convection current sets up. In addition to the above applications, thermally driven turbulence plays a vital role in various industrial applications, such as in heat exchangers, fluid storage, nuclear reactors, solar heating devices, cooling of electronic components, and the metal solidification process.

Rayleigh-Bénard convection (RBC) [8–11] is an ideal model used to study thermal convection in which a thin layer of fluid is heated from the bottom. Figure 1.2 shows the schematic of RBC inside (a) cylindrical and (b) Cartesian cells along with the prevalent coherent structures. At a sufficiently high temperature difference between the isothermal plates, thermal-convective instabilities set the flow in the system, where hot fluid rises to the top and cold fluid sinks to the bottom. While viscous force acts as a stabilizing agent, buoyancy force introduces instability in the system. The relative strength of buoyant force over viscous force is expressed in a non-

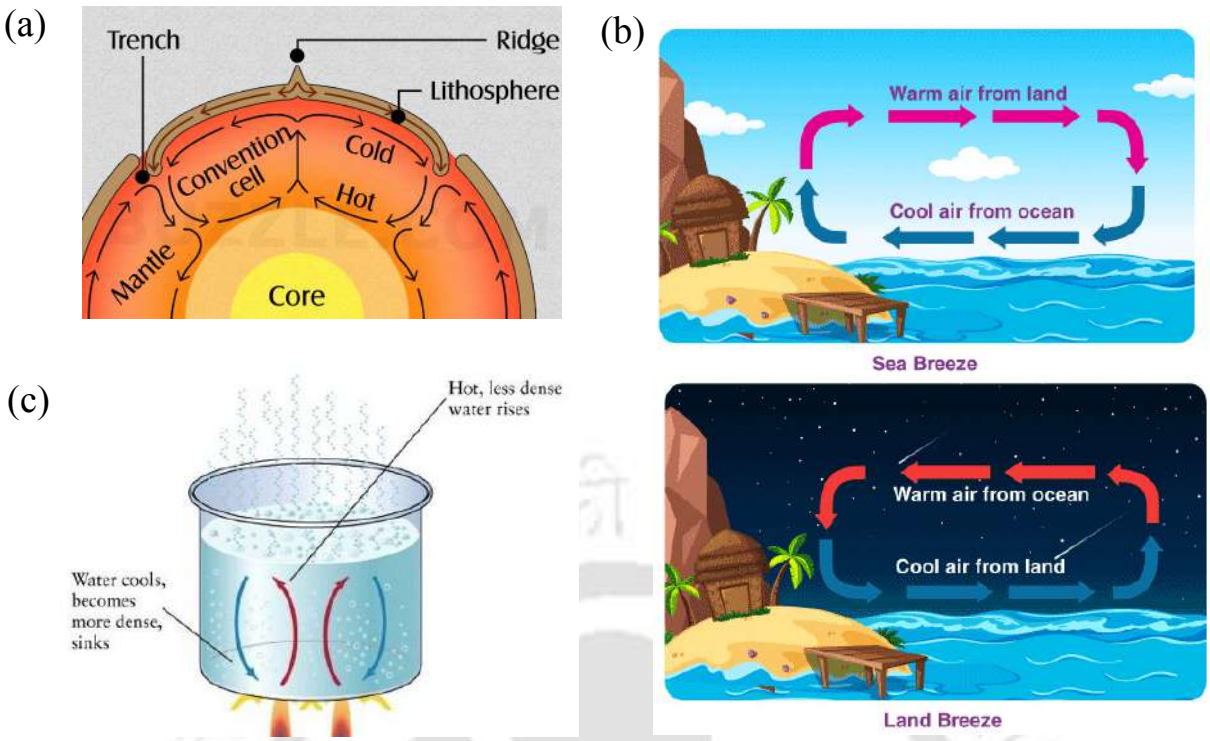

Figure 1.1: Schematic representation of natural convection in (a) Earth's mantle [4], (b) formation of sea and land breezes [5], and (c) boiling of water [6].

dimensional number termed as Rayleigh number, $Ra = \beta g \Delta T H^3/\nu\alpha$. Here, β is the thermal expansion coefficient, ΔT is the temperature difference between the bottom and top plates, g is the acceleration due to gravity, H is the height of the fluid layer, ν is the kinematic viscosity, and α is the thermal diffusivity of the fluid. In addition to Ra, Prandtl number (Pr) is another important parameter that governs the flow dynamics in RBC. It is defined as the ratio of kinematic viscosity to thermal diffusivity of a fluid.

In response to the control parameters (Ra, Pr), Rayleigh-Bénard convection develops in the system, which is characterized by the transport of momentum and thermal energy in terms of Reynolds and Nusselt numbers, respectively. The Reynolds number gives the relative measure of inertial and viscous forces, whereas the Nusselt number signifies the relative contribution of convection over conduction. Mathematically, they are defined in the following manner

$$Re = \frac{UH}{\nu}, \qquad Nu = \frac{Q}{k(\Delta T/H)},$$

where U is the characteristic velocity, k is the thermal conductivity of the fluid, and Q is the total heat flux through the top and bottom walls.

In Fig. 1.3, various stages involved in the transition of the system into a turbulent state with increasing Ra are shown. Above the fixed critical Rayleigh number (Ra_c), instability sets in the RBC system, resulting in fluid motion and an augmented heat transfer rate. The critical

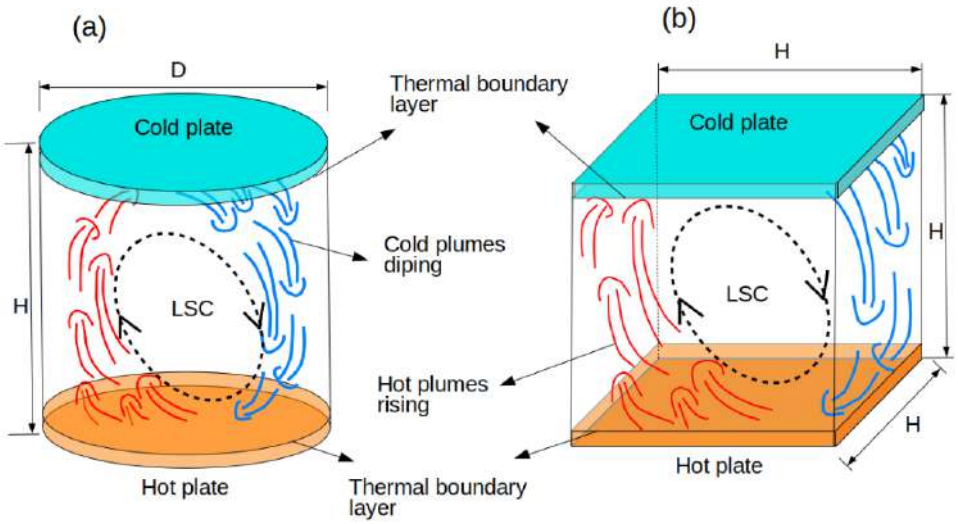

Figure 1.2: Schematic shows the setup of Rayleigh-Bénard convection [7] inside (a) cylindrical and (b) Cartesian cells along with the prevalent coherent structures. The hot thermal plumes originated from the bottom boundary layer (BL) rise to the top while cold plumes descend from the top boundary layer, thus forming a large-scale circulation (LSC).

Rayleigh number (Ra_c) is independent of the Prandtl number but depends on the boundary conditions. For a box geometry, Ra_c assumes 657.5 and 1707 for free slip and no-slip boundary conditions, respectively. It is clear from Fig.1.3 that Ra_c, signifying the transition from conduction to convection state, is constant (1707) for all Pr. In Fig. 1.3, region above curve I marks the onset of convection with steady two-dimensional rolls. The region between curves II and III exhibits steady three-dimensional cellular flow, whereas between curves III and V, the flow is time-dependent and three-dimensional. Beyond curve V, flow becomes turbulent.

For moderate ($Pr \approx 1$) and high Prandtl number ($Pr > 1$) fluids, two-dimensional rolls are realized up to $Ra \approx 2 \times 10^4$, beyond which (see curve II in Fig. 1.3) the steady two-dimensional rolls undergo a transition to steady three-dimensional ones. With further increase in thermal forcing, flow first becomes periodic in time (above curve III) owing to time-dependent instabilities and subsequently loses its temporal coherence (above curve IV) and becomes chaotic. Beyond curve V, the flow exhibits turbulent behavior with randomness in both space and time. However, above a certain threshold Ra, statistical coherence is restored with the appearance of "large-scale circulation" (shown by '$\sim$' in Fig. 1.3) in which on an average flow rises from one side of the lateral wall and descends from the opposite side wall. For low Pr fluids, $Pr << 1$, the transition to the convective state is quite different from high Pr fluids. Here, secondary instabilities appear time-dependent, whereas, for high Pr fluids, three-dimensional convection is observed. Also, for the low Pr regime, the region of the stable two-dimensional state shrinks

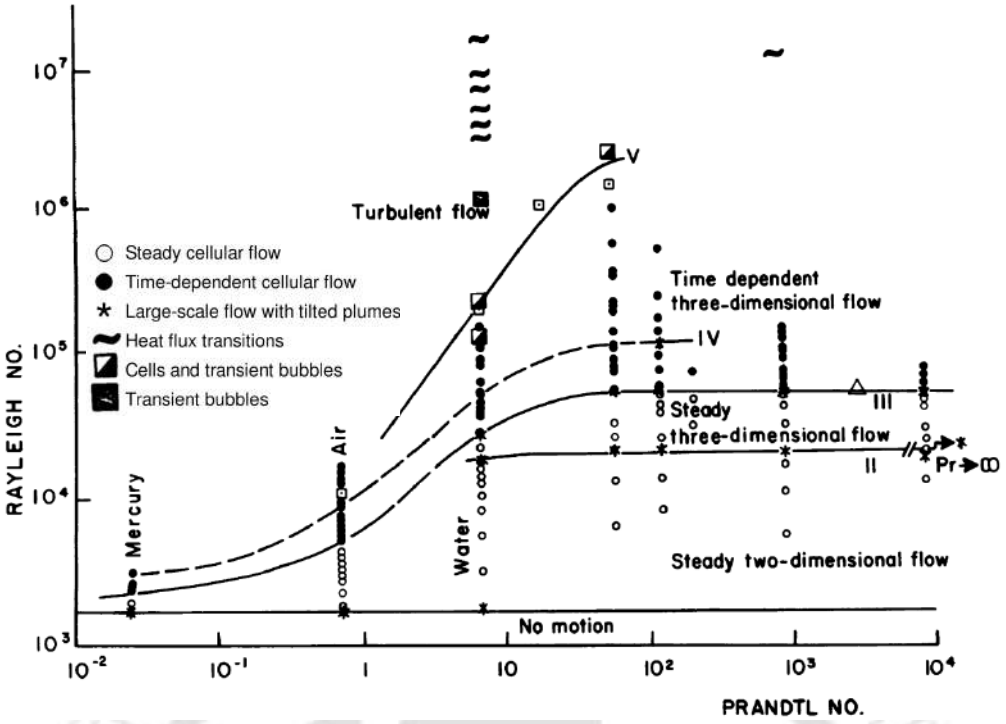

Figure 1.3: Schematic showing various regimes observed for thermal convection as a function of Ra and Pr (adapted from Krishnamurti and Howard [12]). Curves I and II indicate the onset of steady rolls and three-dimensional steady convection patterns, respectively. The region between curves III and V represent time-dependent three-dimensional cellular flow, whereas above V flow becomes turbulent.

considerably. In summary, above the critical Ra, flow undergoes various transitional stages before it becomes fully turbulent.

In turbulent Rayleigh-Bénard convection, constant efforts are made to understand the prevalent heat transport mechanism and its implication on *Nu* relation as a function of the input parameters (Ra, Pr, Γ). The chronological development of heat transport theories and their main results are presented in the next section. Later, we discuss the importance of studying roughness-aided RBC along with the review of existing studies in the literature. Further, the effect of Pr on flow structures and heat transport mechanism is discussed for both rough and smooth cell configurations.

1.2 Scaling theories on heat transport

Various heat transfer theories have been proposed in the past to explain the heat transfer mechanism in RBC, which essentially try to establish the relation of *Nu* with Ra. One of the oldest scaling theories was given by Malkus [13], where the thermal boundary layer is assumed to be

marginally stable such that Ra calculated based on conditions in the thermal boundary layer denotes a critical Rayleigh number (Ra_c). This implies

$$Ra_c \approx Ra(\lambda_\theta) = \beta g \Delta T \lambda_\theta^3 / \nu\alpha$$
$$\implies Ra_c \approx (\lambda_\theta / H)^3 Ra$$

Further, on using $Nu \sim H/\lambda_\theta$ in the above relation yields $Nu \sim Ra^{1/3}$. With $\gamma = 1/3$, *Nu* scaling is termed as "classical" scaling. Priestley [14] proposed an alternate way to obtain the same *Nu* scaling where convective heat flux (q_{conv}) is treated independent of the height of the container (H). The steps are as follows

$$Nu \sim Ra^\gamma$$
$$\implies q_{conv}/q_{cond} = q_{conv} H/k\Delta T \sim \left(\beta g \Delta T H^3/\nu\alpha\right)^\gamma$$
$$\implies q_{conv} \sim k\Delta T \left(\beta g \Delta T/\nu\alpha\right)^\gamma H^{3\gamma-1}$$

From the above step, it is clear that γ should be $1/3$ for q_{conv} to be independent of H. Thus, it can be inferred that realization of $1/3$ scaling inherently involves the decoupling of top and bottom boundary layers.

Kraichnan and Spiegel [15, 16] proposed that in the limit of a very high Rayleigh number, boundary layers (BLs) undergo a transition from being laminar to turbulent. As BLs become turbulent, heat transport process receives negligible resistance from them. In other words, heat flux is solely determined by the bulk dynamics. This high Ra regime is known as the "ultimate" or asymptotic regime. The scaling in this regime is termed as "ultimate scaling" where the scaling exponent has a value of $1/2$. The scaling can be derived using the "free fall" argument [16], where vertical velocity (v) is obtained by the balance of inertia and buoyancy acceleration, $v^2/H \sim \beta g \Delta T$. As contribution of diffusion process in heat transfer is negligible, effective vertical heat flux is given as $q_{conv} \sim v\delta T$. This implies $Nu \sim q_{conv}/q_{cond} \sim H\Delta T\sqrt{\beta g \Delta T H}/\alpha\Delta T \sim (RaPr)^{1/2}$.

Later, Castaing *et al.* [17] proposed the mixing layer theory based on the assumption that thermal plumes exist. They characterized the whole domain into three distinct zones/layers having different physical properties. The first layer is the thermal boundary layer, close to top and bottom isothermal plates, with temperature gradient $\Delta T/2$. Here, plumes of size comparable to the TBL thickness are generated and expelled into the second layer. The Second layer is called the mixing region, whose thickness is greater than the TBL thickness but smaller than the size of the cell height H, where plumes are accelerated due to buoyancy effect. The third layer comprises the central region of the cell with size comparable to the size of the system, where

advection of thermal plumes takes place at constant velocity. Based on this physical picture of the RBC system, *Nu* scaling exponent of $2/7$ is obtained. Shraiman and Siggia [18] also came up with the same $2/7$ scaling law but they envisaged different physical picture for RBC. They asserted that the onset of mean flow happens due to plumes rising from the unstable boundary layer.

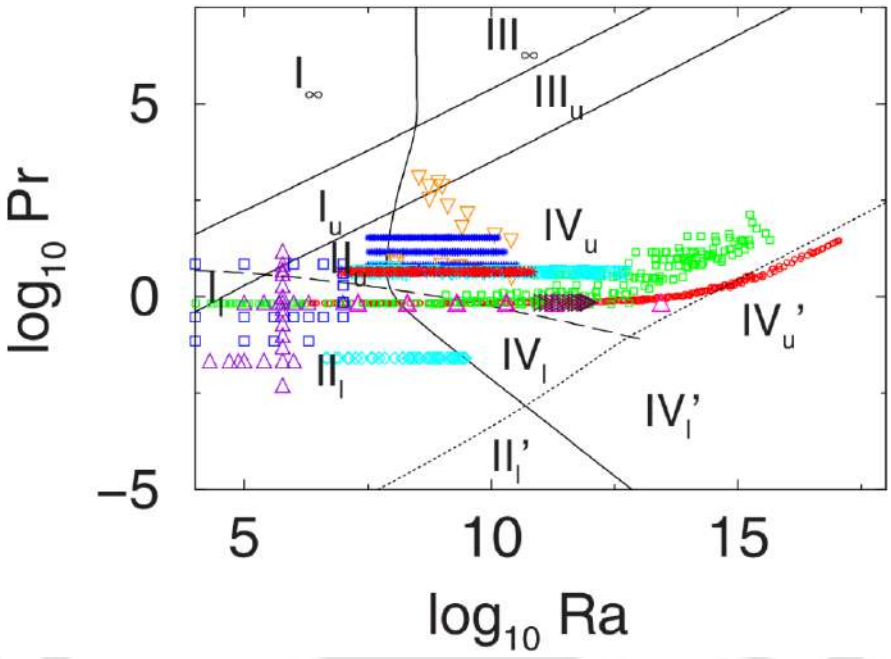

Figure 1.4: Schematic adopted from Ahlers *et al.* [10] shows $Ra-Pr$ phase diagram. The dashed line represents $\lambda_u = \lambda_\theta$, dotted line represents the critical shear Reynolds number ($Re_s^* = 420$) above which kinetic BL is expected to become turbulent (regions $\mathrm{II_l}$', $\mathrm{IV_l}$' and $\mathrm{IV_u}$' have turbulent kinetic BL), topmost solid line represents $Re = Re_c$ and the parallel solid line just below it represents $\epsilon_{u,\mathrm{BL}}$, and the curved solid line signifies $\epsilon_{\theta,\mathrm{BL}} = \epsilon_{\theta,\mathrm{bulk}}$.

With the developments in RBC, various experimental and numerical works suggested different $Nu(Ra, Pr)$ scalings but no single theory could provide a bigger picture explaining the different scalings. It led Grossmann and Lohse [10, 19] to develop a unifying scaling theory (also known as GL theory) which states that there exists no pure scaling law but rather scaling laws are a function of Ra and Pr. One of the basic assumptions in the GL theory is the existence of the large-scale wind which creates a viscous boundary layer around the walls and also stirs the flow in the bulk. In this theory, global dissipation rates (ϵ_u, ϵ_θ) are decomposed into their boundary layer ($\epsilon_{u,\mathrm{BL}}$, $\epsilon_{\theta,BL}$) and bulk contributions ($\epsilon_{u,\mathrm{bulk}}$, $\epsilon_{\theta,bulk}$) which then divides $Ra-Pr$ space into four regions depending on whether bulk or boundary layer contributions dominate the dissipation rates. As shown in Table 1.1, the four different regimes can be characterized as

Regime I: Both ϵ_u and ϵ_θ are dominated by their BL contributions.

Regime II: ϵ_θ is dominated by $\epsilon_{\theta,\text{BL}}$, whereas ϵ_u is dominated by $\epsilon_{u,\text{bulk}}$.

Regime III: ϵ_u is dominated by $\epsilon_{u,\text{BL}}$, whereas ϵ_θ is dominated by $\epsilon_{\theta,\text{bulk}}$.

Regime IV: Both ϵ_u and ϵ_θ are dominated by their bulk contributions.

Further, a regime is subdivided into two zones depending on whether viscous boundary layer thickness (λ_u) is thicker or thinner than λ_θ. Zone with $\lambda_u < \lambda_\theta$ is represented by subscript l and zone where $\lambda_u > \lambda_\theta$ is represented by subscript u. From theoretical point of view, GL theory has managed to identify different regimes and predict the associated *Nu*(Ra, Pr) and $Re(Ra, Pr)$ scaling in those regimes. Further, the GL theory also predicts the existence of the ultimate regime (shown as IV_l in Fig. 1.4), which is the most sought after regime among the research community. For $Pr \approx 1$, the transition to the ultimate regime is predicted to occur at Ra around $10^{13} - 10^{14}$. Despite the theoretical prowess of the GL theory, it has some limitations

1. It is built on Prandtl-Blasius boundary layer theory where temperature is treated as a passive scalar, and only global effect of the plumes is taken into account in the form of large-scale wind.

2. Three-dimensional dynamics of the large-scale wind are not considered.

3. It is not yet conceptualized for RBC with rotation.

Table 1.1: Power laws for *Nu* and Re for different regimes in GL theory.

Regime	Dominance of regime	BL	*Nu*	Re
I_l	$\epsilon_{u,\text{BL}}$, $\epsilon_{\theta,\text{BL}}$	$\lambda_u < \lambda_\theta$	$0.27Ra^{1/4}Pr^{1/8}$	$0.037Ra^{1/2}Pr^{-3/4}$
I_u		$\lambda_u > \lambda_\theta$	$0.33Ra^{1/4}Pr^{-1/12}$	$0.039Ra^{1/2}Pr^{-5/6}$
II_l	$\epsilon_{u,\text{bulk}}$, $\epsilon_{\theta,\text{BL}}$	$\lambda_u < \lambda_\theta$	$0.97Ra^{1/5}Pr^{1/5}$	$0.047Ra^{2/5}Pr^{-3/5}$
II_u		$\lambda_u > \lambda_\theta$	$(\sim Ra^{1/5})$	$(\sim Ra^{2/5}Pr^{-2/3})$
III_l	$\epsilon_{u,\text{BL}}$, $\epsilon_{\theta,\text{bulk}}$	$\lambda_u < \lambda_\theta$	$6.43 \times 10^{-6}Ra^{2/3}Pr^{1/3}$	$5.24 \times 10^{-4}Ra^{2/3}Pr^{-2/3}$
III_u		$\lambda_u > \lambda_\theta$	$3.43 \times 10^{-3}Ra^{3/7}Pr^{-1/7}$	$6.46 \times 10^{-3}Ra^{4/7}Pr^{-6/7}$
IV_l	$\epsilon_{u,\text{bulk}}$, $\epsilon_{\theta,\text{bulk}}$	$\lambda_u < \lambda_\theta$	$4.43 \times 10^{-4}Ra^{1/2}Pr^{1/2}$	$0.036 \times 10^{-4}Ra^{1/2}Pr^{-1/2}$
IV_u		$\lambda_u > \lambda_\theta$	$0.038Ra^{1/3}$	$0.16Ra^{4/9}Pr^{-2/3}$

The realization of the ultimate regime has been an outstanding issue in turbulent Rayleigh-Bénard convection as it is believed to confer the highest possible heat transfer rate with minimum

resistance from the boundary layers. Also, it holds the key to the understanding of the highly turbulent flows prevalent in stellar convection where Ra is as high as 10^{20}. The existence of the ultimate regime has perplexed the scientific community for a very long time and is the most debated topic. In various experiments [20–22], a transition to the ultimate regime has been reported at $Ra \sim 10^{14}$, while others [23–25] denied any sign of ultimate regime. Zhu *et al.* [26] through numerical investigations also ascertained the transition to the ultimate regime at $Ra \sim 10^{13}$. The computational and experimental difficulties in attaining very high Ra pose great challenges in confirming the existence of the ultimate regime. Researchers with the motive of finding a way around developed various strategies to reach the ultimate regime that includes numerical studies involving periodic boundary conditions [27] in all directions to experimental work where radiative heating [28] is introduced to heat the bulk fluid directly, and thus the effect of the BLs is negated. Surface roughness is one of the adopted strategies meant to introduce turbulence in the BLs to seek the realization of the ultimate regime and the associated $1/2$ scaling. In the next section, the role of surface roughness and its impact on heat transfer rate in RBC is introduced.

1.3 Employment of surface roughness in RBC

For a comprehensive understanding of natural convection, it is important to observe the boundary layer dynamics and flow structures over rough surfaces. The study of thermal convection over rough surfaces is inevitable at very high Ra (as in 'ultimate regime') [15]. Any wall roughness becomes influential when the thermal boundary layer thickness becomes smaller than the height of a rough surface. With increasing Ra, the thickness of the thermal boundary layer decreases monotonically, and eventually, it becomes smaller than the height of a rough surface above a particular Ra. Thus, rough surfaces are influential at high Ra, and hence, it becomes essential to study natural convection over them. Thermal convection over rough surfaces is one of the possible ways to achieve enhanced heat transfer. Shen et al. [29] first observed enhancement of heat transfer on using regularly spaced identical pyramids as rough surfaces at the top and bottom plates such that height of the roughness elements is greater than the thermal boundary layer thickness. The increased heat transfer was due to the increase of the prefactor A by 20% in the relation $Nu = ARa^{\gamma}$. However, no change in the scaling exponent γ was observed. Du and Tong [30] also observed enhanced heat transfer with the increase of prefactor A by 76%. Increase in heat transfer was observed because of the enhanced plume emission frequency from the tip of the roughness elements. This deviation of heat transfer could not be explained by a

simple increase in area argument [31] since in terms of area variation, *Nu* could only increase up to 41% instead of 76%. This observation quantitatively confirmed a change in the flow dynamics with rough surfaces. Although an increase in heat transfer was observed, no change in the scaling exponent γ was reported. Later in various experiments, change in the scaling exponent γ was observed.

Roche *et al.* [33] conducted experiment in a cylindrical container with linear V-shaped

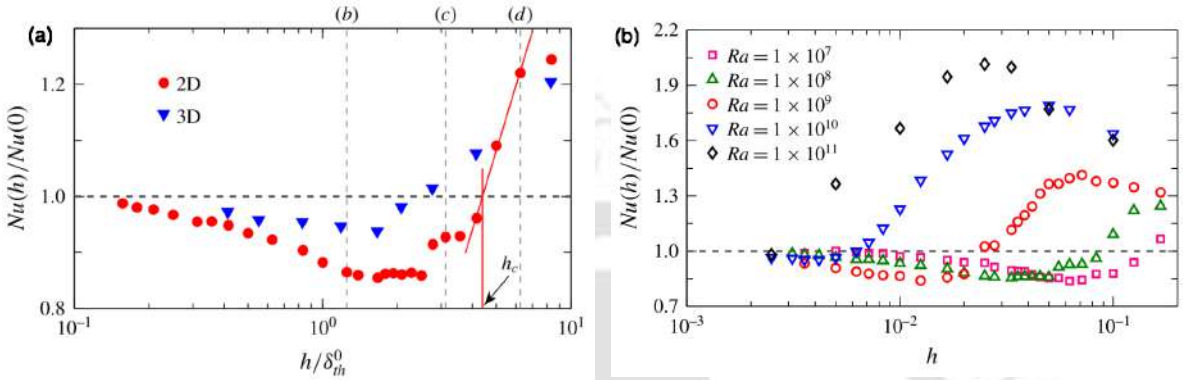

Figure 1.5: Variation of the normalized Nusselt number $Nu(h)/Nu(0)$ as a function of (a) normalized roughness height h/δ°_{th} for $Ra = 10^8$, and (b) roughness height h for different Ra. $Nu(0)$ and δ°_{th} represent Nusselt number and thermal boundary layer thickness for the smooth wall case, respectively. Figure reproduced from Zhang et al. [32].

grooves on both the horizontal plates and sidewall. For $Ra > 2\times10^{12}$, $Nu(Ra)$ dependence was investigated for three different Pr, and γ value was reported as 0.5. Qui et al. [34] also obtained a change in γ value from 0.28 for the smooth walls to 0.35 in the rough surfaces. Xie and Xia [35] experimentally investigated the effect of roughness geometry on turbulent thermal convection in a cylindrical container. On the top and bottom plates, periodically distributed pyramid-shaped roughness elements were considered. Ra was covered in the range $7.5\times10^7 \leq Ra \leq 1.31\times10^{11}$, and Pr varied from 3.57 to 23.34. They considered a parameter λ, defined as the ratio of the height of a roughness element to its base width. Four values of λ (0.5, 1, 1.9, 4) were considered, and the obtained $Nu(Ra)$ scaling was classified into three regimes. In regime I, $Nu(Ra)$ scaling was not affected due to the rough surfaces. This regime was observed for $Ra < 4\times10^8$ where thermal boundary layer thickness was greater than roughness height. However, with an increase in Ra, roughness height became greater than the thermal boundary layer thickness, and enhancement of heat transport was observed in regime II and III, which were distinguished based on different $Nu(Ra)$ scaling. For $Pr = 4.34$, regime II was observed for $4\times10^8 \leq Ra \leq 4\times10^9$, while regime III for $Ra > 4\times10^9$. Increase of λ from 0.5 to 4 brought a change in γ from 0.36 to 0.59 in regime II and 0.3 to 0.5 in regime III. There was a transition from regime II to III,

where viscous boundary layer thickness eventually became smaller than the roughness height which was highlighted as the possible cause for different scalings in regimes II and III.

Wei et al. [36] studied the effect of individual plates on heat transfer by considering different combinations of rough/smooth surfaces. They found that the heat transport property of individual plate differs significantly with dependence on temperature boundary conditions and nature of the opposite plate. Results showed that smooth plates are insensitive to the terrain and temperature boundary condition of the opposite plate. On the other hand, rough plates are found to depend on both nature of the opposite plate and its temperature boundary condition. Tisserand et al. [37] introduced roughness (square plots) at the bottom plate, while top plate was kept smooth. Due to the asymmetry of the plates, temperature drop across the rough plate ($T_H - T_{bulk}$) and smooth plate ($T_{bulk} - T_C$) were different, which were then used to calculate the Nusselt number at the respective plates. Further, it was observed that the scaling exponent (γ) was $1/2$ and $1/3$ for rough and smooth plates, respectively. Various studies have addressed the effect of rough elements on the local dynamics of the turbulent RBC. Du and Tong [38] have shown that enhancement of heat transport is due to the interaction between the large-scale circulation and secondary flow formed inside the cavities of the roughness elements. This interaction enhances the detachment of the thermal boundary layer from the tips of the rough surfaces leading to increase in plume emission. Thus, the enhancement of heat transfer is due to the changed near-wall dynamics because of the rough surfaces.

Direct numerical simulations (DNS) also corroborate experimental findings that an increase in *Nu* scaling exponent is obtained in rough cells. Stringano et al. [40] performed DNS on a cylindrical container of aspect ratio $\Gamma = D/H = 1/2$ with grooves on the top and bottom plates. Rayleigh number covered was in the range $2 \times 10^6 \leq Ra \leq 2 \times 10^{11}$ with fixed Pr = 0.7. Above a threshold Rayleigh number Ra_{th}, scaling exponent γ for grooved surfaces increased from 0.31 to 0.37. Various studies on rough cells indicate that the heat transport maximizes on tuning the geometry of the roughness elements via choosing suitable height and wavelength of the roughness elements. Zhang et al. [32] performed 2D simulations for $10^7 \leq Ra \leq 10^{11}$ with constant Pr = 1, where they varied the height of the roughness elements (h) and wavelength was kept fixed as $2h$. This study highlighted that beyond a critical height (h_c) of the roughness elements, enhanced heat transport is perceived. Further, two regimes were identified using h_c. As shown in Fig. 1.5a, below a critical height h_c for a particular Ra, heat transport is reduced (first regime), and above h_c, enhancement in heat transport is obtained (second regime). Reduction of heat transport at roughness heights smaller than h_c is a result of the entrapment of the

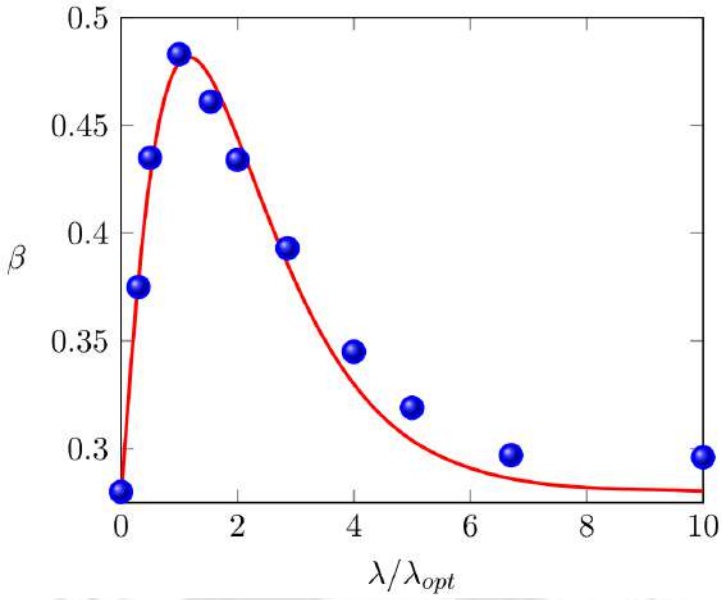

Figure 1.6: Scaling exponent β, in the relation $Nu - 1 = A \times Ra^{\beta}$, is shown as a function of roughness wavelength. Optimal Wavelength signifying maximum value of scaling exponent is $\lambda_{opt} = 0.1$. For $\lambda << \lambda_{opt}$ or $\lambda >> \lambda_{opt}$, planar wall case is retrieved. Figure reproduced from Toppaladoddi et al. [39].

fluid in the roughness facilitated cavities, which makes the bulk flow ineffective in mobilizing the trapped fluid. This accumulation of fluid inside the cavity makes the thermal boundary layer thicker, which causes the heat transfer to reduce. On increasing thermal forcing i.e., Ra, the critical height of the roughness elements follow a decreasing trend, as shown in Fig. 1.5b. It also implies that a certain height of the roughness elements, which decreases heat transfer at a low Ra, may enhance it at a higher Ra. Thus, the heat reduction regime becomes less pronounced at a higher Ra. Moreover, maximal relative enhancement of heat transfer is more for a higher Ra due to the stronger plume emissions.

Toppaladoddi et al. [39] studied two-dimensional RBC, where roughness elements were of sinusoidal shape on both the top and bottom plates with a fixed amplitude of $h = 0.1$. They performed simulations with fixed $Pr = 1$ and Ra in the range $4 \times 10^6 \leq Ra \leq 3 \times 10^9$. It was observed that varying wavelength of the roughness elements causes a change in heat transport, which implies that the scaling exponent of *Nu* depends on the wavelength of the roughness elements. Heat transport scaling exponent β, in the relation $Nu - 1 = A \times Ra^{\beta}$, was calculated from least-squares fit to the $Nu(Ra)$ as a function of wavelength λ of the roughness elements. Optimal wavelength λ_{opt} which yields maximum value of the scaling exponent β was found out as λ_{opt} = 0.1. For λ_{opt}, least-squares fit revealed heat transport scaling as $Nu - 1 = 0.0042 \times Ra^{0.483}$. As shown in Fig. 1.6, when $\lambda << \lambda_{opt}$ or $\lambda >> \lambda_{opt}$ scaling exponent β attains the planar

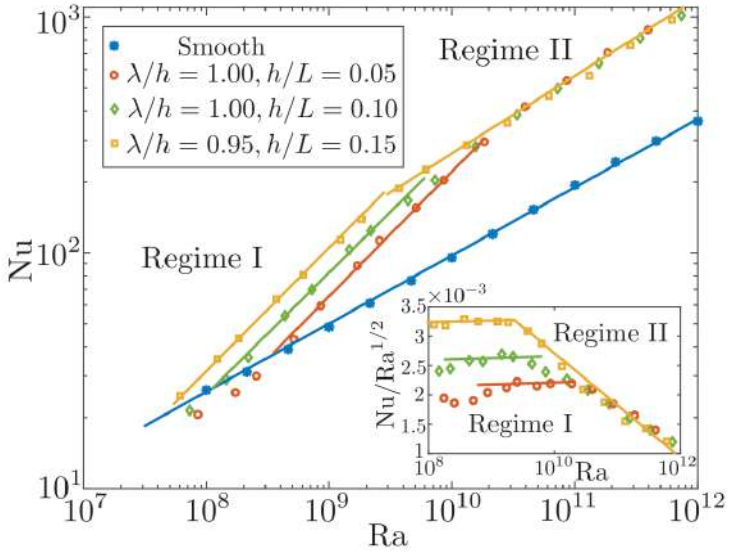

Figure 1.7: Variation of $Nu(Ra)$ for nearly unity aspect ratio of roughness elements ($\lambda/h \approx 1$) at different heights of the roughness elements. Two regimes are demarcated on the basis of *Nu* scaling with Ra ($Nu = ARa^{\gamma}$) when comparing with smooth wall case, where $\gamma = 0.29 \pm 0.01$. Regime I, where scaling exponent is $\gamma = 0.50 \pm 0.02$, and regime II, where $\gamma = 0.33 \pm 0.01$. L denotes height of the domain, whereas h and λ are the height and wavelength of the roughness elements, respectively. Figure reproduced from Zhu et al. [41].

wall value. They have also analyzed optimal wavelength, which characterized maximum heat transport at a particular Ra. As Nusselt number was a function of λ for a given Ra, the λ, for which *Nu* becomes maximum, was termed as optimal wavelength and corresponding *Nu* was termed as optimal Nusselt number Nu_{opt}. Least squares fit revealed $Nu_{opt}(Ra)$ scaling as $Nu - 1 = 0.01 \times Ra^{0.444}$, and variation of λ_{opt} with Ra revealed that for higher Ra (above 10^9), it settles at $\lambda_{opt} = 0.1$.

Zhu et al. [41] performed 2D simulations with sinusoidal roughness elements on both top and bottom plates for even higher Ra in the range $10^8 \leq Ra \leq 10^{12}$ with $Pr = 1$. Both height and wavelength of the roughness elements were manipulated to facilitate increased heat transport. As shown in Fig. 1.7, nearly unit aspect ratio of the roughness elements λ/h was taken for three different heights of the roughness elements. They chose a unit aspect ratio for roughness elements as it provided maximum *Nu* scaling exponent among different aspect ratios considered. Based on the *Nu* scaling with Ra, two regimes were identified. At lower Ra, the first regime, where local scaling exponent of *Nu* with Ra reached up to $1/2$, was observed. Higher the height of the roughness elements was, earlier the system stepped into the first regime. However, at higher Ra, the second regime, where scaling exponent saturated back to a value close to the

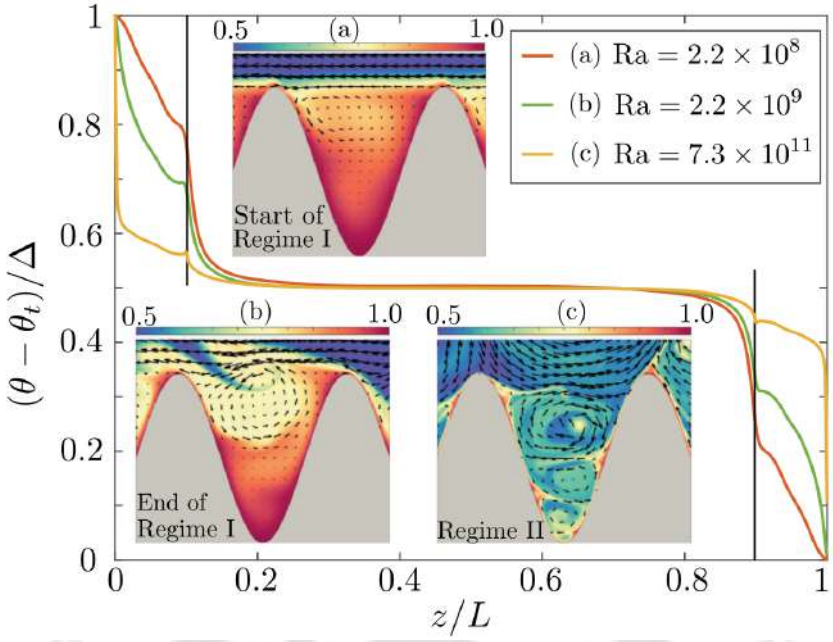

Figure 1.8: Variation of the mean dimensionless temperature in the vertical direction for unit aspect ratio ($\lambda/h = 1$) and h/L_y = 0.1 of sinusoidal rough surface at (a) the beginning of the regime I ($Ra = 2.2 \times 10^8$), (b) the end of the regime I ($Ra = 2.2 \times 10^9$), and (c) regime II ($Ra = 7.3 \times 10^{11}$). Here, Δ represent temperature difference between the top and bottom plates, and θ_t is the temperature of top plate. The inset shows secondary vortices in different regimes. In regime I, there is only one roll, whereas in regime II, multiple rolls are present. Two black vertical lines depict the vertical position of the tip of the roughness elements. Figure reproduced from Zhu et al. [41].

smooth wall case, was observed. In the second regime, the effect of roughness geometry was lost as *Nu* for different roughness geometries collapsed onto a single curve. Enhancement of the heat transport in the first regime was attributed to the protrusion of the roughness elements through the thermal boundary layer, which supposedly introduces perturbations in near-wall regions. In this regime, secondary vortices developed inside the cavities were weak and hence, viscosity still dominated the flow inside them, as shown in Fig. 1.8, which did not effect strong mixing of fluid inside the cavities. Reemergence of classical scaling in the second regime was explained with the fact that there was increased strength of the secondary vortices inside the cavities, which mixed the fluid efficiently inside them, leading to the formation of a cascade of smaller vortices. The stronger mixing inside the cavities led to the formation of a thin boundary layer uniformly covering the entire rough surface, which perfectly mimicked an enlarged wet surface area, and this whole process was explained as a reason why rough surfaces lost their effect in the second regime. To further distinguish both the regimes, variation of thermal dissipation

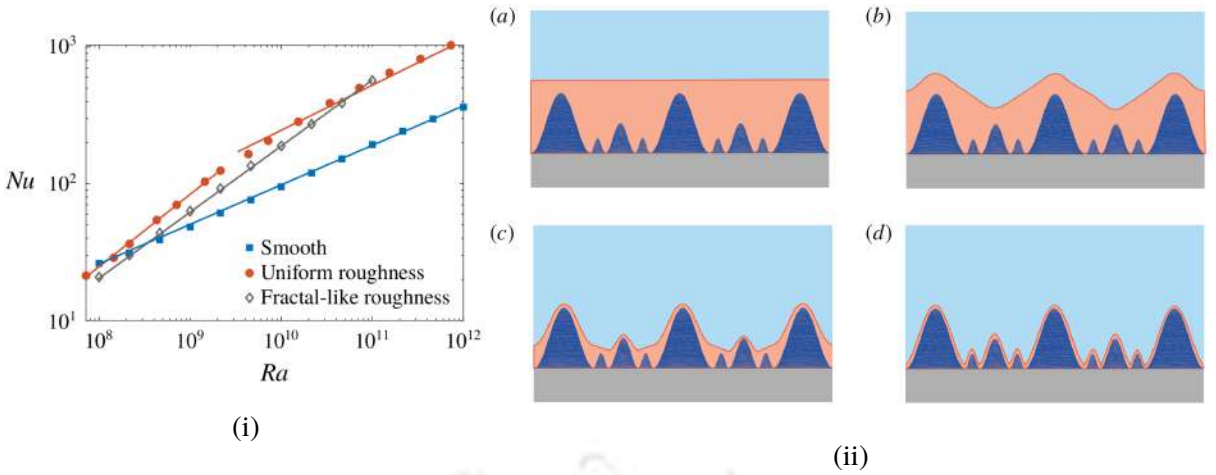

Figure 1.9: (i) Comparison of Nusselt number scaling with Ra for mono-scale roughness, multi-scale roughness and smooth wall case. Mono-scale roughness reference data taken from [41] with roughness height $h = 0.1$. Scaling exponent for the multi-scale roughness was 0.49±0.01 and saturation of the scaling exponent was not achieved. (ii) Schematic shows how multi-scale roughness delays the onset of saturated scaling regime, from (a) to (d) Ra number increases. Figures are reproduced from [42].

rate across the height of the container was observed. In the first regime, bulk contribution in the thermal dissipation dominated, while in the second regime, boundary layer contribution in the thermal dissipation dominated. This result is counterintuitive as one expects bulk contribution to dominate in thermal dissipation rate at a higher Ra, but in this study, boundary layer contributions dominated at higher Ra regime (second regime) and bulk contributions dominated at lower Ra regime (first regime). Thus, it was argued that roughness-facilitated scaling exponent of $1/2$ does not imply the onset of the ultimate regime. The regime I with $1/2$ scaling was recognized as a crossover zone, where bulk contributions dominated, and it was emphasized that the actual transition to the ultimate regime may only be achieved at an even higher Ra.

Zhu et al. [42], introduced multi-scale roughness of the sinusoidal form in two-dimensional RBC. Explored Ra range was $10^8 \leq Ra \leq 10^{11}$ with constant Pr = 1 for aspect ratio $\Gamma = L/H$ = 2. With three different distinct length scales of the roughness elements, obtained local $1/2$ scaling regime extended for a wider range of Ra, as shown in Fig. 1.9(i), and saturation of the local $1/2$ scaling was not observed for the explored range. To explain how they could manage to extend the $1/2$ scaling regime, it was hypothesized that with increasing Ra, as shown in Fig. 1.9(ii), different roughness length scales perturb the thermal BL in an order, starting from the largest (at low Ra) to the smallest (at high Ra), due to which the system stays in the local $1/2$ scaling range for a wider range of Ra. In Table 1.2, the main findings of the important roughness

studies are summarized.

Another fascinating avenue for studies on roughness driven convection is to incorporate the effects of Pr. The close connection of Pr in determining the TBL thickness has the potential to control the activating mechanism of roughness elements in enhancing the plume emission. In the next section, the role of Pr in roughness facilitated convection cell is discussed from the perspective of dominating flow structures and heat transport mechanism.

Table 1.2: Literature review of RBC with rough surfaces

Reference	**Cell and roughness geometry**	**Numerical details**	**Conclusions**
Du and Tong [38]	• Cylindrical cell • Γ = 1 and 0.5 • V-shaped grooves on both top and bottom surfaces • Two rough surfaces were considered with heights h = 9 and 3.2 mm, where wavelength for both cases was $\lambda = 2h$	• Experimental • $10^9 \leq Ra \leq 10^{11}$ • Working fluid is distilled water	• In the *Nu* scaling with Ra ($Nu \sim ARa^{\gamma}$), power law amplitude A increased by 76% • Interaction between the large-scale circulation and secondary flow inside the groove region enhances the detachment of the plumes near the tip of the roughness elements
Stringano *et al.* [40]	• Cylindrical cell • $\Gamma = D/H$ = 1/2 • V-shaped groove elements with a tip angle of 90°	• $2 \times 10^6 \leq Ra \leq 2 \times 10^{11}$ and $Pr = 0.7$ • Non-uniform mesh • Immersed boundary method used to solve governing equations with adiabatic side walls, and all surfaces were no-slip	• Value of scaling exponent γ obtained as 0.37 which reflects an increase of 19% from smooth cell • The presence of grooves not only enhanced plume generation but also their penetration into the bulk
Shishkina and Wagner [43]	• Rectangular cell (2D) with Γ =1 • Roughness elements are rectangular	• Numerical validation of the model developed to check the influence of wall roughness on heat transfer • $Ra = 10^7, 10^8$ and 5×10^7 with $Pr = 1$	• Nusselt number deviations for rough walls can not be solely quantified by the relative increase of area due to rough elements • Heat transport enhanced for slender roughness elements
Toppaladoddi *et al.* [39]	• Rectangular cell (2D) with $\Gamma = 2$ • Roughness elements geometry is sinusoidal	• $4 \times 10^6 \leq Ra \leq 3 \times 10^9$ and Pr= 1 • Lattice Boltzmann method used to solve the governing Boussinesq equations • Height of the roughness elements was fixed as h = 0.1	• At fixed height of the roughness elements, wavelength of the roughness elements can be tuned to get higher heat transport • *Nu* scaling with Ra for optimal wavelength is $(Nu - 1) \propto Ra^{0.483}$

continued ...

...continued

Reference	Cell and roughness geometry	Numerical details	Conclusions
Zhu *et al.* [41]	• Rectangular cell (2D) with Γ =2 • Sinusoidal roughness elements	• $10^8 \leq Ra \leq 10^{12}$ and $Pr = 1$ • Both h and λ of the roughness elements varied independently • h/L_y = 0.05, 0.1 and 0.15 • For each h, wavelength of roughness elements λ/L_y varied from 0.05 to 0.7 • For $Ra = 7.3 \times 10^{11}$, grid resolution is 14336×7168	• Two regimes were identified, regime I, where $Nu(Ra)$ scaling exponent γ increases up to $1/2$ and regime II, where γ saturates with value close to smooth wall case • In regime I, tuning of h and λ enhances $Nu(Ra)$ scaling exponent (γ), while in regime II, saturation of the γ is obtained • Higher the roughness, earlier the system steps in to regime I
Xie and Xia [35]	• Cylindrical cell • Pyramid shaped roughness elements	• Experimental • $7.5 \times 10^7 \leq Ra \leq 1.31 \times 10^{11}$ • $3.57 \leq Pr \leq 23.34$	• Regime I, for $Ra < 4 \times 10^8$, exhibited classical scaling • Beyond regime I, effect of roughness geometry, taken into account via different roughness aspect ratios (λ= 0.5 to 4), was conceived • In regime II (transitional regime), roughness height exceeded thermal boundary layer thickness, and showed an increase of γ from 0.36 to 0.59 with λ increasing from 0.5 to 4. • At further high Ra, regime III obtained, where even viscous boundary layer thickness was exceeded by roughness height, and γ increased from 0.30 to 0.50 with the increase in λ
Xu *et al.* [44]	• Rectangular cell (2D) • $\Gamma = L/H$ =1 • Roughness elements are rectangular fins	• $10^7 \leq Ra \leq 10^{10}$ • Spectral element method used for solving the governing equations • Effect of both Pr and number of fins on flow structures is observed	• In all roughness configurations, heat transport enhanced significantly when Ra exceeds a critical value • Presence of fins greatly influenced the flow structures and dynamics of plumes • For $Pr \geq 1$ and $Ra < 5 \times 10^8$ range, Nusselt number at a particular Ra increased monotonically with Pr
Zhang *et al.* [32]	• Rectangular cell (2D and 3D) • $\Gamma = 1$ (2D) • $H, L = 1, W = 1/4$ (3D) • Triangular roughness elements considered with height h, width $2h$, and Vertex angle = 90°	• $10^7 \leq Ra \leq 10^{11}$ (2D) • $Ra = 10^8$ (3D) • $Pr = 0.7$ • Immersed boundary method used to keep track of the roughness elements • Grid resolution for $Ra = 10^{11}$ is 2560×3456 and $Ra = 10^8$ (3D) is 512×128×624	• Identified a critical height h_c, above which heat transport enhanced and below which it reduced. • h_c decreased with Ra as $h_c \sim Ra^{-0.6}$ • Decrease of h_c with Ra also explained why heat reduction in rough cell was not observed in previous studies at high Ra

continued ...

...continued

Reference	Cell and roughness geometry	Numerical details	Conclusions
Jiang *et al.* [45]	• Rectangular 3D cell with $\Gamma(=L/H)=1$ • Roughness elements are ratchet shaped	• Both experimental and numerical • $Ra=5.7\times10^9$ and $Pr=4.3$ • For $Ra=5.7\times10^9$, grid resolution is $1280\times1280\times256$	• By introducing a small tilt of 3.2° in clockwise or anticlockwise direction, orientation of large-scale circulation was locked • With ratchet surfaces at the top and bottom plates, $Nu(Ra)$ scaling exponent γ increased from smooth cell (around 26%). However, for the two different tilt orientations, different scaling exponents were obtained, for one case γ was 0.38 and for other 0.39
Zhu *et al.* [42]	• Rectangular 2D cell with $\Gamma(=L/H)=2$ • Periodic sinusoidal roughness of three length scales	• $10^8\leq Ra\leq10^{11}$ and $Pr=1$ • For $Ra=10^{11}$, grid resolution is 10240×5120	• Usage of multi-scale roughness was shown to extend local $1/2$ scaling regime to an even higher Ra range.

1.4 Prandtl number effect in RBC

Prandtl number is one of the input control parameters in RBC that influence the global heat flux [19, 46, 47] along with the thermal forcing given by Ra and the cell aspect ratio Γ. It has a strong effect on the prevalent dominating flow structures and the heat transfer mechanism. Verzicco and Camussi [48] demarcated two types of flow regimes in their study inside a cylindrical cell covering $0.022\leq Pr\leq15$ for $Ra\leq2\times10^7$. The first regime was observed for $Pr\leq0.35$, where large-scale circulation dominates and is the major benefactor in vertical heat transfer. Owing to the remarkable contributions, LSC is considered as the "engine" for low Pr convection. Also, in this case, *Nu* was found to increase with Pr. The second regime was observed for $Pr>0.35$, where thermal plumes emerge as the major contributor in heat transfer and the role of large-scale circulation is largely diminished. Here, *Nu* becomes independent of Pr with the scaling exponent being $2/7$. In general, for low Pr fluids, a thicker thermal boundary layer is formed, due to which there is more tendency of diffusive heat transfer, and hence, fewer and weak plume structures are formed. However, with an increase in Pr, the thermal boundary layer becomes thinner, favoring the formation of a greater number of stronger and finer plumes.

Malevsky [49] also highlighted the influence of Pr by observing PDF of θ fluctuation along with its spectra. The PDFs, as shown in Fig. 1.10, exhibit exponential-like concave peaks for small-scale fluctuations, while large-scale fluctuations follow a wide Gaussian-like convex shirt. For high Pr flows, the central peaks of θ PDFs are more pronounced, implying a larger

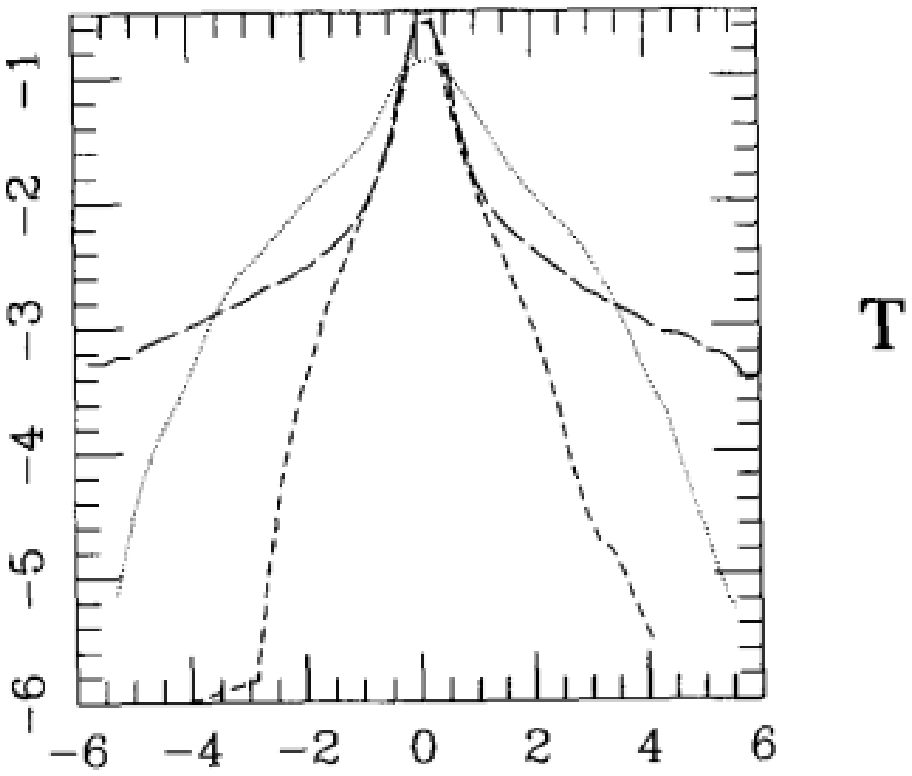

Figure 1.10: PDFs of normalized temperature fluctuations at the midplane for $Ra = 10^7$ at $Pr = 0.7$ (dotted line), $Pr = 7$ (short-dash line), and $Pr = \infty$ (long-dash line). Note, the figure is reproduced from Malevsky [49].

probability of the mean temperature. Also, it suggests thinning of the plumes along with the reduced occupied space by them. However, for low Pr, the increasing dominance of large-scale θ fluctuations with decreasing Pr is observed from the Gaussian-like skirt of the PDFs. Their observations are in line with that of Yakhot [51], Solomon and Gollub [52, 53], where the predominance of large-scale structures is credited in giving Gaussian shape to the PDFs while small-scale structures enforce the exponential shape. As discussed earlier, small Pr flows are dominated by LSC, which explains the Gaussian-like shape of the PDFs. However, high Pr flows are dominated by small-scale isolated thermal plumes, explaining the transformation of the PDFs into exponential. Effect of Pr was also investigated from the spectra of temperature fluctuations measured at different horizontal planes where they were found to be steeper with decreasing Pr. Another interesting feature discovered by Malevsky [49] is the increasing tendency of inverse kinetic energy transfer with the amplification of Pr. The same was manifested from the steeper kinetic energy spectra at higher Pr with the slope of the inertial subrange being close to -11/5 (BO59 scaling [54, 55]). In the literature, BO59 scaling has been shown to be

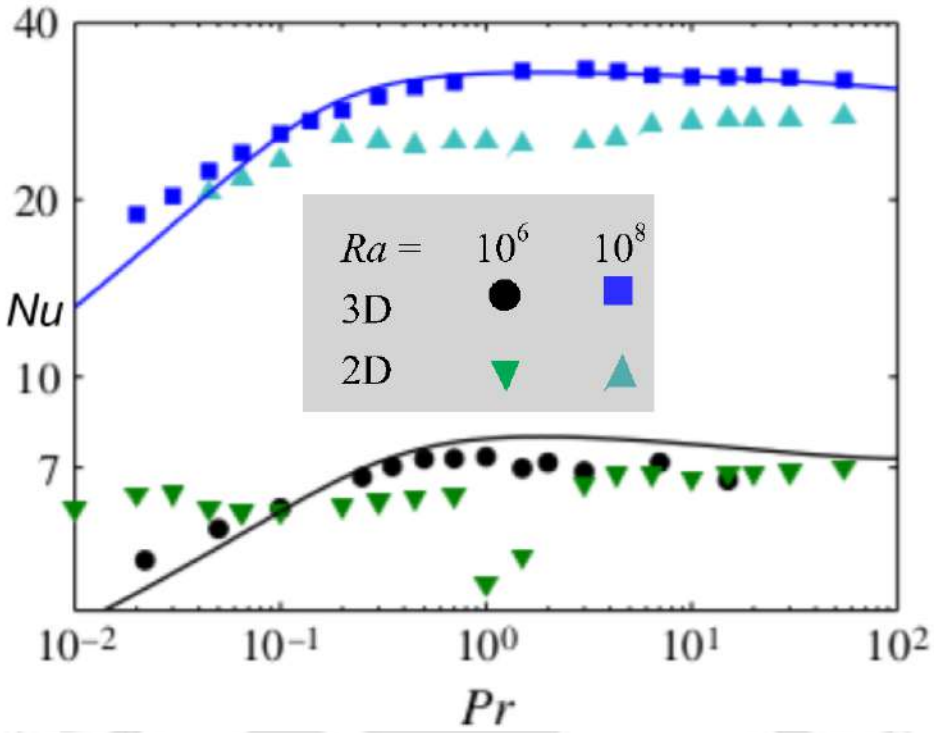

Figure 1.11: Comparison of $Nu(Pr)$ dependence in 2D and 3D cases for $Ra = 10^6$ and $Ra = 10^8$. Downward and upward filled triangles are for 2D cases, whereas square and black circles for the 3D cases, and solid lines represent the prediction of the GL theory. Note, the figure is reproduced from van der Poel *et al.* [50].

closely connected to inverse energy transfer [56, 57].

Huang and Zhou [58] in their 2D study reported anomalous $Nu(Pr)$ relation in comparison to a 3D cylindrical case for a moderate $Ra \leq 10^9$ and $Pr \approx 2 \sim 3$ range, where *Nu* settles for a minimum value rather than attaining maxima as in the 3D case. The reason for the anomaly was attributed to the competition between the corner rolls and LSC creating counter-gradient heat transport, which is a striking feature of 2D convection as the fluid lacks the third direction to escape. Further, heat transfer dependency on Pr was found to diminish with increasing Pr. At higher $Ra \geq 3 \times 10^9$, Pr dependency was qualitatively similar to that observed for the 3D case. van der Poel *et al.* [50] also highlighted the similar behavior of $Nu(Pr)$ in 2D and 3D cases for a large Pr. The same observation is evident from Fig. 1.11, where $Nu(Pr)$ dependence is shown for both 2D and 3D simulations at $Ra = 10^6$ and 10^8. For high Pr, *Nu* data for 2D and 3D cases seems to converge, especially for $Ra = 10^8$. The largest difference in *Nu* is seen at intermediate Pr, which is associated with the difference in LSC dynamics in 2D and 3D cases. In the 2D case, there is an emergence of a stronger LSC with corner rolls, whereas in the 3D case, LSC is less pronounced with smaller rolls. They also observed the Pr dependence

of the global Re, indicating flow strength, based on the rms of the vertical velocity. The flow strength was observed to be monotonically decreasing with growing Pr such that it is always higher for 2D than 3D. However, for a higher Pr, Re for both 2D and 3D converged, which again highlights similar behaviors in both the modes. For a fixed thermal forcing, elevated flow strength with decreasing Pr is a result of the augmented Grashof number ($Gr = Ra/Pr$) which indicates the relative strength of buoyancy over viscous force acting on a fluid. Pandey *et al.* [59] also reported the similarities between 2D and 3D for large Pr convection. On observing the first ten most dominant Fourier modes, close resemblances between 2D and 3D convection were revealed. Similar scaling for kinetic ($E_u(k) \sim k^{-13/3}$) and temperature spectra ($\sim k^{-2}$) further highlighted the behavior in both the cases to be alike. Effect of Pr on $Nu(Ra)$ scaling has also been reported for a rough cell by Xie and Xia [35], where for a larger Pr, higher heat transfer enhancement for roughness elements of larger aspect ratio is observed. The reason for the same was anticipated to be linked with the stronger clustering of thermal plumes.

Yang *et al.* [60] while working with a 2D square rough cell, observed the effect of Pr on the critical height (h_c) of the roughness elements above which an enhancement in heat transfer with respect to a smooth cell can be obtained. They explored $10^7 \leq Ra \leq 10^9$ and $0.01 \leq Pr \leq 100$, where $h_c(Pr)$ revealed three distinct regimes, as shown in Fig. 1.12. The regime at low Pr (shaded in yellow) dominated by LSC shows a decrement of h_c with increasing Pr. Here, the thermal boundary layer (TBL) is thicker, which obstructs the bulk fluid to wash out the fluid inside the roughness cavities. However, augmented Pr leads to thinning of TBL, facilitating disruption of TBL by the roughness elements, which leads to a decrease of h_c. Note, this regime exhibits weaker and fewer plumes due to the large thermal diffusivity of the fluid. The regime at moderate Pr (shaded in pink) exhibits an increasing trend of h_c with Pr. It is characterized by strong competition between the corner rolls and the LSC with the advent of thermal plumes. Here, as Pr increases, the strength and size of corner rolls grow, which introduces counter-gradient heat transport, ultimately leading to suppression of global *Nu*. In order to suppress the effect of corner-rolls, roughness elements of higher amplitudes are required, which explains the increment of h_c with Pr in this regime. Lastly, the regime at high Pr (shaded in cyan) is dominated by plumes with the weakening of large-scale flows due to higher fluid viscosity. Here, h_c is seen to decay with growing Pr. Thermal boundary layer being thinner allows roughness elements to cause perturbations in the near-wall region leading to the emission of stronger plumes capable of sustaining their thermal energy for a long time. The same is evident from Fig. 1.13, where for $Pr = 100$ fine plumes can be seen to erupt from the tips of the roughness elements

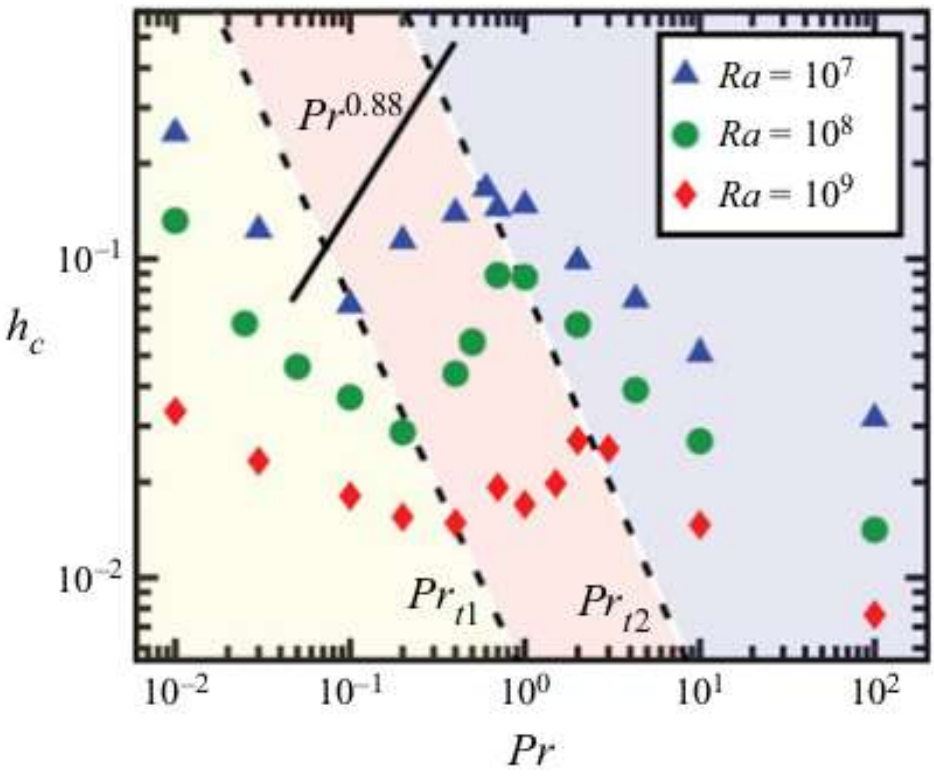

Figure 1.12: Variation of critical roughness height (h_c) as a function of Pr reveals three flow regimes (shaded in distinct colours), where Pr_{t1} and Pr_{t2} are the transitional Prandtl numbers. The low Pr regime is LSC dominated, the moderate Pr regime features strong corner-LSC competition, and the high Pr regime manifests domination by thermal plumes. The figure is adopted from Yang *et al.* [60].

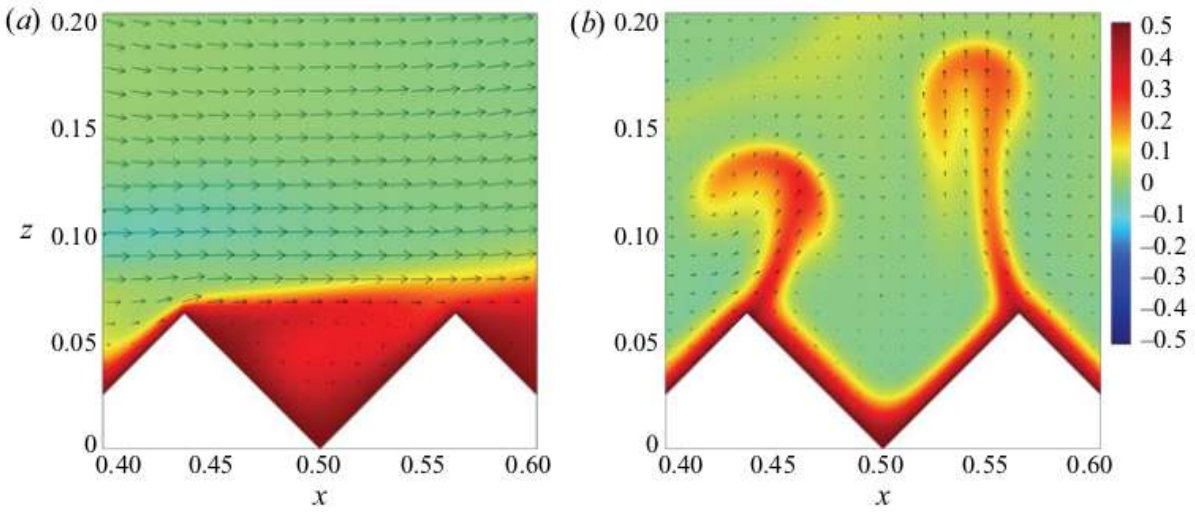

Figure 1.13: Snapshots of the instantaneous temperature field superimposed with velocity vector field shown by Yang *et al.* [60] for the central part of the lower plate at $Ra = 10^8$ for (a) $Pr = 1$ and (b) $Pr = 100$ with the amplitude of the rough plate being $h = 0.0625$.

as opposed to the $Pr = 1$ case. For $Pr = 1$, the cavity fluid is trapped with no significant contributions in plume emission. Thus, higher Pr flows present favorable conditions to trigger plume emission from the roughness elements, which strengthens the heat transport process. It also explains the decreasing trend of h_c in this regime.

1.5 Motivation and objectives

Consideration of rough surfaces in turbulent RBC is inevitable to enhance the understanding of thermal convection occurring in real-life flows. Further, they also seem promising in stimulating turbulence even at a lower Ra and thus, paving the path for realizing an efficient heat transfer mechanism. To date, the effect of only simplified roughness geometry has been explored, the most complex being sinusoidal roughness with three-length scales [42]. However, thermal convection in nature occurs over complex rough surfaces. Taking that into account, we have introduced a complex texture (both in 2D and 3D) that incorporates multiple length scales to emulate such real flow situations. The fascinating flow physics for RBC is revealed in the high Ra range, where flow is highly turbulent. The fact that realizing high Ra in 3D simulations is computationally prohibitive, a number of roughness studies are carried out in 2D in the literature. The choice of 2D simulations with roughness is justified by their ability to explain the dominating heat transfer mechanism and its implication on the *Nu* scaling exponent. For multi-scale triangular roughness, we explore a high Ra range in 2D simulations to test its efficacy in enhancing heat flux. Further, different regions close to the rough plates are explored to unravel the active flow mechanisms and their implication on the heat transfer rate.

In the case of a smooth convection cell, the Prandtl number is shown to have a negligible effect on the global heat transfer rate for moderate to high Pr. However, the study by Xie and Xia [35] argued that Pr might assume a proactive role in deciding the heat flux in the presence of rough surfaces. For the cylindrical cell with periodically distributed pyramid elements, they observed an interesting result where *Nu* corresponding to $Pr = 23.34$ exceeds that observed at a lower $Pr = 3.57$. The result is quite remarkable and unexpected, as in the case of the smooth case, *Nu* peaks around $Pr \sim 3$ to 4. However, the increment was only observed for the cases where the ratio of amplitude to width of the roughness elements was high ($h/\lambda = 1.9$ and 4). It further emphasizes the fact that it takes a specific combination of geometric parameters of the roughness elements to trigger Pr to play a dominant role in deciding the global heat transfer rate. Taking the motivation from this study, we decided to delve into exploring the combined

effect of Pr and the novel multi-scale roughnesses (2D and 3D) adopted in the present work. The main objectives of the present work are as follows:

1. To test the effectiveness of the employed novel multi-scale roughness for a higher Ra range in the 2D set-up.

2. Explore near-wall dynamics, which holds the key for the persistent realization of the enhanced *Nu* scaling exponent.

3. Understand bulk dynamics, sufficiently away from the walls, which holds close relationship with the perturbed near-wall regions

4. Distinguish the prevalent flow mechanisms between the rough and smooth cells.

5. Elucidate the role of Pr in influencing flow structures and heat transfer mechanism in the presence of the roughness for both 2D and 3D set-ups.

1.6 Outline of the thesis

The remainder of the thesis is organized as follows. In chapter 2, important relations in Rayleigh-Bénard convection are discussed. The discussion concerns the characteristic length scales in turbulent flows, Nusselt number calculations based on different measures, theoretical and numerical estimates of thermal and viscous dissipation rates, and the implication of different scalings assumed by structure functions. In chapter 3, the details of mathematical formulation, construction of roughness geometries, numerical procedure, grid generation and parallelization, diffuse interface immersed boundary method to handle rough surfaces, and validation of numerical setup are presented. Subsequently, in chapter 4, we study the effect of multi-scale roughness in 2D in sustaining the roughness facilitated enhanced heat transfer scaling exponent in the higher Ra range. The special focus is on understanding the near-wall regions to unveil the dominant flow mechanism in the throat, tip, and valley regions and its possible effect on the heat transfer rate. The changes brought up by the introduction of rough surfaces in the flow structures and statistics are also taken up by analyzing instantaneous temperature fields, plume statistics, turbulence kinetic energy budget, temporal PDFs and power spectra of temperature and vertical velocity, and orthogonal decomposition of the flow field.

In chapter 5, we incorporate the effect of the Prandtl number on the flow structures and heat transfer mechanism in the 2D roughness setup. Relation of global quantities, $Nu(Pr, Ra)$

and $Re(Pr, Ra)$, instantaneous flow fields, plume volume fractions, temperature and vertical velocity fluctuations, and boundary layer profiles are looked at to ascertain the role of Pr in a roughness facilitated convection cell. In chapter 6, with conical roughness elements on the isothermal plates of a cubical box, the Pr effect is considered for a fixed thermal forcing of $Ra = 10^8$. We observe $Nu(Pr)$ and $Re(Pr)$ relations, dominating heat transport mechanisms functioning at different Pr, role of roughness in disrupting the preferred orientation of the large-scale structures, plume statistics, and different statistical measures quantifying and describing the nature of fluctuations. Finally, we conclude the thesis and present some possible directions for future work in chapter 7.

2

IMPORTANT RELATIONS IN RAYLEIGH-BÉNARD CONVECTION

This chapter contains the details of the important results in Rayleigh-Bénard convection. We first introduce the important characteristic length scales in turbulent RBC, which is followed by a discussion on the theoretical framework for heat transport calculations, where relations for Nusselt number based on thermal and viscous dissipation rates are derived. Further, estimates of theoretical and numerical dissipation rates are presented, followed by a discussion on the Bolgiano scaling and the structure function relations which support its existence.

2.1 Characteristic scales

Turbulent motion exhibits a broad range of length scales, which characterize the size of the eddies. The largest length scales, which are bounded by the physical dimensions of the flow, extract energy from the mean flow. Due to the interaction among eddies at various scales, the energy from the large scales is transferred to successively smaller scales, and finally, at the smallest length scales where viscosity dominates, the energy is dissipated in the form of heat. This smallest length scale where viscous dissipation takes place is known as the Kolmogorov length scale (η). Similarly, for thermal dissipation, the smallest length scale is the Batchelor scale (η_B). Mathematically, these length scales are estimated as

$$\eta = \left(\frac{\nu^3}{\epsilon_u}\right)^{1/4}, \qquad \eta_B = \left(\frac{\nu\alpha^2}{\epsilon_u}\right)^{1/4},$$

where ϵ_u is the kinetic dissipation rate. Resolving the smallest length scales (Kolmogorov and Batchelor scales) is important to obtain accurate results from a turbulent flow simulation. For turbulent RBC, the theoretical estimate of global viscous dissipation is $\langle\epsilon_u\rangle_V = \nu^3(Nu - 1)RaPr^{-2}H^{-4}$[18] (derived later in section 2.3), where $\langle ...\rangle$ represents volume-average. On

substituting this value of ϵ_u in the above relations, one obtains

$$\frac{\eta}{H} = \frac{Pr^{1/2}}{(Nu-1)^{1/4}Ra^{1/4}}, \tag{2.1}$$

$$\frac{\eta_B}{H} = \frac{1}{(Nu-1)^{1/4}Ra^{1/4}} \tag{2.2}$$

From the above equations, it is clear that for $Pr < 1$, Kolmogorov scale η is the smallest dissipative scale, and when $Pr > 1$, Batchelor scale η_B is the smallest scale.

Other important length scales in RBC are the measure of viscous and thermal boundary layer thickness. Viscous boundary layer develops as a result of shearing of the large-scale circulation (LSC), while thermal boundary layer develops due to the presence of the walls offering thermal resistance to the heat transport. Near the top and bottom plates, conductive heat transport (q_{cond}) takes place which is given as

$$q_{cond} = \frac{k\Delta T}{H} \tag{2.3}$$

Since almost entire imposed temperature gradient is lost in the thermal boundary layers, total heat transport (q_{total}) can be written as,

$$q_{total} \approx \frac{k\Delta T}{2\lambda_\theta} \tag{2.4}$$

where λ_θ denotes thermal boundary layer thickness and k thermal conductivity. Now, Nusselt number is defined as the ratio of total heat flux to conductive heat flux. Thus, on using Eq. 2.3 and Eq. 2.4, Nusselt number (Nu) can be written as

$$Nu \approx \frac{H}{2\lambda_\theta} \tag{2.5}$$

or λ_θ can be written as

$$\lambda_\theta \approx \frac{H}{2Nu} \quad \Rightarrow \quad \frac{\lambda_\theta}{H} \approx \frac{1}{2Nu} \tag{2.6}$$

Since Nusselt number is a response parameter, thermal boundary layer thickness (λ_θ) cannot be known a priori. However, an estimate of λ_θ is possible if the value of the Nusselt number for the same input parameter range is available from the previous simulations. From Eq. 2.5, it is also clear that Nu and λ_θ are inversely proportional to each other.

2.2 Theoretical Framework for heat transport calculations

To get the estimates of global heat transport in Rayleigh-Bénard convection, calculation of Nusselt number is important. Constant property (density ρ, specific heat C_p and thermal conductivity

K) energy equation can be cast into the heat flux form as

$$\frac{\partial(\rho C_p T)}{\partial t} + \nabla \cdot (\rho C_p \boldsymbol{u} T) = k\nabla^2 T \tag{2.7}$$

$$\Rightarrow \quad \frac{\partial(\rho C_p T)}{\partial t} + \nabla \cdot (\rho C_p \boldsymbol{u} T - k\nabla T) = 0 \tag{2.8}$$

$$\Rightarrow \quad \frac{\partial(\rho C_p T)}{\partial t} + \nabla \cdot \boldsymbol{q} = 0 \tag{2.9}$$

where total heat flux which is sum of convective and conductive fluxes, is given by $\boldsymbol{q} = \rho C_p \boldsymbol{u} T - k\nabla T$ and velocity field $\boldsymbol{u} = (u, v, w)$. Considering heat transport in the vertical direction (z), Nusselt number being the ratio of convective and conductive heat fluxes can be estimated as

$$Nu = \frac{q_{conv}}{q_{cond}} = \frac{\rho C_p w T - k\frac{\partial T}{\partial z}}{-k(\frac{\partial T}{\partial z}_{cond})} = \frac{\rho C_p w T - k\frac{\partial T}{\partial z}}{k\frac{\Delta T}{H}} = \frac{wT - \alpha\frac{\partial T}{\partial z}}{\alpha\frac{\Delta T}{H}} \tag{2.10}$$

where ΔT is the temperature difference between the hot and cold plates ($\Delta T = T_H - T_C$) and H is the height of the container. Let us consider the domain (rectangular or cylindrical) over which governing equations for RBC are solved has volume V and bounding surface S. If ensemble is considered as Area-time average then average Nusselt number at any arbitrary vertical height (z) is obtained as

$$\langle Nu \rangle_{A,t} = \frac{\langle wT \rangle_{A,t} - \alpha\langle\frac{\partial T}{\partial z}\rangle_{A,t}}{\alpha\frac{\Delta T}{H}} \tag{2.11}$$

Now let us consider a slab of fluid confined between horizontal planes $z = z_1$ and $z = z_2$ which has volume $\mathcal{V}$ and bounding surface $\mathcal{S}$. For this fluid slab, after taking volume average of the energy equation (Eq. 2.9) one obtains

$$\frac{d}{dt}\left(\frac{1}{\mathcal{V}}\int_{\mathcal{V}} \rho C_p T dv\right) + \frac{1}{\mathcal{V}}\int_{\mathcal{V}} \nabla \cdot q dv = 0 \tag{2.12}$$

Under the assumption of steady state flow

$$\frac{d}{dt}\left(\frac{1}{\mathcal{V}}\int_{\mathcal{V}} \rho C_p T dv\right) = 0$$

and thus, Eq. 2.12 reduces to

$$\int_{\mathcal{V}} \nabla \cdot q dv = \int_{\mathcal{S}} q \cdot \hat{n} ds = 0 \tag{2.13}$$

Lateral walls do not contribute in the expression $\int_{\mathcal{S}} q \cdot \hat{n} ds$ and thus, one get

$$q(z_2) = q(z_1) \tag{2.14}$$

where $q(z_1)$ and $q(z_2)$ denotes the total heat flux over the horizontal planes $z = z_1$ and $z = z_2$, respectively. This also implies that under a steady state the total heat flux averaged over

horizontal planes are equal i.e., $\langle Nu \rangle_{A,t}$ is independent of z. Owing to no-slip velocity boundary condition at the top and bottom plates, there is no contribution from convective heat transfer in the total heat flux i.e.,$\langle wT \rangle_{A,t}$ = 0. Another consequence of the above arguments is that planar and volume averaged heat transport are equal under steady state flow assumption. This can be shown as

$$\langle Nu \rangle_{V,t} = \frac{1}{H} \int_0^H \langle Nu \rangle_{A,t} \, dz$$

but $\langle Nu \rangle_{A,t}$ is independant of z and thus,

$$\langle Nu \rangle_{V,t} = \frac{1}{H} \langle Nu \rangle_{A,t} \int_0^H dz = \langle Nu \rangle_{A,t} \tag{2.15}$$

Following the argument that total heat flux is independant of z, Nusselt number averaged over Area and time is obtained as

$$\langle Nu \rangle_{A,t} = \frac{\langle wT \rangle_{A,t} - \alpha \langle \frac{\partial T}{\partial z} \rangle_{A,t}}{\alpha \frac{\Delta T}{H}} = \frac{-H}{\Delta T} \left\langle \frac{\partial T}{\partial z} \right\rangle_{z=0,t} = \frac{-H}{\Delta T} \left\langle \frac{\partial T}{\partial z} \right\rangle_{z=H,t} \tag{2.16}$$

For Volume-time average ensemble, $\langle \cdots \rangle_{V,t}$ written as $\langle \cdots \rangle$, Nusselt number is obtained as

$$\langle Nu \rangle = \frac{\langle wT \rangle - \alpha \langle \frac{\partial T}{\partial z} \rangle}{\alpha \frac{\Delta T}{H}} \tag{2.17}$$

but

$$\left\langle \frac{\partial T}{\partial z} \right\rangle = \overline{\frac{1}{V} \int_V \frac{\partial T}{\partial z} dv} = \overline{\frac{1}{V} \int_V (\nabla T \cdot \hat{k} + T \nabla \cdot \hat{k}) dv} = \overline{\frac{1}{V} \int_V \nabla \cdot (T\hat{k}) dv}$$

where $\hat{k}$ is the unit vector in z direction and overbar denotes time averaging. Now using the divergence theorem

$$\overline{\frac{1}{V} \int_V \nabla \cdot (T\hat{k}) dv} = \overline{\frac{1}{V} \int_S T\hat{k} \cdot \hat{n} ds} = \overline{\frac{1}{V} \int_{z=0} -T_H ds} + \overline{\frac{1}{V} \int_{z=H} -T_C ds} = -\Delta T \left(\frac{A}{V} \right)$$

where A is the surface area of bottom (top) plate.

$$\Rightarrow \left\langle \frac{\partial T}{\partial z} \right\rangle = -\left(\frac{\Delta T}{H} \right) \tag{2.18}$$

On using the above result, one gets

$$\langle Nu \rangle = 1 + \frac{\langle wT \rangle}{\alpha \frac{\Delta T}{H}} \tag{2.19}$$

Now let us consider non-dimensional energy equation

$$\frac{\partial \theta}{\partial T} + \nabla \cdot (\boldsymbol{u}\theta) = \alpha_T \nabla^2 \theta \tag{2.20}$$

where $\theta = (T - T_C)/(T_H - T_C)$ is the normalized temperature having value 1 and 0 at bottom and top plates, respectively. Above equation can also be cast into heat flux form as

$$\frac{\partial \theta}{\partial T} + \nabla \cdot (\boldsymbol{u}\theta - \alpha_T \nabla \theta) = 0$$
$$\Rightarrow \quad \frac{\partial \theta}{\partial T} + \nabla \cdot \boldsymbol{q} = 0$$

where α_T depends on the choice of velocity scale. Thus, considering heat transport in vertical direction (z), *Nu* can be estimated as

$$Nu = \frac{q_{conv}}{q_{cond}} = \frac{w\theta - \alpha_T \frac{\partial \theta}{\partial z}}{-\alpha_T (\frac{\partial \theta}{\partial z}_{cond})} \tag{2.21}$$

In the conduction state, non-dimensional temperature θ varies linearly in vertical direction (z) as

$$\theta_{cond} = 1 - z \quad \Rightarrow \left(\frac{\partial \theta}{\partial z}_{cond}\right) = -1 \tag{2.22}$$

This implies

$$Nu = \frac{1}{\alpha_T}(w\theta) - \frac{\partial \theta}{\partial z} \tag{2.23}$$

If velocity scale is chosen as the diffusive velocity $V^r = \alpha/H$, then α_T = 1. Now let us consider a fluid particle of volume v subject to a density difference $\Delta\rho$ (buoyant force $\Delta\rho v g$) attains kinetic energy equivalent to $\Delta\rho v g H$ as it moves a height H. Thus, a velocity scale can be obtained as $\sqrt{\Delta\rho v g H/\rho v}$. Introducing the isobaric compressibility $\beta = -(1/\rho)(\partial\rho/\partial T)_p$, velocity scale is obtained as $V^r = \sqrt{\rho\beta\Delta T v g H/\rho v} = \sqrt{g\beta\Delta T H}$. Owing to its origin from buoyancy, this scale is termed as the "free fall velocity" and when used it results in $\alpha_T = \sqrt{1/(RaPr)}$. Thus, local heat transfer is obtained as

$$Nu = w\theta - \frac{\partial \theta}{\partial z} \qquad (V^r = \alpha/H) \tag{2.24}$$
$$Nu = \sqrt{RaPr}(w\theta) - \frac{\partial \theta}{\partial z} \qquad (V^r = \sqrt{g\beta\Delta T H}) \tag{2.25}$$

On considering ensemble as Area-time average, Nusselt number is obtained as

$$\langle Nu \rangle_{A,t} = \langle w\theta \rangle_{A,t} - \left\langle \frac{\partial \theta}{\partial z} \right\rangle_{A,t} \qquad (V^r = \alpha/H) \tag{2.26}$$
$$\langle Nu \rangle_{A,t} = \sqrt{RaPr}\langle w\theta \rangle_{A,t} - \left\langle \frac{\partial \theta}{\partial z} \right\rangle_{A,t} \qquad (V^r = \sqrt{g\beta\Delta T H}) \tag{2.27}$$

Further, on considering ensemble as Volume-time average, *Nu* can be written as

$$\langle Nu \rangle = \langle w\theta \rangle - \left\langle \frac{\partial \theta}{\partial z} \right\rangle \qquad (V^r = \alpha/H) \tag{2.28}$$
$$\langle Nu \rangle = \sqrt{RaPr}\langle w\theta \rangle - \left\langle \frac{\partial \theta}{\partial z} \right\rangle \qquad (V^r = \sqrt{g\beta\Delta T H}) \tag{2.29}$$

Now,

$$\left\langle \frac{\partial \theta}{\partial z} \right\rangle = \overline{\frac{1}{V}\int_V \frac{\partial \theta}{\partial z} dv} = \frac{1}{V}\left\{ \frac{\theta|_{z=1} - \theta|_{z=0}}{(z=1)-(z=0)} \right\} V = -1$$

This implies

$$\langle Nu \rangle = 1 + \langle w\theta \rangle \qquad (V^r = \alpha/H) \tag{2.30}$$

$$\langle Nu \rangle = 1 + \sqrt{RaPr}\langle w\theta \rangle \qquad (V^r = \sqrt{g\beta\Delta T H}) \tag{2.31}$$

where Rayleigh number $Ra = g\beta\Delta T H^3/\nu\alpha$ and Prandtl number $Pr = \nu/\alpha$.

2.2.1 Nusselt number based on thermal and viscous dissipation rates

The non-dimensional energy equation can be written as

$$\frac{\partial \theta}{\partial t} + \nabla \cdot (\boldsymbol{u}\theta) = \alpha_T \nabla^2 \theta \tag{2.32}$$

where $\alpha_T = 1$ or $(RaPr)^{-1/2}$ for $V^r = \alpha/H$ and $\sqrt{g\beta\Delta T H}$, respectively. Owing to the normalization $\theta|_{z=0} = 1$ and $\theta|_{z=1} = 0$ while $\nabla\theta \cdot \hat{n} = 0$ on lateral (vertical) walls due to adiabatic condition. Note, in case of periodic boundary condition, $\nabla\theta$ is same but $\hat{n}$ is opposite in sign. If the above equation is multiplied by θ and each term is simplified as $\theta\partial\theta/\partial t = \partial(1/2\theta^2)/\partial\theta$, $\theta\nabla\cdot(\boldsymbol{u}\theta) = \theta\boldsymbol{u}\cdot\nabla\theta = \boldsymbol{u}\cdot\nabla(1/2\theta^2) = \nabla\cdot(1/2\boldsymbol{u}\theta^2)$ and $\theta\nabla^2\theta = \theta\nabla\cdot(\nabla\theta) = \nabla\cdot(\theta\nabla\theta) - |\nabla\theta|^2$ one obtains the following form

$$\frac{\partial(\frac{1}{2}\theta^2)}{\partial t} + \nabla \cdot (\frac{1}{2}\boldsymbol{u}\theta^2) = \alpha_T\{\nabla \cdot (\theta\nabla\theta) - |\nabla\theta|^2\} \tag{2.33}$$

Integrating it over the volume V surrounded by the surface S gives

$$\frac{d}{dt}\int_V (\frac{1}{2}\theta^2) dv + \int_V \nabla \cdot (\frac{1}{2}\boldsymbol{u}\theta^2) dv = \alpha_T \left\{ \int_V \nabla \cdot (\theta\nabla\theta) dv - \int_V |\nabla\theta|^2 dv \right\} \tag{2.34}$$

as V does not change with t. Using the divergence theorem it further reduces to

$$\frac{d}{dt}\int_V (\frac{1}{2}\theta^2) dv + \int_S (\frac{1}{2}\boldsymbol{u}\theta^2) \cdot \hat{n} ds = \alpha_T \int_S (\theta\nabla\theta) \cdot \hat{n} ds - \alpha_T \int_V |\nabla\theta|^2 dv \tag{2.35}$$

Owing to $\boldsymbol{u} = 0$ on the no-slip walls and $\boldsymbol{u}\theta^2$ same but $\hat{n}$ opposite on periodic boundaries

$$\int_S (\frac{1}{2}\boldsymbol{u}\theta^2) \cdot \hat{n} ds = 0$$

Also on adiabatic wall $\nabla\theta \cdot \hat{n} = 0$ and on periodic walls $\nabla\theta$ is same but $\hat{n}$ being opposite, the first integral on the right hand side reduces to the surface integrals at top and bottom walls

$$\int_S (\theta\nabla\theta) \cdot \hat{n} ds = \theta|_{z=1} \int_{z=1} \frac{\partial\theta}{\partial z} ds - \theta|_{z=0} \int_{z=0} \frac{\partial\theta}{\partial z} ds = \int_{z=0} -\frac{\partial\theta}{\partial z} ds \tag{2.36}$$

as $\theta(z=0)=1$ and $\theta(z=1)=0$. Thus, Eq. 2.35 becomes

$$\frac{d}{dt}\int_V (\frac{1}{2}\theta^2)dv = -\alpha_T \int_{z=0} \frac{\partial\theta}{\partial z}ds - \alpha_T \int_V |\nabla\theta|^2 dv \tag{2.37}$$

Now multiply Eq. 2.32 by z and simplify the resulting terms as $z\partial\theta/\partial t = \partial(z\theta)\partial t$, $z\nabla\cdot(\boldsymbol{u}\theta) = \nabla\cdot(z\boldsymbol{u}\theta) - (\boldsymbol{u}\theta)\cdot\nabla z = \nabla\cdot(z\boldsymbol{u}\theta) - w\theta$ since $\nabla z = (0,0,1)$ and finally $z\nabla^2\theta = z\nabla\cdot(\nabla\theta) = \nabla\cdot(z\nabla\theta) - \nabla z\cdot\nabla\theta = \nabla\cdot(z\nabla\theta) - \partial\theta/\partial z$ to obtain

$$\frac{\partial(z\theta)}{\partial t} + \nabla\cdot(z\boldsymbol{u}\theta) - w\theta = \alpha_T\{\nabla\cdot(z\nabla\theta) - \frac{\partial\theta}{\partial z}\} \tag{2.38}$$

Integrating Eq. 2.38 over the volume V yields

$$\int_V \frac{\partial(z\theta)}{\partial t}dv + \int_V \nabla\cdot(z\boldsymbol{u}\theta)dv - \int_V w\theta dv = \alpha_T\left\{\int_V \nabla\cdot(z\nabla\theta)dv - \int_V \frac{\partial\theta}{\partial z}dv\right\} \tag{2.39}$$

According to the Leibiniz theorem, if we consider any function $f(x,t)$ such that both function and its partial derivatives $\partial_x f(x,t)$ are continuous in x and t, then,

$$\frac{d}{dx}\left(\int_{a(x)}^{b(x)} f(x,t)dt\right) = \int_{a(x)}^{b(x)} \frac{\partial f(x,t)}{\partial x}dt + f[x,b(x)]\frac{d\{b(x)\}}{dx} - f[x,a(x)]\frac{d\{a(x)\}}{dx}$$

If limits of integration are constant then the above rule reduces to

$$\frac{d}{dx}\left(\int_a^b f(x,t)dt\right) = \int_a^b \frac{\partial f(x,t)}{\partial x}dt$$

That is, integral and differential operators can interchange if limits of integration are constant. Here, volume of the domain V is constant which implies

$$\int_V \frac{\partial(z\theta)}{\partial t}dv = \frac{d}{dt}\int_V z\theta dv$$

On using the the the divergence theorem

$$\int_V \nabla\cdot(z\boldsymbol{u}\theta)dv = \int_S (z\boldsymbol{u}\theta)\cdot\hat{n}ds$$
$$\int_V \nabla\cdot(z\nabla\theta)dv = \int_S (z\nabla\theta)\cdot\hat{n}ds$$

By the virtue of no-slip boundary conditions on horizontal plates and no-slip/periodic boundary condition on lateral walls,

$$\int_S (z\boldsymbol{u}\theta)\cdot\hat{n}ds = 0$$

Now, S is a piece-wise continuous surface and owing to adiabatic or periodic boundary conditions $\nabla\theta\cdot\hat{n} = 0$ on the lateral walls. Thus, one obtains

$$\int_S (z\nabla\theta)\cdot\hat{n}ds = 1\int_{z=1}\frac{\partial\theta}{\partial z}ds - 0\int_{z=0}\frac{\partial\theta}{\partial z}ds = \int_{z=1}\frac{\partial\theta}{\partial z}ds$$

Thus, Eq. 2.39 reduces to

$$\frac{d}{dt}\int_V z\theta dv - \int_V w\theta dv = \alpha_T(\int_{z=1}\frac{\partial\theta}{\partial z}ds - \int_V \frac{\partial\theta}{\partial z}dv) \tag{2.40}$$

In addition, on integrating energy equation (Eq. 2.32) over the volume results in

$$\int_V \frac{\partial\theta}{\partial t}dv + \int_V \nabla\cdot(\boldsymbol{u}\theta)dv = \int_V \alpha_T\nabla^2\theta dv \tag{2.41}$$

For constant V,

$$\int_V \frac{\partial\theta}{\partial t}dv = \frac{d}{dt}\int_V \theta dv \quad \text{(using Leibiniz theorem)}$$

and on using the the divergence theorem

$$\int_V \nabla\cdot(\boldsymbol{u}\theta)dv = \int_S(\boldsymbol{u}\theta)\cdot\hat{n}ds$$
$$\int_V \alpha_T\nabla^2\theta dv = \alpha_T\int_S \nabla\theta\cdot\hat{n}ds$$

Thus, Eq. 2.41 reduces to

$$\frac{d}{dt}\int_V \theta dv + \int_S(\boldsymbol{u}\theta)\cdot\hat{n}ds = \alpha_T\int_S\nabla\theta\cdot\hat{n}ds \tag{2.42}$$

Owing to no-slip boundary conditions on horizontal plates and no-slip/periodic boundary condition on the lateral walls,

$$\int_S(\boldsymbol{u}\theta)\cdot\hat{n}ds = 0$$

Thus, Eq. 2.42 reduces to

$$\frac{d}{dt}\int_V\theta dv = -\alpha_T\int_{z=0}\frac{\partial\theta}{\partial z}ds + \alpha_T\int_{z=1}\frac{\partial\theta}{\partial z}ds \tag{2.43}$$

Adding Eq. 2.37 and Eq. 2.41 and subtracting from the above Eq. 2.43 results in

$$\frac{d}{dt}\int_V(\theta - \frac{1}{2}\theta^2 - z\theta)dv + \int_V w\theta dv = \alpha_T\int_V\frac{\partial\theta}{\partial z}dv + \alpha_T\int_V|\nabla\theta|^2dv \tag{2.44}$$

Now let u consider a bounded function $f(t)$ such that

$$|f(t)| \leq C < \infty$$

where C is any real constant. Time average of derivative of the bounded function $f(t)$ can be written as

$$\overline{\frac{df}{dt}} = \lim_{T\to\infty}\frac{1}{T}\int_t^{t+T}\frac{df(t')}{dt'}dt' = \lim_{T\to\infty}\frac{1}{T}(f(t+T) - f(t))$$

Maximum value of this function can be obtained as

$$max\{f(t+T) - f(t)\} = max\{f(t+T)\} - min\{f(t)\} = C - (-C) = 2C$$

Thus ,

$$\overline{\frac{df}{dt}} \leq \lim_{T\to\infty} \frac{2C}{T} = 0 \tag{2.45}$$

On taking time average of the Eq. 2.44, one gets

$$\overline{\frac{d}{dt}\int_V (\theta - \frac{1}{2}\theta^2 - z\theta)dv} + \overline{\int_V w\theta dv} = \alpha_T \overline{\int_V \frac{\partial\theta}{\partial z}dv} + \alpha_T \overline{\int_V |\nabla\theta|^2 dv} \tag{2.46}$$

where,

$$\overline{\frac{d}{dt}\int_V (\theta - \frac{1}{2}\theta^2 - z\theta)dv} = 0 \quad \text{(using the result from Eq. 2.45)}$$
$$\overline{\int_v \frac{\partial\theta}{\partial z}dv} = \overline{\frac{\theta|_{z=1} - \theta|_{z=0}}{(z=1)-(z=0)}V} = -V$$

$\partial\theta/\partial z$ when summed up over the volume reduces to the above as the intermediate values get cancelled out. Thus, Eq. 2.46 can be written as

$$\overline{\int_V w\theta dv} = \alpha_T\overline{(-V)} + \alpha_T \overline{\int_V |\nabla\theta|^2 dv} \tag{2.47}$$

Dividing by V on both sides of Eq. 2.47 gives

$$\frac{1}{V}\overline{\int_V w\theta dv} = \alpha_T(-1 + \frac{1}{V}\overline{\int_V |\nabla\theta|^2 dv}) \tag{2.48}$$
$$\langle w\theta\rangle = \alpha_T(-1 + \langle|\nabla\theta|^2\rangle) \tag{2.49}$$

If $V^r = \alpha/H$ then $\alpha_T = 1$ and $Nu = 1 + \langle w\theta\rangle$. Thus,

$$Nu = 1 - 1 + \langle|\nabla\theta|^2\rangle = \langle|\nabla\theta|^2\rangle \tag{2.50}$$

On the other hand, for $V^r = \sqrt{g\beta\Delta TH}$, $\alpha_T = (RaPr)^{\frac{-1}{2}}$ and $Nu = 1 + (RaPr)^{\frac{1}{2}}\langle w\theta\rangle$. Thus,

$$Nu = 1 + (RaPr)^{\frac{-1}{2}}(RaPr)^{\frac{1}{2}}(-1 + \langle|\nabla\theta|^2\rangle) = \langle|\nabla\theta|^2\rangle \tag{2.51}$$

Now consider the non-dimensional momentum equation

$$\frac{\partial \boldsymbol{u}}{\partial t} + \boldsymbol{u}\cdot\nabla(\boldsymbol{u}) = -\nabla P + \alpha_u\nabla^2\boldsymbol{u} + \alpha_b\theta\delta_{iZ} \tag{2.52}$$

Here, for $V^r = \alpha/H$, $\alpha_u = Pr$ and $\alpha_b = RaPr$ while $\alpha_u = (Pr/Ra)^{1/2}$ and $\alpha_b = 1$ for $V^r = \sqrt{g\beta\Delta TH}$, and δ is the kronecker delta. Above equation is contracted by $\boldsymbol{u}$ and first term of left hand side $\partial_t\boldsymbol{u}$ becomes,

$$\boldsymbol{u}\cdot\frac{\partial\boldsymbol{u}}{\partial t} = \frac{\partial(\frac{1}{2}U^2)}{\partial t}$$

where U is the magnitude of the velocity vector $\boldsymbol{u}$. Contraction of $\boldsymbol{u}\cdot\nabla\boldsymbol{u}$ is as follows

$$\boldsymbol{u}\cdot\{\boldsymbol{u}\cdot\nabla\boldsymbol{u}\} = u_i u_j\frac{\partial u_i}{\partial x_j} = \frac{\partial(u_i^2u_j)}{\partial x_j} - u_i\frac{\partial(u_iu_j)}{\partial x_j} = \frac{\partial(u_i^2u_j)}{\partial x_j} - u_i\left\{u_j\frac{\partial u_i}{\partial x_j} + \frac{\partial u_j}{\partial x_j}\right\}$$

But since $\dfrac{\partial u_j}{\partial x_j} = 0$,

$$u_iu_j\frac{\partial u_i}{\partial x_j} = \frac{\partial(u_i^2u_j)}{\partial x_j} - u_iu_j\frac{\partial u_i}{\partial x_j} \Rightarrow u_iu_j\frac{\partial u_i}{\partial x_j} = \frac{\partial(\frac{1}{2}u_i^2u_j)}{\partial x_j} \Rightarrow \boldsymbol{u}\cdot\{\boldsymbol{u}\cdot\nabla\boldsymbol{u}\} = \nabla\cdot(\frac{1}{2}U^2\boldsymbol{u})$$

∇P is contracted in the following manner

$$\boldsymbol{u}\cdot\nabla P = \nabla\cdot(\boldsymbol{u}p) - p\nabla\cdot\boldsymbol{u} = \nabla\cdot(\boldsymbol{u}p),$$

whereas for $\nabla^2\boldsymbol{u}$ following steps used

$$\boldsymbol{u}\cdot\nabla^2\boldsymbol{u} = u_i\frac{\partial^2u_i}{\partial x_k\partial x_k} = u_i\frac{\partial}{\partial x_k}(\frac{\partial u_i}{\partial x_k}) = \frac{\partial}{\partial x_k}(u_i\frac{\partial u_i}{\partial x_k}) - \frac{\partial u_i}{\partial x_k}\frac{\partial u_i}{\partial x_k} = \nabla\cdot(\boldsymbol{u}\cdot\nabla\boldsymbol{u}) - |\nabla\boldsymbol{u}|^2$$

and finally, $\alpha_b\theta\delta_{iz}$ after contraction follows

$$\boldsymbol{u}\cdot\alpha_b\theta\delta_{iz} = \alpha_bw\theta$$

Thus, the above equation simplifies to

$$\frac{\partial(\frac{1}{2}U^2\boldsymbol{u})}{\partial t} + \nabla\cdot(\frac{1}{2}U^2\boldsymbol{u}) = -\nabla\cdot(\boldsymbol{u}p) + \alpha_u\nabla\cdot(\boldsymbol{u}\cdot\nabla\boldsymbol{u}) - \alpha_u|\nabla\boldsymbol{u}|^2 + \alpha_bw\theta \tag{2.53}$$

Integrating the above equation over the entire volume V gives

$$\begin{aligned}\int_V\frac{\partial(\frac{1}{2}U^2\boldsymbol{u})}{\partial t}dv + \int_V\nabla\cdot(\frac{1}{2}U^2\boldsymbol{u})dv = &-\int_V\nabla\cdot(\boldsymbol{u}p)dv + \int_V\alpha_u\nabla\cdot(\boldsymbol{u}\cdot\nabla\boldsymbol{u})dv \\ &-\int_V\alpha_u|\nabla\boldsymbol{u}|^2dv + \int_V\alpha_bw\theta dv\end{aligned} \tag{2.54}$$

With the constant V and using the the divergence theorem we get

$$\begin{aligned}\frac{d}{dt}\int_V(\frac{1}{2}U^2)dv + \int_S(\frac{1}{2}U^2\boldsymbol{u})\cdot\hat{n}ds = &-\int_S(\boldsymbol{u}p)\cdot\hat{n}ds + \int_S\alpha_u(\boldsymbol{u}\cdot\nabla\boldsymbol{u})\cdot\hat{n}ds \\ &-\int_V\alpha_u|\nabla\boldsymbol{u}|^2dv + \int_V\alpha_bw\theta dv\end{aligned} \tag{2.55}$$

Owing to no-slip boundary conditions on horizontal plates and no-slip/periodic boundary condition on the lateral walls,

$$\int_S(\frac{1}{2}U^2\boldsymbol{u})\cdot\hat{n}ds = 0$$

$$\int_S(\boldsymbol{u}p)\cdot\hat{n}ds = 0$$

$$\int_S\alpha_u(\boldsymbol{u}\cdot\nabla\boldsymbol{u})\cdot\hat{n}ds = 0$$

Thus,

$$\frac{d}{dt}\int_V (\frac{1}{2}U^2)dv = -\int_V \alpha_u |\nabla \boldsymbol{u}|^2 dv + \int_V \alpha_b w\theta dv \tag{2.56}$$

Taking time average and subsequently dividing it by the volume results in

$$\overline{\frac{1}{V}\frac{d}{dt}\int_V (\frac{1}{2}U^2)dv} = \overline{-\frac{1}{V}\int_V \alpha_u |\nabla \boldsymbol{u}|^2 dv} + \overline{\frac{1}{V}\int_V \alpha_b w\theta dv} \tag{2.57}$$

However, using the result from Eq. 2.45

$$\overline{\frac{1}{V}\frac{d}{dt}\int_V (\frac{1}{2}U^2)dv} = 0$$

This implies,

$$\langle w\theta \rangle = \frac{\alpha_u}{\alpha_b}\langle |\nabla \boldsymbol{u}|^2 \rangle \tag{2.58}$$

For $V^r = \alpha/H, \alpha_u = Pr, \alpha_b = RaPr$, and from Eq. 2.30

$$\begin{aligned} \langle Nu \rangle &= 1 + \langle w\theta \rangle \\ \Rightarrow \langle Nu \rangle &= 1 + \frac{1}{Ra}\langle |\nabla \boldsymbol{u}|^2 \rangle \end{aligned} \tag{2.59}$$

On the other hand, for $V^r = \sqrt{g\beta\Delta T H}, \alpha_u = (Pr/Ra)^{1/2}, \alpha_b = 1$, and from Eq. 2.31

$$\begin{aligned} \langle Nu \rangle &= 1 + \sqrt{RaPr}\langle w\theta \rangle \\ \Rightarrow \langle Nu \rangle &= 1 + Pr\langle |\nabla \boldsymbol{u}|^2 \rangle \end{aligned} \tag{2.60}$$

2.3 Theoretical estimates of thermal and viscous dissipation

The dimensional governing equations for turbulent RBC are written as

$$\frac{\partial u_i}{\partial t} + \frac{\partial (u_i u_j)}{\partial x_j} = -\frac{\partial p}{\partial x_i} + \nu \frac{\partial^2 u_i}{\partial x_j \partial x_j} + \beta g (T - T_C)\delta_{iz} \tag{2.61}$$

$$\frac{\partial T}{\partial t} + u_j \frac{\partial T}{\partial x_j} = \alpha \frac{\partial^2 T}{\partial x_j \partial x_j} \tag{2.62}$$

$$\frac{\partial u_i}{\partial x_i} = 0 \tag{2.63}$$

When momentum equation is contracted by u_i it results in

$$\frac{\partial (\frac{1}{2}u_i u_i)}{\partial t} + \frac{\partial (\frac{1}{2}u_i u_i u_j)}{\partial x_j} = -\frac{\partial (p u_i)}{\partial x_i} + \nu \frac{\partial}{\partial x_j}\left(u_i \frac{\partial u_i}{\partial x_j}\right) - \nu \frac{\partial u_i}{\partial x_j}\frac{\partial u_i}{\partial x_j} + \beta g u_i (T - T_C)\delta_{iz}$$

After taking volume-time average of the above equation, one obtains

$$\begin{aligned} \left\langle \frac{\partial (\frac{1}{2}u_i u_i)}{\partial t} \right\rangle + \left\langle \frac{\partial (\frac{1}{2}u_i u_i u_j)}{\partial x_j} \right\rangle = &-\left\langle \frac{\partial (p u_i)}{\partial x_i} \right\rangle + \nu \left\langle \frac{\partial}{\partial x_j}\left(u_i \frac{\partial u_i}{\partial x_j}\right) \right\rangle \\ &- \nu \left\langle \frac{\partial u_i}{\partial x_j}\frac{\partial u_i}{\partial x_j} \right\rangle + \beta g \left\langle w(T - T_C) \right\rangle \end{aligned} \tag{2.64}$$

As volume V is constant, on applying Leibiniz theorem one obtains

$$\left\langle \frac{\partial(u_i u_i)}{\partial t} \right\rangle = \frac{d}{dt}\left\langle \frac{1}{2} u_i u_i \right\rangle$$

If flow is assumed to be in statistically stationary state then

$$\frac{d}{dt}\langle \cdot \rangle_{V,t} = 0.$$

This implies

$$\frac{d}{dt}\left\langle \frac{1}{2} u_i u_i \right\rangle = 0$$

According to the divergence theorem

$$\left\langle \frac{\partial(u_i u_i u_j)}{\partial x_j} \right\rangle = \overline{\frac{1}{V}\int_V \frac{\partial(u_i u_i u_j)}{\partial x_j} dv} = \overline{\frac{1}{V}\int_S u_i u_i u_j n_j ds}$$
$$-\left\langle \frac{\partial(p u_i)}{\partial x_i} \right\rangle = \overline{\frac{1}{V}\int_V \frac{\partial(p u_i)}{\partial x_i} dv} = \overline{\frac{1}{V}\int_S -p u_i n_i ds}$$
$$\left\langle \frac{\partial}{\partial x_j}\left(u_i \frac{\partial u_i}{\partial x_j} \right) \right\rangle = \overline{\frac{1}{V}\int_V \frac{\partial}{\partial x_j}\left(u_i \frac{\partial u_i}{\partial x_j} \right) dv} = \overline{\frac{1}{V}\int_S u_i \frac{\partial u_i}{\partial x_j} n_j ds}$$

Owing to no-slip boundary condition on horizontal walls and no-slip/periodic boundary on lateral walls

$$\overline{\frac{1}{V}\int_S u_i u_i u_j n_j ds} = 0, \ \overline{\frac{1}{V}\int_S -p u_i n_i ds} = 0, \text{ and } \overline{\frac{1}{V}\int_S u_i \frac{\partial u_i}{\partial x_j} n_j ds} = 0$$

Now Eq. 2.64 reduces to

$$\nu\langle |\nabla \boldsymbol{u}|^2 | \rangle = \beta g \langle w(T - T_C) \rangle \tag{2.65}$$

This implies

$$\langle \epsilon_u \rangle = \beta g \big\{ \langle wT \rangle - \langle wT_C \rangle \big\}$$

But it is known that $\langle w \rangle = 0$ and thus,

$$\langle \epsilon_u \rangle = \beta g \langle wT \rangle \tag{2.66}$$

Further,

$$\langle Nu \rangle = 1 + \frac{\langle wT \rangle}{\alpha \frac{\Delta T}{H}}$$
$$\Rightarrow \langle wT \rangle = \big\{ \langle Nu \rangle - 1 \big\} \alpha \frac{\Delta T}{H}$$

Now on putting this value in Eq. 2.66 we get

$$\langle \epsilon_u \rangle = \beta g \alpha \frac{\Delta T}{H} \big\{ \langle Nu \rangle - 1 \big\}$$

After further simplification,

$$\langle \epsilon_u \rangle = \frac{\nu^3}{H^4}(Nu - 1)RaPr^{-2} \tag{2.67}$$

where *Nu* represents global heat transport and is equal to $\langle Nu \rangle_{V,t}$ or $\langle Nu \rangle_{A,t}$. Now let us consider dimensional energy equation

$$\frac{\partial T}{\partial t} + u_j \frac{\partial T}{\partial x_j} = \alpha \frac{\partial^2 T}{\partial x_j \partial x_j}$$

On contracting the above equation with temperature T

$$\begin{aligned} &\frac{\partial(\frac{1}{2}T^2)}{\partial t} + u_j \frac{\partial(\frac{1}{2}T^2)}{\partial x_j} = \alpha T \frac{\partial^2 T}{\partial x_j \partial x_j} \\ \Rightarrow\ &\frac{\partial(\frac{1}{2}T^2)}{\partial t} + \frac{\partial(\frac{1}{2}T^2 u_j)}{\partial x_j} = \alpha \left\{ \frac{\partial}{\partial x_j}\left(T \frac{\partial T}{\partial x_j} \right) - \frac{\partial T}{\partial x_j}\frac{\partial T}{\partial x_j} \right\} \end{aligned} \tag{2.68}$$

On taking volume-time average of the above equation, we get

$$\frac{d}{dt}\left\langle \frac{1}{2}T^2 \right\rangle + \left\langle \frac{\partial(\frac{1}{2}T^2 u_j)}{\partial x_j} \right\rangle = \alpha \left\{ \left\langle \frac{\partial}{\partial x_j}\left(T \frac{\partial T}{\partial x_j} \right) \right\rangle - \left\langle \frac{\partial T}{\partial x_j}\frac{\partial T}{\partial x_j} \right\rangle \right\} \tag{2.69}$$

Now due to assumption of statistically stationary state

$$\frac{d}{dt}\left\langle \frac{1}{2}T^2 \right\rangle = 0$$

After applying the divergence theorem and invoking no-slip boundaries on horizontal walls, and no-slip/periodic boundaries on lateral walls

$$\left\langle \frac{\partial(\frac{1}{2}T^2 u_j)}{\partial x_j} \right\rangle = \overline{\frac{1}{V}\int_V \frac{\partial(\frac{1}{2}T^2 u_j)}{\partial x_j} dv} = \overline{\frac{1}{V}\int_S \frac{1}{2}T^2 u_j n_j ds} = 0$$

Now Eq. 2.69 reduces to

$$\alpha \langle |\Delta T|^2 \rangle = \alpha \left\langle \frac{\partial}{\partial x_j}\left(T \frac{\partial T}{\partial x_j} \right) \right\rangle \tag{2.70}$$

This implies

$$\langle \epsilon_T \rangle = \overline{\frac{\alpha}{V}\int_V \frac{\partial}{\partial x_j}\left(T \frac{\partial T}{\partial x_j} \right) dv} = \overline{\frac{\alpha}{V}\int_S T \frac{\partial T}{\partial x_j} n_j ds} \tag{2.71}$$

Now S is a piecewise continuous surface and net contribution of lateral walls in the above expression is zero. This implies

$$\langle \epsilon_T \rangle = \frac{\alpha}{V} A \left\{ -T_H \left\langle \frac{\partial T}{\partial z} \right\rangle_{z=0,t} + T_C \left\langle \frac{\partial T}{\partial z} \right\rangle_{z=H,t} \right\} \tag{2.72}$$

where A is the surface area of top (bottom) wall. It is known that area-time averaged Nusselt number over any horizontal plane is same and thus,

$$\langle Nu \rangle_{A,t} = \frac{\langle wT \rangle_{A,t} - \alpha \langle \frac{\partial T}{\partial z} \rangle_{A,t}}{\alpha \frac{\Delta T}{H}} = \frac{-H}{\Delta T}\left\langle \frac{\partial T}{\partial z} \right\rangle_{z=0,t} = \frac{-H}{\Delta T}\left\langle \frac{\partial T}{\partial z} \right\rangle_{z=H,t}$$

This implies

$$\left\langle \frac{\partial T}{\partial z} \right\rangle_{z=0,t} = \left\langle \frac{\partial T}{\partial z} \right\rangle_{z=H,t} = -Nu\left(\frac{\Delta T}{H}\right)$$

On using the above result, Eq. 2.72 becomes

$$\begin{aligned} \langle \epsilon_T \rangle &= \frac{\alpha}{H}(Nu\, T_H - Nu\, T_C)\frac{\Delta T}{H} \\ \Rightarrow \langle \epsilon_T \rangle &= \alpha\left(\frac{\Delta T}{H}\right)^2 Nu \end{aligned} \tag{2.73}$$

2.4 Dissipation rates calculations

Dissipation rates of kinetic and thermal energy are estimated numerically as

$$\langle \epsilon_u \rangle = \nu \langle |\nabla \boldsymbol{u}|^2 \rangle \tag{2.74}$$

$$\langle \epsilon_T \rangle = \nu \langle |\nabla T|^2 \rangle \tag{2.75}$$

while theoretical estimates [18] (discussed in Section 2.3) are given as

$$\langle \epsilon_u^{Th} \rangle = \nu^3 H^{-4}(Nu - 1)RaPr^{-2} \tag{2.76}$$

$$\langle \epsilon_T^{Th} \rangle = \alpha(\Delta T)^2 Nu H^{-2} \tag{2.77}$$

Comparison of numerical and theoretical estimates of ϵ_u and ϵ_θ provides information of spatial resolution of the simulations. Non-dimensionalizing the numerical estimate of ϵ_u,

$$\begin{aligned} \langle \epsilon_u \rangle &= \nu \langle |\nabla \boldsymbol{u}|^2 \rangle \\ \langle \epsilon_u \rangle &= \frac{\nu (V^r)^2}{H^2} \langle |\nabla \boldsymbol{u}^*|^2 \rangle \end{aligned}$$

If velocity scale is chosen as $V^r = \sqrt{\beta g \Delta T H}$ then

$$\frac{HV^r}{\nu} = \sqrt{\frac{Ra}{Pr}}$$

which implies

$$\langle \epsilon_u \rangle = \frac{(V^r)^3}{H}\sqrt{\frac{Pr}{Ra}} \langle |\nabla \boldsymbol{u}^*|^2 \rangle$$

But $(V^r)^3/H$ is the dimensional scale of viscous dissipation rate and thus, non-dimensional kinetic energy dissipation is obtained as

$$\langle \epsilon_u^* \rangle = \sqrt{\frac{Pr}{Ra}} \langle |\nabla \boldsymbol{u}^*|^2 \rangle \tag{2.78}$$

Numerical estimate of ϵ_T can be non-dimensionalized as

$$\langle \epsilon_T \rangle = \alpha \langle |\nabla T|^2 \rangle \tag{2.79}$$

$$\langle \epsilon_T \rangle = \alpha \frac{\Delta T^2}{H^2} \langle |\nabla \theta|^2 \rangle \tag{2.80}$$

As $(HV^r)/\alpha = \sqrt{RaPr}$ for free fall velocity scale,

$$\langle \epsilon_T \rangle = \frac{\Delta T^2 V^r}{H} \frac{1}{\sqrt{RaPr}} \langle |\nabla \theta|^2 \rangle$$

But since $(\Delta T^2 V^r)/H$ represents dimensional scale of thermal dissipation rate, non-dimensionalized thermal dissipation can be written as

$$\langle \epsilon_\theta \rangle = \frac{1}{\sqrt{RaPr}} \langle |\nabla \theta|^2 \rangle \tag{2.81}$$

Similarly, non-dimensionalized theoretical estimates of dissipation rates are obtained as

$$\langle \epsilon_u^{*Th} \rangle = \frac{(Nu - 1)}{\sqrt{RaPr}} \tag{2.82}$$

$$\langle \epsilon_\theta^{Th} \rangle = \frac{Nu}{\sqrt{RaPr}} \tag{2.83}$$

Thus, the ratio of the numerical to theoretical estimates of the non-dimensionalized dissipation rates is

$$\frac{\langle \epsilon_u^* \rangle}{\langle \epsilon_u^{*Th} \rangle} = \frac{\langle |\nabla \boldsymbol{u}^*|^2 \rangle Pr}{(Nu - 1)} \tag{2.84}$$

$$\frac{\langle \epsilon_\theta \rangle}{\langle \epsilon_\theta^{Th} \rangle} = \frac{\langle |\nabla \theta|^2 \rangle}{Nu} \tag{2.85}$$

To check for spatial resolution, $\langle \epsilon_u \rangle$ and $\langle \epsilon_\theta \rangle$ are calculated at different mesh sizes and are compared with the theoretical estimates. Stevens et al. [61] observed that for fully resolved simulations the thermal dissipation rates are higher and for under-resolved simulations the gradients are smeared out and thus $\langle \epsilon_u \rangle$ and $\langle \epsilon_\theta \rangle$ are underestimated.

2.5 Bolgiano scaling

In turbulent thermal convection, scaling of the velocity and temperature fluctuations in the inertial range is of immense importance as it reveals the nature of the flow and also provides the physical picture explaining energy cascade. From literature, it is known that for homogenous and isotropic thermal convection, temperature acts as a passive scalar and small scale fluctuations follow Kolmogorov (1941) scaling [62] where dominant energy balance is between the

kinetic energy transfer and viscous dissipation, whereas for anisotropic flow, temperature acts as an active scalar and Bolgiano scaling [63] is expected where dominant balance is between the kinetic energy and buoyant production. Yakhot [64] has given the following expressions

$$\langle \delta v_{//}(r)^3 \rangle = \frac{-4}{5}\epsilon_u r + \frac{2\beta g}{r^4}\int_0^r r'^4 \langle \delta T(r')\delta v_{//}(r')\rangle dr' + 6\nu \frac{\partial}{\partial r}\langle \delta v(r)^2 \rangle \tag{2.86}$$

$$\langle \delta v_{//}(r)\delta T(r)^2 \rangle = \frac{-4}{3}\epsilon_\theta r + \frac{2}{r^2}\int_0^r y^2 \langle \delta T(y)\delta v_z(y)\rangle dy \frac{\partial \theta}{\partial z} + 6\alpha \frac{\partial}{\partial r}\langle \delta T(r)^2 \rangle \tag{2.87}$$

where ϵ_u and ϵ_θ are the mean rate of energy dissipation and temperature dissipation, respectively, whereas $\delta v_{//}(r)$ and $\delta T(r)$ are the velocity and temperature fluctuations, respectively, which are defined as

$$\delta v_{//}(r) = \left[\boldsymbol{v}(\boldsymbol{x}+\boldsymbol{r}) - \boldsymbol{v}(\boldsymbol{x})\right].\boldsymbol{r}$$

$$\delta T(r) = T(x+r) - T(x)$$

First-term on the right-hand side of the Eq. 2.86 and Eq. 2.87 contribute to the homogeneous and isotropic behavior of the flow. However, the second term contribute to the anisotropic behavior of the flow. Hence, Eq. 2.86 and Eq. 2.87 act as a useful guideline to distinguish the flow, whether it is homogeneous and isotropic, or anisotropic. If one neglects the intermittency effects from Eq. 2.87, a scaling relation is obtained as

$$\delta v(r)\delta T(r)^2 \simeq \epsilon_\theta r \tag{2.88}$$

In Eq. 2.86, depending on whether the first or second-term on the right-hand side dominates, two different regimes are unveiled. For the latter case, the following balance is obtained

$$\delta v^3(r) \sim \beta g \delta T(r)\delta v(r)\, r \tag{2.89}$$

Now, using Eq. 2.88 one obtains

$$\delta v^2(r) \sim \beta g r \delta T(r) \simeq \beta g r \left(\frac{\epsilon_\theta r}{\delta v(r)}\right)^{1/2} \tag{2.90}$$

Further, Eq. 2.90 can be rephrased as

$$\begin{aligned} \delta v(r)^{5/2} &\simeq \beta g r (\epsilon_\theta r)^{1/2} \\ \implies \delta v &\simeq (\beta g)^{2/5}\epsilon_\theta^{1/5} r^{3/5} \end{aligned} \tag{2.91}$$

Using the result of Eq. 2.91, and putting it in Eq. 2.88, one obtains temperature fluctuations scaling in the following manner

$$\delta T(r) \simeq \left(\frac{\epsilon_\theta\, r}{\delta v(r)}\right)^{1/2} \implies \delta T(r) \simeq \left(\frac{\epsilon_\theta\, r}{(\beta g)^{2/5}\epsilon_\theta^{1/5} r^{3/5}}\right)^{1/2} \simeq (\beta g)^{-1/5}\epsilon_\theta^{2/5}\, r^{1/5}$$

Hence, one gets

$$\delta T(r) \simeq (\beta g)^{-1/5} \epsilon_\theta^{2/5}\, r^{1/5} \tag{2.92}$$

The scaling represented by the Eq. 2.91 and Eq. 2.92 is termed as Bolgiano scaling. Using the Bolgiano scaling, the second term of the right-hand side of Eq. 2.86 can be written as

$$\begin{aligned}
\frac{2\beta g}{r^4}\int_0^r r'^4 \langle \delta T(r')\delta v_{//}(r')\rangle dr' &\simeq \beta g \delta T(r)\delta v(r)\, r \\
&\simeq (\beta g)\left\{(\beta g)^{-1/5}\epsilon_\theta^{2/5}\, r^{1/5}\right\}\left\{(\beta g)^{2/5}\epsilon_\theta^{1/5} r^{3/5}\right\} r \\
\implies \frac{2\beta g}{r^4}\int_0^r r'^4 \langle \delta T(r')\delta v_{//}(r')\rangle dr' &\simeq (\beta g)^{6/5}\epsilon_\theta^{3/5} r^{9/5}
\end{aligned} \tag{2.93}$$

Now, we know that the Bolgiano scaling exists when the second term of the right-hand side in Eq. 2.86 dominates over the first term, which gives a consistency condition in terms of the scale $r = L_B$. Now for Bolgiano scaling to exist

$$(\beta g)^{6/5}\epsilon_\theta^{3/5} L_B^{9/5} > \epsilon\, L_B \tag{2.94}$$

This gives

$$L_B \equiv \frac{\epsilon^{5/4}}{\epsilon_\theta^{3/4}(\beta g)^{3/2}} \tag{2.95}$$

where L_B is the Bolgiano length scale. For $r < L_B$, the scaling is obtained as

$$\delta v(r) \simeq \epsilon_u^{1/3} r^{1/3} \tag{2.96}$$

$$\delta T(r) \simeq \epsilon_\theta^{1/2}\epsilon_u^{-1/6} r^{1/3} \tag{2.97}$$

where Eq. 2.96 represents the Kolmogorov (1941) scaling and Eq. 2.97 is the scaling of a passive scalar. Further, global Bolgiano length scale can be obtained on using theoretical estimates of global kinetic and thermal energy dissipation rates [18] as follows

$$\begin{aligned}
\langle \epsilon_T \rangle_V &= \alpha\left(\frac{\Delta T}{H}\right)^2 Nu \\
\langle \epsilon_u \rangle_V &= \nu^3 H^{-4} Pr^{-2} Ra(Nu - 1) \\
\implies L_{B,global} &= \left\{\nu^3 H^{-4} Pr^{-2} Ra(Nu-1)\right\}^{5/4}\left\{\alpha\left(\frac{\Delta T}{H}\right)^2 Nu\right\}^{-3/4}(\beta g)^{-3/2} \\
&= (Nu-1)^{5/4} Nu^{-3/4} Ra^{5/4} Pr^{-5/2}\left\{\alpha\left(\frac{\Delta T}{H}\right)^2\right\}^{-3/4}(\beta g)^{-3/2}\left(\frac{\nu^3}{H^4}\right)^{5/4}
\end{aligned}$$

On further solving, one gets

$$L_{B,global} = (Nu-1)^{5/4} Nu^{-3/4} (RaPr)^{-1/4} \tag{2.98}$$

which is a theoretical estimate to calculate the global Bolgiano length scale. Numerical estimate of the Bolgiano length in non-dimensionalized form can be obtained as follows

$$L_B = \left\{\nu\langle|\nabla \boldsymbol{u}|^2\rangle\right\}^{5/4}\left\{\alpha\langle|\nabla T|^2\rangle\right\}^{-3/4}(\beta g)^{-3/2}$$

Now, the velocity $\boldsymbol{u}$ is normalized by $V_r = \sqrt{\beta g \Delta T H}$, and temperature T is normalized by $\theta = (T - T_C)/(T_H - T_C)$. This leads to

$$L_B = \nu^{5/4}\left(\frac{V_r}{H}\right)^{5/2}\alpha^{-3/4}\left(\frac{\Delta T}{H}\right)^{-3/2}(\beta g)^{-3/2}\langle|\nabla \boldsymbol{u^*}|^2\rangle^{5/4}\langle|\nabla\theta|^2\rangle^{-3/4}$$

On solving further, one gets

$$L_B^* = \frac{L_B}{H} = PrRa^{-1/4}\frac{\langle|\nabla \boldsymbol{u^*}|^2\rangle^{5/4}}{\langle|\nabla\theta|^2\rangle^{3/4}} \tag{2.99}$$

Now, non-dimensionalized numerical estimates of thermal and viscous dissipation rates (for free fall velocity scale $V_r = \sqrt{\beta g \Delta T H}$) are already known as

$$\langle\epsilon_u^*\rangle = \sqrt{\frac{Pr}{Ra}}\langle|\nabla u^*|^2\rangle$$
$$\langle\epsilon_\theta\rangle = \sqrt{\frac{1}{RaPr}}\langle|\nabla\theta|^2\rangle$$

On using the above values in Eq. 2.99, one gets

$$L_B^* = \frac{\langle\epsilon_u^*\rangle^{5/4}}{\langle\epsilon_\theta\rangle^{3/4}} \tag{2.100}$$

.

It is to be noted that the global Bolgiano length scale cannot be used as a reliable indicator of the presence of the Bolgiano scaling in RBC, as significant variation in dissipation rate is observed between the boundary layer and bulk region. Kunnen *et al.* [65] and Kunnen and Clercx [66] proposed that L_B should be considered locally, taking into account the fact that dissipation rate is significantly higher in the boundary layer regions compared to the bulk. They reported that L_B exhibits smaller values in proximity to the isothermal walls and larger ones in the bulk region. As a result, when assessing the existence of Bolgiano scaling, it is essential to consider both the global and local perspectives of L_B. Confirming Bolgiano scaling is further complicated by the prevalent occurrence of large-scale circulation [63] in RBC which introduces additional complexity and inhomogeneity to the system.

Table 2.1: Scaling laws expected for the small scale statistics in the K41 and BO59 scaling.

	Temperature		Velocity	
	K41	BO59	K41	BO59
Spectra	$\sim k^{-5/3}$	$\sim k^{-7/5}$	$\sim k^{-5/3}$	$\sim k^{-11/5}$
SF	$\sim r^{p/3}$	$\sim r^{p/5}$	$\sim r^{p/3}$	$\sim r^{3p/5}$

2.6 Scaling of structure function and spectra in thermal convection

To describe small scale dynamics in thermal convection, scaling properties of structure functions and spectra are analyzed. As discussed in Section 2.5, classical view of the scaling in inertial range is that when temperature acts as a passive scalar, Kolmogorov scaling (K41) [62] is expected for velocity fluctuations, while temperature fluctuations follow Obukhov and Corsine (OC) [67, 68] scaling, which is a result of generalization of the Kolmogorov's K41 scaling. However, when temperature behaves as an active scalar, Bolgiano and Obukhov scaling (BO59) [54, 55] is observed for both velocity and temperature fluctuations above a length scale L_B (Bolgiano length) where buoyancy force becomes dominant. According to K41 scaling, velocity and temperature structure functions of a pth order can be described as

$$S_u^p(r) = \langle |\boldsymbol{u}(\boldsymbol{x}+\boldsymbol{r}) - \boldsymbol{u}(\boldsymbol{x})|^p \rangle \sim \epsilon_u^{p/3} r^{p/3},$$
$$S_\theta^p(r) = \langle |\theta(\boldsymbol{x}+\boldsymbol{r}) - \theta(\boldsymbol{x})|^p \rangle \sim \epsilon_\theta^{p/2} \epsilon_u^{-p/6} r^{p/3},$$

while BO59 scaling is tagged with the following scaling laws

$$S_u^p(r) = \langle |\boldsymbol{u}(\boldsymbol{x}+\boldsymbol{r}) - \boldsymbol{u}(\boldsymbol{x})|^p \rangle \sim \epsilon_\theta^{p/5} r^{3p/5},$$
$$S_\theta^p(r) = \langle |\theta(\boldsymbol{x}+\boldsymbol{r}) - \theta(\boldsymbol{x})|^p \rangle \sim \epsilon_\theta^{2p/5} r^{p/5},$$

where $\boldsymbol{r}$ is the separation vector, $r = |\boldsymbol{r}|$, and $\langle \cdots \rangle$ represents volume-time average. In terms of Fourier transform, K41 scaling, observed for wavenumber $k >> 1/L_B$, describes kinetic energy and temperature spectra by $k^{-5/3}$ decay law, whereas in the BO59 scaling ($k << 1/L_B$) energy and temperature spectra obey $k^{-11/5}$ and $k^{-7/5}$ scaling laws, respectively. Above described scaling laws are summarized in Table 2.1

In turbulent RBC, realization of BO59 scaling is of particular interest to the research community. Camussi et al. [69] characterized the flow dynamics via spectra and SFs scaling for different

regions of a cylindrical cell with $\Gamma = 1/2$ for $Pr = 0.7$ and $Ra = 2 \times 10^{10}$ and 2×10^{11}. For lateral walls Kolmogorov -5/3 decay law was obtained for both velocity and temperature spectra, while central region exhibited -7/5 law for both temperature and velocity spectra, i.e., only temperature spectra followed Bolgiano scaling in the central region. Kunnen et al. [65] performed DNS in a cylindrical cell of aspect ratio $D/H = 1$ for $10^8 \leq Ra \leq 10^9$ where Pr was either 4 or 6.4. They measured SFs of velocity and temperature in the centre of cell and in the analysis local Bolgiano length scale (for central region), which increases with Ra, was considered rather than its global estimate. Consistent with the above argument, Bolgiano scaling regime reduced with an increase in Ra and K41 scaling became more pronounced at high Ra. Kaczorowski and Xia [70] evaluated SFs for vertical velocity and temperature via DNS in the central region of a cubic box for $3 \times 10^5 \leq Ra \leq 3 \times 10^9$ where $Pr = 0.7$ and 4.38. To estimate the existence of the BO59 scaling, the local Bolgiano length scale volume averaged over the central region ($L_{B,centre}$) was calculated. It was observed that velocity SFs in the buoyancy direction approach K41 scaling with an increase in Ra, while temperature SFs approached BO59 scaling for $r > L_{B,centre}$. Also, mixed vertical velocity-temperature SFs obeyed $4/5$ scaling for $Pr = 4.38$ above $r > L_{B,centre}$. It was concluded that BO59 scaling might be observed vividly at moderate Ra and high Pr. Lohse and Xia [63] highlighted the main obstacle in realizing clear separation between Kolmogorov scaling ($r < L_B$) and Bolgiano scaling ($r > L_B$) simultaneously at the same location. It was pointed out that with an increase in Ra, Kolmogorov length scale (η) decreases with an increase in Ra whereas local Bolgiano length scale increases. This opposite dependence on Ra poses difficulties in realizing both scalings simultaneously. Hence, it was proposed that one should choose suitable Ra and Pr range, aspect ratio of the cell, and different regions of the convection cell should be analyzed for different scalings. To realize BO59 scaling, near boundary region should be analyzed, whereas for K41 scaling central (bulk) region should be considered.

3 NUMERICAL DETAILS

This chapter presents the mathematical formulation of Rayleigh-Bénard convection along with the necessary numerical details required for the simulations. We start with describing the governing equations in the non-dimensionalized form along with the details of the flow domain and prescribed boundary conditions. This is followed by discussion on the construction of rough surfaces, numerical procedure to solve the governing conservation laws, grid generation and parallelization techniques, and diffuse interface immersed boundary method to handle the rough surfaces. Lastly, the validation of the numerical setup with existing roughness studies is shown. In addition, we show that the global heat transport properties do not change for different flow realizations.

3.1 Mathematical formulation

Governing non-dimensional continuity, momentum and energy equations for incompressible buoyancy driven flows using the Boussinesq approximation are given as

$$\frac{\partial u_i}{\partial x_i} = 0 \tag{3.1}$$

$$\frac{\partial u_i}{\partial t} + \frac{\partial (u_i u_j)}{\partial x_j} = -\frac{\partial p}{\partial x_i} + \sqrt{\frac{Pr}{Ra}} \frac{\partial^2 u_i}{\partial x_j \partial x_j} + \theta \delta_{ib} \tag{3.2}$$

$$\frac{\partial \theta}{\partial t} + \frac{\partial (u_j \theta)}{\partial x_j} = \frac{1}{\sqrt{RaPr}} \frac{\partial^2 \theta}{\partial x_j \partial x_j} \tag{3.3}$$

where u_i is the non-dimensional velocity in x_i direction, b is the buoyancy direction, p is the pressure, and $\theta = (T - T_C)/(T_H - T_C)$ is the non-dimensional temperature with T_H and T_C

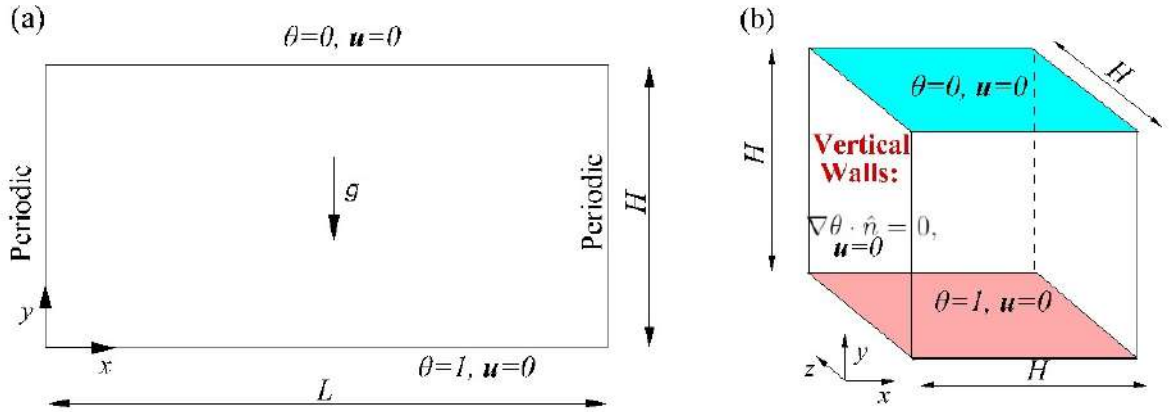

Figure 3.1: Schematic of RBC in (a) 2D rectangular cell, (b) 3D cubic cell with applicable boundary conditions.

are the temperatures of the bottom and top plates, respectively. The above set of equations are non-dimensionalized using reference scales for length, velocity, temperature, and time as vertical height H, free-fall velocity $\sqrt{\beta g \Delta T H}$, $\Delta T = T_H - T_C$, and $(H/\beta g \Delta T)^{1/2}$, respectively. Typical schematics of RBC in 2D rectangular and 3D cubic cells are shown in Fig. 3.1 with the boundary conditions. Top and bottom plates are maintained at constant temperatures with no-slip velocity boundary condition, while lateral walls are either treated as adiabatic with no-slip velocity or considered periodic. Usually lateral walls are treated periodic when the focus is on realizing higher turbulent intensity with minimal boundary effects in the domain.

We have carried out roughness facilitated simulations in a 2D rectangular box of aspect

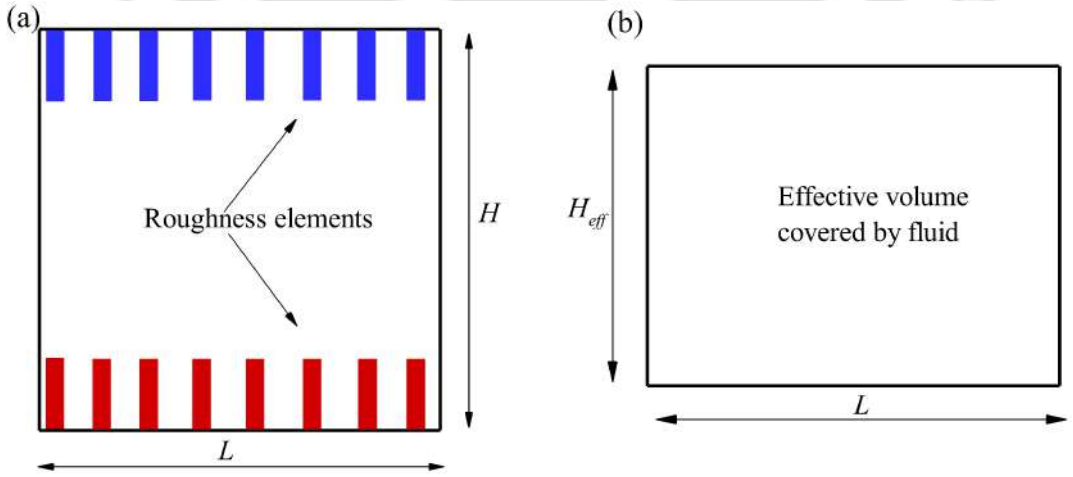

Figure 3.2: Schematic of 2D convection cell comprising (a) both fluid and rough surfaces, (b) effective volume covered by fluid in a smooth cell.

ratio $\Gamma = 2$, while 3D flows are investigated in a cubical box. Due to the introduction of rough surfaces on the isothermal plates, effective volume covered by the fluid decreases. Hence, the

characteristic length scale for the rough case is computed as the height of the equivalent hypothetical smooth cell for the same volume of fluid, as shown in Fig. 3.2. The calculation of H_{eff} is given as

$$H_{eff} = \frac{\text{Net volume occupied by fluid in the rough cell}}{\text{Base area of the smooth cell}} \tag{3.4}$$

Based on H_{eff}, we have calculated effective Rayleigh number (Ra_{eff}) as

$$Ra_{eff} = Ra\left(\frac{H_{eff}}{H}\right)^3 \tag{3.5}$$

To handle rough surfaces while solving the governing conservation laws, we have employed diffuse interface immersed boundary method (DIIBM), the details of which are described later in section 3.5.

3.2 Construction of rough surfaces

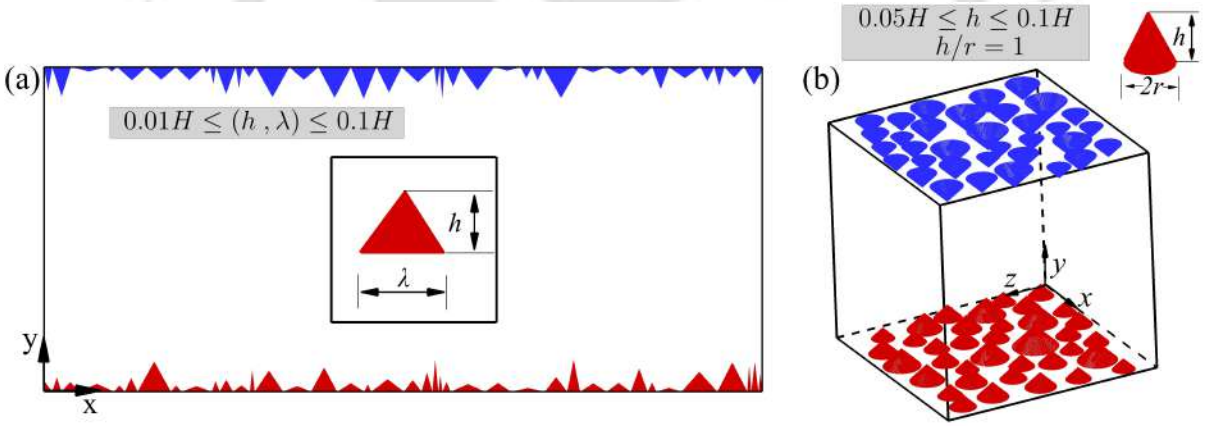

Figure 3.3: Schematic of (a) triangular roughness used in the 2D rectangular cell of aspect ratio 2, and (b) conical roughness employed in the 3D cubic cell.

Introduction of rough surfaces is identified in the literature as a viable means to enhance the global heat transfer rate [29, 30, 33]. Majority of the studies in the past considered uniform or mono-scale rough surfaces, which cease to confer augmented heat transport scaling in the higher Ra range [41, 42]. With the idea of facilitating natural selection and incorporating multiple length scales of the roughness elements on the isothermal plates, we have employed the standard random number generator available. It allows randomly assigning the values of different geometric attributes of the roughness elements. The rough surfaces used in 2D and 3D frameworks are shown in Fig. 3.3. In 2D setup, roughness elements are isosceles triangles such that their height or amplitude (h) and width or wavelength (λ) are set to vary independently

between 1% to 10% of the height of the cell. This arrangement allows continuous fuelling of plumes in the system, such that taller elements are predominantly active at a lower Ra, while smaller elements perturb TBL in the higher Ra range. In case of 3D setup, we have employed conical shaped roughness elements in the cubical cell. The aspect ratio of a conical element, defined as the ratio of its height to radius, is kept unity. Using the random number generator, the amplitude and location of the centroid of the base of cone is assigned. The amplitude of the conical elements vary within 5% to 10% of H. The chosen range of elements allows sufficient penetration of TBL by them for the fixed $Ra = 10^8$. The addition of further smaller roughness elements ($h < 0.05H$) is avoided as they hinder heat transport for the chosen thermal forcing. The cones are populated in such a way that a minimum clearance of $0.01H$ is established between them. Further, the maximum change in heat transfer area due to the addition of conical elements is restricted to 20% of the base area for each isothermal plate.

Note that though the construction of the rough surfaces in 2D and 3D is accomplished using the random number generator imparting uniform distribution of roughness elements, the spectrum of height/base is random only to a limited extent owing to the finite axial length of the cell. As a result of which the number of elements that can be accommodated are also finite. Nevertheless, the rough surfaces employed are fairly good representation of the ones encountered in real life flows containing multiple length scales.

3.3 Numerical Procedure

The governing equations are solved using a non-staggered finite volume approach in conjunction with a diffuse interface immersed boundary method (DIIBM) [71] to handle the roughness elements. Boundary of the object (roughened plates) is first linearized in order to ascertain its relation with the computing cells surrounding it. Computing cells are classified into fluid or body cells based on the volume fractions, which is the fraction of a computing cell lying inside an object. Since DIIBM does not essentially demarcate the body surface from the fluid region, a universal momentum equation, which smoothly blends the Navier-Stokes equations with the velocity boundary conditions, is solved in the entire physical domain regardless of whether the computing cell belongs to fluid or solid body. Buoyancy, pressure and diffusive terms in the momentum equation are handled using the 2nd order implicit Crank-Nicolson scheme while the non-linear convective term is approximated using the explicit Adams-Bashforth scheme. The aforementioned treatment of different terms confers the stability and robustness of the time

marching procedure. A two-step predictor-corrector technique is employed in the solver. In the first step, the provisional velocity field is calculated using the known pressure field, and in the second step, it is corrected by solving the pressure Poisson equation, which enforces mass balance indirectly. All the resulting sparse linear systems are solved using the BiCGSTAB technique preconditioned by a highly scalable block diagonal version of the modified strongly implicit (MSI) procedure. The solver used for the computations is parallelized with standard MPI libraries to speed up the calculations. For further details of the numerical technique, Peter and De [72] and De *et al.* [73] can be referred.

To ensure adequate spatial resolution, Kolmogorov length scale [$\eta = Pr^{1/2}(RaNu)^{-1/4}$] is resolved such that maximum grid spacing is always smaller than η ($\Delta x_{max}/\eta, \Delta y_{max}/\eta, \Delta z_{max}/\eta < 1$). For sufficient resolution of the rough surfaces, a refined mesh in the vertical direction close to the isothermal plates is employed. Also, the resolution of the roughness elements is kept comparable to that of the grid. Time increment (Δt) for a stable time marching is kept smaller than the Kolmogorov time scale (τ_η), which is analytically obtained as $\tau_\eta = \sqrt{Pr/(Nu-1)}$. Further, the value of maximum Courant number never exceeds 0.2.

3.4 Grid generation and parallelization

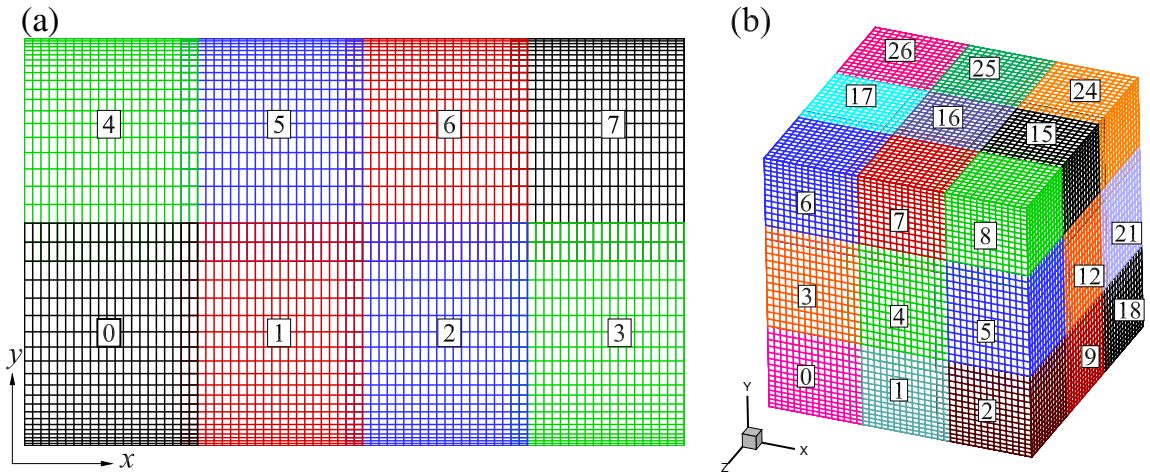

Figure 3.4: Schematic of the sample non-uniform grid in vertical direction y is shown for (a) 2D rectangular and (b) 3D cubic boxes. The sample grid for 2D is decomposed into 8 sub-domains, while for 3D, the number of divisions of the domain are 27.

We have employed a structured grid, non-uniform in the vertical direction to allow refinement near the isothermal plates. As a consequence of which minimum vertical grid spacing is present

close to the isothermal plates, while the maximum spacing prevails in the center of the domain. Let us suppose that a grid containing N_x points and spanning length L is created in x direction, then its $(i+1^{th})$ coordinate is given by [74]

$$x_{i+1} = L\frac{(\beta+2\alpha)(\frac{\beta+1}{\beta-1})^{\frac{\eta-\alpha}{1-\alpha}} - \beta + 2\alpha}{(1+2\alpha)(1+(\frac{\beta+1}{\beta-1})^{\frac{\eta-\alpha}{1-\alpha}})} \tag{3.6}$$

Here, $\eta\ \big((i-1)/(N_x-1)\big)$ corresponds to the uniform grid, and α and β are the parameters which control refinement of the grid. The parameter α decides the region where refinement is applied, while β controls the level of refinement. The value of β is always greater than 1. The closer the value of β is to 1, greater is the refinement. When the value of α is specified as 0, then the refinement is applied only near $x = L$. To enforce equal refinement at both end of the domain ($x = 0$ and $x = L$), α is specified as 0.5. Due to the presence of rough surfaces on both top and bottom isothermal plates, grid refinement is required near both the walls. Thus, α is set as 0.5 in the simulations for the vertical direction. For sufficient resolution of the rough surfaces, β is assigned a value closer to 1 ($\beta \approx 1.1$). To avoid the loss of spatial resolution due to heavy refinement close to the walls, a very fine grid is used so that the maximum grid spacing in the center of the domain does not exceed the Kolmogorov length scale.

The parallelization of the numerical code is based on the distributed memory allocation. To speed up the calculations, the computational domain is decomposed into sub-domains, such that each of them is uniquely assigned to a processor. Each processor performs computations independently and has no knowledge of its neighbours. The task of establishing communication of solution variables at the interfaces of the sub-domains is accomplished using Message passing interface (MPI) protocols to coordinate computations among the processors. In Fig. 3.4, we show sample grids in 2D and 3D configurations distributed over 8 and 27 processors, respectively. It is a convention to denote the processors by rank, starting from 0. Note that the processors are assigned equal number of computing cells to ensure identical load distribution on them. For 2D simulations in a rectangular cell, the most demanding case of $Ra = 10^{11}$ consisted of 40 million computing cells distributed over 162 processors. For 3D simulations in a cubical box, we have used a grid consisting of 27 million computing cells spread over 100 processors to simulate $Ra = 10^8$. The exploration of higher Ra in 3D, demanding higher spatial and temporal resolutions, is extremely prohibitive. This is the reason we restricted 3D simulations to $Ra = 10^8$.

3.5 Diffuse interface immersed boundary method

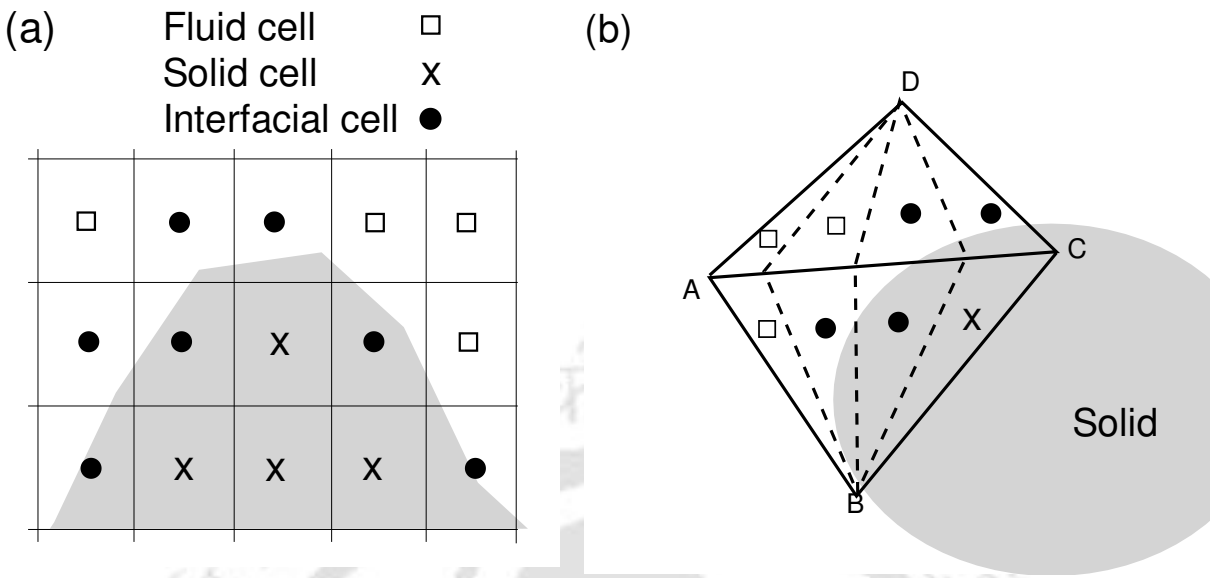

Figure 3.5: (a) Characterization of computing cells into fluid, solid and interfacial based on level set function and (b) computation of volume fraction.

Consistent with the idea of the diffuse interface immersed body method, the relation of the computing cells surrounding the linearized rough surface is determined using the volume fraction criterion, which categorizes the cells into three types. The volume fraction (ϕ) of a cell specifies the fraction of it that lies inside the object/body (here, rough surfaces). Mathematically, ϕ is represented as $\phi = V_s/V_p$, where V_s is the portion of the cell volume covered by the body, and V_p is the total volume of the computing cell. The three types of computing cells are distinguished based on ϕ as fluid ($\phi = 0$), body ($\phi = 1$), and interfacial ($0 < \phi < 1$) cells, as shown in Fig. 3.5. Accurate and efficient calculation of volume fractions holds the key in the reconstruction of body surfaces [71]. The rendered volume of the surfaces using zero-level set function, $V_{body} = \sum_{cell} \phi_i V_{pi}$ is checked with the original volume of the linearized surfaces. The lesser the difference between the two is, better is the reconstruction of the body. A universal equation combining momentum conservation and rigid body motion obtained through the volume fraction is solved in the entire domain,

$$(1-\phi)[\frac{u_{i,P}^{n+1} - u_{i,P}^{n}}{\Delta t} V_P + \aleph(\frac{\partial(u_i u_j)}{\partial x_j}) + \aleph(\frac{\partial p}{\partial x_i}) - \sqrt{\frac{Pr}{Ra}}\aleph(\frac{\partial^2 u_i}{\partial x_j \partial x_j}) + \theta\delta_{ib}] - \phi\frac{u_{i,P}^{n+1} - u_{i,B}}{\Delta t} V_P = 0, \tag{3.7}$$

where $\aleph$ denotes the numerical approximation, ϕ represents volume fraction of a computing cell denoted by P and having volume V_P, i is the Cartesian component, $u_{i,B}$ is the i-th component

of body velocity and $n+1$ is the desired time step index. The boundary conditions are enforced indirectly through the global equations in a volume average sense such that their scope is limited to a computational cell. It implies that on reducing the size of a computing cell, identical results as obtained with the sharp interface method are approached. In other words, a sufficiently refined mesh in the wall normal direction is required to resolve the rough surfaces sufficiently.

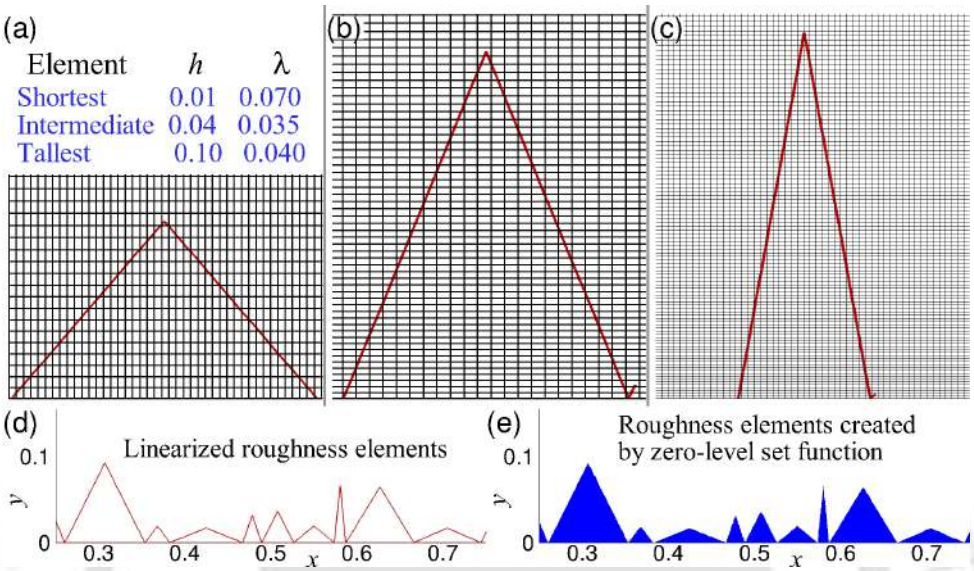

Figure 3.6: (a-c) Grid resolution of three extreme roughness elements extracted from the rough bottom plate at the lowest $Ra = 10^8$. As one moves from left to right, the amplitude of the selected roughness elements increases. Note, frames (a-c) are not shown on the same scale. Adequate spatial resolution near the roughness elements is ensured with at least 13 cells (N_{min}) containing in the vertical direction for the shortest element. For the highest $Ra = 10^{11}$ (not shown), N_{min} is 50. In (d) A portion of the bottom surface using linearized elements is shown while (e) shows volume rendering of the roughness geometry using the zero-level set function. It can be seen that nuances of the roughness geometry are identically reproduced. The error in the reconstructed volume (using volume fractions) with respect to the original one (linearized) is as low as 0.08% for $Ra = 10^8$ and 0.05% for $Ra = 10^{11}$.

In Fig. 3.6(a-c), grid resolution for the three roughness elements of extreme dimensions in 2D rectangular cell at the lowest $Ra = 10^8$ is shown. The choice of this Ra for the grid representation is in line with the fact that a smaller thermal forcing (Ra) demands coarser resolution and thus, there is a possibility of under-resolution of the near-wall roughness elements. Here, the element with the smallest amplitude is in the left frame, while the tallest one is on the right. A minimum of 13 cells (N_{min}) is always placed inside the roughness elements. The aforementioned provision other than satisfying the Kolmogorov length scale criterion ensures a spatial

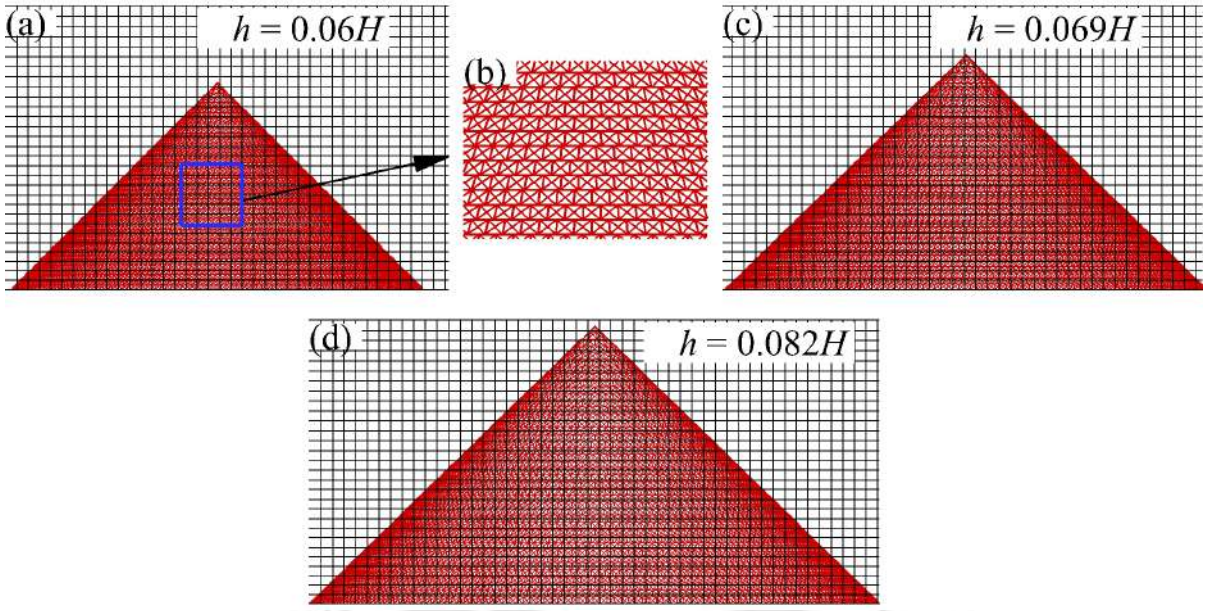

Figure 3.7: (a,c,d) Grid resolution close to three extreme conical elements of the bottom plate of the cube, such that height of the elements is increased sequentially. In (b), magnified view of the highlighted conical region in (a) shows triangular elements used for the construction of the surface.

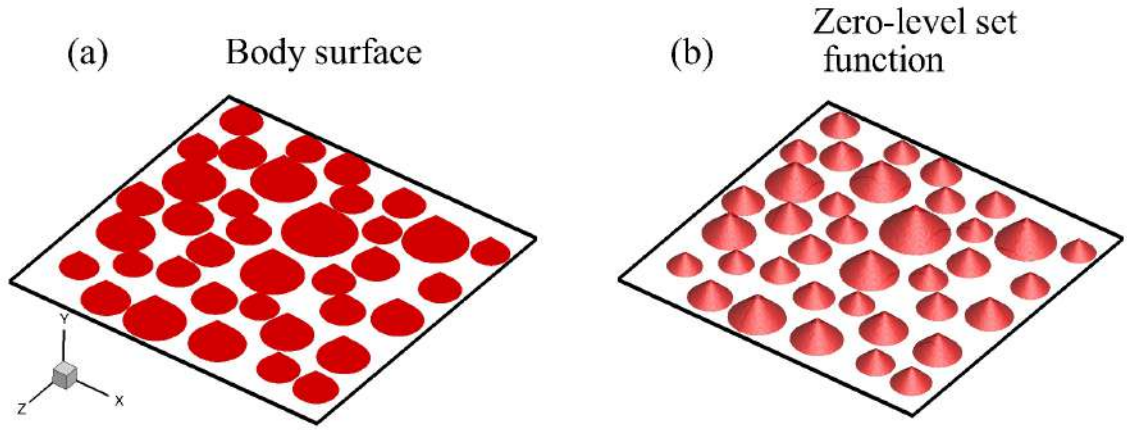

Figure 3.8: (a) Triangulated conical rough surface on the bottom isothermal plate is shown along with its b) zero-level set function representation. For simplicity and better visualization, only bottom surface is shown.

resolution close to the roughness elements which is more than reasonable. The excellent resolution of the elements is reflected from the volume rendering of zero-level set function, see frame (e), reproducing identically the exact linearized rough bottom plate as shown in frame (d). Note,

Table 3.1: Error in reproduction of linearized rough surfaces using volume fractions (ΔV_{error}) for the 2D and 3D simulations. Note that N_{min} represents the number of grid points inside the smallest roughness element in the vertical direction.

Case	Ra	Mesh	N_{min}	$\Delta V_{error}(\%)$
2D	10^8	1201×601	13	0.080
	10^9	2201×1101	15	0.030
	10^{10}	5041×2521	30	0.007
	10^{11}	9001×4501	50	0.050
3D	10^8	$300 \times 300 \times 300$	20	0.247

for simplicity in representation, only a small portion of the bottom plate is shown in frames (d) and (e). The error in reconstruction is calculated by $\Delta V_{error} = \left|1 - \frac{V_{body}}{V_{analytical}}\right|$. In 2D framework, the error in reconstruction of the rough surfaces is always less than 0.08%, refer Table 3.1. Further, as we have kept the resolution of the rough surfaces comparable to that of the grid, the error in reconstruction of the rough surfaces is diminished with increasing Ra. It results in highly precise and accurate identification of the rough surfaces. At $Ra = 10^{10}$ and $Ra = 10^{11}$, the above mentioned error diminishes to 0.007% and 0.05%, respectively. It emphasizes the excellent spatial resolution used for the larger Ra cases. Note that in case of $Ra = 10^{10}$, the ratio of body to grid resolution is 1.26, while for $Ra = 10^{11}$, it is 2.25. The slight increase of the error for $Ra = 10^{11}$ may be attributed to the above mentioned reason. For further details of the simulation parameters, refer chapter 4.

In the same line, we have ensured adequate grid resolution close to the conical roughness elements in the 3D cubical box at $Ra = 10^8$, refer Fig. 3.7. In addition to satisfying the Kolmogorov length scale criterion, a minimum of 20 computing cells in the vertical direction are contained in the conical elements, which highlights the excellent spatial resolution close to the rough surfaces. In Fig. 3.8, the excellent reproduction of conical surfaces using their zero-level set function representations is readily evident. The error in reconstruction of the rough surfaces for a grid size of $300 \times 300 \times 300$, refined close to the isothermal walls, is 0.247%. It highlights the robustness of the present set-up in resolving rough surfaces with deviations in the rendered volume being trivial. Note that the numerical set-up employed in the present work has been successfully used to solve a variety of complex flow problems that involve stationary [75, 76] and moving boundaries [77, 78].

3.6 Validation of the numerical setup and flow realizations

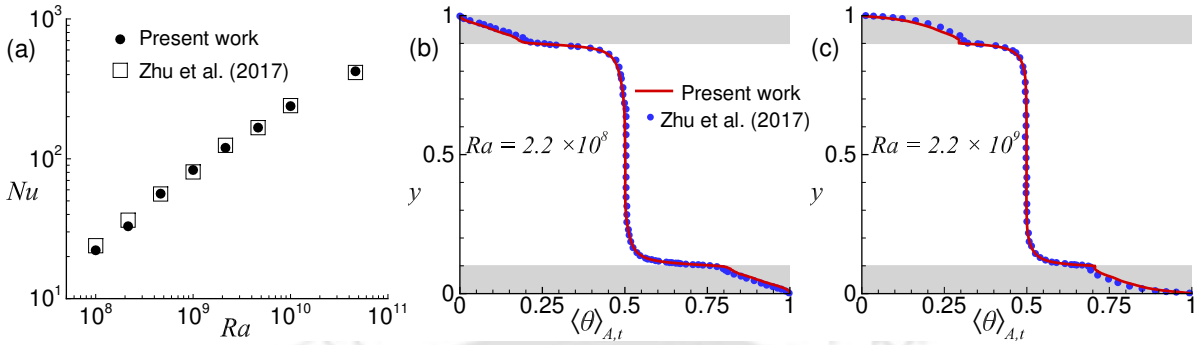

Figure 3.9: Comparison of (a) mean $Nu(Ra)$, and (b,c) vertical mean temperature $\left(\langle\theta\rangle_{A,t}\right)$ profiles for the sinusoidal roughness case ($h = \lambda = 0.1$) reported by Zhu *et al.* [41]. Note, the height of the shaded portions is representative of the maximum amplitude of the roughness elements.

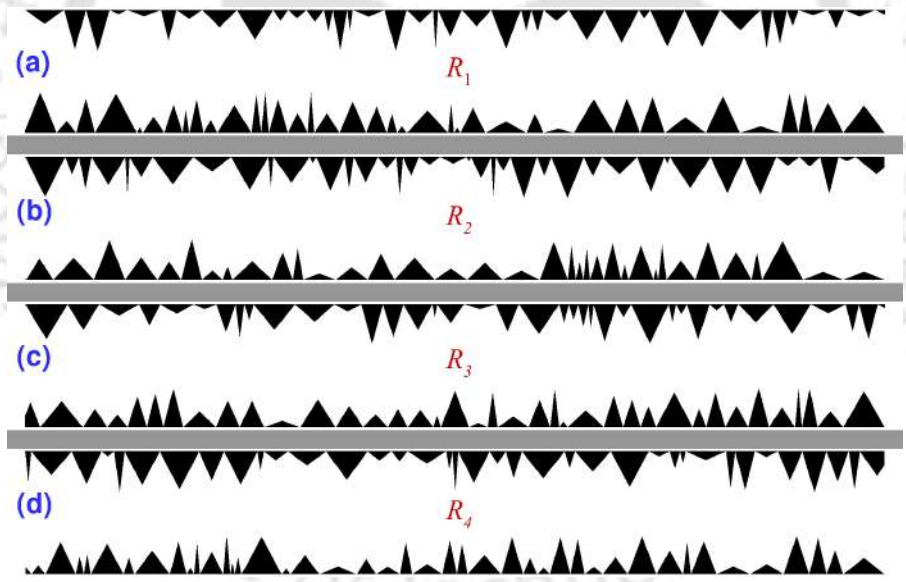

Figure 3.10: Schematic showing rough surfaces employed on top and bottom plates such that range of values admissible for width and height of the roughness elements is kept same (from 1 to 10% of H) for different flow realizations at $Ra = 1.5 \times 10^9$.

To check the ability of the present numerical set-up, results reported by Zhu *et al.* [41] (numerical study) for sinusoidal roughness, both amplitude (h) and wavelength (λ) being 0.1, on horizontal plates are reproduced. As shown in Fig. 3.9(a), $Nu(Ra)$ agrees well with an average and maximum variation of 3% and 7%, respectively, which is reasonable given the complexity of the problem, difference in the numerical methods and a large range of *Nu* data. The comparison

of *Nu* is limited to $Ra = 10^{10}$ due to the higher computational cost involved. Moreover, vertical mean temperature profiles for $Ra = 2.2 \times 10^8$ and 2.2×10^9, shown in Figs. 3.9(b) and (c), respectively, compare accurately with the reference data which highlights the effectiveness of the present set-up in dealing with the rough surfaces.

The present work incorporates irregular rough surfaces on the isothermal plates. To identify whether the arrangement of the irregular roughness elements plays a role in deciding the global heat transport properties, we observe global *Nu* and variance of the temperature fluctuations corresponding to different flow realizations. For the 2D setup, we observed four different flow realizations for R_1, R_2, R_3, and R_4 rough surfaces at $Ra = 1.5 \times 10^9$. In Fig. 3.10, the top and bottom rough surfaces employed for different flow realizations are shown. The details of the obtained global *Nu* and variance of the temperature fluctuations, $\langle \sigma_\theta^2 \rangle_V$, are listed in Table 3.2.

Table 3.2: Global Nusselt number and variance of temperature fluctuations observed for different realizations in the 2D setup at $Ra = 1.5 \times 10^9$ is listed along with the total wetted area (A_{wet}) of the top and bottom rough surfaces.

Realization	$\langle Nu \rangle_{V,t}$	A_{wet}	$\langle \sigma_\theta^2 \rangle_V$ $(\times 10^{-3})$
R_1	96.05	10.01	3.447
R_2	95.74	9.74	3.439
R_3	94.04	9.64	3.604
R_4	94.80	10.19	3.476

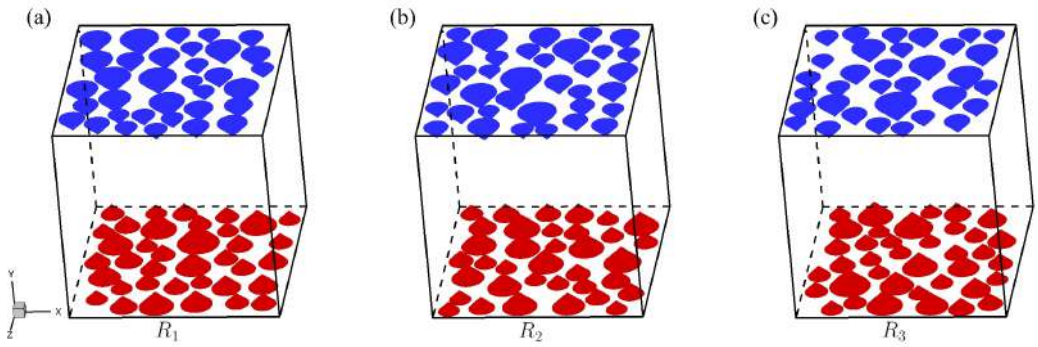

Figure 3.11: Schematic shows rough surfaces on a cubic box for different flow realizations at $Ra = 10^8$ and $Pr = 1$. Admissible amplitude of the conical elements ($0.05H \leq h \leq 0.1H$) and change in heat transfer area due to addition of the rough surfaces (20% of base area of the isothermal plates) are kept same for the realizations.

It can be observed that $\langle Nu \rangle_{V,t}$ and $\langle \sigma_\theta^2 \rangle_V$ converge for different realizations when total wetted area (A_{wet}) of the rough surface is comparable. The maximum variation between any two flow realizations does not exceed 2.1% and 4.8%, respectively, for $\langle Nu \rangle_{V,t}$ and $\langle \sigma_\theta^2 \rangle_V$. The obtained results are in agreement with that reported by Toppaladoddi *et al.* [79] for the fractal roughness, where *Nu* was reported to converge while higher-order moments differed significantly for different flow realizations.

In the same manner, we observed three different flow realizations for the 3D cubical box

Table 3.3: Global Nusselt number and variance of temperature fluctuations observed for different realizations in the 3D cubical box at $Ra = 10^8$ and $Pr = 1$ is listed along with the total number of conical elements N_{cones} on the isothermal plates.

Realization	$\langle Nu \rangle_{V,t}$	N_{cones}	$\langle \sigma_\theta^2 \rangle_V$ $(\times 10^{-3})$
R_1	48.23	71	4.81
R_2	48.48	72	4.962
R_3	47.97	77	4.79

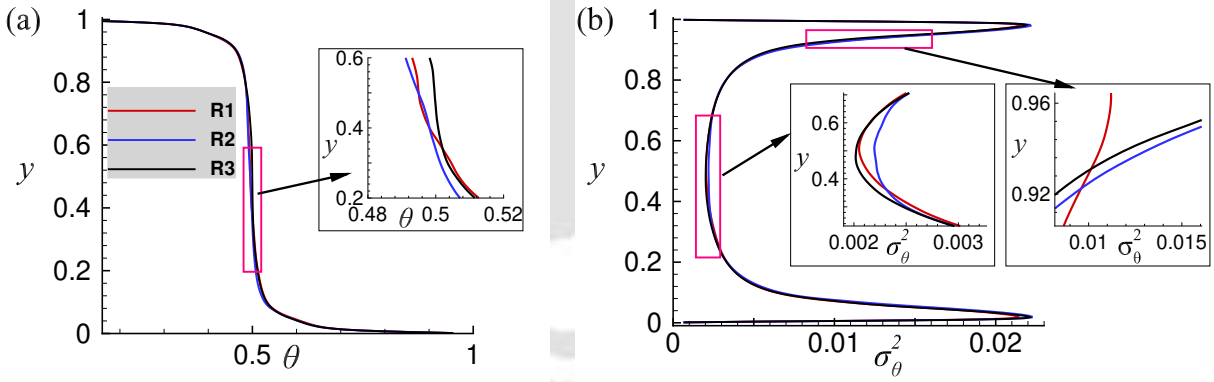

Figure 3.12: Horizontally-averaged vertical profiles of (a) temperature (b) variance are shown for different flow realizations. The insets show the magnified view of the highlighted profile regions.

endowed with rough conical surfaces R_1, R_2, and R_3 at $Ra = 10^8$ and $Pr = 1$. In Fig. 3.11, the top and bottom rough surfaces employed for different flow realizations are shown. From Table 3.3, the convergence of both $\langle Nu \rangle_{V,t}$ and $\langle \sigma_\theta^2 \rangle_V$ is readily evident. It can be observed that the maximum variation between any two realizations for $\langle Nu \rangle_{V,t}$ and $\langle \sigma_\theta^2 \rangle_V$ does not exceed 1.05% and 3.42%, respectively. Further, we compared vertical profiles of horizontally-averaged mean

temperature and variance for the flow realizations, as shown in Fig. 3.12. It is clearly evident that the profiles match quite well with trivial deviations in the bulk and near-wall regions, signifying convergence of flow statistics for different flow realizations.

4

ENHANCED *Nu* SCALING IN HIGH Ra REGIME

In this chapter, we present the results of a two-dimensional numerical study of turbulent Rayleigh-Bénard convection with air as the working fluid over multi-scale randomly roughened surface in a rectangular box of aspect ratio 2 over three decades of Rayleigh number ($10^8 \leq Ra \leq 10^{11}$). It is observed that the varied response of the roughness elements at different Ra allows the retention of the enhanced heat transfer scaling ($\gamma = 0.41$) throughout the explored Ra range. The plume emission process is triggered from the taller roughness elements at a lower Ra, while smaller elements contribute significantly at higher Ra. Increased plume emission frequency compared to smooth case is reflected from the enhanced volume fraction and thermal dissipation rate of plumes. Tip of the roughness elements exhibits the highest temperature and vertical velocity fluctuations, while washing out of the trapped fluid in the throat region holds the key to enhanced heat flux at higher Ra. Increased localized pockets of fluid at higher Ra indicates better inter-scale energy transfer which is reflected in higher energy content at all scales in the computed temperature spectra. The decomposition of the flow field into orthogonal modes reveals heat transfer enhancement at higher Ra is associated with multiple small-scale structure. Owing to better energy transfer and intense localized fluctuations, modal distribution of energy is less severe for higher Ra and stable twin large-scale rolls do not favor an efficient heat transport process.

4.1 Introduction

One of the central issues in the study of the turbulent RBC is to determine the global heat transfer mechanism and scaling law that describes it. For the scaling law of heat transfer, $Nu(Ra)$ is proposed in the form $Nu = ARa^{\gamma}$ [19]. One of the main motives of the ongoing research is to increase heat transfer for a given Ra, which can be achieved with an increase in A, γ or

both. Various heat transfer theories have been proposed in the past to quantify the heat transfer mechanism, and nearly all of them focus strongly on the dynamics in the boundary layer (BL) region. Malkus [13] assumed the marginal stability of the thermal boundary layers (TBLs) and predicted $\gamma = 1/3$, which also suggests that heat flux is independent of H or in other words, top and bottom TBLs do not communicate. Kraichnan [15] and Spiegel [80] predicted that at extremely large Ra, BLs undergo a transition from laminar to turbulent state, which leads to a regime known as asymptotic or 'ultimate' regime where $\gamma = 1/2$. In this regime, heat is transported ballistically with negligible resistance from the diffusivities of a fluid. Following a rigorous analysis based on the decomposition of the kinetic and thermal dissipation rates into bulk and BL contributions, Grossmann and Lohse [19, 46] proposed a unifying scaling theory, where scaling laws are dependent on the Ra and *Pr* regimes rather than being universal ones. In this theory, ultimate regime is also predicted as one of the regimes. But whether the ultimate regime exists or not, has perplexed the scientific community for a very long time and is the most debated topic.

In various experiments [20–22], a transition to the ultimate regime has been reported at $Ra \sim 10^{14}$, while others [23–25] denied any sign of ultimate regime. Zhu *et al.* [26] through numerical investigations also ascertained the transition to the ultimate regime at $Ra \sim 10^{13}$. Various strategies have been made to reach the ultimate regime that includes numerical studies involving periodic boundary conditions [27] in all directions to experimental work where radiative heating [28] is introduced to heat the bulk fluid directly, and thus the effect of the BLs is negated. Surface roughness is also one of the adopted strategies meant to introduce turbulence in the BLs to seek the realization of the ultimate regime and the associated $1/2$ scaling.

Though roughness facilitates enhanced heat transport scaling, the effect is observed to be transitional [41] as the classical scaling returns at a higher Ra range. The limitation is now being challenged with the introduction of multi-scale rough surfaces [42] as opposed to simple mono-scale and periodic ones, allowing sustenance of the enhanced scaling for an even larger Ra range. It is well established that any wall roughness becomes influential (increases heat transfer) only above a certain Ra when the TBL thickness is smaller than the height of a rough surface. Enhancement of heat transfer due to rough walls may or may not lead to an increase in the scaling exponent (γ). Shen *et al.* [29] and Du and Tong [30] reported an increase in heat transfer but with no change in γ. The amplified heat transfer rate could not be solely attributed to the increase in wetted area because of the rough surfaces [31]. Later in various experiments [33, 34, 81], enhanced scaling exponent γ was observed.

Direct numerical simulations (DNS) also corroborate experimental findings that an increase in *Nu* scaling exponent is obtained in rough cells. Stringano *et al.* [40] performed DNS in a cylindrical container of aspect ratio $\Gamma = D/H = 1/2$ with grooves on the top and bottom plates. Rayleigh number covered was in the range $2 \times 10^6 \leq Ra \leq 2 \times 10^{11}$ with fixed Pr = 0.7. Above a threshold Rayleigh number, scaling exponent γ for grooved surfaces increased from 0.31 to 0.37. Various studies on rough cells indicate that the heat transport maximizes on tuning the geometry of the roughness elements via choosing suitable height and wavelength of the roughness elements. Shishkina and Wagner [43] performed two-dimensional (2D) simulations with surface roughness in the form of rectangular elements on the horizontal plates. Results revealed that *Nu* does not solely depend on the wall surface area, and average heat flux was more for slender roughness elements when the distance between them exceeded their height. For closely spaced roughness elements, a decrease in heat transfer rate is observed as fluid becomes stagnant in the space between them. Zhang *et al.* [32] performed 2D simulations for $10^7 \leq Ra \leq 10^{11}$ with constant Pr = 1, where they varied the height of the roughness elements (h) and wavelength was kept fixed as $2h$. This study highlighted that beyond a critical height (h_c) of the roughness elements, enhanced heat transport is perceived. They reported that h_c decreases with an increase in Ra as $h_c \sim Ra^{-0.6}$, which also implies that a certain height of the roughness elements decreasing heat transfer at low Ra may enhance it at a higher Ra. Thus, the enhancement in heat transfer due to roughness is more pronounced at higher Ra.

Toppaladoddi *et al.* [39] studied 2D RBC with sinusoidal roughness on both the horizontal plates, where height of the roughness elements was kept fixed. For an optimum wavelength of the roughness elements, $\gamma = 0.483$ was obtained on fitting the data in $4 \times 10^6 \leq Ra \leq 3 \times 10^9$ range, which was misinterpreted as the onset of the ultimate regime. Later, Zhu *et al.* [41] extended the above study for an even higher Ra ($10^8 \leq Ra \leq 10^{12}$) and clarified that the regime with $\gamma = 1/2$ is transient as with a further increase in Ra, classical scaling regime ($\gamma = 1/3$) is restored. Reemergence of the classical scaling regime was attributed to the strong mixing of the fluid inside the roughness cavities. The vigorous mixing led to the formation of a thin TBL, which uniformly covered the entire rough surface and perfectly mimicked an enlarged wet surface area. Zhu *et al.* [42], introduced multi-scale roughness of the sinusoidal form in two-dimensional RBC. Explored Ra range was $10^8 \leq Ra \leq 10^{11}$ with constant Pr = 1 for aspect ratio $\Gamma = L/H$ = 2. With three different distinct length scales of the roughness elements, the local $1/2$ scaling regime got extended and the restoration of the classical $1/3$ scaling was put off. While explaining the efficacy of the multi-scale roughness, it was hypothesized that with

increasing Ra, different roughness length scales perturb the TBL in an order, starting from the largest (at low Ra) to the smallest (at high Ra).

Emran and Shishkina [82] performed 3D DNS simulations with ring-shaped obstacles in a cylindrical cell, where for an optimum height and gap between the obstacles, an increased γ was observed. Recently, Toppaladoddi *et al.* [79] also reported increased γ with the application of the fractal boundaries in a 2D cell. To the best of our knowledge, the effect of a complex roughness on flow dynamics has not been studied extensively. In the present work, a complex random roughness that incorporates multiple length scales, contrary to three scales employed by Zhu *et al.* [42], is introduced in a 2D rectangular convection cell to emulate real flow-like situations with an objective to unravel the heat transport mechanism and the associated flow dynamics in different regions of the convection cell. The reason for choosing 2D simulations is the luxury of exploring the flow physics at a higher Ra range which is computationally prohibitive for 3D simulations [41, 42].

4.2 Numerical details

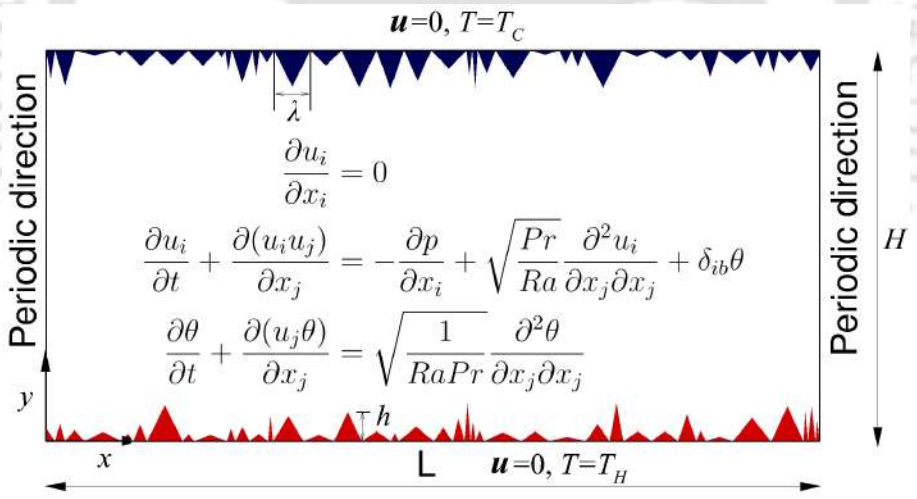

Figure 4.1: Schematic showing 2D rectangular convection cell with random triangular roughness elements at the top and bottom plates. Here, h and λ denotes height and width (wavelength) of the roughness elements, respectively.

The simulations are carried out in a 2D rectangular cell of aspect ratio $\Gamma = L/H$ = 2 with air as the working fluid ($Pr = 0.7$) for $10^8 \leq Ra \leq 10^{11}$. Top and bottom horizontal walls are endowed with rough surfaces, consisting of random triangular elements with no-slip velocity and isothermal temperature boundary conditions imposed on them, while the lateral walls are

smooth and periodic, see Fig. 4.1.

Table 4.1: Details of simulation parameters starting from the left: Ra is the Rayleigh number; Nu_{ref} the reference Nusselt number taken from Zhu *et al.* [42]; Nu_c the calculated Nusselt number, η the Kolmogorov length scale estimated as $\eta \approx Pr^{1/2}/(RaNu)^{1/4}$; $\Delta t/\eta_\tau$ the ratio of time step to Kolmogorov time scale $\left(\eta_\tau = \sqrt{Pr/(Nu-1)}\ \right)$; N_x and N_y are the grid resolution in x and y directions, respectively; $\Delta y_{max}/\eta$ the ratio of maximum grid spacing in y direction to the Kolmogorov length scale η; N_{min} represents the no: of grid points inside the smallest roughness element in the y direction; $\Delta_{body}/\Delta x_{max}$ the ratio of resolution of the roughness elements to the maximum grid spacing in x direction; t_{sampl} represents the data sampling duration.

Ra	Nu_{ref}	Nu_c	η	$\Delta t/\eta_\tau$	$N_x \times N_y$	$\Delta y_{max}/\eta$	N_{min}	$\Delta_{body}/\Delta x_{max}$	t_{sampl}
10^8	20.8	28.06	3.92×10^{-3}	2.66×10^{-3}	1201×601	0.611	13	1.08	1000
2.15×10^8	30.1	38.80	2.95×10^{-3}	1.29×10^{-3}	1601×801	0.609	18	1.12	1000
4.64×10^8	43.6	54.60	2.22×10^{-3}	1.56×10^{-3}	1801×901	0.604	14	1.08	1000
10^9	63.1	77.03	1.67×10^{-3}	1.88×10^{-3}	2201×1101	0.624	15	1.10	660
2.15×10^9	92.2	106.85	1.25×10^{-3}	1.14×10^{-3}	3001×1501	0.591	19	1.20	500
4.64×10^9	130.3	145.80	9.49×10^{-4}	6.80×10^{-4}	3801×1901	0.616	24	1.14	280
10^{10}	189.2	200.2	7.13×10^{-4}	3.28×10^{-4}	5041×2521	0.604	30	1.26	135
2.15×10^{10}	273	261.2	5.38×10^{-4}	3.94×10^{-4}	6241×3121	0.643	37	1.56	120
4.64×10^{10}	390.5	352	4.06×10^{-4}	2.36×10^{-4}	8065×4033	0.657	37	2.02	100
10^{11}	580.7	455	3.03×10^{-4}	2.88×10^{-4}	9001×4501	0.775	50	2.25	100

A grid that is uniform in x and non-uniform in y is employed such that the regions close to rough surfaces are resolved sufficiently. At a particular Ra, maximum grid spacing in y (Δy_{max}) is kept comparable to the global Kolmogorov length scale (η) estimated as $Pr^{1/2}(RaNu)^{-1/4}$ such that $\Delta y_{max}/\eta$ is always less than 0.8. Triangular elements are resolved in such a way that their resolution is comparable to that of the grid. Further, at least thirteen computing cells in the vertical y direction are kept inside the smallest roughness element ($h = 0.01$). Refer Table 4.1 for details of the simulation parameters. Time increment is chosen in such a way that it is smaller than Kolmogorov time scale (η_τ) and the maximum Courant number is always less than 0.2. For simulation runs, the flow field of a lower Ra is linearly interpolated and subsequently used as the initial condition for the next higher Ra case to speed up attainment of the statistically stationary state after which data is sampled. Details of the data sampling duration (t_{sampl}) are listed in Table 4.1. While for the highest Ra, the sampling time is kept as large as 1000 free-fall time units to realize the fully developed turbulent state, a sampling of 100 units is found adequate for the highly turbulent highest Ra case, which also involves a very high spatial resolution.

To ensure adequate grid resolution, a mesh refinement study at $Ra = 10^9$ is carried out by employing four progressively increasing grids (M_i, $i = 1$ to 4). The variation in the global $\langle Nu \rangle_{V,t}$ along with the variance of temperature fluctuations (σ_θ^2) is reported in Table 4.2. We observe that the variation in *Nu* and σ_θ^2 between any two successive grids never exceed 1 and 3.8%, respectively. Note, the choice of mesh is strictly limited by the Kolmogorov length scale, and thus, mesh resolution can not be coarsened arbitrarily. The refinement test clearly establishes the requisite spatial resolution in the simulations and the robustness of the implemented numerical code. Note, M_3 is the grid whose results are reported in the present study. For more numerical details, reader is referred to chapter 3.

Table 4.2: Details of the grid independence study performed at $Ra = 10^9$ are in the order starting from the left: Mesh M_i, $N_x \times N_y$ is the grid resolution, $\langle Nu \rangle_{V,t}$ is the calculated volume-time averaged Nusselt number, and $\langle \sigma_\theta^2 \rangle_V$ represents global variance of the temperature fluctuations. Note, $\langle \sigma_\theta^2 \rangle_V$ is calculated as $\left\langle \overline{\phi(\boldsymbol{x},t)^2} - \left(\overline{\phi}\right)^2 \right\rangle_V$, where overbar represents temporal average, and $\langle \cdots \rangle_V$ represents volume average.

Mesh (M_i)	$N_x \times N_y$	$\langle Nu \rangle_{V,t}$	$\langle \sigma_\theta^2 \rangle_V$ ($\times 10^{-3}$)
M_1	1801×901	76.89	3.6302
M_2	1981×991	76.76	3.6076
M_3	2201×1101	77.03	3.6355
M_4	2431×1516	76.23	3.497

4.3 Heat transport mechanism

One of the key challenges in turbulent RBC is to understand the heat transport phenomena, where thermal plumes and large scale circulation (LSC) serve as thermal carriers in transporting heat from the bottom heated to top cooled plate. With the introduction of rough surfaces, flow dynamics in a thermal convection cell is believed to be altered which often favors augmented heat transport at a sufficiently high thermal forcing. In Fig. 4.2, snapshots of the instantaneous temperature field are shown for Ra ranging from 10^8 to 10^{11}, where evolution of the flow structures with increasing Ra can be observed. At the lowest $Ra = 10^8$, flow inside the cavities (formed between the roughness elements) is still viscosity dominated which is evident from the entrapment of fluid inside the cavities and thus, a thick TBL is seen to form. As a result of which

significant enhancement in heat transport is not achieved. The major contribution to the plume emission comes from the taller roughness elements as shorter elements are embedded inside the TBL and are unable to perturb the BL region. With the increase in Ra, fluid trapped inside the cavities becomes accessible to the bulk flow and is eventually washed away, resulting in better mixing and a thin TBL. As the height of the smaller elements become comparable to TBL thickness, they start to contribute to plume emission. At the highest $Ra = 10^{11}$, the flow is highly turbulent and homogeneous with the emergence of very fine flow structures. Large scale diffuse structures are mainly seen to carry heat at the smaller Ra. This causes interdependency between the plumes, which often deters heat transfer enhancement. However, as flow structures become finer and intense, localized effects become important, and the plume emission process is triggered even at the sloping sides. As nucleation sites multiply, heat transport also magnifies.

To further elucidate the heat transport process, local instantaneous heat flux is decomposed

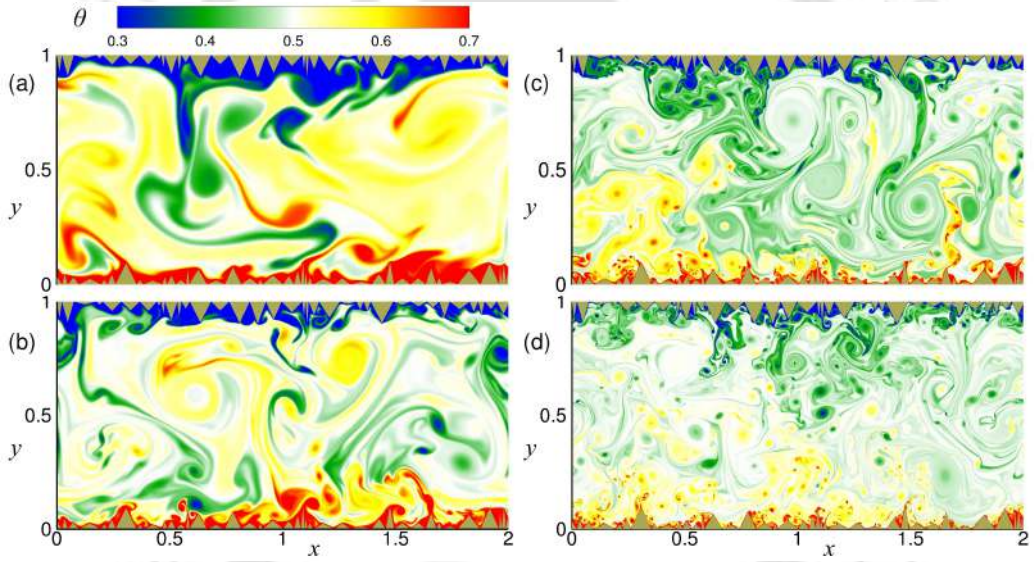

Figure 4.2: Snapshots of instantaneous temperature field for (a) $Ra = 10^8$, (b) $Ra = 10^9$, (c) $Ra = 2.15 \times 10^{10}$, and (d) $Ra = 10^{11}$.

into the contributions from diffusion and convection, defined as

$$Nu = \underbrace{\sqrt{RaPr}\,(v\theta)}_{convection} + \underbrace{(-\partial_y \theta)}_{diffusion}$$
$$= \quad H_{conv} \quad + \quad H_{diff}$$

which are shown in Fig. 4.3. As convective heat flux (H_{conv}) is associated with the product $v\theta$, it represents the transfer of heat by the vertical component of the fluid velocity. H_{conv} is positive for the ascent of the fluid ($v > 0$), while it is negative for the descent ($v < 0$). Clearly, a larger magnitude of $v\theta$ corresponds to a stronger convective effect. Diffusive heat flux (H_{diff}), on the

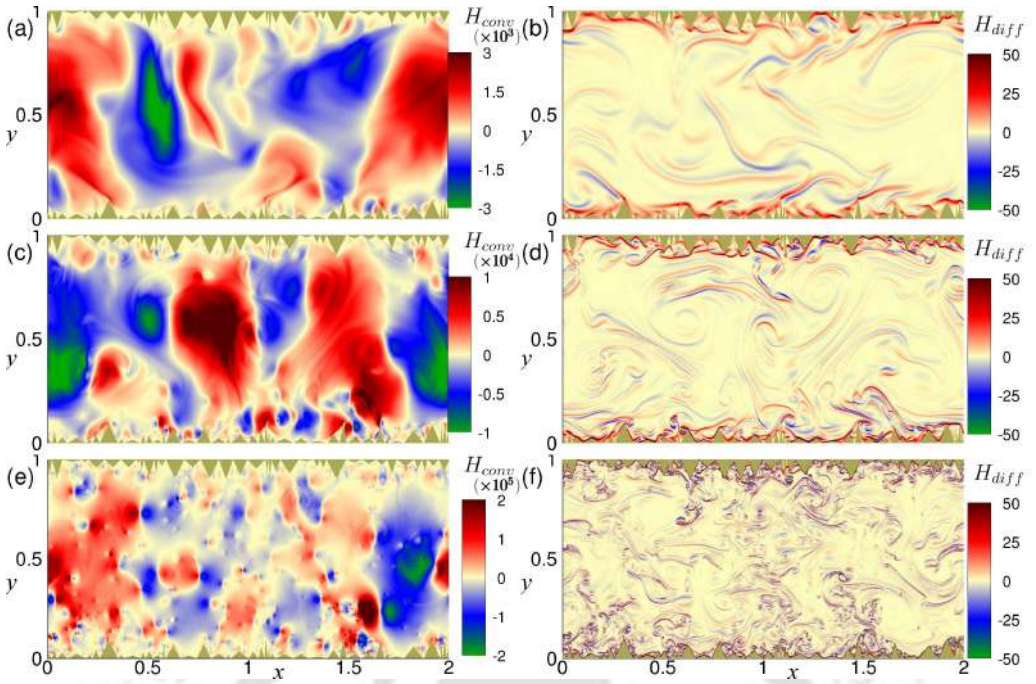

Figure 4.3: Instantaneous local convective and diffusive heat flux fields are shown for $Ra = 10^8$ (top row), $Ra = 10^9$ (middle row), and $Ra = 10^{11}$ (bottom row). Here, $H_{conv} = \sqrt{RaPr}\, v\theta$ is the convective flux, while $H_{diff} = -\partial_y \theta$ is the diffusive flux. Note, the data sets correspond to the same instances as in Fig. 4.2

other hand, takes into account the heat transfer due to vertical temperature gradient, $\partial_y \theta$. In the expression for H_{diff}, $\partial_y \theta$ is preceded by a negative sign, which signifies that diffusive contribution of the heat flux is positive in the direction of buoyancy. Near the BL regions, diffusive contribution is predominant owing to the strong temperature gradient in comparison to the bulk region. Also, plumes detaching from roughness elements exhibit high H_{diff} at their interfaces, which distinguishes them from the rest of the fluid. In view of this, it can be seen that at the lowest $Ra(= 10^8)$, there are fewer plume emitting spots, while at the highest $Ra(= 10^{11})$, we observe significantly increased plume emission sites with visibly finer plumes. As for convective contributions, they are expected to increase with increasing Ra (prefactor $\sqrt{RaPr}$ of H_{conv} increases with Ra) and the same is evident in Fig. 4.3. At the highest $Ra = 10^{11}$, maximum convective heat flux is of the order of 10^5, which is nearly two orders of magnitude higher than that at the lowest $Ra = 10^8$. Plume regions are clearly identified by high H_{conv}. Thus, at all Ra, plumes are observed to be the most potent coherent structures in enhancing the heat transfer. Interestingly, the shape of these regions does not change even at the highest Ra. This clearly indicates that though visibly plumes become finer at higher Ra, their spread and thus the convective effects brought about by them increases in magnitude while they control the heat transfer

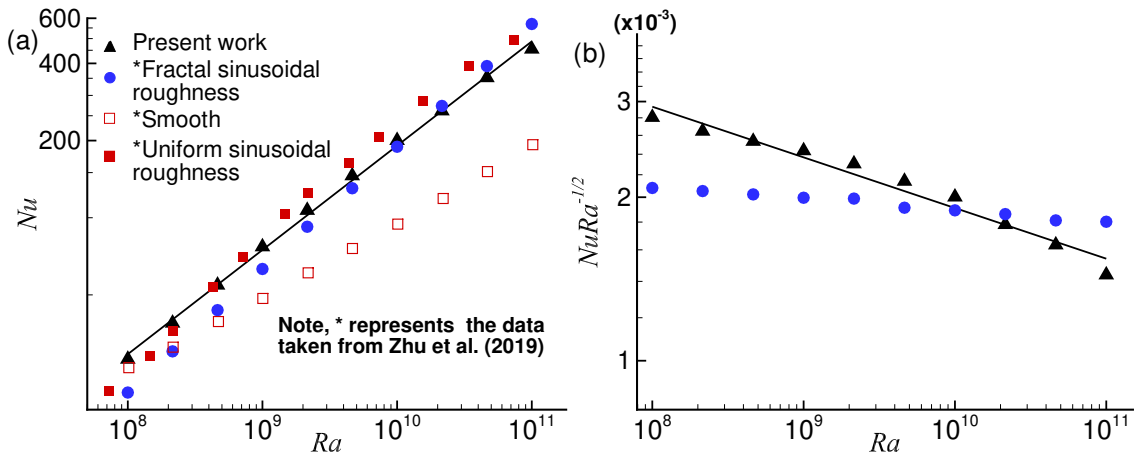

Figure 4.4: (a) $Nu(Ra)$ scaling is shown for three decades of Ra ($10^8 \leq Ra \leq 10^{11}$). For comparison, the data for smooth, mono-scale and fractal-like sinusoidal roughness taken from Zhu *et al.* [42] are also shown. Using the least-squares fitting, the scaling relations for multi-scale cases are obtained as $Nu = 0.016\,Ra^{0.41}$ (present work), and $Nu_{ref} = 0.003\,Ra^{0.48}$. (b) Compensated $NuRa^{-1/2}$ plots for the multi-scale cases.

away from the walls. Note, H_{diff} contributions are trivial in comparison to H_{conv} in the flow field, though high values of the former in the vicinity of the roughness elements show the signatures of the plumes.

Next, we analyze how the global heat flux represented by $\langle Nu\rangle_{V,t} = \sqrt{RaPr}\langle v\theta\rangle_{V,t} - \langle \partial_y \theta\rangle_{V,t}$ evolves with increasing Ra, as shown in Fig. 4.4. Using the least-squares fit, heat transport scaling relation is obtained as $Nu = 0.016\,Ra^{0.41}$, which highlights the attainment of the augmented scaling [41]. For comparison, Nusselt number reported by Zhu *et al.* [42] (numerical study) for the smooth wall, mono-scale and fractal-like sinusoidal roughness are also shown. Least-squares fitting to their data for fractal-like roughness revealed the scaling relation as $Nu = 0.003\,Ra^{0.48}$. It can be observed that for the first two decades, $10^8 \leq Ra \leq 10^{10}$, present roughness configuration yields higher Nu, while in the last decade $10^{10} < Ra \leq 10^{11}$, it is comparable with the reference Nu. Figure 4.4(b) clearly highlights the difference in the two scalings, where $NuRa^{-1/2}$ is plotted against Ra. The larger intercept on $NuRa^{-1/2}$ axis for the present work signifies a greater prefactor, while comparatively flatter fitting for the reference data implies the exponent is closer to 1/2. Note, Zhu *et al.* [42] chose the optimized parameters ($h/\lambda = 1$) for their roughness configuration to realize the maximum possible scaling exponent in comparison to other combinations of the amplitude and wavelength of the roughness elements. However, in the present work with the random roughness, there is no preference to any particular combination of the amplitude and wavelength of the roughness elements. The above argument highlights

the possible reason for the difference in the scaling exponents. Nevertheless, this study corroborates the finding of Zhu *et al.* [42] that multi-scale roughness extends the Ra range up to which augmented scaling ($1/3 < \gamma \leq 1/2$) is realized. Also, it can be inferred that use of an optimized and simplified roughness may overpredict the scaling exponent as opposed to its realistic version where all possible responses of the roughness elements are present.

Next, we delve into the production and dissipation of the turbulent kinetic energy (TKE) to see how they fare for the rough surfaces. Dynamical equation for the TKE budget is obtained by contracting the equation of velocity fluctuation and then effecting a suitable ensemble average (represented by overbar). The resulting TKE budget is

$$\underbrace{\frac{\partial}{\partial t}\left(\frac{1}{2}\overline{u_i'u_i'}\right) + U_j\frac{\partial}{\partial x_j}\left(\frac{1}{2}\overline{u_i'u_i'}\right)}_{A_K} = \underbrace{-\overline{u_i'u_j'}S_{ij}}_{P_S} + \underbrace{\overline{u_i'\theta'}\delta_{iy}}_{P_B} - \underbrace{2\sqrt{\frac{Pr}{Ra}}\overline{s_{ij}'s_{ij}'}}_{\epsilon} - \underbrace{\frac{\partial}{\partial x_j}\left(\overline{u_j'p'} + \frac{1}{2}\overline{u_i'u_i'u_j'} - 2\sqrt{\frac{Pr}{Ra}}\overline{u_i's_{ij}'}\right)}_{T_K}, \tag{4.1}$$

where the terms (left to right) are cast as advection A_K, shear production P_S, buoyancy production P_B, dissipation ϵ, and transport T_K of $1/2\ \overline{u_i'u_i'}$. Production terms P_S and P_B feed energy to the system to sustain turbulence, while ϵ denotes dissipation of energy due to viscous forces in action at small scales. In buoyancy driven flows, P_B is expected to be higher than P_S as the flow is driven by thermo-convective instabilities. An important insight about thermal convection is revealed when global contributions of the different terms in the TKE budget are considered. The volume-time averaged contributions of A_K, T_K, and P_S being negligible result in an exact balance between global buoyancy production (P_B) and turbulent dissipation (ϵ). In Table 4.3, a direct comparison is made between the present rough and the smooth surface [83] cases for volume-time averaged P_B, ϵ, and the Nusselt number. Note, in the present roughness configuration, there is a slight digression from the expected balance between the global P_B and ϵ. The exact reasons contributing to the deviation could not be comprehended. However, it is suspected that the nature of the roughness terrain plays a large role in determining how well the velocity gradients at the interface of the fluid and rough surfaces are calculated. The complex roughness terrain employed in the present study might be responsible for the observed slight imbalance. From Table 4.3, it can be observed that both $\langle P_B\rangle_{V,t}$ and $\langle\epsilon\rangle_{V,t}$ are higher for the present study. At the lowest Ra, P_B, ϵ, and *Nu* are comparable with their smooth surface counterparts, implying no change is induced by the roughness. However, at $Ra = 10^{10}$, both $\langle P_B\rangle_{V,t}$ and $\langle\epsilon\rangle_{V,t}$ are approximately two times higher (highlighted in bold) than their smooth surface counterparts. Increased P_B is a clear indicator of the enhanced heat transport, which highlights the usefulness

of employing roughness in RBC. It is important to address how roughness contributes to the enhanced buoyancy production. Zhang *et al.* [84] reported that rising and falling plumes exhibit high turbulent heat flux ($v'\theta'$) as well as high turbulent dissipation rates. In the same line we have shown above how plume emission multiplies at higher Ra. Thus, we may reason the augmentation of plume emission frequency as the cause of enhanced heat transport at higher Ra which appears through an increased buoyancy production.

Table 4.3: The effect of employing rough surfaces is highlighted by drawing a direct comparison with smooth surface case [83] for volume-time averaged turbulent buoyancy production P_B, dissipation (ϵ), and the Nusselt number (Nu).

	Smooth surface			Rough surface (present study)			Ratios (rough/smooth)		
Ra	$\langle P_B\rangle_{V,t}$ ($\times10^{-3}$)	$\langle\epsilon\rangle_{V,t}$ ($\times10^{-3}$)	$\langle Nu\rangle_{V,t}$	$\langle P_B\rangle_{V,t}$ ($\times10^{-3}$)	$\langle\epsilon\rangle_{V,t}$ ($\times10^{-3}$)	$\langle Nu\rangle_{V,t}$	$P_{B_{ratio}}$	ϵ_{ratio}	Nu_{ratio}
10^8	2.87	-2.87	24.97	3.22	-2.84	28.06	**1.12**	**0.99**	**1.12**
3×10^8	2.27	-2.28	34.14	3.09	-2.72	47.83	1.36	1.19	1.40
10^9	1.77	-1.73	47.37	2.87	-2.46	77.03	1.62	1.42	1.63
3×10^9	1.42	-1.41	66.44	2.52	-2.20	122.95	1.77	1.56	1.85
10^{10}	1.09	-1.01	93.28	2.38	-2.11	200.2	**2.18**	**2.09**	**2.15**

4.4 Plume statistics

Thermal plume is the coherent structure that contributes substantially in the heat transport process. A number of visualization studies [85–87] have identified thermal plumes as either mushroom or sheet-like structures. Plumes are formed near the isothermal walls from where they drift to the bulk region while carrying heat with them. To detect plumes from the turbulent background, the threshold technique suggested by Emran and Schumacher [88], where strong positive correlation between the vertical velocity (v') and temperature (θ') fluctuations indicate plume dominated regions, is implemented in the present work. Temperature fluctuation is defined as $\theta'(\boldsymbol{x},t)=\theta(\boldsymbol{x},t)-\langle\theta(\boldsymbol{x})\rangle_{A,t}$, while owing to $\langle v\rangle_{A,t}=0$, velocity fluctuation is taken as $v'(x,t)=v(x,t)$, where $\langle\,\rangle_{A,t}$ denotes averaging over horizontal plane and time. In the present study, decomposition of the whole domain, based on whether a region is dominated by plumes or background, is carried out using the following criteria,

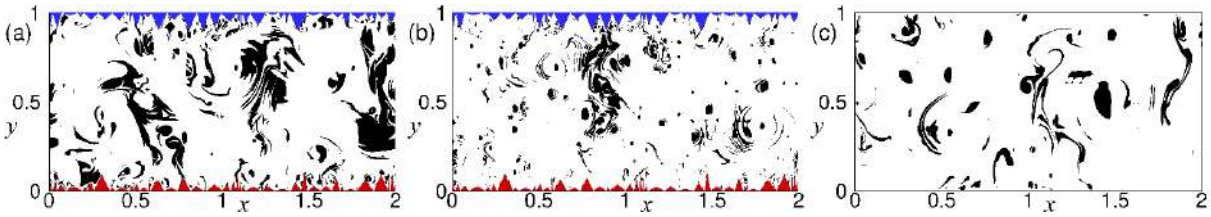

Figure 4.5: Plume (black) and background (white) regions are identified using a threshold $\delta = 5\%$ for (a) $Ra = 10^{10}$, (b) $Ra = 10^{11}$, and (c) $Ra = 10^{10}$ for the plane surface case. Note, frames (a) and (b) correspond to the same time instances as in Fig. 4.2.

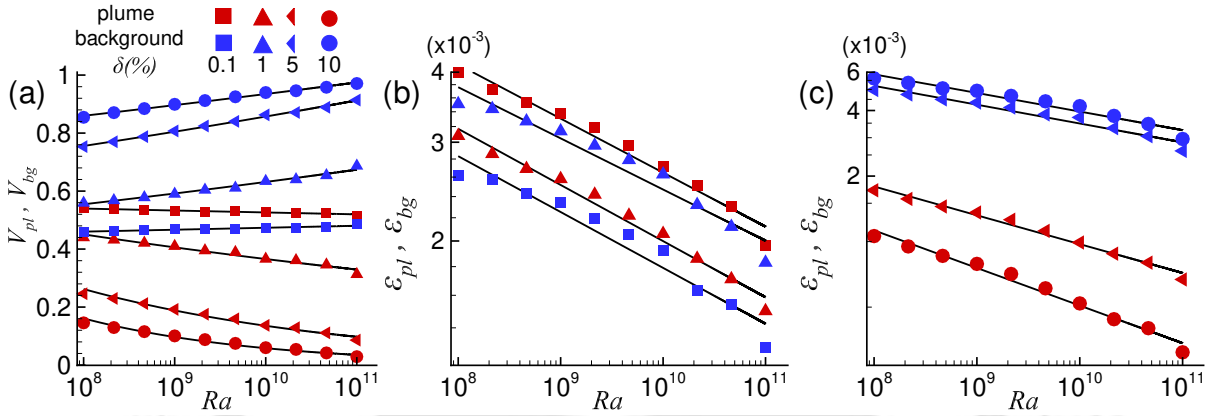

Figure 4.6: Ra and δ dependency of (a) volume fractions of plumes (V_{pl}) and background (V_{bg}) , (b) and (c) dissipation rates of plumes (ϵ_{pl}) and background (ϵ_{bg}). Note, ϵ_{pl} and ϵ_{bg} are shown for $\delta = 0.1$ and 1% in (b), whereas for $\delta = 5$ and 10% in (c). Symbols in red and blue correspond to plume and background, respectively, while solid black lines represent power law fittings.

$$V_{pl} = \boldsymbol{x} \in V : v'\theta'/\Gamma' > \delta$$
$$V_{bg} = \boldsymbol{x} \in V : v'\theta'/\Gamma' \leq \delta. \tag{4.2}$$

Here, V_{pl} and V_{bg} are the volume fractions of the plume and background dominated regions, respectively, Γ' represents instantaneous global maximum of $v'\theta'$, and δ is a free parameter that imposes the threshold criterion. The idea behind using different threshold values is to observe cut off dependency for plumes, if any. In the present work, four threshold values, δ = 0.1, 1, 5 and 10%, are used. In Fig. 4.5, instantaneously extracted plumes and background regions using the above criteria with $\delta = 5\%$ are shown for $Ra = 10^{10}$ and 10^{11} along with a case for the smooth surface at $Ra = 10^{10}$. Plume regions are clearly seen to expand with the introduction of roughness. While traces of remnant plumes are found near the roughened surface, they become stretched and scattered at higher Ra. Dependency of the volume fractions for plume and background regions on Ra for different threshold (δ) values is shown in Fig. 4.6(a). It can be observed that irrespective of δ, a decreasing trend of plume volume fractions is obtained with

Ra, while the background fractions compensate it. Clearly, a larger threshold turns out to be a stricter condition for a region to qualify as a plume.

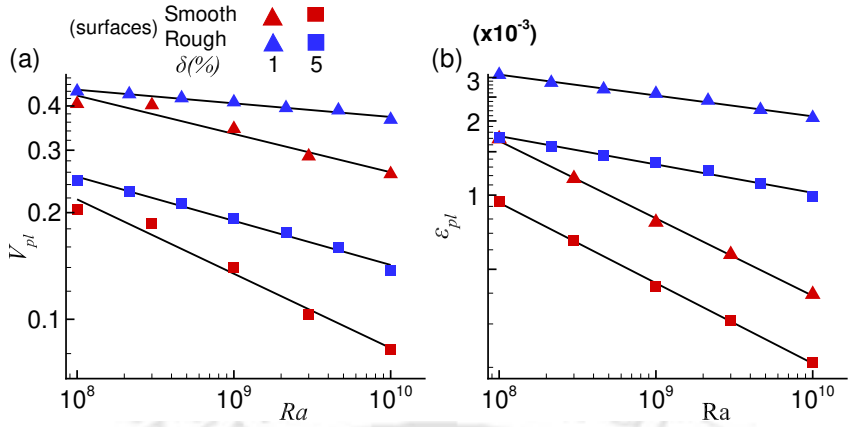

Figure 4.7: A comparison is made for the variation of (a) V_{pl} and (b) ϵ_{pl} with Ra between rough and smooth surfaces for $\delta = 1$ and 5%. Symbols in red and blue represent data for smooth [83] and present rough surfaces, respectively, and solid black lines represent power law fittings.

Table 4.4: Prefactor and exponent of the power-law fit, ARa^m, for the volume fractions and dissipation contributions of the plume and background at different thresholds.

	Volume fraction				Thermal dissipation			
δ (%)	A_{pl}	m_{pl}	A_{bg}	m_{bg}	A_{pl}	m_{pl}	A_{bg}	m_{bg}
0.1	0.597	−0.005	0.410	0.006	0.024	−0.096	0.018	−0.1
1	1.04	−0.045	0.329	0.028	0.02	−0.1	0.02	−0.091
5	3.67	−0.143	0.456	0.027	0.021	−0.132	0.026	−0.086
10	9.3	−0.22	0.615	0.018	0.027	−0.173	0.028	−0.085

A comparison of thermal dissipation rates, $\epsilon_\theta = (RaPr)^{-1/2}|\nabla\theta|^2$, of plume ($\epsilon_{pl}$) and background regions (ϵ_{bg}), which are obtained as

$$\epsilon_{pl} = \left\langle \int_{V_{pl}} \epsilon_\theta(\boldsymbol{x}, t) dV \right\rangle_t \qquad \text{and} \qquad \epsilon_{bg} = \left\langle \int_{V_{bg}} \epsilon_\theta(\boldsymbol{x}, t) dV \right\rangle_t,$$

indicate dominant heat transfer agent in the flow. Note, ϵ_{pl} and ϵ_{bg} represent total time-averaged contributions in thermal dissipation from plumes and background dominated regions, respectively. In Figs. 4.6(b) and 4.6(c), the variations of ϵ_{pl} and ϵ_{bg} are shown with increasing Ra. It can be observed that for all threshold (δ) values, contributions of both ϵ_{pl} and ϵ_{bg} decline as Ra increases. Interestingly, for $\delta = 0.1\%$, ϵ_{pl} exceeds ϵ_{bg} at all Ra, whereas for $\delta = 1, 5, 10\%$, ϵ_{bg} exceeds ϵ_{pl}. On the other hand, at a given Ra, with the increase in δ, ϵ_{bg} grows while ϵ_{pl}

decays. A larger δ allows larger background, which implies ϵ_{bg} contributions are incorporated from larger regions. On the other hand, for plumes, a larger δ yields smaller V_{pl} and hence ϵ_{pl} drops.

Further, using least squares fitting, power laws of the form ARa^m are obtained for both volume fractions and dissipation rate contributions of plumes and background at different δ values. The obtained fitting parameters are shown in Table 4.4. We observe that for all δ, m_{pl} is negative for V_{pl}, while m_{bg} is positive for V_{bg}. It implies that with increase in Ra, the effective region covered by plumes diminishes which is taken up by the background. The scaling exponents for both ϵ_{pl} and ϵ_{bg} are negative, implying reduced thermal dissipation at higher Ra. Note, the non-dimensional thermal dissipation rate (ϵ_θ) should not be confused with the dimensional one. The global dimensional thermal dissipation rate, denoted as $\epsilon_T = \alpha(\Delta T/H^2)Nu$, augments with increasing Ra owing to the elevated ΔT and *Nu*. However, the former obeys the following relation, $\langle\epsilon_\theta\rangle_V = \langle Nu\rangle_V/\sqrt{RaPr}$, which explains the observed diminution of net thermal dissipation rate ($\epsilon_{pl} + \epsilon_{bg}$) on amplification of the thermal forcing. For $\delta = 0.1\%$, the scaling exponents for volume fractions are very low indicating negligible variation of the volumes of plumes and background with increasing Ra, which is also evident from Fig. 4.6(a). It can be observed that with increase in δ, the scaling exponents for both V_{pl} and ϵ_{pl} increase in absolute sense, while for V_{bg} and ϵ_{bg}, they appear to be more stable. Further, to explain how roughness alters plume regions, variation of V_{pl} and ϵ_{pl} with Ra is compared with smooth surface case [83] for $\delta = 1$ and 5% in Fig. 4.7. It is clear that irrespective of δ, both V_{pl} and ϵ_{pl} are higher for the roughened surface with slower decay over increasing Ra. This re-emphasizes the effectiveness of rough surfaces in enhancing the plume emission process. Also, a slower decay rate of V_{pl} and ϵ_{pl} indicate that effect of roughness is sustained even at higher Ra. Though at higher threshold, plume regions follow a near identical behavior, dissipation contribution continues to dominate for the rough surface configuration.

4.5 Near-wall dynamics

Rough surfaces significantly alter the BL dynamics, which is responsible for the augmented heat flux above a threshold Ra. The ability of a rough surface in facilitating extra plume generation spots is its biggest asset in influencing flow structures and dynamics. In smooth surfaces, plume eruption is purely driven by buoyancy, whereas for rough surfaces, sharp edges promote flow separation and act as the active source of plume emission [40]. Three types of localized re-

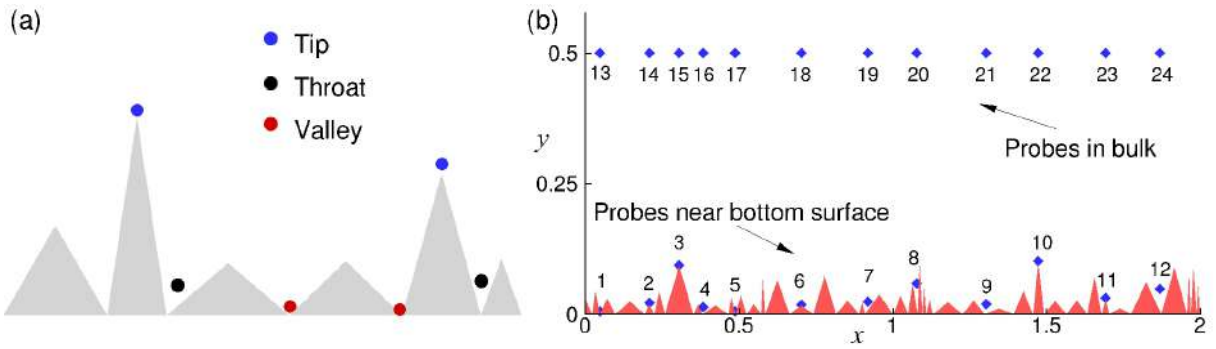

Figure 4.8: (a) A Schematic diagram showing tip, throat, and valley regions associated with a rough surface. (b) Location of numerical probes chosen in the vicinity of the bottom rough surface and bulk region shown in a magnified view.

gions with distinct flow features can be associated with a rough surface; above the tips, between two roughness elements (throat) and the lower point between them (valley). These regions are schematically shown in Fig. 4.8(a).

The region above the tip of the roughness elements (especially sharp ones) records high heat flux due to frequent emission of plumes whereas the throat and cavity regions exhibit the lowest heat flux due to immobility of the trapped fluid. Motion of fluid inside the cavities is enhanced with the increase in Ra and eventually the fluid becomes accessible to the bulk flow. Note, if the cavity region is too closely packed then fluid remains struck at even higher thermal forcing (Ra). To effectively study flow dynamics in the near-wall and bulk region, we have considered a total of 24 probes, half near the bottom rough surface and rest in the bulk region, as shown in Fig. 4.8(b). At the probes, time series data is recorded at a non-dimensional sampling rate of 100 units (after every $\Delta t = 10^{-2}$).

The transition of the flow states with increasing Ra in the throat and tip regions can be identified using the temperature and velocity fluctuations. In Fig. 4.9, time series of vertical velocity and temperature are shown for regions near the bottom rough surface for a small window of 5 time units at three different $Ra = 10^8, 10^{10}$, and 10^{11}. At the lowest $Ra = 10^8$, we observe both temperature and velocity fluctuations are minimum, with low vertical velocity and high mean temperature for both the tip and throat regions. It essentially indicates that the flow is nearly stagnant near the rough surface. With an increase in thermal forcing, the fluctuations increase for both the regions as bulk fluid approaches near-wall regions more effectively. Also, note that in general, both vertical velocity and temperature show larger fluctuations near the tips than throat regions at all Ra explored, which suggests that the major source of plume emission is the tip area of the roughness elements. At one extreme, deep down the throat, large-scale inhomogeneity is

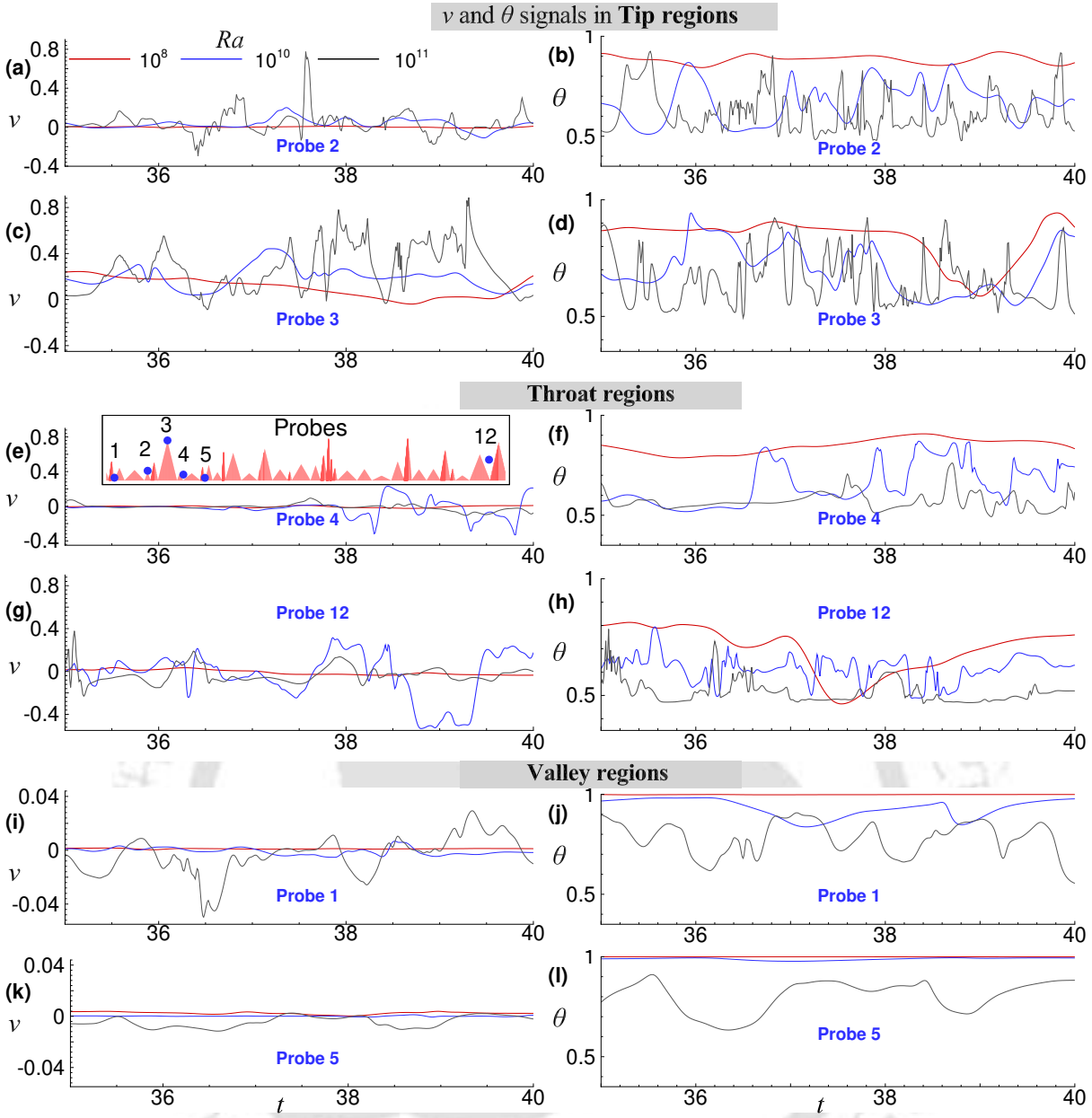

Figure 4.9: Time series of vertical velocity (left column) and temperature (right column) recorded from probes placed near the bottom rough surface are shown at $Ra = 10^8$, 10^{10}, and 10^{11} for a small window of 5 time units. Location of the probes (magnified view) is shown in the inset of frame (e).

evident as circulating fluid cannot reach there (see frames g and h). On the other extreme, near the tip of taller roughness, large oscillations are recorded owing to the interaction between newly formed plumes and large-scale rolls (see frames c and d). Greater mixing at the higher Ra is clearly seen through large fluctuations in vertical velocity with lower mean temperature. Thus, different relative locations near the wall do not contribute to plume emission and mixing with the same intensity. It indicates varied responses of the elements at different Ra owing to their

relatively distinct geometric features that essentially occur on a random surface texture.

In Fig. 4.10, PDFs (probability density functions) of temperature and vertical velocity, com-

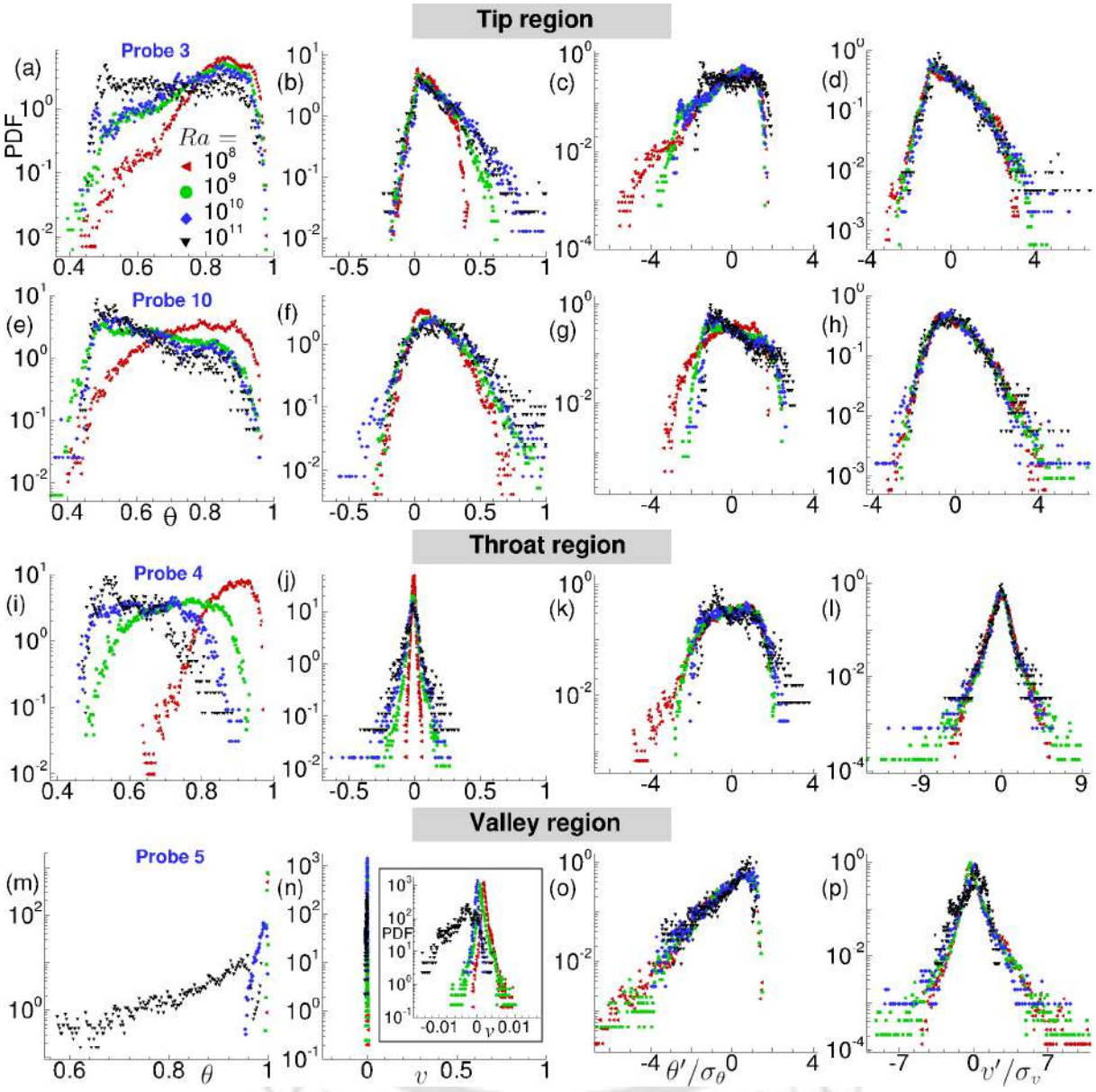

Figure 4.10: Columns from left to right shows PDFs of θ, v, θ'/σ_θ and v'/σ_v for probes placed near the bottom plate at different Ra. Note, each row represents the data for a particular probe, the inset in frame (n) shows the magnified view, and for location of the probes, Fig. 4.8(b) can be referred.

puted from the above signals, are shown in frames (a-h), while for their normalized fluctuations in frames (i-p). Note, to normalize the fluctuations their rms are used, which for a quantity ϕ is defined as $\sigma_\phi^2 = \overline{\phi(t)^2} - \left(\overline{\phi}\right)^2$, where overbar denotes temporal average. From temperature PDFs, it can be observed that, in general, at the lowest $Ra = 10^8$, higher mean temperature (especially in throat region) is expected as peaks of the temperature PDFs are skewed towards high

temperature. However, with increase in Ra, there is increased probability of the lower temperature readings, and at the highest $Ra = 10^{11}$, the peaks are skewed towards the lower temperature. This also hints that at lower Ra, either plume emission frequency is lower or fluid is stuck. On the other hand, at higher Ra, hot plumes are emitted frequently and cold fluid rushes towards the plume emitting spots, which explains the lower mean temperature. PDFs of the normalized temperature fluctuations are seen to collapse onto one another in the core, while the tails show deviation. However, the PDFs have overall different shapes for different regions, implying temperature fluctuations are locally influenced by the roughness elements.

Vertical velocity PDFs being narrower at the lowest $Ra = 10^8$ clearly signify immobility of the fluid. However, with the increased Ra, occurrence of events with large vertical velocity is augmented. The PDFs for the tip regions have longer positive tails which further extend with increase in Ra, whereas in the throat regions, they are symmetric about the zero-mean. Also, they exhibit nearly equal affinity for both positive and negative vertical velocity in the throat regions such that the maximum absolute v is less than that is observed in the tip regions. Peak regions which are surrounded by the roughness of different aspect ratio show clearly different flow behavior. Though probes 3 and 10 are closer to the bulk, the slender one (probe 10) exhibits a near-symmetric Gaussian distribution for v, while at location 3, no extreme events for $v < 0$ are recorded. This again indicates the varied response of the peaks to the nearest large-scale roll. Similarly different cavity regions evolve differently with Ra. For instance, probes 4 and 5 exhibit totally contrasting PDFs for both θ and v. Fluid region depicted by probe 5 is too closely packed between the neighboring elements such that it is inaccessible to the bulk flow even at a higher Ra whereas probe 4 is accessible to the bulk flow at higher Ra. Also, the role played by the tip regions in emitting plumes is highlighted from the PDFs of the vertical velocity exhibiting a higher probability for the positive fluctuations. Thus, we show that a randomly distributed roughness has a varied influence on the flow dynamics, and it cannot be characterized unilaterally.

Use of rough surfaces is desired to yield enhancement in heat transport which is not easily achieved at a lower Ra. Improvement of plume emission process is reflected in the increased temperature and vertical velocity fluctuations. In Fig. 4.11, rms of temperature and vertical velocity fluctuations, denoted by σ_θ and σ_v, respectively, are shown for the throat and tip regions in the explored Ra range. It can be observed that, in general σ_θ and σ_v are higher near the tips. While velocity fluctuation is seen to increase monotonically, temperature fluctuation peaks at an intermediate Ra ($\approx 2.15 \times 10^9$) followed by a drop at a higher Ra. The reason for the decrease

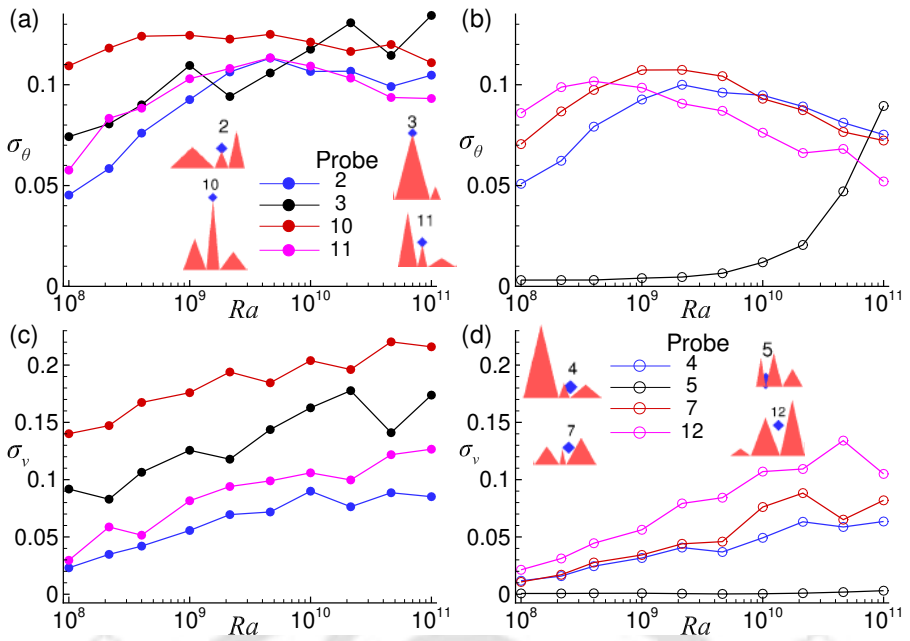

Figure 4.11: Root mean square of fluctuations of temperature (σ_θ) and vertical velocity (σ_v) are shown for probes in throat and tip regions as a function of Ra. At the lowest $Ra = 10^8$, σ_θ is lowest as rough surfaces are embedded inside the thermal boundary layer (TBL). As they start to perturb TBL, increase in σ_θ is perceived. However, enhanced penetration of the bulk flow inside the near-wall regions at higher Ra damps out σ_θ. For σ_v, a consistent increasing trend with Ra is observed, signifying mobility of the flow in the cavities.

of σ_θ in throats is attributed to the effective bulk-BL interaction where a nearly homogeneous bulk fluid is now accessing and mixing well with the fluid in the cavity regions. With increasing influence of the bulk-BL interaction, temperature fluctuations are damped out, though vertical velocity fluctuations continue to amplify as fluid now can move quickly in or out of the cavity regions. In the higher Ra range, drop in σ_θ is more prominent in the throats as tip regions continue to be the preferred spots for nucleation of the plumes, which explains why σ_θ for tips is higher even at the higher Ra range. For vertical velocity fluctuations, near-tip regions corresponding to taller roughness elements (probe 10), and spacious throat regions (probe 12) yield higher σ_v owing to the greater mobility in these regions. Note, the fluid region corresponding to probe 5, which is closely packed between the neighboring roughness elements, shows negligible vertical velocity fluctuations, whereas temperature fluctuations are enhanced above $Ra = 10^{10}$. It implies that fluid is severely trapped in this region, and only in the higher Ra range significant temperature fluctuations are observed.

We observe that more spacious the throat region is, sooner σ_θ attains the peak. It indicates why maximum σ_θ for probe 12 is attained at $Ra = 4.64 \times 10^8$, while for probes 4 and 7 it is

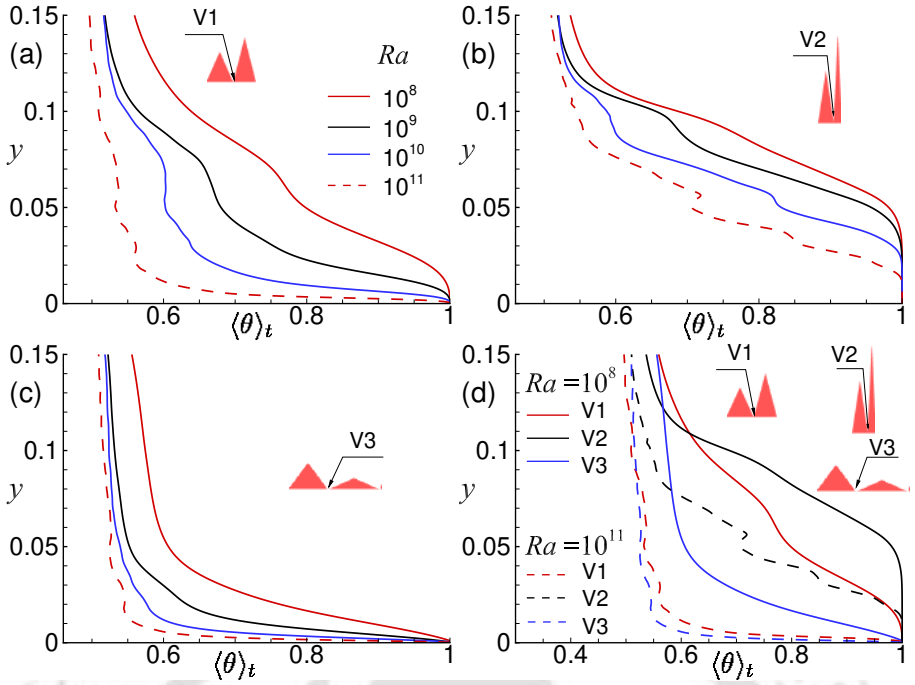

Figure 4.12: Vertical mean temperature $\left(\langle\theta\rangle_t\right)$ profile passing through three different valley regions V1, V2, and V3 near the bottom plate shown in frames (a), (b), and (c), respectively, with increasing Ra. In frame (d), $\langle\theta\rangle_t$ profiles for the valley regions are compared for the two extreme Ra (10^8 and 10^{11}). Note, frames (a-c) follow the same legends.

delayed to $Ra = 2.15 \times 10^9$. It is to be noted that closely packed regions can only be ventilated effectively by the bulk fluid at a higher Ra, where temperature fluctuations are damped. This is the reason why σ_θ monotonically increases for probe 5. At the higher end of Ra, bulk fluid finally washes out the trapped fluid from the throat region of probe 5 and effects strong mixing leading to a decrease in temperature fluctuations. Further, it can be observed that flow near smaller peaks (2 and 11) have lower values of σ_θ at $Ra = 10^8$, but with the increase in Ra, σ_θ increases such that for $Ra > 10^9$, it becomes comparable to that observed for taller roughness elements (3 and 10). This implies that small-scale roughness elements are particularly activated at a higher Ra, causing increased temperature fluctuations because of the increased plume emission.

Next, we attempt to bring out the effect of different cavity regions on flow behavior by analyzing vertical time-averaged temperature, $\langle\theta\rangle_t$, profiles. In Fig. 4.12, mean temperature profiles at different valleys (V1, V2 and V3) near the bottom plate are shown with increasing Ra. The region corresponding to valley V3 is most spacious, while valley V2 is highly confined. It can be observed that the mean temperatures for V1 and V2 valleys, at $Ra = 10^8$, are nearly unity for a layer of fluid close to the wall. Note, the fluid layer with nearly zero temperature gradient is

thicker in V2 than V1. However, for V3, this layer is hardly visible as fluid is least confined, and hence, heat is diffused effectively in the vertical direction. Due to the severe confinement of fluid near the valley region, such a layer is observed. In the absence of confinement, a linearly varying thin layer is observed where temperature drops sharply. With the increase in Ra, temperature gradient increases significantly resulting in a very thin layer over which practically half of the net imposed temperature drop occurs.

Note, in the succeeding discussion, the layer with a steep temperature gradient is discussed

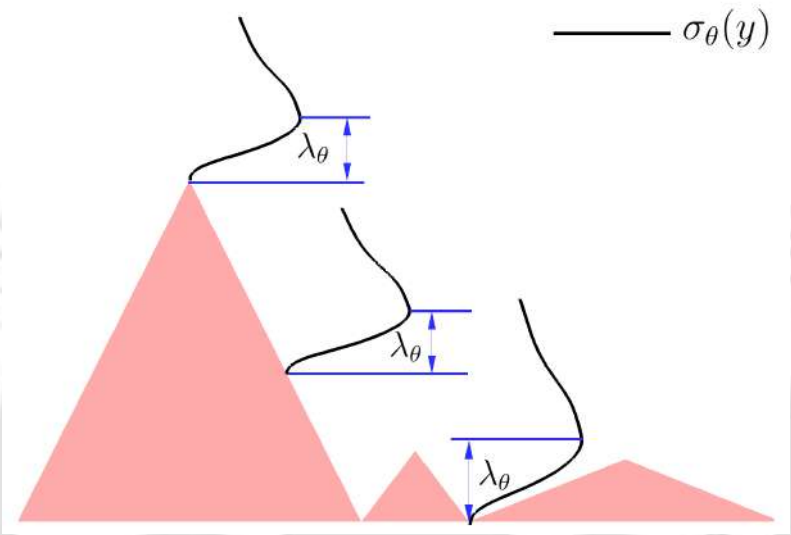

Figure 4.13: Schematic showing geometrical construction of TBL thickness (λ_θ). Note, profiles of temperature fluctuation starts on the surface of a roughness element and λ_θ is measured accordingly.

for the valleys, while the layer with trivial temperature gradient is not taken into consideration. It can be observed that $\langle\theta\rangle_t$ is steepest for V3, while for V2, it is flattest for any Ra. At the highest $Ra = 10^{11}$, $\langle\theta\rangle_t$ profiles for V1 and V3 are nearly same, as shown in frame (d) of Fig. 4.12, while V2 still exhibits smaller temperature gradients. This implies that as V1 is effectively washed out at $Ra = 10^{11}$, the flow characteristics become similar to V3, which is least confined and ventilated effectively by bulk fluid even at lower Ra. However, as V2 is severely confined, heat is diffused slowly in the vertical direction even at $Ra = 10^{11}$ with the cavity region is just starting to get washed out, resulting in flattest $\langle\theta\rangle_t$.

In the present work, $\langle\theta\rangle_t$ profiles passing through three different valleys of the bottom plate illustrates the effect of roughness wavelength on the heat transfer. It has been observed that flow structures are dependent on both Ra and wavelength of the roughness elements [32, 39, 41, 42]. When elements are well spaced, and thermal forcing is strong enough to effect mixing in the

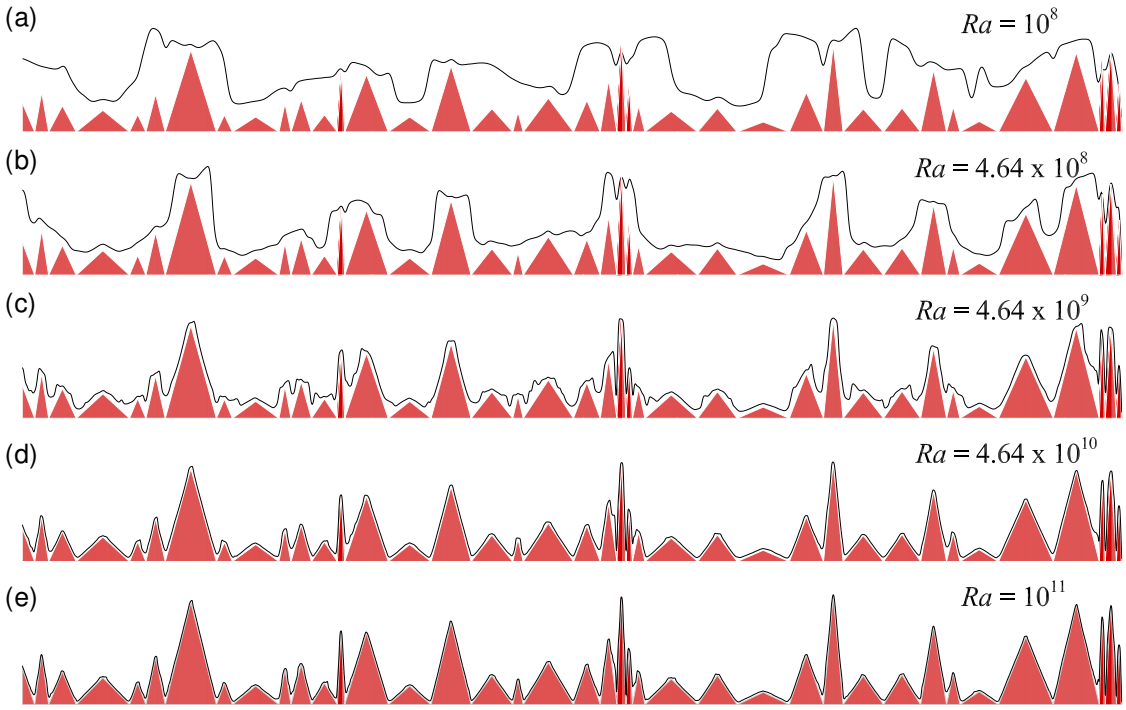

Figure 4.14: Variation of TBL thickness (λ_θ) over the bottom rough surface with increasing Ra where λ_θ is shown by black solid lines. At the lowest $Ra = 10^8$, only taller roughness elements protrude TBL, but with the increase in Ra, smaller elements start to protrude. At the highest $Ra = 10^{11}$, a thin uniform TBL, except at the valleys, is seen to cover the rough surface.

cavities, steeper $\langle\theta\rangle_t$ similar to the one in smooth surfaces is observed early. But for closely packed cavities, effective mixing of fluid is achieved at a much higher Ra, and hence, steeper $\langle\theta\rangle_t$ profiles are achieved late. Highly confined cavity regions do not assist in enhancing heat transfer at low to moderate Ra owing to the lack of mobility of the fluid inside them. However, in the higher Ra range, as flow structures become finer, mobility is increased and hence, these regions start to augment heat transfer. The same observation can be made from $\langle\theta\rangle_t$ profiles for V2. As the profiles, even at the highest $Ra = 10^{11}$, are still making the transition to a steeper smooth-surface like profiles, flow behavior in these regions is still influenced by the rough surfaces. It is also known that when cavities are only partly washed by the bulk flow, enhanced heat transport scaling is achieved [41]. This explains why closely packed regions yield favorable results in the higher Ra. The cavities which are dormant (stagnant fluid) at lower Ra range starts to get washed away by the bulk fluid in the higher Ra range. This implies that at the higher Ra, roughness elements of smaller amplitude (small tips) or smaller wavelength (highly confined regions) are useful in retarding the arrival of the classical $1/3$ scaling. Note, it is expected that for a very high thermal forcing $Ra >> 10^{11}$, the effect of the regions with smaller wavelength

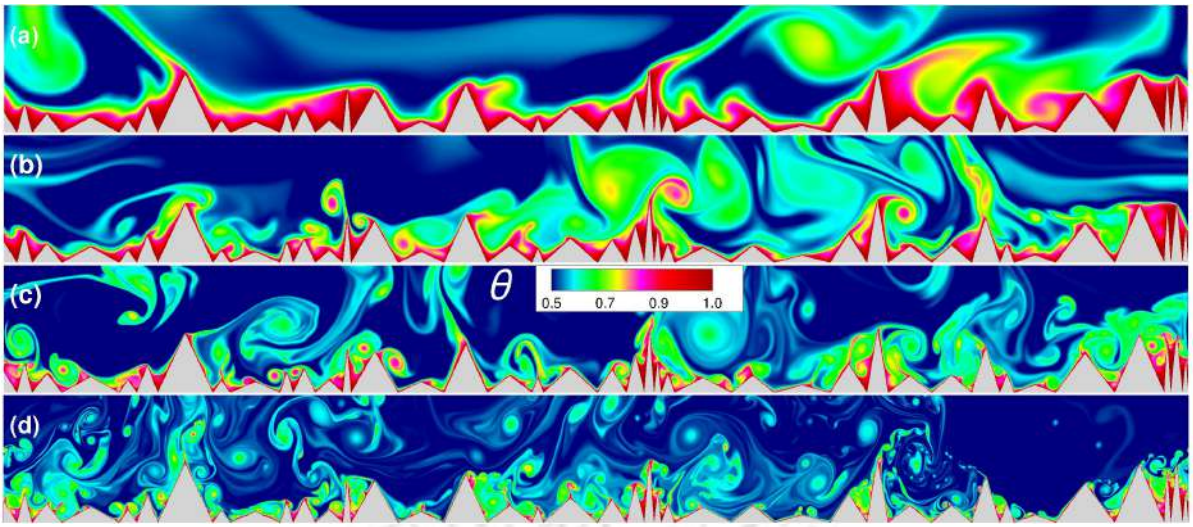

Figure 4.15: Instantaneous temperature field for near-wall region corresponding to the hot bottom plate for (a) $Ra = 10^8$, (b) 10^9, (c) 10^{10}, and (d) 10^{11}. At the lowest Ra, plumes are of larger size with a few emitting spots, however, as Ra increases there is a surge in plume emitting spots with visibly finer flow structures. Also, the ability of the bulk fluid to invade highly confined cavity or tip regions of the smaller roughness elements is significantly enhanced at a higher Ra, which augments heat transfer.

or severe confinement would also cease to exist, where $\langle\theta\rangle_t$ profiles for V1, V2, and V3 will become identical. Thus, inclusion of very small wavelength elements acts as a remedy to cast away the classical scaling and thus, extending the range of the augmented heat transfer scaling.

In thermal convection role of TBL (λ_θ) is pivotal. The transition of TBL attached to the isothermal plate to turbulent state is still believed to have links with the so-called $1/2$ scaling regime. For the smooth plates, BL dominated flow at low Ra makes a transition to bulk dominated flow [10, 19] at high Ra, rendering $1/2$ scaling regime. This idea has recently been modified. With the addition of roughness, bulk-dominated flow at lower Ra was reported [41] to change to BL based at high Ra, reviving the classical $1/3$ scaling. It also implies that the roles of BL and bulk are reversed. A thin covering of TBL in the higher Ra range was reasoned to explain the fallback to $1/3$ scaling [41] after a stint in $1/2$ scaling [39]. In the current work, λ_θ is calculated by taking the edge of the TBL at the position where temperature fluctuations are maximum [89], as shown by a schematic in Fig. 4.13. The computed BL profile along the x direction is shown in Fig. 4.14 where roughness elements are also placed for better visibility of λ_θ. At the lowest $Ra = 10^8$, taller roughness elements protrude the TBL and thus are the major benefactor in enhancing heat transfer. With an increase in Ra, λ_θ becomes thinner, and smaller roughness elements start to protrude TBL. The smaller elements play an important role

in sustaining the plumes emission at higher Ra. At the highest $Ra = 10^{11}$, a nearly thin uniform TBL, except at the valleys, is formed along the rough surface. Note that for the valley regions, where the fluid is least mobile, a higher λ_θ is obtained. It is interesting to note that more the confinement is, thicker λ_θ is. Previously, Zhu *et al.* [42] predicted that the formation of a thin uniform TBL would lead to the classical $1/3$ scaling. Remarkably, in spite of a thin covering of the TBL with increasing Ra, the $Nu(Ra)$ scaling does not saturate to the classical $1/3$ law at a very high Ra when random roughness is used. This again indicates the complex role of multi-scale roughness in turbulent convection.

To visualize local flow structures, instantaneous temperature field in the near-wall region of the bottom hot plate is shown in Fig. 4.15. It is evident that at $Ra = 10^8$, the roughness elements are covered by a thick layer of hot fluid, implying flow is stagnant near the surface. Also, plumes, which are emitted from the taller elements, are of larger size. With the increase in Ra, the layer of hot fluid covering the surface starts to become thinner, and the fluid inside the cavities starts to move out of it. Also, plumes become finer with a surge in nucleation sites owing to the increased contributions from the smaller elements. At the highest $Ra = 10^{11}$, plumes are extremely fine, and almost all the elements are actively participating in plume emission. Further, penetration of the bulk fluid inside the cavities is maximized, due to which highly confined regions also start to become accessible to the bulk. Though flow structures become finer, enhancement in heat transfer occurs with the increase in plume emission sites at the highest Ra, which primarily contributes in sustaining the enhanced heat transport regime.

Enhancement in heat transfer depends on the amplitude [32] and wavelength [39] of roughness elements. When the amplitude is of the order of the TBL thickness enhancement in heat transfer is perceived, which is observed in the present study from instantaneous temperature contours, PDFs, and time series of temperature and vertical velocity. This explains why smaller roughness elements play an important role in sustaining heat transfer at the higher Ra range. Previously, Toppaladoddi *et al.* [39] explored the effect of the wavelength through sinusoidal roughness on the scaling exponent, where it was observed that too large or small wavelength yields the scaling exponent close to $1/3$. However, the range ($4 \times 10^6 \leq Ra \leq 3 \times 10^9$) explored by them was not high to realize the propitious results of the rough surface with a small wavelength. Later, Zhang *et al.* [32], in their study with mono-scale triangular roughness, established the efficacy of the rough surfaces with smaller amplitude by highlighting that the critical height (h_c) of the rough surfaces signifying enhanced heat transfer in comparison to smooth surfaces decreases with Ra as $h_c \sim Ra^{-0.6}$. Zhu *et al.* [41, 42] took into account the effect of both

the parameters together by introducing roughness aspect ratio defined as the ratio of amplitude to the wavelength of roughness elements. Also, they ran different tests to ascertain the optimum roughness aspect ratio yielding maximum scaling exponent, which was reported as unity. This implies that rough surfaces with smaller amplitude and wavelength are highly effective at a higher Ra. The results obtained for our multi-scale random roughness configuration are in agreement with the above observations. Hence, the inclusion of random roughness has proved to be highly beneficial in sustaining enhanced heat transfer even at the higher Ra range owing to the creation of different local regions which get activated at different thermal forcings.

The attempt of incorporating multi-scale roughness paid off outstandingly such that different relative locations contributed differently in the plume emission process to avoid saturation of the increased heat transfer scaling. Taller roughness elements exhibited large temperature fluctuations at lower Ra while throat regions were dormant initially. However, with increasing thermal forcing, contributions from the throat regions further propelled the separation of the plumes from the tip regions. Though a thin TBL is formed at a higher Ra, increased contributions from the small-scale elements and the activation of the highly confined regions continued to amplify the overall perturbations in the near-wall regions leading to enhanced heat transport. TBL envelopes roughness elements hierarchically, starting from the tallest to the shortest with increasing thermal forcing. However, the complex texture of the roughness acts as a deterrent to uniform covering of TBL over it. Thus, the earlier reported state where the rough surfaces were practically reduced to smooth only with extended wetted surface area is deferred.

4.6 Bulk dynamics

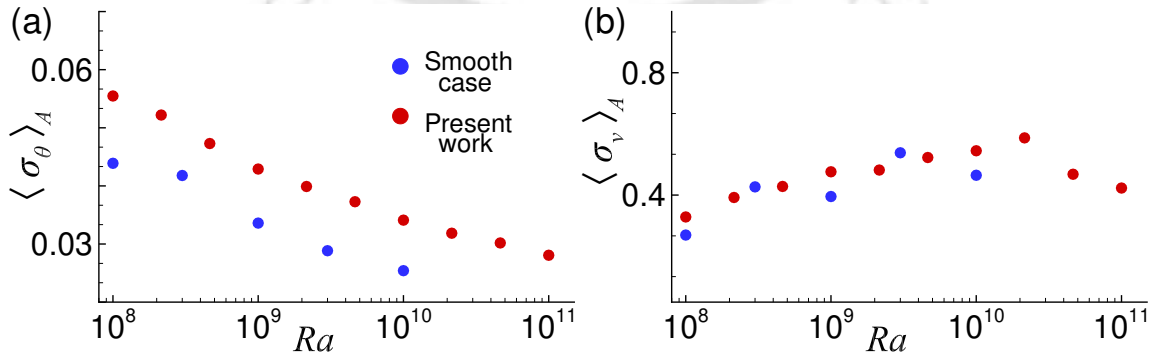

Figure 4.16: Variation of horizontally averaged root mean square of fluctuations of (a) temperature (σ_θ) and (b) vertical velocity (σ_v) at mid-height of the cell ($y = 0.5$) as a function of Ra. For comparison, the data corresponding to the smooth surface [83] is also shown.

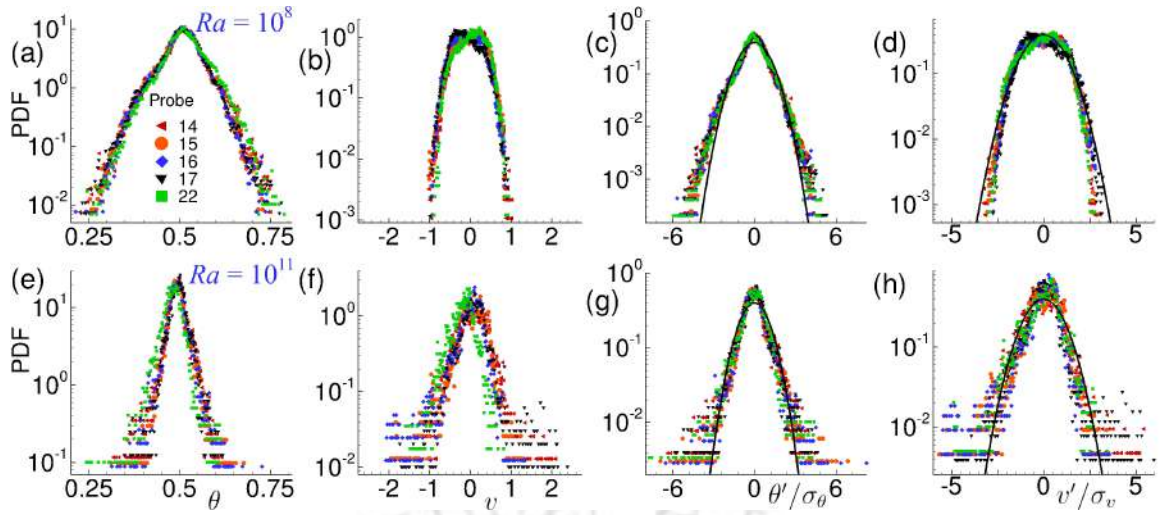

Figure 4.17: PDFs of (a,e) temperature (θ), (b,f) vertical velocity (v), normalized fluctuations of (c,g) temperature (θ'/σ_θ) and (d,h) vertical velocity (v'/σ_v) for probes in bulk. Note, top row corresponds to the lowest $Ra = 10^8$ while bottom row is for the highest $Ra = 10^{11}$, the solid lines in the last two columns represent the Gaussian function, and location of the probes can be referred from Fig. 4.8(b).

We now turn our attention to the flow dynamics away from the rough surfaces. With plumes emitting from the rough surfaces and moving into the bulk region, the fluctuations are brought about by them. In line with the results of a number of studies [40, 90], the increased temperature fluctuations in comparison to the smooth case are observed in the present study. In Fig. 4.16, horizontally averaged rms of temperature (σ_θ) and vertical fluctuations (σ_v) at midheight of the cell ($y = 0.5$) are shown along with the smooth case counterparts [83] as a function of Ra. It is clearly evident that σ_θ is magnified in the presence of the rough surfaces, while σ_v is comparable to that observed in smooth case. Also, distinct nature of v' and θ' is unveiled with σ_θ decreasing monotonically with increasing Ra, while large amplitude v' are marked by the peak in σ_v at higher Ra. Surprisingly, σ_v, as opposed to σ_θ, increases monotonically before reaching a peak near $Ra = 2.15 \times 10^{10}$. The difference in the trend for σ_v and σ_θ can be attributed to the interaction of the high-intensity rolls with the background, which causes large-amplitude vertical velocity fluctuations at a higher Ra while temperature oscillations are damped out due to vigorous mixing of the fluid.

The scattered and skewed distribution of θ' is not expected in the bulk as polarized fluctuations near the wall give way to oscillations about the bulk mean temperature. In Fig. 4.17 we observe that the PDFs, corresponding to different probes in bulk, overlap with each other at a particular Ra, signifying that the overall flow behavior is nearly the same at different horizontal

locations in the bulk. At the lowest $Ra = 10^8$, they are wider about the mean ($\theta = 0.5$), but with the increase in Ra, they become narrower, implying the probability of occurrence of the structures with large temperature gradient is diminished, and at the same time, bulk fluid approaches a uniform temperature ($\theta = 0.5$). Non-obeyance of the Gaussian distribution [2, 91, 92] near the tails of the PDFs of v' and θ' at $Ra = 10^{11}$ reflects the intermittent appearance of the large amplitude events in the bulk, which are significantly enhanced with the introduction of the random rough surface.

Power spectra of the vertical velocity and temperature in the bulk can be analyzed to evaluate energy cascade and the associated small-scale dynamics. The slope in the inertial subrange [63, 93] is of particular interest to the research community. The classical view of the scaling in the inertial subrange is that for a homogeneous and isotropic flow, temperature and velocity fluctuations follow Kolmogorov's (K41) [62, 67, 68] scaling. Obeyance of the K41 scaling implies that temperature is a passive scalar. However, for an anisotropic flow, BO59 scaling proposed by Bolgiano [55] and Obukhov [54] is expected for the fluctuations where temperature exhibits characteristics of an active scalar. According to the K41 scaling, the slope in the inertial subrange for both velocity and temperature spectra is $-5/3$, while for the BO59 scaling, the slope becomes $-7/5$ for temperature as opposed to $-11/5$ for velocity.

In Fig. 4.18, power spectra of temperature and vertical velocity are shown for three probes in the bulk, one above a throat region while remaining two are directly above the tips, at three different $Ra = 10^9, 10^{10}$ and 10^{11}. It can be observed that both temperature and velocity follow BO59 scaling as the slope in the inertial subrange is close to $-7/5$ and $-11/5$ for temperature and velocity, respectively. The same observation is also evident from compensated plots of temperature and vertical velocity spectra in frames (d-f) and (j-l) of Fig. 4.18, respectively. It is evident that with the increase in Ra, the inertial range obeying BO59 scaling also widens. Previously, Stringano *et al.* [40] in their study in a cylindrical cell with grooved surfaces reported BO59 scaling for temperature and K41 scaling for vertical velocity in the bulk of the flow. However, in the present study, we observe that temperature behaves as a pure active scalar. Also, the spectra for the present work are compared with that observed for the smooth surface case [83] at $Ra = 10^8$ and 10^{10} at mid-height of the cell, as shown in Fig. 4.19. At $Ra = 10^8$, both temperature and velocity spectra are comparable with that observed for the smooth case, which signifies nearly same level of fluctuations. However, at $Ra = 10^{10}$, both the spectra show increased energy at all scales of the flow in comparison to smooth surface, highlighting the effectiveness of the roughness at higher Ra. Thus, the presence of the random roughness is perceived in the

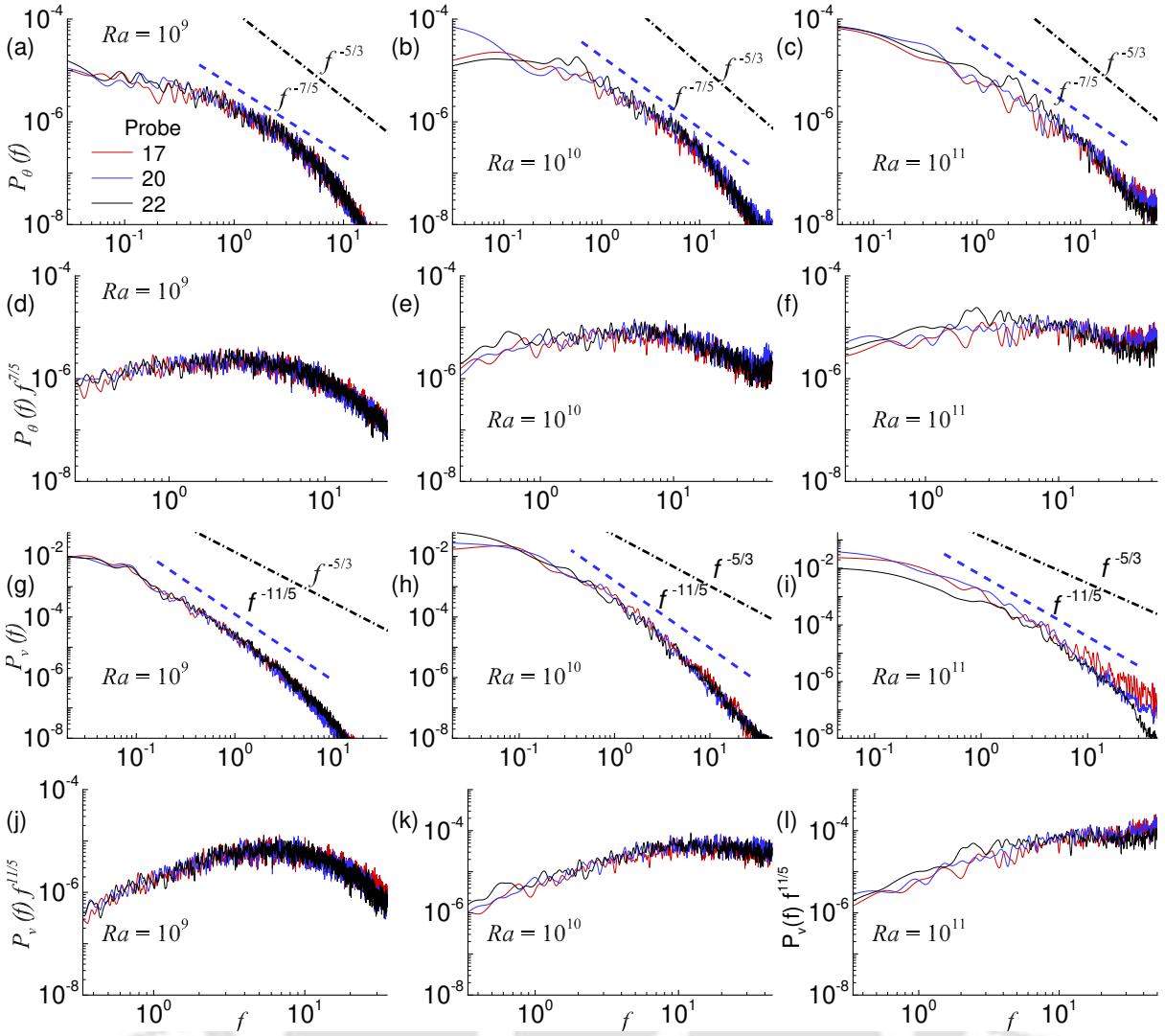

Figure 4.18: Power spectra of temperature (a-c) and vertical velocity (g-i) for the bulk at three different $Ra = 10^9, 10^{10}$ and 10^{11}. The corresponding compensated plots of temperature (d-f) and vertical velocity (j-l) spectra are also shown. Note, the dashed line represents Bolgiano and Obukhov's (BO59) scaling [54, 55] whose slope is $-7/5$ and $-11/5$ for temperature and vertical velocity spectra, respectively. Further, the dash-dot line serving as a reference for Kolmogorov's (K41) scaling is shown. For location of the probes refer Fig. 4.8(b).

bulk through increased temperature fluctuations in comparison to the smooth cell. Though flow homogeneity in temperature sense increases with Ra, its fluctuations continue to be higher than the smooth cell due to the increased presence of plumes emitted from the rough surfaces in the bulk.

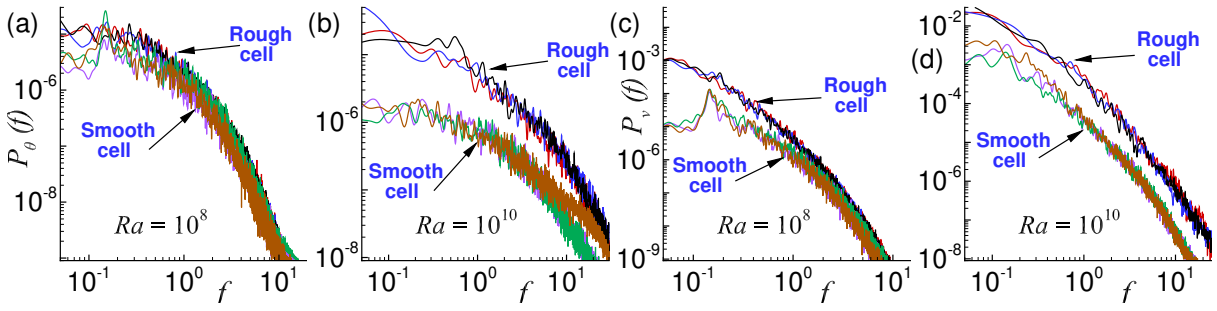

Figure 4.19: Power spectra of temperature (a-b) and vertical velocity (c-d) for the rough cell are compared with that observed for the smooth surface case [83] at $Ra = 10^8$ and 10^{10} for probes considered at mid-height of the cells at three different horizontal locations ($x = 0.5, 1, 1.5$).

4.7 Small-scale statistics

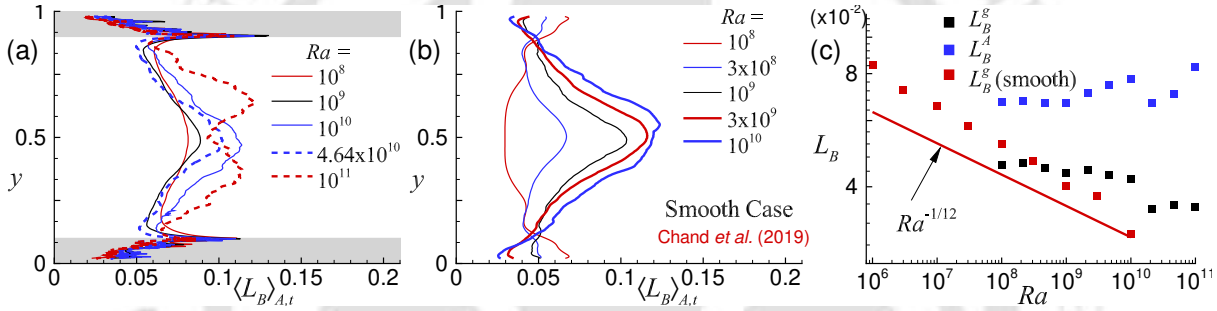

Figure 4.20: Variation of horizontally-time averaged Bolgiano length scale $\langle L_B \rangle_{A,t} = \langle \epsilon_u \rangle_{A,t}^{5/4} \langle \epsilon_\theta \rangle_{A,t}^{-3/4}$ as a function of vertical distance y in (a) the present roughness set-up and (b) smooth surface case [83] for different Ra. (c) Global Bolgiano length scale L_B^g and L_B^A as a function of Ra. Also, L_B^g for smooth plates [83] is shown. Note, $L_B^g = \langle \epsilon_u \rangle_{V,t}^{5/4} \langle \epsilon_\theta \rangle_{V,t}^{-3/4}$, while L_B^A is obtained by taking vertical average of $\langle L_B \rangle_{A,t}$. The vertical extent of the shaded regions in frame (a) represents the maximum height of the roughness elements.

In turbulent RBC, the imposed temperature difference between the plates induces buoyancy force, which sets the fluid in motion. According to Richardson [94], the energy from the large-scale eddies is passed on to the smaller eddies till it is dissipated at small scales where molecular diffusivity becomes predominant. The process of transfer of energy in the inertial subrange holds the answers to various scaling laws followed by velocity and temperature fluctuations [63, 65, 69, 70]. In view of homogeneous and isotropic flow [62, 67, 68], temperature is treated as a passive scalar and the effect of buoyancy force at small scales is neglected. The scalings for the fluctuations can be found out by invoking energy balance between the energy transfer and

dissipation

$$\epsilon_u \sim \frac{(\delta u)^3}{l}, \qquad \epsilon_T \sim \frac{\delta u(\delta T)^2}{l}$$
$$\implies \delta u \sim \epsilon_u^{1/3}\ l^{1/3}, \qquad \delta T \sim \epsilon_u^{-1/6}\epsilon_T^{1/2} l^{1/3},$$

where δu and δT are the difference in velocity (u) and temperature between two points separated by a distance l, respectively, ϵ_u is the viscous dissipation while ϵ_T represents thermal dissipation. Another viewpoint for scaling in the inertial subrange was proposed by Bolgiano [55] and Obukhov [54], where above a characteristic length scale, defined as the Bolgiano length scale (L_B), buoyancy forces become important. Now the scaling for the velocity fluctuations are found out by invoking energy balance between the down-scale energy transfer and buoyancy production, while for temperature fluctuations, the energy transfer is again balanced by the thermal dissipation

$$\frac{(\delta u)^3}{l} \sim \beta g\, \delta u\, \delta T, \qquad \epsilon_T \sim \frac{\delta u(\delta T)^2}{l}$$
$$\implies \delta u \sim (\beta g)^{2/5}\epsilon_T^{1/5} l^{3/5}, \qquad \delta T \sim (\beta g)^{-1/5}\epsilon_T^{2/5} l^{1/5}$$

Ideally, for scales $\eta \ll l \ll L_B$, the Kolmogorov's K41 scaling should be realized while for $L_B \ll l \ll H$, Bolgiano and Obukhov's BO59 scaling is expected [63], where η and H are the Kolmogorov length scale and height of the cell, respectively. The cross-over between these two scalings yields the Bolgiano length scale, which implies

$$\epsilon_u^{1/3} L_B^{1/3} = (\beta g)^{2/5}\epsilon_T^{1/5} L_B^{3/5} \qquad \text{or} \qquad \epsilon_u^{-1/6}\epsilon_T^{1/2} L_B^{1/3} = (\beta g)^{-1/5}\epsilon_T^{2/5} L_B^{1/5}$$
$$\implies L_B = (\beta g)^{-3/2}\epsilon_u^{5/4}\epsilon_T^{-3/4}$$

In the non-dimensionalized form, L_B is found as

$$L_B = \epsilon_u^{5/4}\epsilon_\theta^{-3/4} \tag{4.3}$$

where $\epsilon_u, \epsilon_\theta$ are computed from the non-dimensional field. In turbulent RBC, simultaneous existence of both the scalings is usually not observed [63]. Also, whether BO59 scaling, which was first proposed for stably stratified flows, exists for RBC is still unresolved. Kunnen *et al.* [65] and Kunnen and Clercx [66] addressed the relation between mean Bolgiano length scale (using global values of the dissipation rates) and BO59 scaling. They proposed that L_B should be considered locally while looking for BO59 scaling as the order of magnitude of the dissipation rates is substantially high in the near-wall regions in comparison to the bulk. Local L_B attains small values close to the isothermal walls, while it has large values in the bulk region. Further,

it increases with an increase in Ra in the bulk region, while mean/global L_B decreases with Ra. This highlights the subtleties to consider while deducing the relationship between the order of L_B and the possible scaling for the fluctuations.

To verify the existence of the Bolgiano scaling in the bulk region, as observed from Fig. 4.18, we explore different measures of L_B. In Fig. 4.20(a), vertical variation of horizontally time-averaged Bolgiano length $\langle L_B \rangle_{A,t} = \langle \epsilon_u \rangle_{A,t}^{5/4} \langle \epsilon_\theta \rangle_{A,t}^{-3/4}$ as a function of Ra is shown. It can be observed that in general $\langle L_B \rangle_{A,t}$ increases with Ra in the bulk region. However, the maximum value is of the order of $H/10$ which is far separated from H. This partly supports the existence of the Bolgiano scaling observed earlier in v and θ spectra. Further, for comparison, $\langle L_B \rangle_{A,t}$ for smooth surface case [83] is shown in Fig. 4.20(b). The trend and the order of L_B are comparable to what is observed in the present work away from the walls. Clearly, owing to a high ϵ_θ near the walls, local measure of L_B drops there significantly. However, in the bulk it shows global maximum as the flow is nearly homogeneous. We observe a consistent trend both in the rough and smooth geometry with L_B increases marginally with Ra.

Theoretically, global estimate of L_B can be approximated by using global estimates of thermal and kinetic dissipation rates [18] in Eq. (4.3), as shown below

$$\begin{aligned} \langle \epsilon_u \rangle_{V,t} = \frac{Nu-1}{\sqrt{RaPr}}, \quad \langle \epsilon_\theta \rangle_{V,t} = \frac{Nu}{\sqrt{RaPr}} \\ \implies L_B^g = \langle \epsilon_u \rangle_{V,t}^{5/4} \langle \epsilon_\theta \rangle_{V,t}^{-3/4} = \left(\frac{Nu-1}{\sqrt{RaPr}} \right)^{5/4} \left(\frac{Nu}{\sqrt{RaPr}} \right)^{-3/4} \\ \implies L_B^g \approx Nu^{1/2}/(RaPr)^{1/4} \quad (\text{for } Nu >> 1) \end{aligned} \tag{4.4}$$

A second global measure of L_B can also be obtained by vertically integrating $\langle L_B \rangle_{A,t}$

$$L_B^A = \int_0^H \langle L_B \rangle_{A,t}(y) dy$$

While L_B^g includes the spatial inhomogeneity of ϵ_θ arising from bulk-plume interaction, L_B^A strikes a compromise between the gap in $\langle L_B \rangle_{A,t}$ in the bulk and near-wall region. We show their variation in Fig. 4.20(c) as a function of Ra. With $Nu \sim Ra^{1/2}$ scaling, the above scaling predicts an $Ra-$invariant L_B^g. Both the global measures nearly conform to this argument. Further, we note both L_B^g and L_B^A have smaller magnitudes than $\langle L_B \rangle_{A,t}$ as they are not as sensitive to ϵ_θ as the local measure is. Also, L_B^g for smooth surface [83] is appended in Fig. 4.20(c), where it is seen to drop with increasing Ra. The classical $Nu \sim Ra^{1/3}$ scaling when inserted in Eq. (4.4), one obtains $L_B^g \sim Ra^{-1/12}$. The power law fitting of $Ra^{-1/12}$ closely follows the smooth surface data. In the current work, L_B is found to be in the admissible limits (not greater than H) for the realization of the Bolgiano scaling for the explored Ra range, which is

in agreement with the spectra obtained for temperature and velocity fluctuations in the bulk. In addition, global Bolgiano length appears to support the classical $1/3$ scaling for the smooth surface data, while the much elusive $1/2$ scaling shows encouraging signs of consistency with the estimate $L_B^g \approx Nu^{1/2}/(RaPr)^{1/4}$. Note, in spite of substantial evidence in favour of existence of the BO59 scaling from different estimates of L_B, the result can only be claimed incontestable when complemented by the results of the spatial structure functions of temperature and velocity. Also, the two-dimensionality of the problem introduces further complications due to the effect of inverse energy cascade [95]. Thus, in view of the above considerations, a caution is to be exercised while invoking the BO59 scaling.

4.8 Decomposition into orthogonal modes

In order to identify the dominant organized mode of heat transfer mechanism and the much elusive coherent structure, we have decomposed the flow field into a number of orthogonal modes. The basic principle behind proper orthogonal decomposition (POD) [96] is to seek an optimal basis of orthogonal spatial modes or eigenfunctions for a vector field $\boldsymbol{U}(\boldsymbol{r},t)$ based on its energy content $\int \langle \boldsymbol{U}(\boldsymbol{r},t)^2 \rangle_t \, d\boldsymbol{r}$. The vector field $\boldsymbol{U}(\boldsymbol{r},t)$ can be written as a superposition of the spatial modes $\boldsymbol{\phi}_n(\boldsymbol{r})$ scaled by their temporal amplitudes $a_n(t)$ in the following manner

$$\boldsymbol{U}(\boldsymbol{r},t) = \sum_{n=1}^{\infty} a_n(t)\boldsymbol{\phi}_n(\boldsymbol{r}). \tag{4.5}$$

Note, the POD modes are arranged in the decreasing order of their energy indicated by the eigenvalues of an algebraic problem discussed below. To represent the vector field $\boldsymbol{U}(\boldsymbol{r},t)$ in a low-dimensional subspace, the decomposition can be restricted to the first few modes encapsulating a large portion of the energy of $\boldsymbol{U}(\boldsymbol{r},t)$. While applying POD to the natural convection problem, one needs to decide whether to treat velocity and temperature jointly or independently [97–99]. The former treatment takes into account the coupling of temperature and velocity with the introduction of a scaling factor γ. In the present work, the vector field considered is $\boldsymbol{U}(\boldsymbol{r},t) = [u, v, \gamma\theta]$, where γ is calculated as

$$\gamma = \left(\left\langle \frac{\int [u^2(\boldsymbol{r},t) + v^2(\boldsymbol{r},t)] d\boldsymbol{r}}{\int \theta^2(\boldsymbol{r},t) d\boldsymbol{r}} \right\rangle_t \right)^{1/2}, \tag{4.6}$$

which essentially allows the energy of both temperature and velocity fields to be equal. The value of γ is obtained as 1.303.

The most energetic modes of POD have been consistently looked up to observe the large-scale structures and determine their role in the heat transfer process. A better understanding of these structures holds the key to achieve a greater heat transfer rate. Verdoold *et al.* [100] observed the primary mode consists of a single roll covering the entire width of the cell at $Ra = 6\times10^8$, while fluctuating modes revealed two types of flow patterns. In the first type, higher-order modes had an increased number of rolls. However, for the second type, second and third-order fluctuating modes depicted diagonal flow patterns. Both types of fluctuating modes appeared randomly in repeated experiments for the same thermal forcing. Podvin and Sergent [101] using the LES data predicted that the first two most energetic modes, major benefactors in the vertical heat transfer, consist of rolls aligned in the transverse dimension, while for the subsequent modes they align in the longitudinal direction. Later, Podvin and Sergent [98, 102] used the POD modes to investigate the flow structures to seek reasons for the observed flow reversals and cessations. 2D geometry was preferred as it locks the LSC allowing the disentanglement of the different mechanisms involved in flow reversals. The first three POD modes revealed the dominant structures as large-scale circulation consisting of a single-roll, symmetry breaking two rolls, and a quadrupolar flow. They observed that flow reversals are associated with the instability of the transient double-roll symmetry breaking mode. So far the POD has mainly been used as a tool to study the features of LSC and its reversals, notably in the low Ra range.

To extract the POD modes, we have implemented the method of snapshots [103], which essentially allows the modes to be written as a linear combination of N instantaneous snapshots of the vector field $\boldsymbol{U}(\boldsymbol{r},t)$ taken at different time instances t_i

$$\boldsymbol{\phi}_n(\boldsymbol{r}) = \sum_{i=1}^{N} \boldsymbol{U}(\boldsymbol{r},t_i)\varphi_n^i \tag{4.7}$$

The vectors $\boldsymbol{\varphi}_n$ are followed from the algebraic eigenvalue problem

$$\boldsymbol{C}\boldsymbol{\varphi}_n = \lambda_n\boldsymbol{\varphi}_n \tag{4.8}$$

where $\boldsymbol{C}$ is the temporal correlation matrix of the snapshots, calculated as

$$C_{ij} = \frac{1}{N}\int_V \left(\boldsymbol{u}(\boldsymbol{r},t_i)\cdot\boldsymbol{u}(\boldsymbol{r},t_j) + \gamma^2\theta(\boldsymbol{r},t_i)\theta(\boldsymbol{r},t_j)\right) d\boldsymbol{r} \tag{4.9}$$

For the lowest $Ra(=\ 10^8)$, a total of 400 snapshots are extracted at an interval of 2.5 time units, while for the highest $Ra(=\ 10^{11})$ case nearly 100 discrete temporal frames recorded at an interval of 0.5 time units are used to construct the eigen modes. Such a choice is driven by collection of adequate number of time frames to include all possible random events without

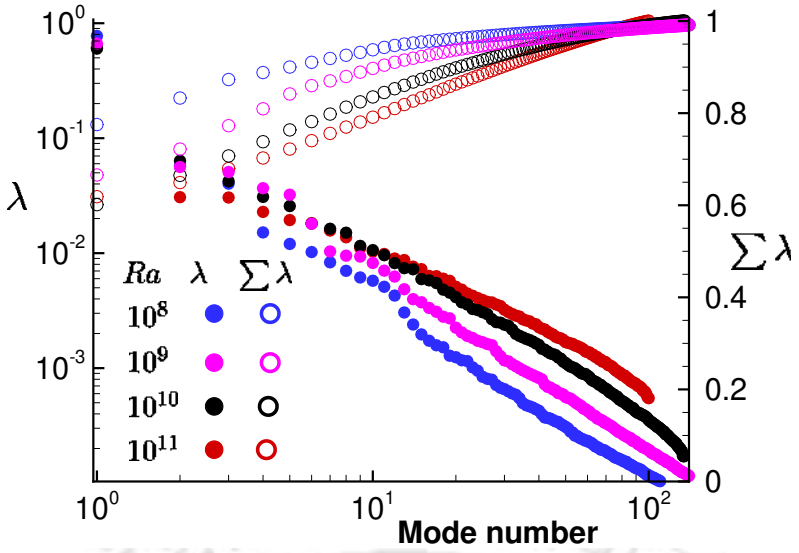

Figure 4.21: Normalized POD eigenspectrum (filled symbols), where $\Sigma_N \lambda_j = 1$, is shown along with the associated cumulative spectrum (unfilled symbols) for $Ra = 10^8, 10^9, 10^{10}$ and 10^{11}. The difference in energy content between the first and higher-order modes indicates better mixing and inter-scale energy transfer at higher Ra.

significant overlap. In Fig. 4.21, POD eigenspectrum normalized by $\Sigma_N \lambda_i$ is shown along with the cumulative spectrum for $Ra = 10^8, 10^9, 10^{10}$ and 10^{11}. Note, owing to such normalization the cumulative sum $\Sigma_i \lambda_i$ approaches unity as one moves towards the right end of the spectrum. It can be observed that the first mode captures most of the energy. For $Ra = 10^8$, the energy captured by the first mode is 77%, while for $Ra = 10^{11}$, it is 62%. The cumulative spectrum indicates that with increase in Ra energy content in higher order modes is non-trivial. This occurs owing to the enhanced inter-scale energy transfer and complexity of flow modes at higher thermal forcing.

Temperature field superimposed with velocity vectors is shown for the first and second modes for $Ra = 10^8, 10^{10}$ and 10^{11} in Fig. 4.22. The first mode is seen to weakly represent the mean flow field, where a layer with very hot (bottom plate) or cold (top plate) fluid covering the rough surfaces is revealed. Also, the layer enclosing large temperature gradients diminishes with increased thermal forcing, though not uniformly, due to the intricate texture of the rough surfaces. It also signifies thinning of the TBL. In the bulk, the mean temperature field is nearly homogeneous with higher θ at $Ra = 10^8$ in comparison to $Ra = 10^{10}$ and 10^{11}, where it approaches 0.5. The temperature field corresponding to the second mode is at first inhomogeneous, but at the highest $Ra = 10^{11}$ we observe increased homogeneity. In the dominant mode, nearly half of the total temperature drop is noticed near the isothermal walls with a large homogeneous

bulk region. The second mode is clearly underdeveloped whose contribution in heat transport is rather insignificant. Interestingly, the covering of TBL on the rough surface is only detected in the dominant first mode while the subsequent mode only exhibits trapped fluid scattered around the throats of the roughness.

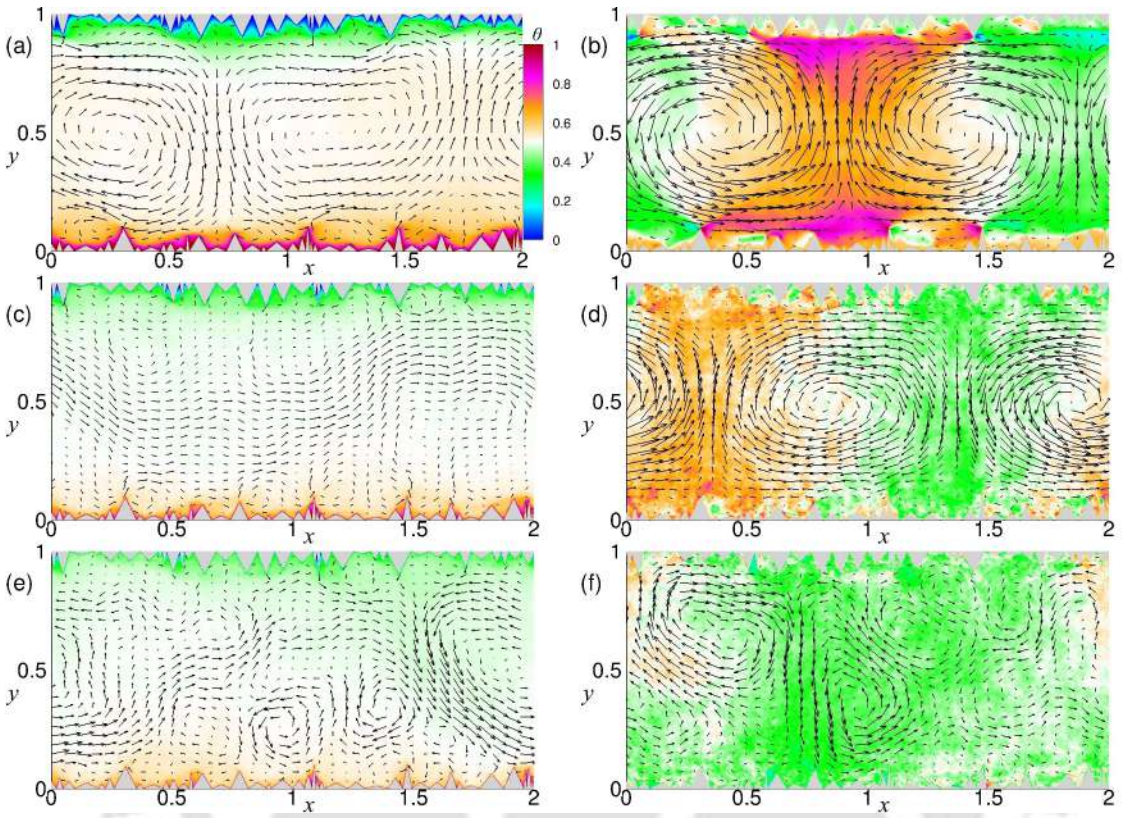

Figure 4.22: First (left column) and second POD modes (right column) representing temperature field superimposed with velocity vectors for $Ra = 10^8$ (top row), 10^{10} (middle row) and 10^{11} (bottom row). The bulk region clearly assumes a better homogeneous state with near bulk-mean temperature in the first mode while underdeveloped and unmixed hot (or cold) plumes constitute the second mode.

From velocity vector field shown in Fig. 4.22, dominant double roll structure (DRS) at $Ra = 10^8$, readily observed from the first mode, are seen to transform into multiple small-scale rolls at the higher Ra. Increased turbulence with emergence of the small structures from numerous sites near the rough surfaces supports disintegration of the large-scale rolls leading to the formation of the local vortices. The second POD mode for both $Ra = 10^8$ and 10^{10} correspond to the double roll state while at $Ra = 10^{11}$ multiple small-scale rolls are evident. The above observation hints that with increasing thermal forcing, organization of the flow with multiple small-scale rolls becomes the natural choice. While DRS at smaller Ra induces a stronger lateral motion, multiple small rolls at higher Ra promotes direct injection of plumes

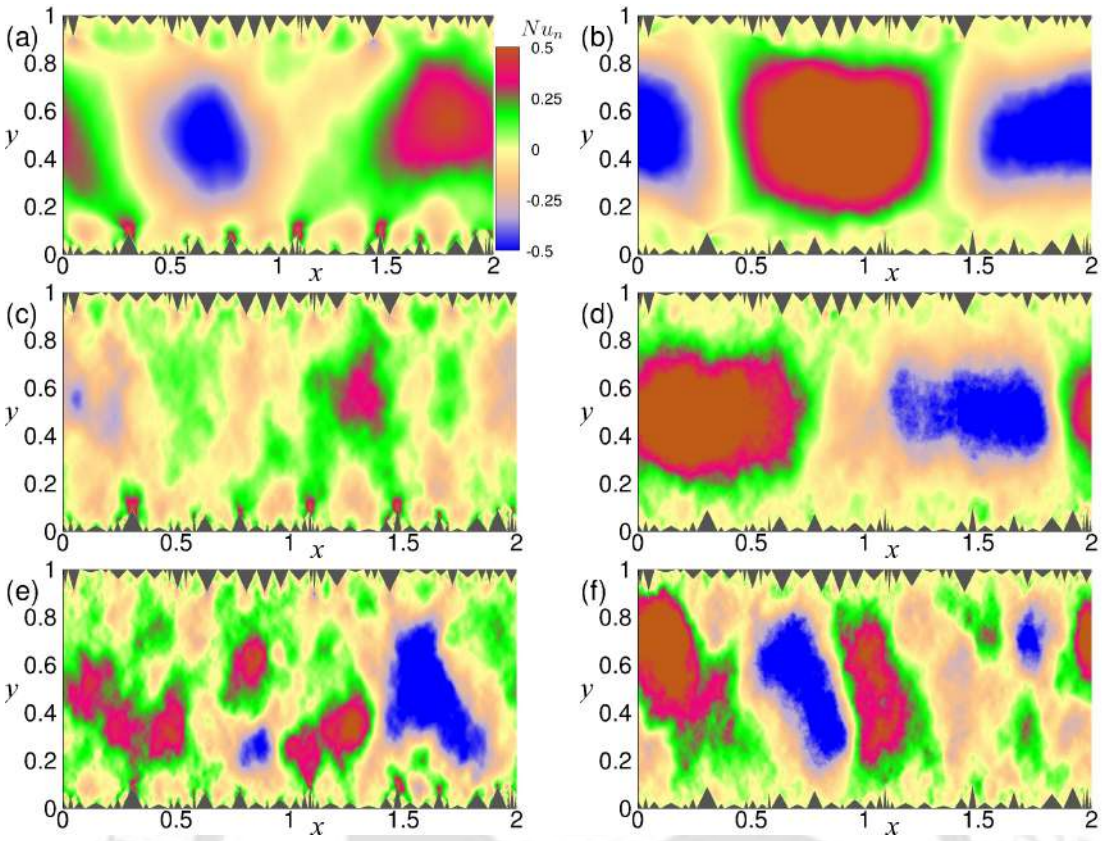

Figure 4.23: Normalized Nusselt number Nu_n calculated from the first (left column) and second mode (right column) are shown for $Ra = 10^8$ (top row), 10^{10} (middle row) and 10^{11} (bottom row). Note, maximum value of *Nu* is used for its normalization. Dominant mode of heat transfer occurs with multiple unstable structures while the secondary mode mainly shows the stable double-roll state.

into the bulk, causing an increased $v\theta$ correlation responsible for enhanced heat flux. In Fig. 4.23 we show normalized Nusselt number given by $Nu = (RaPr)^{1/2}v\theta - \partial_y\theta$ computed from the first two modes for the selected Ra. Note the global maximum of *Nu* is used to normalize it. In agreement with our previous observation, at the lowest Ra, dominant flow structures carrying a large amount of thermal energy are larger in size, while at higher Ra, fine structures are responsible for the transport of heat. A greater vertical motion induced by multiple small-scale plumes improves the *Nu* distribution at higher Ra, which is seen to be confined at smaller Ra. Thus, stable DRS as a principal carrier of heat does not favor an enhanced heat flux regime while multiple small pockets of intense plume distribute thermal energy efficiently and also create numerous nucleation sites for plumes. Break down of DRS into multiple rolls is triggered by the sharp peaks and uneven valleys near the isothermal surfaces.

4.9 Summary

The present work explored the effect of random triangular roughness on the flow dynamics and heat transport properties in a two-dimensional rectangular cell. The inclusion of varied elements enriched the flow physics such that they and the associated regions assumed distinct roles to enable the sustenance of the enhanced heat transfer scaling throughout the explored three decades of Ra. At lower Ra, only taller elements are active in enhancing plume emission from their tips, while at higher Ra, substantial contributions from the smaller elements are received, which play a pivotal role in casting aside the saturation of the enhanced heat transport scaling. Plume regions are clearly identified by high convective heat flux and are observed to be the most potent coherent structures in enhancing the heat transfer at all thermal forcings. Increased plume emission frequency in comparison to the smooth surface case is quantified from turbulent buoyancy production and dissipation, and volume fraction of plumes. Detailed analysis of the near-wall dynamics reveals the complex role of the roughness elements and the associated throat, valley, and tip regions. Throat regions are inaccessible to the bulk flow at lower Ra. However, with increasing thermal forcing, penetration of the bulk fluid improves, which is also reflected through increased velocity fluctuations. Similarly, tip regions associated with smaller roughness elements get activated at higher Ra such that they start to protrude the TBL and incite plume emissions which are recorded from temperature fluctuations.

Also, distinct flow dynamics in different throat regions are revealed through vertical profiles of mean temperature passing through the associated valleys. Evolution of the flatter linear profiles to the steeper ones, identical to that observed in a smooth cell for highly confined cavities from the lowest Ra to higher Ra, marks the washing away of the cavities. When profiles become identical to that of the smooth cell, effect of the cavity regions in perturbing the nearby flow is largely diminished. Depending on whether throat regions are spacious or confined, the transition to enhanced local heat flux regime undergoes at different thermal forcings. It implies that the propitious effect of the roughness elements is not lost altogether. Activation of small-scale roughness elements and highly confined regions at higher Ra promotes the sustenance of the enhanced heat transfer scaling. Further, the effect of perturbations induced by the roughness elements in the near-wall regions is felt in the form of increased temperature fluctuations, which are substantially higher than the smooth surface case. Also, increased movement of the plumes in the bulk is observed from the long tails of the PDFs of temperature and vertical velocity. From temporal power spectra of temperature and vertical velocity, increased energy at nearly all scales of the flow is seen in comparison to the smooth cell at sufficiently high Ra.

In the previous fractal roughness studies [42, 79], the effect of the roughness parameters on the global quantities, *Nu* and Re, are observed. However, the present study not only deals with the global parameters but also explores the varying local flow dynamics related to the distinct regions associated with the rough surface. The distinct flow dynamics and their evolution with Ra shed light on the applicability of the small-scale elements at a higher thermal forcing. Thus, the possible mechanism responsible for sustenance of the enhanced heat transfer scaling at higher Ra is explored in detail. Also, the various facets pertaining to the altered flow dynamics and structures with respect to smooth surface case are investigated from different perspectives to establish a clear distinction between the two cases.

In all, the random multi-scale roughness alters the flow dynamics with diverse responses of the roughness elements, ultimately aiding in retaining the enhanced heat transfer scaling by pushing off the arrival of the classical 1/3 scaling. Also, presence of multi-scale random roughness is clearly a better manifestation of the real-life rough surfaces and thermal convection over them. Hence, the observations from the above study are expected to provide deeper insights into understanding of real-life flows occurring in nature.

5

ROLE OF THE PRANDTL NUMBER IN AUGMENTING *Nu*

The present study numerically investigates the effect of Prandtl number ($0.1 \leq Pr \leq 100$) *on the flow structures and heat transport mechanism in a two-dimensional rectangular rough cell of aspect ratio* 2, *for more than two decades of Rayleigh number* ($10^7 \leq Ra \leq 5 \times 10^9$). *Large-scale diffuse structures transform into finer ones with either increase in* Ra *or* Pr. *The height of roughness elements relative to the thermal boundary layer (TBL) thickness establishes the level of perturbations introduced into the system. A stronger thermal forcing or larger* Pr *facilitates a thinner TBL which triggers a quicker response from the elements in the emission of plumes. In comparison to the smooth case, heat transport is enhanced significantly with the introduction of roughness. The near invariance of Nu with* Pr *in smooth cells is overcome in the rough cell, where a monotonically increasing heat flux is obtained. A greater presence of plumes in the domain is identified by an augmented volume fraction and thermal dissipation from plumes. Flow intensity measured in terms of global Reynolds number* (Re) *shows significant improvement for* $10^8 \leq Ra \leq 5 \times 10^9$ *and* $5 \leq Pr \leq 100$ *in comparison to the smooth case. Stagnation of the fluid inside the roughness cavities is responsible for a lower* Re *at a smaller* Ra *or* Pr. *The strength of velocity and temperature fluctuations are observed to decay with increasing* Pr. *However, in comparison to the smooth cell, greater fluctuations are observed for the rough cell, especially in the bulk region.*

5.1 Introduction

In addition to thermal forcing, Prandtl number has a strong effect on the prevalent dominating flow structures and the heat transfer mechanism [19, 46, 47]. Verzicco and Camussi [48] demarcated two types of flow regimes in their study inside a cylindrical cell covering $0.022 \leq Pr \leq 15$ for $Ra \leq 2 \times 10^7$. The first regime was observed for $Pr \leq 0.35$, where large-scale circulation

(LSC) dominates and is the major benefactor in vertical heat transfer. Owing to the remarkable contributions, LSC is considered as the "engine" for low *Pr* convection. Also, in this case, *Nu* was found to increase with *Pr*. The second regime was observed for $Pr > 0.35$, where thermal plumes emerge as the major contributor in heat transfer and the role of large-scale circulation is largely diminished. Here, *Nu* becomes independent of *Pr* with the scaling exponent being $2/7$. In general, for low *Pr* fluids, a thicker thermal boundary layer (TBL) is formed, due to which there is more tendency of diffusive heat transfer, and hence, fewer and weak plume structures are formed. However, with an increase in *Pr*, the thermal boundary layer becomes thinner, favoring the formation of a greater number of stronger and finer plumes.

Malevsky [49] also highlighted the influence of *Pr* by observing PDF (Probability density function) of θ fluctuation along with its spectra. For low *Pr*, the increasing dominance of large-scale structures with decreasing *Pr* leads to the Gaussian-like skirt of the PDFs, while at high *Pr*, the emergence of the small-scale structures in the form of isolated fine plumes is responsible for the exponential-like shape. The above observation is in line with that of Yakhot [51], Solomon and Gollub [52, 53], where the predominance of large-scale structures is credited in giving Gaussian shape to the PDFs while small-scale structures enforce the exponential shape. The spectra of temperature fluctuations measured at different horizontal planes also revealed the *Pr* dependence where they were found to be steeper with decreasing *Pr*. Another interesting feature discovered by Malevsky [49] is the increasing tendency of inverse kinetic energy transfer with the amplification of *Pr*. The same was manifested from the steeper kinetic energy spectra at higher *Pr* with the slope of the inertial subrange being close to -11/5 (BO59 scaling [54, 55]). In the literature, BO59 scaling has been shown to be closely connected to the inverse energy transfer [56, 57].

Huang and Zhou [58] in their 2D study reported anomalous $Nu(Pr)$ relation in comparison to a 3D cylindrical case for a moderate $Ra \leq 10^9$ and $Pr \approx 2 \sim 3$ range, where *Nu* settles for a minimum value rather than attaining maxima as in the 3D case. The reason for the anomaly was attributed to the competition between the corner rolls and LSC creating counter-gradient heat transport, which is a striking feature of 2D convection as the fluid lacks the third direction to escape. Further, heat transfer dependency on *Pr* was found to diminish with increasing *Pr*. At higher $Ra \geq 3 \times 10^9$, *Pr* dependency was qualitatively similar to that observed for the 3D case. Yang *et al.* [104] also obtained a lack of *Pr* dependence in heat transfer rate for their experimental investigation inside a cylindrical cell for $2.63 \times 10^8 \leq Ra \leq 3.89 \times 10^{10}$ and $3.58 \leq Pr \leq 9.40$. However, Reynolds number showed significant dependence on *Pr* ($Re = Ra^{0.47}Pr^{-0.72}$) such that its value dropped with an increase in Pr. They also observed that the local temperature

fluctuations weaken with increasing *Pr*.

van der Poel *et al.* [50] also highlighted the similar behavior of $Nu(Pr)$ in 2D and 3D cases for a large *Pr*, where *Nu* data for both the cases converged. The largest difference in *Nu* is seen at intermediate *Pr*, which is associated with the difference in LSC dynamics in 2D and 3D cases. In the 2D case, there is an emergence of a stronger LSC with corner rolls, whereas in the 3D case, LSC is less pronounced with smaller rolls. They also observed the *Pr* dependence of the global Re, where the flow strength was observed to be monotonically decreasing with growing *Pr* such that it is always higher for 2D than 3D. However, for a higher *Pr*, Re for both 2D and 3D converged, which again highlights similar behavior in both the modes. Pandey *et al.* [59] reported the similarities between 2D and 3D for large *Pr* convection. On observing the first ten most dominant Fourier modes, close resemblances between 2D and 3D convection were revealed. Similar scaling for kinetic ($E_u(k) \sim k^{-13/3}$) and temperature spectra ($\sim k^{-2}$) further highlighted the behavior in both the cases to be alike. Li *et al.* [105] experimentally investigated the effect of *Pr* on heat transport and flow structures in a quasi 2D rectangular convection cell for $6 \times 10^8 \leq Ra \leq 3 \times 10^{10}$ and $11.7 \leq Pr \leq 650.7$. It was observed that a well-defined LSC exists for *Pr* up to 145.7. In this range, the increase of *Pr* is accompanied by a lesser number of thermal plumes traversing through the central region of the cell. For the two extreme $Pr = 345.2$ and 650.7, LSC disappears, and in place of that, slender thermal plumes that move randomly in the cell emerge. The breakdown of LSC also resulted in a regime transition in the $Re(Ra, Pr)$ scaling law.

Zhang *et al.* [106] simulated 2D flow with uniform triangular roughness for $10^7 \leq Ra \leq 10^{11}$ with constant $Pr = 1$. It was reported that it takes a critical height (h_c) of the roughness elements to realize enhancement in heat transport. Below h_c, rough surfaces inhibit heat transport. However, h_c was observed to decrease with Ra, which explains the prevalence of augmentation of heat transfer rate at higher Ra. Toppaladoddi *et al.* [39] using optimized roughness parameters for sinusoidal roughness in a 2D cell of double aspect ratio obtained a heat transfer scaling exponent of 0.483 for $4 \times 10^6 \leq Ra \leq 3 \times 10^9$. They interpreted it as the attainment of the ultimate scaling. However, Zhu *et al.* [41], refuted the above claim by exploring a wider $10^8 \leq Ra \leq 10^{12}$ range. They reported that the roughness facilitated $1/2$ scaling is temporary, and the classical $1/3$ scaling returns at a higher Ra range. To overcome the saturation of the much sought after $1/2$ scaling, Zhu *et al.* [42] introduced three scales of roughness. The above provision allowed them to sustain $1/2$ scaling for a wider Ra range, $10^8 \leq Ra \leq 10^{11}$. It was hypothesized that different roughness length scales introduce thermal boundary layer perturba-

tions at different Ra. Large scale elements are activated at a lower Ra, while smaller elements require a larger thermal forcing to assist enhancement in heat transport. To investigate the influence of spatial arrangement of roughness elements on heat transport mechanism and flow structures, Dong *et al.* [107] performed 2D simulations in a square cavity with rough horizontal walls. They observed that the *Nu* scaling exponent varies depending on how the roughness elements are populated (dense/sparse). However, the Reynolds number was observed to be insensitive to the spatial arrangement in the employed roughness models.

Xie and Xia [35] experimentally explored *Pr* influence on $Nu(Ra)$ scaling in a cylindrical rough cell with periodically distributed pyramid-shaped elements for $7.5 \times 10^7 \leq Ra \leq 1.31 \times 10^{11}$ and $3.57 \leq Pr \leq 23.34$. They classified three regimes based on $Nu(Ra)$ scaling. Regime I experienced no influence of the roughness on $Nu(Ra)$, whereas regimes II and III revealed enhanced heat transport scaling. The transition from regime I to II happens with the TBL becoming thinner than the roughness height, whereas the transition from regime II to III is accompanied by the viscous boundary layer (BL) becoming thinner than the roughness height. Further, they reported that the larger the *Pr* is, the higher the enhancement in heat transfer is possible when a larger aspect ratio of the roughness elements is considered. The reason for the same was anticipated to be linked with the stronger clustering of thermal plumes.

Recently, Yang *et al.* [60] while working with a 2D square rough cell, observed the effect of *Pr* on the critical height (h_c) of the roughness elements above which an enhancement in heat transfer with respect to a smooth cell can be obtained. They explored $10^7 \leq Ra \leq 10^9$ and $0.01 \leq Pr \leq 100$, where $h_c(Pr)$ revealed three distinct regimes. The regime at low *Pr* dominated by LSC shows a decrement of h_c with increasing *Pr*. The regime at moderate *Pr*, characterized by strong competition between the corner rolls and the LSC with the advent of thermal plumes, experiences an increment of h_c with the magnified *Pr*. Lastly, the regime at high *Pr* features fine plumes with the weakening of the large-scale flows, where h_c follows a decreasing trend with *Pr*. To the best of our knowledge, the effect of *Pr* in a multi-scale roughness setup has not been explored, which calls for an in-depth study exploring how flow structures evolve and are altered at different Ra and *Pr* in the rough cell.

5.2 Numerical details

All the simulations are carried out in a 2D rectangular cell of aspect ratio $\Gamma = L/H$ = 2 covering $10^7 \leq Ra \leq 5 \times 10^9$ for $0.1 \leq Pr \leq 100$. Figure 5.1 shows the schematic diagram of

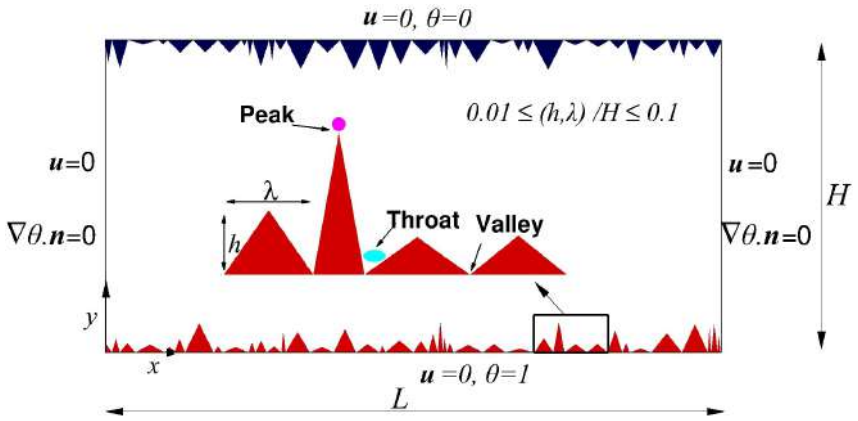

Figure 5.1: Schematic of the 2D rectangular convection cell featuring irregular triangular roughness on the horizontal plates. A blown up view of a small portion of the bottom plate depicts peak, throat and valley regions associated with the roughness elements. Here, h and λ are height (amplitude) and width (wavelength) of the roughness elements, respectively.

the convection cell with the applied boundary conditions and the detailed roughness geometry implanted on the top and bottom plates. The horizontal plates consist of irregular rough surfaces with triangular elements. All the walls admit the no-slip velocity boundary condition. While the lateral walls are kept adiabatic, the top and bottom horizontal plates are maintained at constant temperatures.

A grid that is uniform in the horizontal and non-uniform in the vertical direction is employed such that the regions close to rough surfaces are resolved sufficiently. For adequate spatial resolution, Kolmogorov length scale ($\eta \approx Pr^{1/2}/(RaNu)^{1/4}$) is resolved. Also, grid independence of the simulations, which is discussed later, is ensured for the accuracy of the results. In Table 5.1, details of the simulation parameters are listed for the rough cases. Note, we have also performed adequately resolved simulations for the smooth case for the same input parameters to enable a direct comparison with the rough cases. From Table 5.1, it can be observed that for $Pr = 0.1$ cases, the flow adequately resolves Kolmogorov length scale such that for the most demanding case, $Ra = 5\times10^9$, $\Delta x_{max}/\eta$ and $\Delta y_{max}/\eta$ are 0.97 and 1, respectively. For $Pr \geq 1$ cases, the resolutions in the horizontal and vertical direction are kept at least 0.85 times of the Kolmogorov length scale. Note, the reference Nusselt number for calculation of η is taken from Chand *et al.* [76]. For temporal resolution, time increment (Δt) is chosen in such a way that it is smaller than the Kolmogorov time scale $\left(\eta_\tau = \sqrt{Pr/(Nu-1)}\right)$ and the maximum Courant number is always less than 0.2. For the most demanding case ($Ra = 5 \times 10^9$ and $Pr = 0.1$), the ratio $\Delta t/\eta_\tau$ is as small as 8.78×10^{-6}, and it never exceeds 0.01 for all simulations. The simulations are started from the conduction state, and once a statistically stationary state is reached,

Table 5.1: Details of simulation parameters for different Ra cases starting from the left: Pr is the Prandtl number, N_x and N_y are the grid resolution in the x and y directions, $\Delta x_{max}/\eta$ and $\Delta y_{max}/\eta$ are the ratio of maximum grid spacing in x and y directions, respectively, to the Kolmogorov length scale ($\eta \approx Pr^{1/2}/(RaNu)^{1/4}$), and $\langle Nu\rangle_{V,t}$ is the calculated global Nusselt number. Note, for $Pr \geq 1$, the *Nu* is listed for the increasing order of Pr i.e., for $Pr = 1, 5, 10, 20, 50, 100$, respectively.

Pr	$N_x \times N_y$	$\Delta x_{max}/\eta$	$\Delta y_{max}/\eta$	$\langle Nu\rangle_{V,t}$
		Ra $= 10^7$		
0.1	1321×1081	0.49	0.43	10.5
≥ 1	1001×601	0.20	0.25	(10.9, 13.75, 15.52, 17.31, 18.86, 19.31)
		Ra $= 10^8$		
0.1	1561×1081	0.85	0.89	23.64
≥ 1	1201×601	0.38	0.55	(27.40, 31.57, 38.32, 39.15, 44.60, 47.2)
		Ra $= 10^9$		
0.1	3241×2281	0.84	0.86	55.02
≥ 1	2041×1081	0.52	0.70	(77.34, 81.21, 90.28, 101.135, 114.05, 120.65)
		Ra $= 5 \times 10^9$		
0.1	4681×3241	0.97	1	105.57
≥ 1	2521×1561	0.73	0.85	(147.63, 165.28, 170.161, 177.36, 190.21, 204.05)

sampling of the data is carried out.

To check the effect of resolution on the solution, four progressively refined meshes (M_i, i = 1 to 4) are tested for convergence of global *Nu*, and variance of temperature fluctuations, $\langle\sigma_\theta^2\rangle_V$, at $Ra = 5 \times 10^9$ for $Pr = 1$ and 100. The global Nusselt number and variance are calculated as $\langle Nu\rangle_{V,t} = \sqrt{RaPr}\langle v\theta\rangle_{V,t} - \langle\partial_y\theta\rangle_{V,t}$ and $\langle\sigma_\theta^2\rangle_V = \left\langle\left\langle\theta(\boldsymbol{x},t)^2\right\rangle_t - \left\langle\theta(\boldsymbol{x},t)\right\rangle_t^2\right\rangle_V$. The details of the mesh refinement study are listed in Table 5.2. It can be observed that for $Pr = 1$ case, the maximum variation in $\langle Nu\rangle_{V,t}$ and $\langle\sigma_\theta^2\rangle_V$ between any two successive grids does not exceed 1.4

and 7.6%, respectively. For $Pr = 100$, the maximum variation is 1.76 and 7.2% in $\langle Nu \rangle_{V,t}$ and $\langle \sigma_\theta^2 \rangle_V$, respectively. A slightly higher variance of higher order moments is also observed by Toppaladoddi *et al.* [79] while considering different flow realizations with fractal roughness. Note, mesh M_3, the chosen one for the simulations, is a perfect blend of adequate spatial resolution and accuracy of the solution. The mesh refinement study clearly establishes the employment of requisite spatial resolution of the flow field along with the robustness of the current numerical setup.

Table 5.2: Details of the grid independence study performed at $Ra = 5 \times 10^9$ for $Pr = 1$ and 100 are listed. Here, M_3 is the adopted mesh, $N_x \times N_y$ is the grid resolution, $\langle Nu \rangle_{V,t}$ is the calculated mean Nusselt number, and $\langle \sigma_\theta^2 \rangle_V$ is the global variance of temperature fluctuations.

		$Pr = 1$		$Pr = 100$	
Mesh (M_i)	$N_x \times N_y$	$\langle Nu \rangle_{V,t}$	$\langle \sigma_\theta^2 \rangle_V$ ($\times 10^{-3}$)	$\langle Nu \rangle_{V,t}$	$\langle \sigma_\theta^2 \rangle_V$ ($\times 10^{-4}$)
M_1	2101×1381	147.12	2.36	200.64	7.036
M_2	2301×1453	149.18	2.318	200.52	6.832
M_3	2521×1561	147.63	2.494	204.05	7.324
M_4	2771×1681	148.64	2.389	203.98	7.192

5.3 Nusselt number dependence on Ra and Pr

Scaling relation of the global heat transfer rate with imposed thermal forcing is at the heart of thermal convection. It is calculated as $\langle Nu \rangle_{V,t} = \sqrt{RaPr}\langle v\theta \rangle_{V,t} - \langle \partial_y \theta \rangle_{V,t}$. In Fig. 5.2, Nusselt number dependence on Pr is explored for both the rough and smooth cells at different Ra. We observe that the heat transfer rate is lowest for $Pr = 0.1$. Distinct heat transport mechanism prevalent in the rough cell is manifested in $Nu(Pr)$ relation. For the smooth cell, Nu is invariant for $Pr \geq 1$. This observation is in line with that reported in various previous studies [48, 50, 58]. Also, for comparison, we have plotted the data of van der Poel *et al.* [50] (numerical study) and Li *et al.* [105] (experimental study). It can be observed that the present data agree well with the reference data of van der Poel *et al.* [50] for a smooth cell of unit aspect ratio at $Ra = 10^8$ and $0.1 \leq Pr \leq 20$. Also, the data of Li *et al.* [105] (quasi 2D study), exhibit weak Pr dependence

($Ra = 10^9$), but the value of *Nu* is slightly higher. The slightly higher value can be attributed to the quasi 2D nature of the problem as *Nu* is observed to have a higher value in 3D than 2D [48, 50, 58]. In contrast to the trend followed by $Nu(Pr)$ for the smooth cell, the heat transfer rate in the rough cell does not saturate for high Pr flows. Here, higher Pr flows are seen to offer an augmented heat transfer rate. It is quite an interesting result, where the roughness configuration is seen to alter the role of Pr in the heat transfer process. Also, it is clearly evident that *Nu* in the rough cell is higher in comparison to the smooth cell except for the low Pr cases at the lowest $Ra = 10^7$.

To establish a $Nu(Pr) = APr^m$ relation for $Pr \geq 1$, the least-squares fitting is applied to the data. Note, the data for low Pr (< 1) is not included because of lack of enough data points to reveal the flow behavior, which is different from the one observed for moderate to large Pr flows. The details of the fitting parameters are listed in Table 5.3 for both the rough and smooth cells. It can be observed that the prefactor A amplifies with increasing Ra, whereas the scaling exponent m drops for both rough and smooth cells. Note, the scaling exponent m is a measure of how rapidly *Nu* varies with Pr. The drop of m with increasing Ra is an indicator of declining effect of Pr on *Nu* for higher Ra. However, m being significantly higher for the rough case indicates that the state of *Nu* becoming invariant of Pr is largely deferred in comparison to the smooth cell.

Table 5.3: Prefactor and exponent of the least-squares fit $Nu(Pr) = APr^m$ at different Ra are listed below for $Pr \geq 1$ for both the smooth and rough cells.

	Rough		Smooth	
Ra	A	m	A	m
10^7	11.215	0.129	12.856	0.029
10^8	27.267	0.123	25.775	0.017
10^9	73.247	0.106	50.919	0.008
5×10^9	146.91	0.067	79.896	0.009

Next, the relation of *Nu* as a function of Ra is observed at different Pr. In Fig. 5.3(a) and Fig. 5.3(b), the Nusselt number variation as a function of Ra is presented for rough and smooth cells, respectively. Further, the compensated plot of $NuRa^{-1/3}$ for the rough and $NuRa^{-2/7}$ for the smooth cell are shown as a function of Ra in Fig. 5.3(c) and Fig. 5.3(d), respectively. Note the solid lines in frames (a) and (b) of Fig. 5.3 represent the power-law fitting to $Pr = 0.1, 1$ and 100. The lines of best power fit are not shown for other Pr cases to avoid clutter. From frames (a) and (b), again, distinct *Nu* behavior in rough and smooth cells is evident. For the rough case,

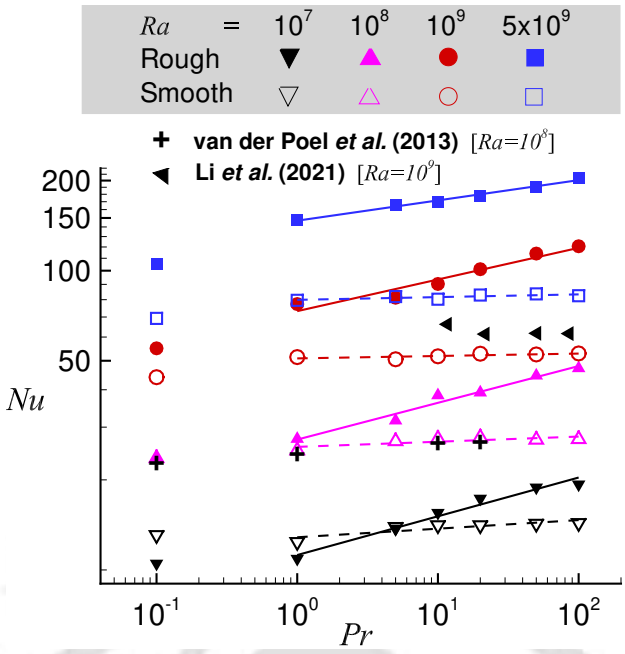

Figure 5.2: Variation of *Nu* as a function of Pr is shown at different Ra for both the smooth and rough cells. Note, the power-law fit for $Pr \geq 1$ is indicated by solid and dashed lines for rough and smooth cells, respectively. Data taken from the studies by van der Poel *et al.* [50] and Li *et al.* [105] is also plotted for comparison.

Nu exhibits Pr dependence. For a higher Pr at a given Ra, a greater value of *Nu* is evident, whereas for the smooth case, *Nu* is nearly the same for $Pr \geq 1$. To gain insights into the growth rate of $Nu(Ra)$, the details of the scaling exponent and prefactor for $Nu(Ra) = BRa^n$ are listed in Table 5.4. It can be observed that the scaling exponent n is least for $Pr = 0.1$, while for $Pr = 1$, it is highest (valid for both smooth and rough cells). Further, it can be observed that the scaling exponent n is always higher for the rough cases at any Pr. For smooth surfaces, n assumes a value close to $2/7$. In the higher end of Pr, the scaling exponent, n, is observed to be nearly constant and invariant of Pr in both cells. The compensated plots shown in frames (c) and (d) reveal how closely the scaling laws $Ra^{1/3}$ and $Ra^{2/7}$ are followed at different Pr for the rough and smooth cells, respectively. The flatter the data points are at a particular Pr, the better is their agreement with the perceived scaling exponent. From frame (d), it is evident that for the smooth cell, the scaling exponent of $n = 2/7$ is followed closely. However, the data points for the rough cell at a fixed Pr follow an increasing trend with the increasing Ra (see frame b), which reveals that n is higher than $1/3$. The above observations highlight that Pr assumes an active role in the presence of roughness to significantly enhance the heat transfer rate in comparison to the smooth case where *Nu* is lower and nearly invariant for moderate to large Pr. Further, note that in frames (a) and (c), experimental $Nu(Ra)$ data reported by Xie and Xia

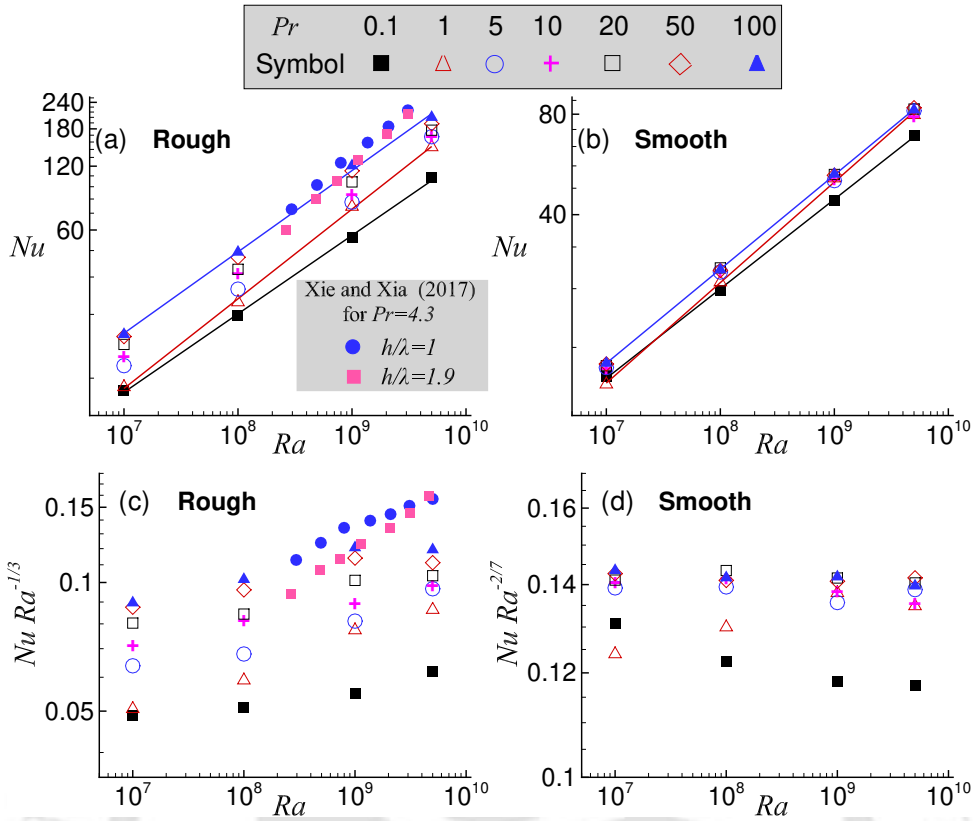

Figure 5.3: In (a) and (b), *Nu* variation with Ra is shown at different Pr for the rough and smooth cells, respectively. Note, the solid lines, representing power-law fit, are shown only for $Pr = 0.1, 1$ and 100 to avoid clutter. The compensated plots of $NuRa^{-1/3}$ and $NuRa^{-2/7}$ as a function of Ra are shown in (c) and (d) for the rough and smooth cells, respectively. In (a) and (c), *Nu* data reported by Xie and Xia [35] for pyramidal roughness elements with $h/\lambda = 1$ and $h/\lambda = 1.9$ is also shown for comparison at $Pr = 4.3$.

[35] for pyramidal-shaped roughness elements is shown for cases with aspect ratio, $h/\lambda = 1$ and 1.9, of the roughness elements at $Pr = 4.3$. Similar to our observation, they have also reported an augmented heat transfer scaling exponent in the presence of roughness. A higher value of the *Nu* scaling exponent is observed for a roughness configuration with a greater h/λ. van der Poel *et al.* [50], in their study involving the comparison of 2D and 3D results, reported a higher heat flux in 3D for the same input parameters, Ra and Pr. Lower *Nu* in the present 2D simulations compared to that reported by Xie and Xia [35] (experimental study) agrees well with the observation of van der Poel *et al.* [50] (numerical work).

Note that the scaling exponent obtained in the present study is greater than $1/3$, but the ultimate $1/2$ scaling is not realized. In contrast to the roughness studies by Zhu *et al.* [42] and Toppaladoddi *et al.* [39], where scaling exponent close to $1/2$ is achieved, the roughness parameters (h and λ) are not optimized in the present study. Here, irregular roughness elements

are incorporated such that there is no bias for any particular combination of h and λ. It highlights the possible reason for *Nu* scaling exponents deviating from $1/2$.

Table 5.4: Prefactor and exponent of the least-squares fit $Nu(Ra) = BRa^n$ at different Pr are listed for both the smooth and rough cells.

	Rough		Smooth	
Pr	B	n	B	n
0.1	0.026	0.37	0.171	0.268
1	0.012	0.423	0.097	0.301
5	0.021	0.4	0.144	0.284
10	0.032	0.384	0.157	0.279
20	0.038	0.379	0.145	0.284
50	0.044	0.377	0.145	0.284
100	0.040	0.383	0.152	0.282

5.4 Flow topology and heat transfer mechanism

Prevalent flow structures in RBC have a close connection with the primary heat transfer mechanism. In addition to the applied thermal forcing, which is represented by Ra, the Prandtl number serves as an important input parameter that influences flow structures [19, 46]. It is a widely accepted notion that in a rough convection cell, flow dynamics and structures are altered in comparison to a smooth convection cell [30, 38, 41, 42], which enhances the heat transfer rate when thermal boundary layer thickness becomes comparable with the height of the rough surface. The efficacy of employing rough surfaces is recently concluded to be dependent on thermal forcing [41]. For periodic rough surfaces, enhanced heat transport scaling exponent ceases to exist at higher Ra range when flow perturbations due to rough surfaces diminish. Efforts to prolong the propitious effect of rough surfaces in enhancing heat transfer led to the introduction of multi-scale rough surfaces [42], which provided augmented heat transport for an even larger Ra range. The success of the multi-scale surfaces at large thermal forcing is attributed to the thermal plumes triggered by small-scale elements. Till now, majority of roughness studies explored the response of a rough cell for varying Ra. However, there are only a few studies in a rough cell that take into account the role of Pr in connection to the flow structures and heat transfer mechanism.

In Fig. 5.4(I), snapshots of instantaneous temperature field are shown for the rough cell for $Ra = 10^8$, 10^9, and 5×10^9 at $Pr = 0.1$, 10, and 100. The evolution of flow structures with

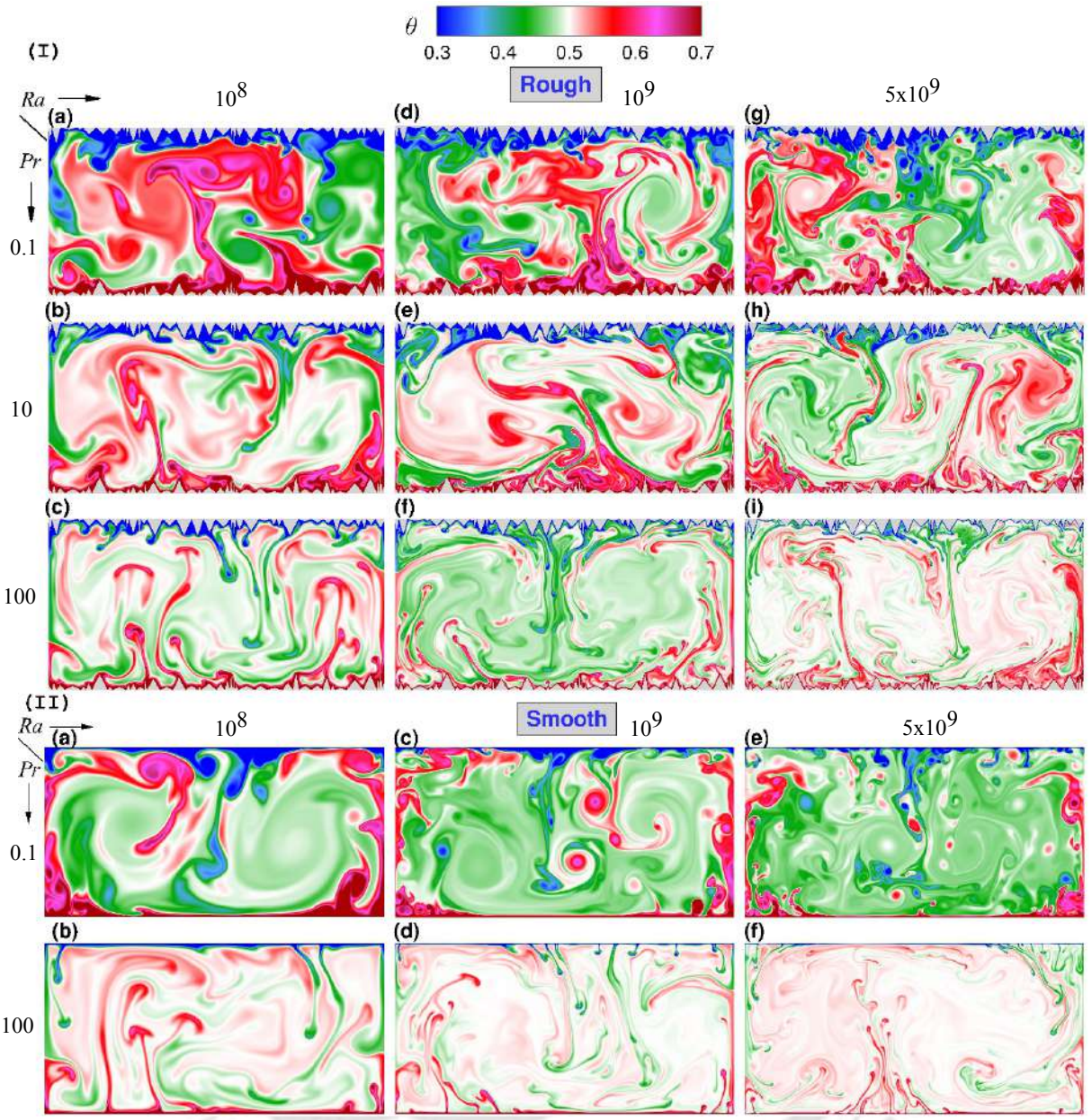

Figure 5.4: Snapshots of the instantaneous temperature field for the (I) rough convection cell are shown at $Ra = 10^8$ (a-c), $Ra = 10^9$ (d-f) and $Ra = 5 \times 10^9$ (g-i) for $Pr = 0.1, 10$ and 100. In (II), temperature field is shown for the smooth cell at $Ra = 10^8$ (a-b), $Ra = 10^9$ (c-d) and $Ra = 5 \times 10^9$ (e-f) for the extreme $Pr = 0.1$ and $Pr = 100$.

increasing Ra and Pr can be observed from the temperature fields. For low $Pr = 0.1$, a thick thermal boundary layer (TBL) over the rough surface is evident at $Ra = 10^8$ (see frame a). There are only a few plumes, which are of larger size, emanating mainly from the taller roughness elements. There is no significant contribution from small-scale elements as they are buried deep inside the thermal boundary layer, incapable of promoting plume emission. As Ra increases, the fluid layer of very high/low temperature on the bottom/top surface becomes thinner (see frames

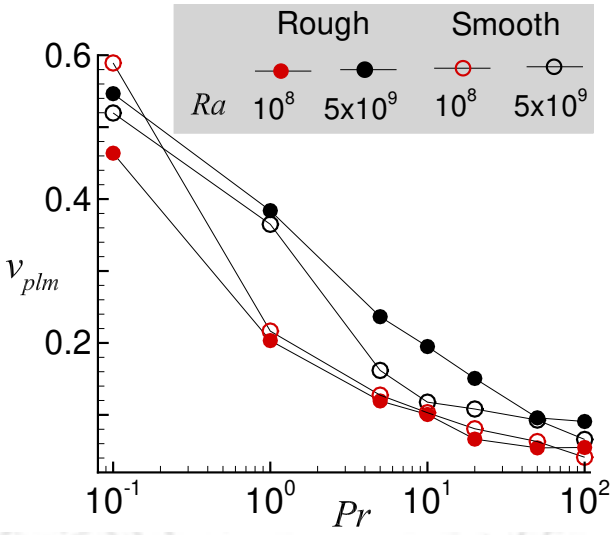

Figure 5.5: Variation of mean vertical velocity of plumes (v_{plm}) as a function of Pr is compared between the rough and smooth cells for $Ra = 10^8$ and $Ra = 5 \times 10^9$.

d and g). It leads to more number of roughness elements now protruding the TBL, the effect of which is evident in terms of a surge in plume nucleation sites. At $Ra = 5 \times 10^9$, flow structures appear to be extremely fine and are highly localized. It can be observed that nearly all the roughness elements are involved in the plume nucleation and emission process.

It can be observed that for a given thermal forcing, an increase in Pr leads to the emergence of finer flow structures with a thinner TBL (see frames b, e, and h). For $Pr = 100$ (frames c, f, and i), there is strong clustering of fine mushroom-shaped plumes near the rough surfaces. It is interesting to note that for a thermal forcing as low as $Ra = 10^8$ (frame c), plume emission sites are significantly higher for $Pr = 100$ in comparison to lower Pr cases (see frames a-c). The reason for the increased plume nucleation sites can be attributed to the activation of the small-scale roughness elements. The thinner TBL, in case of large Pr, allows early activation of the small-scale elements. Hence, stronger and increased flow perturbations are perceived in the flow at higher Pr even for a lower Ra. Another interesting observation is that though flow structures become finer with increasing Ra, they still manifest contrasting features for varied Pr. For instance, at the highest $Ra = 5 \times 10^9$ and $Pr = 100$, plumes are visibly finest and immensely localized in comparison to other Pr cases.

To compare the flow structures with a smooth convection cell for the same input parameters, we observe the snapshots of instantaneous temperature field data for the two extreme Pr ($= 0.1$ and 100), as shown in Fig. 5.4(II). The progression of large-scale flow structures into fine-scale intense structures is evident here also when either thermal forcing or Pr is increased. However, the intensity of the emitted plumes is relatively weaker than observed for the rough cells.

Also, there is trivial plume-bulk interaction in contrast to the rough cells, where the localized emission of plumes, i.e., from the tips of the roughness elements, promotes better plume-bulk interaction. The existence of a strong temperature gradient at the tip of roughness elements is responsible for the stimulation of intense plume emission. In line with the general expectation, it can be observed that bright detached flow structures (plumes) visibly span a larger portion of the convection cell for the roughened cells. The prominent presence of plumes in a rough cell, which are comparatively more energetic than that observed in a smooth cell, is an indication of enhanced heat transfer.

An estimate of the intensity of thermal plumes can be obtained by observing mean instantaneous vertical velocity of the plumes. The procedure for demarcation of the fluid volumes into plume or background dominated regions is described in detail in section 5.5. The mean vertical velocity (v_{plm}) is obtained by taking volume average of the absolute vertical velocity over the plume regions as described below

$$v_{plm} = \frac{1}{V_\Omega}\int_\Omega |v| dv \quad \text{such that} \quad \Omega : |v'\theta'|/\Gamma' > \delta \tag{5.1}$$

Note, Ω refers to the regions which satisfy the plume criterion, V_Ω is the volume of the plume regions, Γ' signifies the instantaneous global maximum of $|v'\theta'|$ and δ is the threshold parameter whose value is chosen as 5% for identifying plumes. In Fig. 5.5, v_{plm} is shown as a function of Pr at $Ra = 10^8$ and 5×10^9 for both smooth and rough cases. It can be observed that, in general, v_{plm} is comparable for the rough and smooth cases at $Ra = 10^8$. At a lower Ra, viscous forces remain largely stronger that hinder the emergence of the energetic plumes even from the rough surfaces. For the flow at the lowest $Pr = 0.1$, there is clearly a significant reduction in v_{plm} because of the formation of a thicker TBL, which not only obstruct the motion of flow inside the roughness cavities but also the formation of potent plumes. The true benefits of roughness are realized with the increase of thermal forcing, where the protrusion of roughness elements over the TBL yields stronger and greater number of plumes. The same is evident for 5×10^9, where v_{plm} is found to be significantly higher for the rough case. A higher v_{plm} serves as an indicator of the increased plume strength, which is realized with roughness at a higher thermal forcing.

5.5 Plume statistics

Thermal plumes are one of the most important flow structures that act as thermal carriers in transporting heat in bottom heated configuration. The introduction of rough surfaces is intimately linked to augmenting the emission of extra thermal plumes, which ultimately manifests

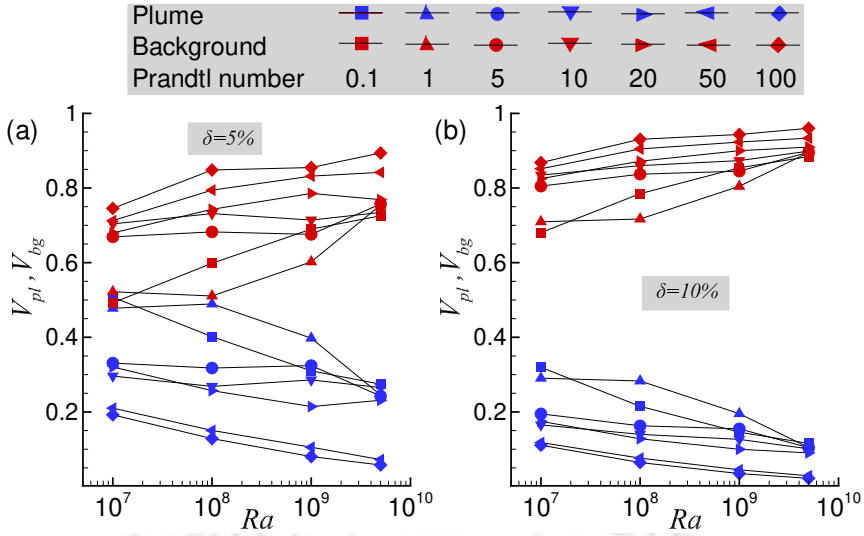

Figure 5.6: Variation of volume fraction of plumes (V_{pl}) and background (V_{bg}) as a function of Ra is explored for different Pr at threshold (a) $\delta = 5\%$ and (b) $\delta = 10\%$ for the rough cell.

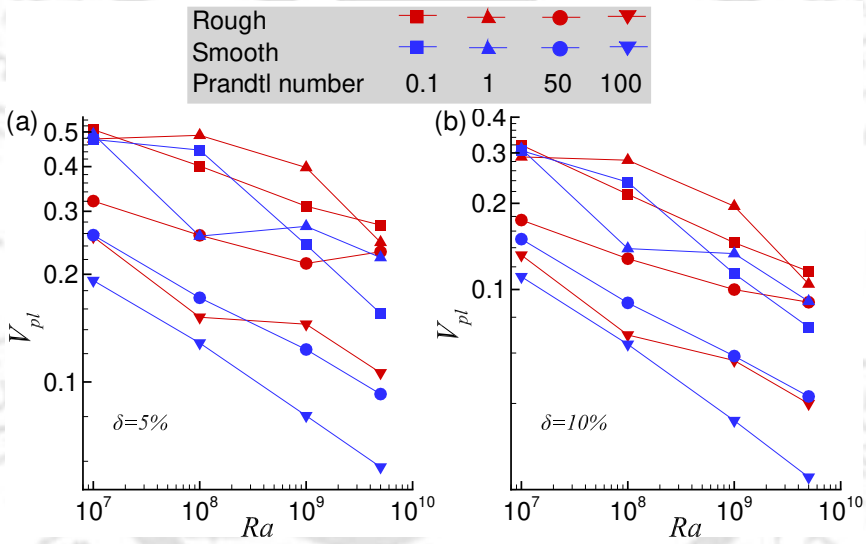

Figure 5.7: Plume volume fraction (V_{pl}) as a function of Ra is compared between the rough and smooth cells for different Pr at (a) $\delta = 5\%$ and (b) $\delta = 10\%$.

in the form of enhanced heat transfer compared to the smooth case. To detect plume-dominated regions from the turbulent background, Emran and Schumacher [88] suggested that plumes are associated with a strong correlation between vertical velocity (v') and temperature (θ') fluctuations. Temperature fluctuation is calculated as $\theta'(\boldsymbol{x},t) = \theta(\boldsymbol{x},t) - \langle\theta(\boldsymbol{x})\rangle_{A,t}$, whereas vertical velocity fluctuation is defined as $v'(\boldsymbol{x},t) = v(\boldsymbol{x},t)$ as $\langle v\rangle_{A,t} = 0$. The criteria for detection of plume and background regions employed in the present study is modified as,

$$\begin{aligned} V_{pl} &= \boldsymbol{x} \in V : |v'\theta'|/\Gamma' > \delta \\ V_{bg} &= \boldsymbol{x} \in V : |v'\theta'|/\Gamma' \leq \delta. \end{aligned} \tag{5.2}$$

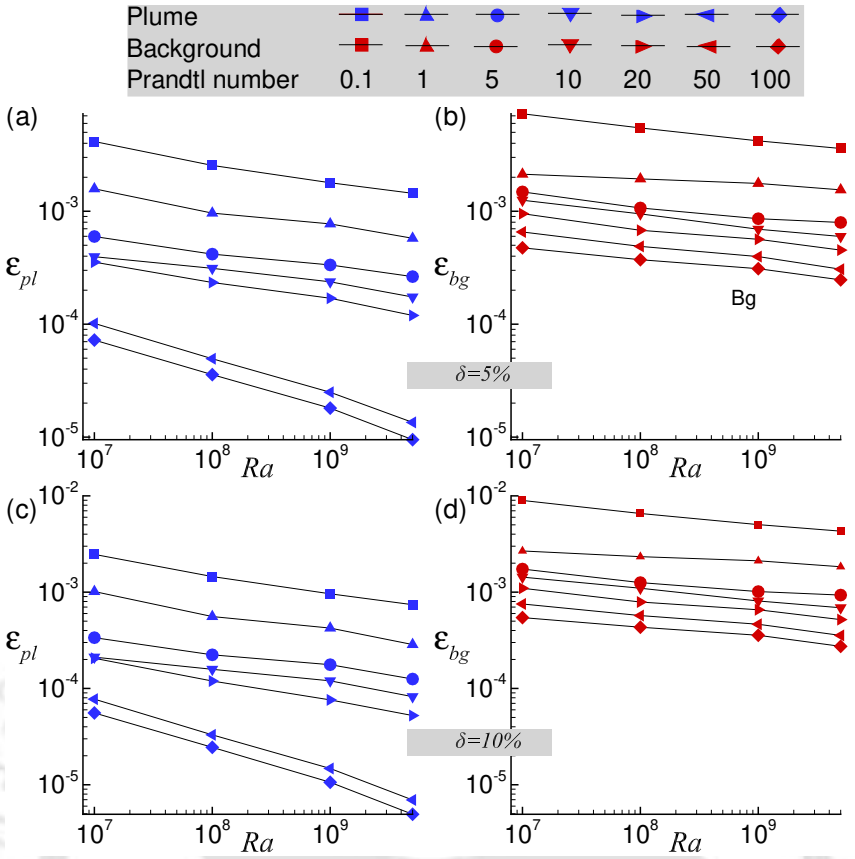

Figure 5.8: Thermal dissipation contributions from plumes (ϵ_{pl}) and background (ϵ_{bg}) are shown as a function of Ra at different Pr. Top row shows the data based on $\delta = 5\%$ criterion, while for the bottom row, δ is 10%. Note, frames (a,c) show data for ϵ_{pl}, while (b,d) represent data for ϵ_{bg}.

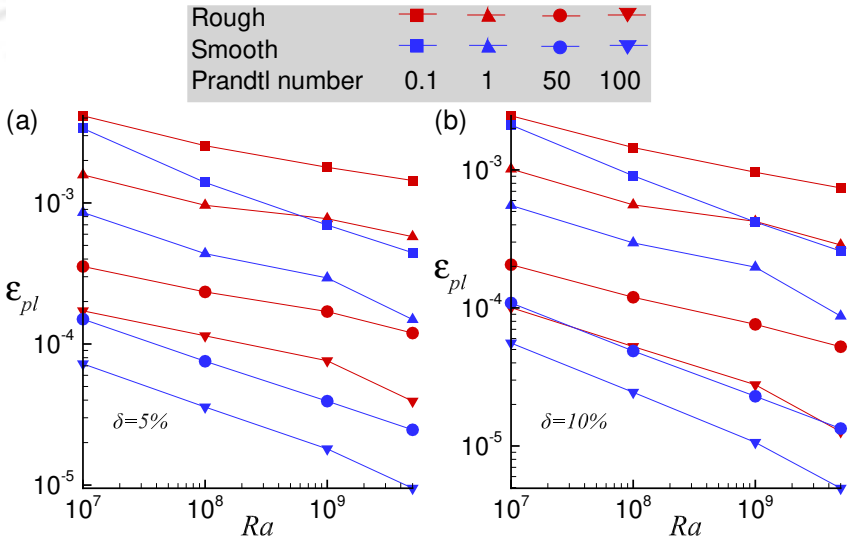

Figure 5.9: Variation of ϵ_{pl} as a function of Ra is compared between the rough and smooth cells at different Pr based on (a) $\delta = 5\%$ and (b) $\delta = 10\%$.

Here, V_{pl} and V_{bg} represent the volume fractions of plume and background dominated regions, respectively, Γ' is the instantaneous global maximum of $|v'\theta'|$, and δ is a free parameter controlling the threshold scale. Note, to account for the previously ignored yet significant anomalous motion of the plumes, i.e., the downward motion of hot plumes or upward motion of cold plumes, the absolute value of $|v'\theta'|$ is used as opposed to the signed correlation proposed by Emran and Schumacher [88]. This provision is important as a 2D configuration lacks an extra direction for the fluid to escape. It explains the need to incorporate the non-intuitive motion of plumes. If the conventional plume detection method is used, then plumes exhibiting anomalous motion, in other words, negative $v'\theta'$, go undetected and are misinterpreted as background regions.

In Fig. 5.6, the variation of volume fractions of plume (V_{pl}) and background (V_{bg}) regions as a function of Ra is shown for different Pr at thresholds $\delta = 5$ and 10%. Note, the two different thresholds identifies plumes reasonably well and are used to see their effect on the volume fractions. It can be observed that for all Pr cases, irrespective of δ, V_{pl} drops with increasing Ra, while V_{bg} climbs in order to compensate for the diminishing V_{pl}. The results are in agreement with the general consensus that higher the thermal forcing is, greater is the extent and role of the turbulent background. Note, in general, higher the Pr is, smaller is the value of V_{pl}, which is in line with the observation that plume structures emerge finer as Pr is increased and are likely to cover a relatively smaller fraction of the cell volume.

The increased plume emission in the rough case is expected to exhibit a higher V_{pl} than the smooth counterpart. In Fig. 5.7, a direct comparison is made between V_{pl} of smooth and rough cells for different Pr as a function of Ra at $\delta = 5$ and 10%. It is clearly evident that the rough cases have significantly higher V_{pl} for all Pr when $Ra \geq 10^8$. At $Ra = 10^7$ and $Pr = 0.1$ and 1, the heat transfer rate remains comparable in both the cells. However, for $Pr = 50$ and 100, *Nu* is significantly higher in the rough cases. At the lower Pr, owing to a thicker TBL, fluid is stuck inside the cavities and is unable to effect perturbations in the flow, which explains the inability of a rough cell in augmenting the heat transfer. However, at a higher Pr, a greater number of roughness elements introduce perturbations in the system because of a thinner TBL, which ultimately yields a larger *Nu*.

Further, the variation of thermal dissipation, $\epsilon_\theta = (RaPr)^{-1/2}|\nabla\theta|^2$, contributed by the plume (ϵ_{pl}) and background (ϵ_{bg}) regions with Ra is explored in Fig. 5.8, for different Pr at $\delta = 5$ and 10%. The dissipation contributions are calculated as

$$\epsilon_{pl} = \left\langle \int_{V_{pl}} \epsilon_\theta(\boldsymbol{x}, t) dV \right\rangle_t \text{ and } \epsilon_{bg} = \left\langle \int_{V_{bg}} \epsilon_\theta(\boldsymbol{x}, t) dV \right\rangle_t,$$

where, $\epsilon_\theta(\boldsymbol{x}, t)$ is the local non-dimensional thermal dissipation rate. We observe plume and background regions tend to contribute less to ϵ_θ as Ra is increased. The same is evident from the monotonic decrease of both ϵ_{pl} and ϵ_{bg} with increasing Ra for all Pr. Note, the decay of the net thermal dissipation rate ($\epsilon_{pl} + \epsilon_{bg}$) is in accordance with the exact relation $\langle \epsilon_\theta \rangle_V = \langle Nu \rangle_V / \sqrt{RaPr}$. For a fixed thermal forcing, a lower Pr flow exhibits higher ϵ_{pl} and ϵ_{bg}, while they drop significantly as Pr increases. Another observation is that irrespective of δ or Pr, ϵ_{bg} is higher than ϵ_{pl}. It is a general expectation that a higher V_{bg} should yield a higher ϵ_{bg}. Now, if we refer Fig. 5.6, it can be readily observed that V_{bg} exceeds V_{pl} almost for all cases irrespective of δ, which explains the perceived dominance of ϵ_{bg}. Also, a direct comparison between smooth and rough cells is made for ϵ_{pl} as a function of Ra and Pr at $\delta = 5$ and 10%, as shown in Fig. 5.9. It can be observed that in line with the higher V_{pl} in the rough cell, ϵ_{pl} is found to be substantially higher than the smooth cell at all Ra and Pr. Note, the decay rate of ϵ_{pl} in the rough cell is smaller than that observed for the smooth cell. It essentially highlights that the extra plume contributions received from roughness elements are sustained for the entire explored Ra range.

5.6 Reynolds number dependence on Ra and Pr

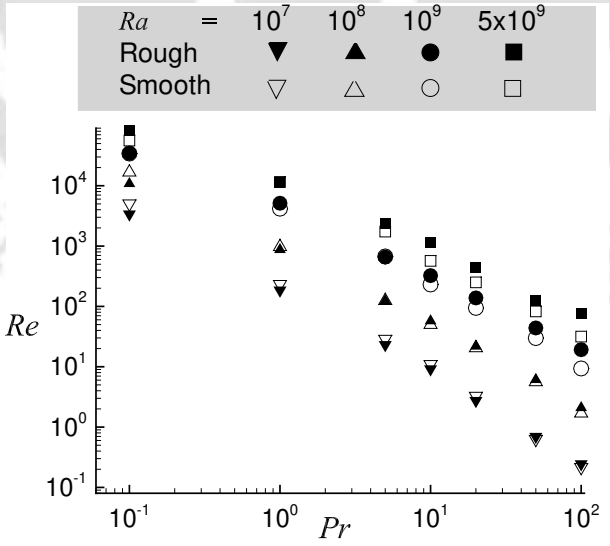

Figure 5.10: Re-dependence on Pr is explored for different thermal forcings in rough and smooth cells.

Flow strength developed in the convection cell due to the applied thermal forcing exhibits a strong dependence on the type of fluid used and has close links to the heat transport process.

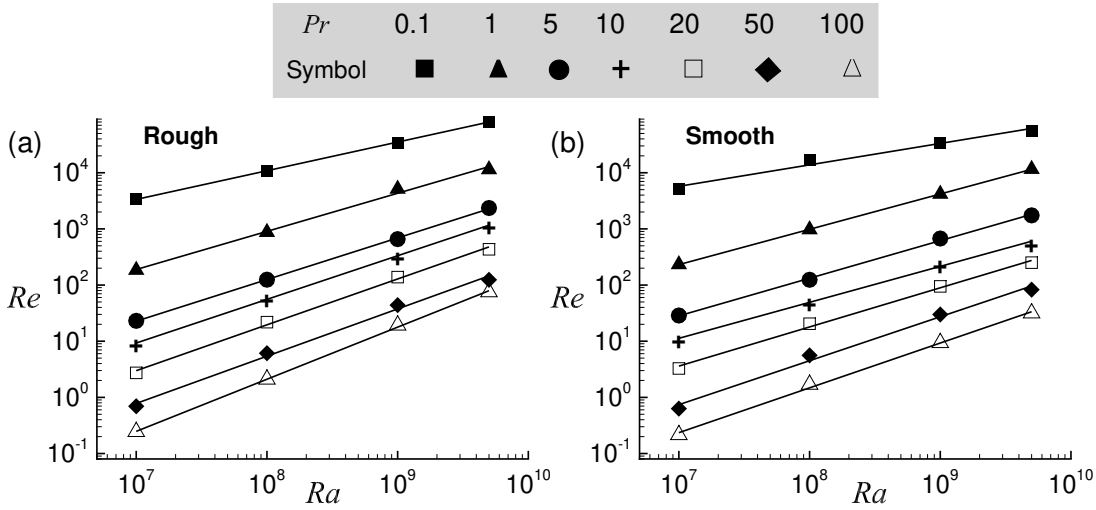

Figure 5.11: Variation of Re with Ra is shown at different Pr for (a) rough and (b) smooth cells. Note, the solid black lines correspond to the least-squares fit to the data.

Table 5.5: Prefactor and exponent of the least-squares fit $Re(Ra) = ARa^n$ at different Pr are listed for both the smooth and rough cells.

	Rough		Smooth	
Pr	A	n	A	n
0.1	0.895	0.51	12.176	0.382
1	3.358×10^{-3}	0.679	9.158×10^{-3}	0.629
5	1.477×10^{-4}	0.741	5.798×10^{-4}	0.670
10	3.377×10^{-5}	0.777	3.708×10^{-4}	0.640
20	5.764×10^{-6}	0.816	4.751×10^{-5}	0.697
50	1.007×10^{-6}	0.841	2.458×10^{-6}	0.783
100	7.937×10^{-8}	0.928	6.119×10^{-7}	0.798

Intensity of the flow is usually described in terms of the Reynolds number [50, 106], which can be quantified as

$$Re = \sqrt{\langle \boldsymbol{u} \cdot \boldsymbol{u} \rangle_{V,t}\, Ra/Pr}$$

In Fig. 5.10, Reynolds number dependence on Pr is shown for both smooth and rough cells at different Ra. It can be observed that for a fixed Pr, a higher Ra yields a stronger flow strength. However, for a fixed Ra, increasing Pr is seen to attenuate the flow intensity. On comparing Re between smooth and rough cells, enhanced flow strength in the rough cell is clearly evident for $10^8 \leq Ra \leq 5 \times 10^9$ and $5 \leq Pr \leq 100$. For lower $Pr = 0.1$ and 1, the enhancement of Re due to rough surfaces is observed only in the higher Ra range ($\geq 10^9$). The reason for not realizing an enhanced Re for lower Ra is associated with the immobility of fluid inside the cavities, where the flow is largely viscosity dominated. However, at higher Pr, owing to the thinner TBL,

cavity regions are easily ventilated by the bulk flow, promoting stronger fluid motion, which is responsible for an increased Re. Note, contrary to our previous observation that *Nu* loses its dependence on Pr in the smooth cell, $Re(Pr)$ dependence is not lost in either of the cells.

In Fig. 5.11, Re dependence on Ra is observed for both the rough and smooth cell configurations. The increasing trend of Re with Ra is clearly evident here for both the smooth and rough configurations. From Fig. 5.11, it is easy to observe that at the highest $Ra = 5 \times 10^9$, a higher Re exists for the rough cell at all Pr when compared to the smooth cell. To establish a relation of the form $Re(Ra) = ARa^n$, we have applied the least-squares fitting to the data. The details of the scaling exponent and prefactor are listed in Table 5.5. In general, it can be observed that the scaling exponent, n, increases as Pr is increased, while the prefactor (A) diminishes with Pr in both the cells. Most importantly, at any fixed Pr, n is higher for the rough cells. Increased exponent highlights that the flow strength is largely influenced by the introduction of rough surfaces.

5.7 Statistics of temperature and vertical velocity fluctuations

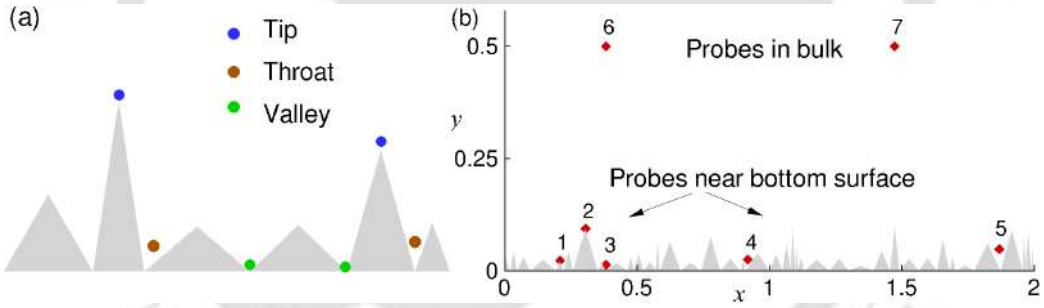

Figure 5.12: (a) Schematic diagram representing tip, throat and valley regions corresponding to a rough surface. (b) Location of numerical probes selected in the vicinity of the bottom surface and bulk region is shown in a magnified view.

Observing fluctuations of temperature and velocity reveal a great deal of information about the dominating flow structures and dynamics in different regions of a convection cell. Distinct flow regions associated with a rough surface can be mainly categorized as above the tips, between two roughness elements (throat) and the area deeply embedded between them (valley). The regions are shown schematically in Fig. 5.12(a). To unravel flow characteristics of different regions in the cell, we have chosen numerical probes at suitable locations, shown in Fig. 5.12(b). Note, time series data is recorded at a non-dimensional sampling rate of 100 units, i.e., data is stored after every 10^{-2} non-dimensional time units.

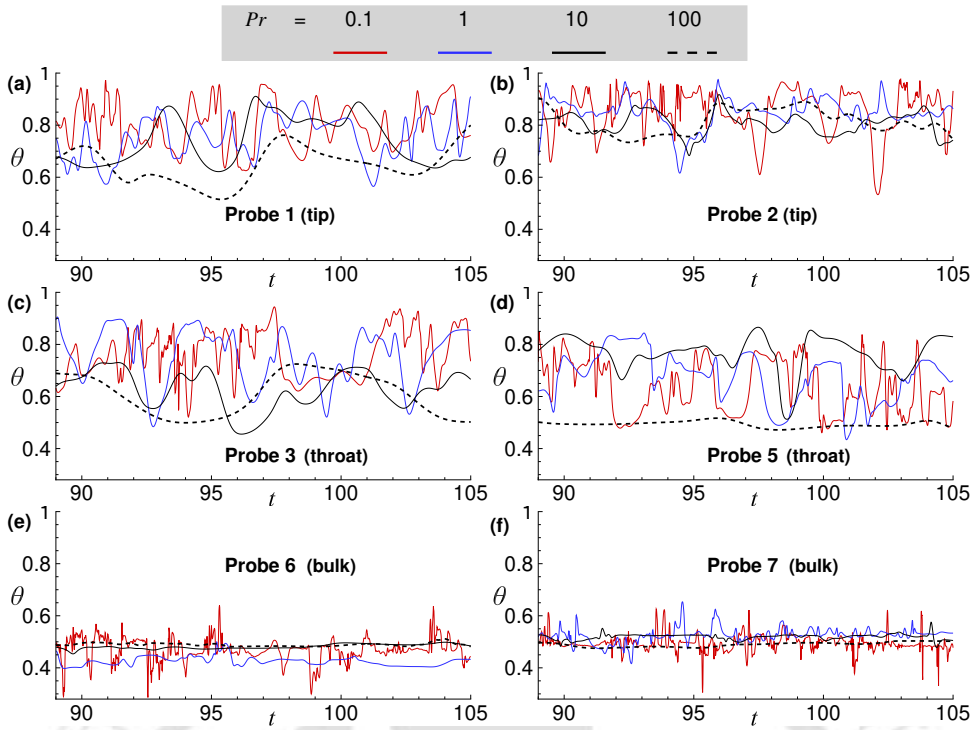

Figure 5.13: Time series of temperature for a short interval of time is shown for probes in the tip (a-b), throat (c-d), and bulk (e-f) regions for $Ra = 10^9$ at different Pr. Location of the probes can be referred from Fig. 5.12(b).

In Fig. 5.13 and Fig. 5.14, time series of temperature and vertical velocity, respectively, are observed for the selected probes above the tips (Probes 1 and 2), in the throat (Probes 3 and 5), and in the bulk (Probes 6 and 7) for $Ra = 10^9$ over a short span of time. It is easy to observe that probes close to the wall regions exhibit greater temperature fluctuations than the ones in the bulk where flow is nearly homogeneous. For a fixed region, both temperature (θ') and vertical velocity (v') fluctuations exhibit large magnitude for the lowest $Pr = 0.1$. As Pr is increased, they are largely diminished, and the flow becomes quieter. In contrast to θ', v' is large in the bulk and it diminishes in the near-wall regions. The distinct nature of v' and θ' in the bulk is because of the nearly homogeneous temperature field, while v is position-dependent. It other words, temperature fluctuations always fluctuate around the mean $\theta \sim 0.5$. However, mean vertical velocity varies with horizontal direction in the bulk because of the influence of the multiple large scale rolls present in the system.

To compare the intensity of the fluctuations between rough and smooth cells, variance of temperature (σ_θ^2) and vertical velocity (σ_v^2) fluctuations as a function of vertical height (y) is observed for $Ra = 5 \times 10^9$ at different Pr, as shown in Fig. 5.15. Note, the variance of a quantity ϕ at a given vertical height (y) is calculated as $\sigma_\phi^2(y) = \left\langle \langle \phi(\boldsymbol{x},t)^2 \rangle_t - \langle \phi(\boldsymbol{x},t) \rangle_t^2 \right\rangle_A$,

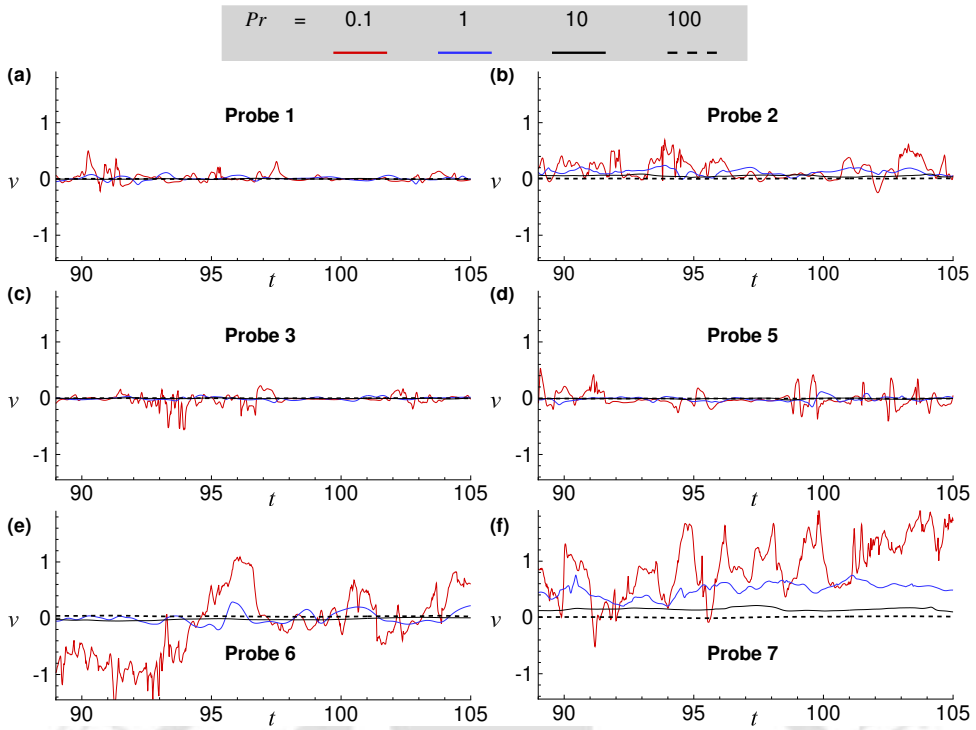

Figure 5.14: A segment of time traces of vertical velocity is shown for probes in the tip (a-b), throat (c-d), and bulk (e-f) regions for $Ra = 10^9$ at different Pr. For location of the probes, refer Fig. 5.12(b).

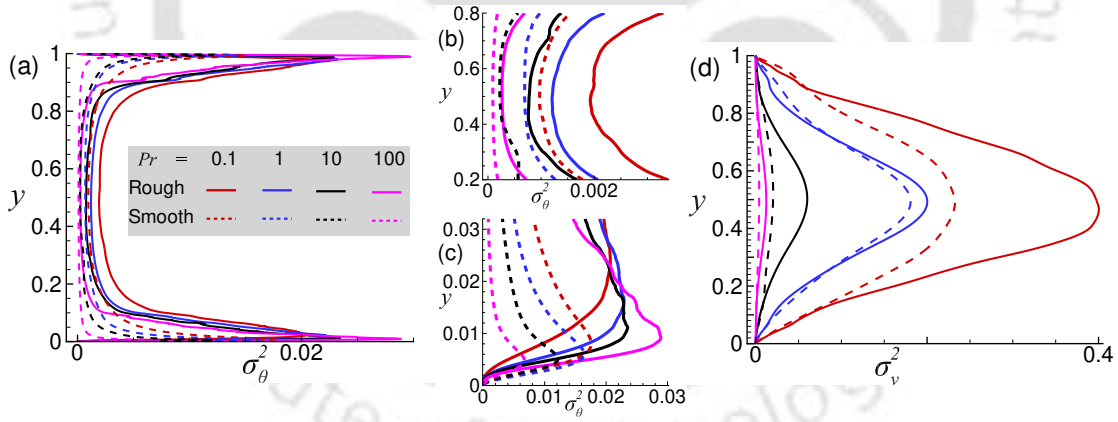

Figure 5.15: A comparison is made between the rough and smooth cells for variance of (a) temperature (σ_θ^2) and (d) vertical velocity (σ_v^2) as a function of the vertical height at the highest $Ra = 5 \times 10^9$. Frames (b) and (c) show the magnified view of the variation of σ_θ^2 in the bulk and near-wall region of the bottom plate, respectively.

where $\langle\rangle_A$ represents horizontal line average. As evident from Fig. 5.15(a), σ_θ^2 is higher for the rough cell at all Pr. In Fig. 5.15(b), magnified view of the variation of σ_θ^2 for the bulk region is shown, where amplification of temperature fluctuations is easily evident in the rough cell. A close up view close to the bottom plate shown in Fig. 5.15(c) also corroborates the finding of

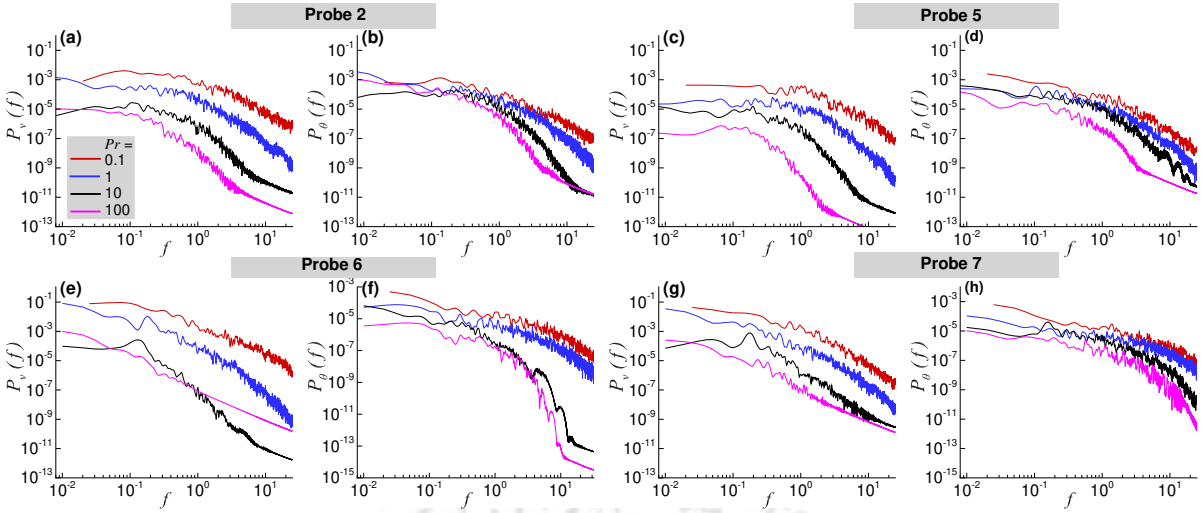

Figure 5.16: Power spectra of temperature (b,d,f,h) and vertical velocity (a,c,e,g) are shown for probes in the near-wall (a-d) and bulk regions (e-h) for $Ra = 5 \times 10^9$. For location of the probes refer Fig. 5.12(b).

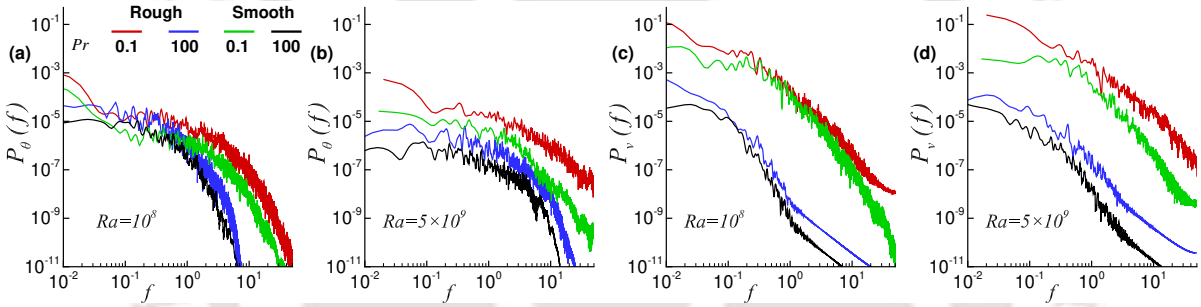

Figure 5.17: Power spectra of temperature (a-b) and vertical velocity (c,d) are compared between the rough and smooth cells in the bulk region at mid-height of the cell at $Ra = 10^8$ and $Ra = 5 \times 10^9$.

the increased θ fluctuation for the rough case. Note, θ fluctuations in the bulk are maximum for the lowest $Pr = 0.1$, and the increase of Pr results in diminishing of strength of the fluctuation for both the smooth and rough cells. However, in contrast to the bulk region, the maximum fluctuation for the rough cell is observed for the highest $Pr = 100$. As Pr decreases, there is a reduction in intensity of θ fluctuation. For the smooth cell, θ fluctuation follows a similar trend as observed in the bulk region, i.e, temperature fluctuation is maximum for the lowest Pr. The reverse role of Pr close to the rough walls is associated with the activation of plume emission sites. A large Pr flow with a thinner TBL expedites the activation of the roughness elements in emitting energetic plumes, which is responsible for the increased θ fluctuation. The strength of vertical velocity fluctuations, as shown in Fig. 5.15(d), is also significantly enhanced with the introduction of the rough surfaces. In agreement with our previous observation that the lower

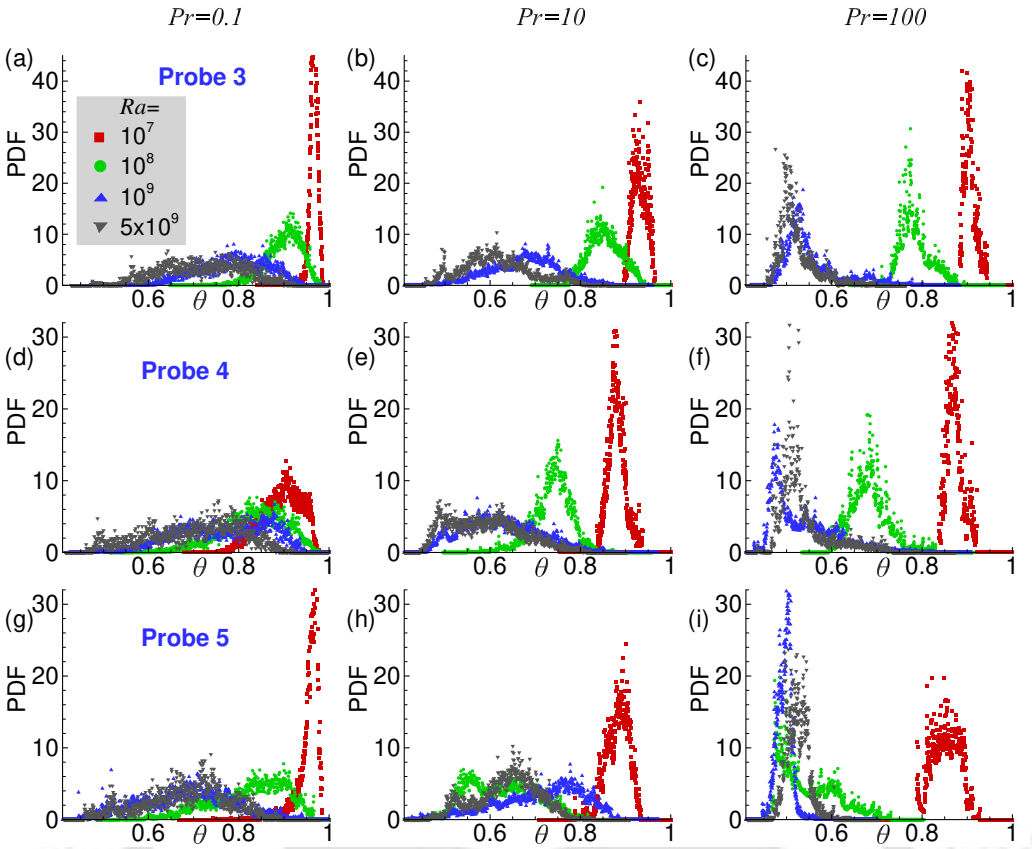

Figure 5.18: Evolution of temporal PDFs of temperature is observed for the probes in the throat regions for varying Pr and Ra. Frames (a-c), (d-f), and (g-i) represent data for probes 3, 4, and 5, respectively. For a given probe, the effect of increasing Pr can be observed by comparing the frames from left to right. Refer Fig. 5.12(b) for location of the probes.

Pr flows are highly turbulent, the maximum values of σ_θ^2 and σ_v^2 are obtained corresponding to the lowest $Pr = 0.1$ in the bulk region, while they are substantially dampened at the highest $Pr = 100$. The increased strength of temperature fluctuation close to the rough surfaces at a higher Pr flow is a result of the increased perturbations from the roughness elements.

Power spectra of velocity and temperature fluctuations reveal information about the energy cascade and the associated small-scale dynamics prevalent in the system. In Fig. 5.16, power spectra of temperature and vertical velocity are shown for probes near the bottom plate and in the bulk region at $Ra = 5 \times 10^9$ for different Pr. It can be observed that the energy content for both v and θ fluctuations are particularly higher for a lower Pr, and with the increase in Pr, it diminishes. The observation is in line with our previous discussion based on vertical profiles of variance of the fluctuations.

Further, we compare the spectra for rough and smooth cases in Fig. 5.17 at $Ra = 10^8$ and 5×10^9 for the lowest and highest $Pr = 0.1$ and 100, respectively. It can be observed that the v

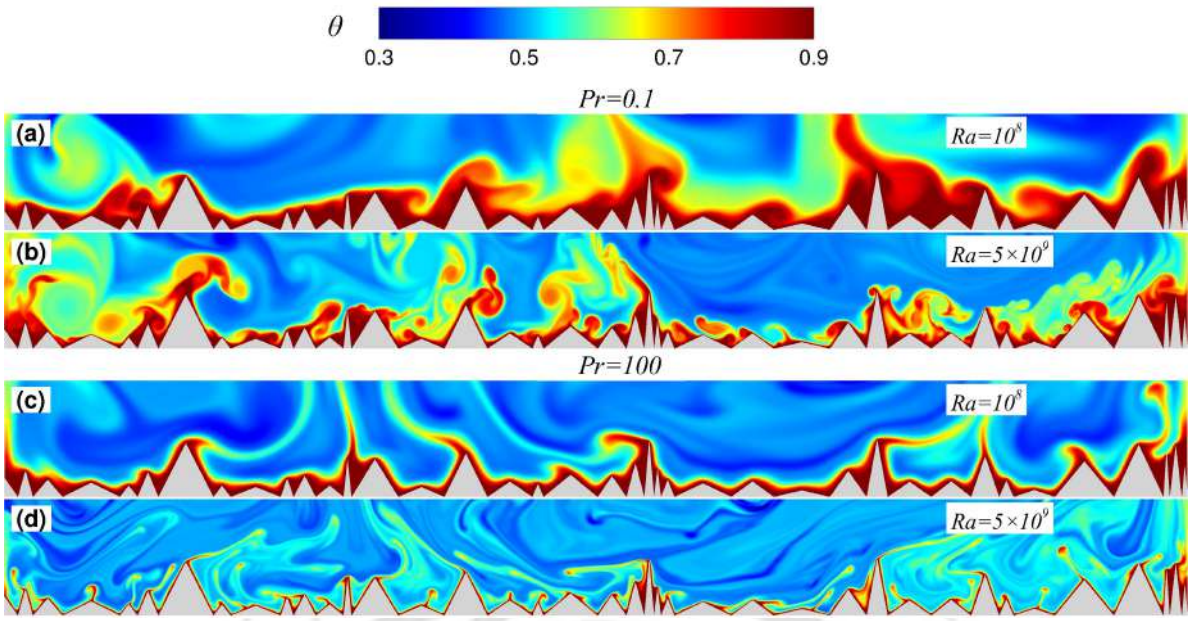

Figure 5.19: Snapshots of instantaneous temperature field for near-wall region close to the bottom plate are shown for (a-b) $Pr = 0.1$ and (c-d) $Pr = 100$ at $Ra = 10^8$ and 5×10^9.

and θ spectra for smooth and rough cases are comparable at $Ra = 10^8$. However, at the highest $Ra = 5 \times 10^9$, the spectra corresponding to rough surfaces show significantly increased energy levels at nearly all scales of the flow. The increased energy content for the rough cell is attributed to the activation of the small-scale roughness elements at a higher Ra in emitting plumes. At a lower Ra, the immobility of fluid due to stronger viscous force hinders the introduction of roughness facilitated perturbations in the system, which is responsible for the comparable energy content between smooth and rough cells.

In Fig. 5.18, the evolution of temporal PDFs of temperature for probes 3, 4, and 5 (throat regions of the rough bottom surface) is observed as a function of Ra for three different Pr. At any fixed Pr, we observe that the mean temperature is maximum for the lowest $Ra = 10^7$, where fluid is trapped inside the roughness cavities. As thermal forcing increases, flow mobility leads to ventilation inside the cavities, which is reflected from the reduced mean temperature as the peaks of the PDFs shift towards the lower temperature. Also, the PDFs acquire a wider skirt/base as Ra is increased. For the lowest $Pr = 0.1$ (first column of Fig. 5.18), though increase in Ra leads to a wider skirt yet no clear peak of the PDFs is perceived. However, for the highest $Pr = 100$, a wider skirt and a distinct peak of the PDFs are observed with increasing Ra. It again highlights the distinct flow dynamics prevalent in the near-wall regions at different Pr. At a fixed thermal forcing, varying Pr from 0.1 to 100 results in augmented occurrence of low temperature events. The most probable temperature or the peak of the PDFs starts to shift

towards $\theta = 0.5$, which is an indicator of a stronger penetration of the bulk fluid inside the throat regions. The result can also be understood from the fact that for higher Pr flows, TBL is thinner, which allows a quicker invasion of the cavity regions by the bulk in comparison to a lower Pr flow.

Distinct evolution of temporal PDFs with Ra, as observed above for the throat regions at different Pr, can be explained by observing instantaneous temperature field close to the bottom plate. In Fig. 5.19, snapshots of instantaneous θ field are shown for $Pr = 0.1$ (a-b) and $Pr = 100$ (c-d) at $Ra = 10^8$ and 5×10^9. It can be observed that at $Ra = 10^8$, throat regions are covered by a thick layer of high-temperature fluid, which is responsible for a higher mean temperature. It is clearly evident that TBL is thinner for $Pr = 100$. For the highest $Ra = 5 \times 10^9$, the flow is highly homogeneous for $Pr = 100$ with very fine flow structures in comparison to $Pr = 0.1$. Also, the cavity regions are largely invaded by the bulk fluid. This is the reason for the realization of a mean temperature close to $\theta = 0.5$ in the form of clearer peaks in the θ-PDFs. Note the plume contributions from the roughness elements are still present for $Pr = 100$, but as plumes are finer in size and highly streamlined while moving into the bulk region, their effect in stimulating θ fluctuations is not perceived appreciably in the cavity regions. The time-series data shown in Fig. 5.13 also substantiates the above finding. However, for $Pr = 0.1$, the flow even at the highest $Ra = 5 \times 10^9$ exhibits relatively larger thermal structures emanating from the roughness elements, which periodically makes their way inside the roughness cavities. In other words, the intermittent burst of relatively large hot thermal structures from the roughness elements adds to the inhomogeneity in the cavities and thus, responsible for the occurrence of high temperature events inside them. Owing to the above reasons, we still observe an augmented weightage to the high-temperature events. Hence, the distinct peaks of the PDFs are not pronounced even at the highest $Ra = 5 \times 10^9$.

5.8 Boundary layer profiles

Thermal boundary layer bears a strong relationship with the heat transport mechanism in natural convection. The oldest scaling theory given by Malkus [13] relates the decoupling of top and bottom TBLs with the classical scaling law, $Nu \sim Ra^{1/3}$. Later, Kraichnan and Spiegel [15, 16] proposed that in the limit of a very high Ra, BLs undergo a transition from laminar to turbulent state, resulting in an enhanced heat transport with negligible resistance due to momentum and thermal diffusivities. The aforementioned high Ra regime is known as the "ultimate" or

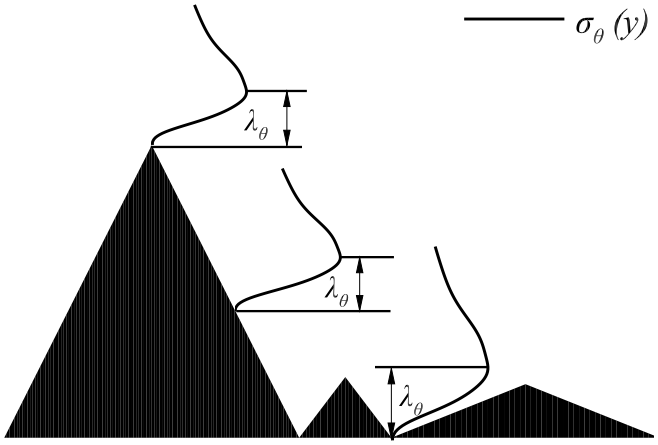

Figure 5.20: (a) Schematic shows the procedure employed for the estimation of local TBL thickness (λ_θ). Note, the vertical distance away from the walls with maximum temperature fluctuation gives λ_θ.

"asymptotic" regime with the scaling law, $Nu \sim Ra^{1/2}$. In the roughness context, it is now well established that the augmented heat transport is realized with the thickness of TBL being comparable to the amplitude of the roughness elements. Since both Ra and Pr influence the behavior of different scales of roughness elements, it is interesting to observe the connection between TBL thickness and the level of perturbations introduced into the system by rough surfaces.

In Fig. 5.20, the procedure employed to determine the edge of TBL is illustrated, where the vertical location of maximum temperature fluctuation away from the wall [89] gives local λ_θ. In Fig. 5.21(a-b), variation of TBL along the horizontal direction is observed as a function of Pr at $Ra = 10^8$ and 5×10^9, respectively. From frame (a), it can be observed that TBL thickness decreases with increase in Pr. For $Ra = 5 \times 10^9$, TBL is thinner and is starting to envelope the rough surface. The differences in TBL thickness at different Pr are largely diminished as thermal forcing is increased. Further, from Fig. 5.21(c-d), horizontal variation of TBL is observed for different Ra at $Pr = 0.1$ and $Pr = 100$, respectively. It is clearly evident that TBL is thickest for the lowest $Ra = 10^7$ and $Pr = 0.1$. The reason for the same can be attributed to a weaker buoyancy force, which is responsible for the immobility of the fluid inside the cavities. TBL for $Pr = 100$ cases is comparatively thinner than $Pr = 0.1$ with a better conformity with the rough surface texture. A thinner TBL at a higher Pr allows stronger participation of roughness elements in emitting plumes, which is responsible for significant enhancement in heat transfer rate.

Further, we have computed the global TBL thickness using the horizontally-time averaged

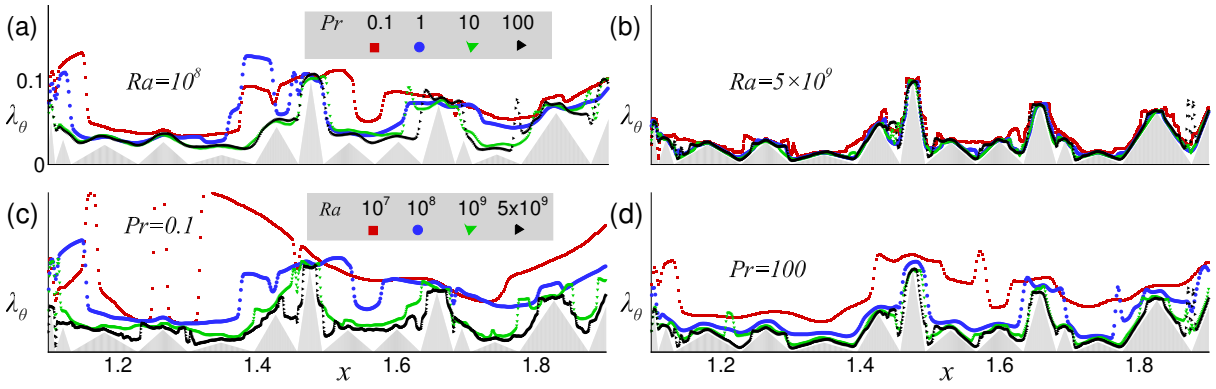

Figure 5.21: Horizontal variation of local TBL thickness is shown as a function of Pr in (a) at $Ra = 10^8$ and (b) $Ra = 5 \times 10^9$, while in (c) and (d), the variation is shown with Ra for fixed $Pr = 0.1$ and $Pr = 100$, respectively. Note, for simplicity in presentation, only a portion of the bottom surface is shown.

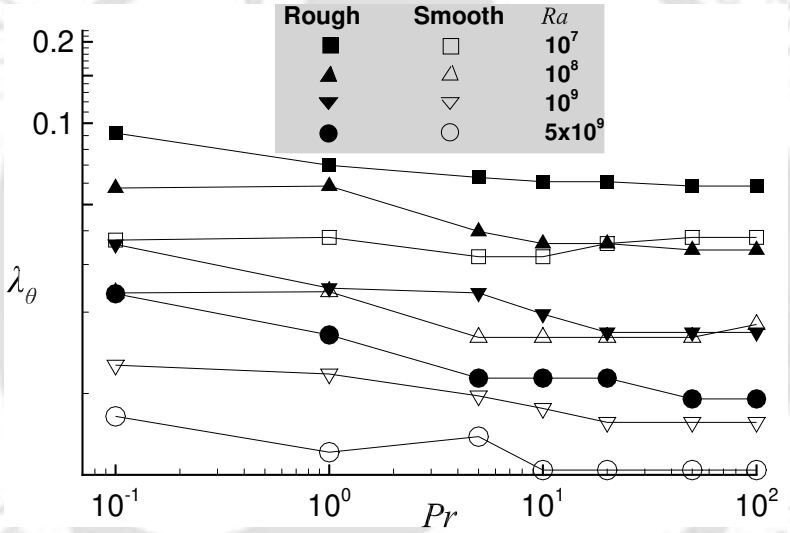

Figure 5.22: Variation of global TBL thickness as a function of Pr is shown for different Ra for both smooth and rough cases.

rms profile of temperature fluctuation. In Fig. 5.22, variation of λ_θ as a function of Ra and Pr can be observed for both the smooth and rough cells. At a fixed Pr, the decrease of λ_θ with increasing Ra is clearly evident here. Note, for the rough case, λ_θ is significantly thicker because of the fluid entrapment inside the cavities. For the rough cell, it can be observed that, in general, λ_θ decreases with Pr. In the higher Pr range, the change in λ_θ is observed to be marginal. For the smooth case, λ_θ is observed to be nearly invariant for $Ra \geq 10^8$ in $Pr \geq 5$ range. From the above discussion, it can be inferred that the choice of the input parameters, Ra and Pr, is seen to influence the growth of TBL. As the effectiveness of the rough surfaces depends on the relative size of the roughness elements and TBL thickness, the flow dynamics can be largely controlled

by Ra and Pr to realize an enhanced heat transfer rate.

5.9 Summary

The present work attempts to find the role of Pr in influencing flow structures and the prevalent heat transport mechanism in a two-dimensional rough rectangular convection cell. We show the importance of the choice of fluid, in addition to the applied temperature forcing, in realizing augmented heat transfer rate from the roughened cell. The distinct role played by Pr in the presence of roughness is evident in the form of a monotonic increase of *Nu* with increasing Pr. The result is a significant improvement to the nearly invariant *Nu* observed in the smooth cell. At a lower Pr, a thick layer of hot/cold fluid is observed above the top/bottom plate, while a higher Pr is associated with a thinner thermal boundary layer (TBL). For the former, large-scale diffuse structures are prevalent, while for the latter, fine mushroom-shaped structures are discharged from the near-wall regions. At a lower Ra, since roughness elements are embedded beneath the TBL, plume emission from them is thwarted. The creation of numerous nucleation sites and subsequent frequent plume emission is observed at higher Pr as more and more roughness elements penetrate the TBL. At a given Ra, since a high Pr flow boasts of a thinner TBL, roughness elements become thermally active quickly. This results in augmented *Nu* at higher Pr.

In comparison to the smooth case, plumes are observed to span a wider extent of the domain in the rough cell. Also, they are more localized and intense, which finally yield greater heat transport. The level of flow perturbations effected by rough surfaces can be controlled by either increasing Ra or Pr or both. A direct comparison of flow intensity measured in terms of the global Reynolds number between rough and smooth cells reveal that Re is superior for the rough cell for a larger Ra or Pr. The diminished flow intensity for extremely low Ra or Pr can be attributed to the entrapment of fluid inside the roughness cavities, where the flow is largely viscosity dominated. Further, the comparison of variance of temperature and vertical velocity between the smooth and roughened cells shows that the fluctuations are strengthened in the bulk in the presence of roughness. The increased energy of the fluctuations in the rough case is also substantiated by their power spectra. At a given thermal forcing, the fluctuations attenuate on increasing Pr, which is an indicator of the flow becoming quiescent. Temporal PDFs of temperature in the throat regions highlight the distinct flow behavior at varying Pr. The appearance of a distinct sharp peak of the PDFs around $\theta = 0.5$ for the highest $Ra = 5 \times 10^9$ at

$Pr = 100$ indicates effective penetration of the bulk fluid inside the cavities. However, for the lowest $Pr = 0.1$, an intermittent burst of large plumes from the roughness elements continue to mark their presence in the throat regions, which does not allow the development of a distinct peak in the PDF, and the mean temperature is still quite higher than the bulk mean temperature (0.5).

Lastly, distinct behavior of TBL over rough and smooth surfaces at different Pr is explored. Global TBL thickness is observed to be relatively thicker for the rough case and follows a decreasing trend with Pr. In the smooth cell, the invariant nature of global λ_θ is observed in the higher Pr and Ra range. Further, we observe that the ability of rough surfaces to influence flow structures depends on the geometric parameters of the roughness elements and the input parameters, Ra and Pr. At the lowest $Pr = 0.1$ and $Ra = 10^7$, TBL is thickest with nearly no interaction with the rough surfaces. However, as Ra and Pr are increased, thickness of the TBL becomes comparable with the height of the roughness elements, which assists detachment of thermal structures from the rough surfaces and enhances the heat transfer rate.

6

DOMINANT HEAT TRANSFER MECHANISM WITH CONICAL ROUGHNESS

In this chapter, the effect of Prandtl number in heat transfer mechanism in turbulent Rayleigh-Bénard convection is explored in a cubical box endowed with conical roughness elements on the isothermal plates. The simulations are carried out at the fixed $Ra = 10^8$ *with* Pr *varying from* 1 *to* 50*. It is observed that the trends followed by Nu in 2D and 3D configurations are different. In contrast to the monotonic increasing trend of Nu (Nu* $\sim Pr^{0.27}$*) in the 2D roughness explored previously in chapter 5, Nu assumes an invariant behavior (Nu* $\sim Pr^{0.012}$*) as a function of* Pr *though it is approximately* 50% *higher than its smooth counterpart. Flow intensity, measured in terms of Reynolds number, shows comparatively lower values for the 3D configuration with a general decreasing trend with* Pr*. The addition of the roughness elements is observed to have an effect on the preferred orientation of LSC. The effect is predominant for low* Pr*, where the roughness interferes most with the natural bias of LSC towards the diagonal planes of the cubical box. Further, we have distinguished the active flow mechanism in different* Pr *using plume statistics, temporal PDFs, power spectra, and variance of vertical velocity (*v*) and temperature* θ*, thermal and viscous dissipation rates, and cross-correlation of* v *and* θ *fluctuations.*

6.1 Introduction

Though 2D simulations reveal a great deal of information about global heat transport scaling laws prevalent in high Ra flows, they are not the actual representation of the flows occurring in nature. Real-life flows are innately predisposed to 3D. To enhance our understanding of real-life flows, we carry out 3D simulations in a rectangular cell at $Ra = 10^8$ with $1 \leq Pr \leq 50$, where both the top and bottom plates are populated with cones as roughness elements, as shown in Fig. 6.1. The location, geometric parameters, amplitude and radius, of a roughness element are

randomly assigned on both the plates such that the ratio of amplitude to radius of all the elements remains unity.

Distinct flow behavior in 2D and 3D smooth cells has been previously highlighted in various studies [50, 58, 59]. The differences are divulged in LSC behavior, plume dynamics, heat transfer mechanism, flow intensity as well as in the energy cascade process. Huang and Zhou [58], while comparing their 2D data with the 3D results in a cylindrical cell, observed anomalous $Nu(Pr)$ relation. They found that for a moderate $Ra \leq 10^9$ and $Pr \approx 2 \sim 3$ range, *Nu* attains a minimum value rather than a maximum as observed in the 3D case. The reason for this behavior was attributed to the manifestation of a strong competition between corner rolls and LSC, which creates a strong counter gradient heat transport and, thus, results in a diminished overall heat transfer rate. With the increase in Pr, the difference in heat transfer rate between 2D and 3D cells is diminished [50]. In the higher Ra range, Pr dependency is observed to be qualitatively similar in both 2D and 3D cases [50]. The lack of extra direction in 2D promotes stronger LSC [50] with corner rolls. The effect of which is evident in a stronger flow strength in comparison to a 3D case where plumes are not confined in a particular plane. The behavior of fluctuations in 2D and 3D cases in the inertial subrange is also observed to be distinct. It is observed that 2D flows mainly exhibit the inverse energy cascade process [63, 95]. In other words, energy is transferred from smaller eddies to larger ones, and not the other way around.

In the above discussion, the effect of dimensionality on fluid turbulence emerges without

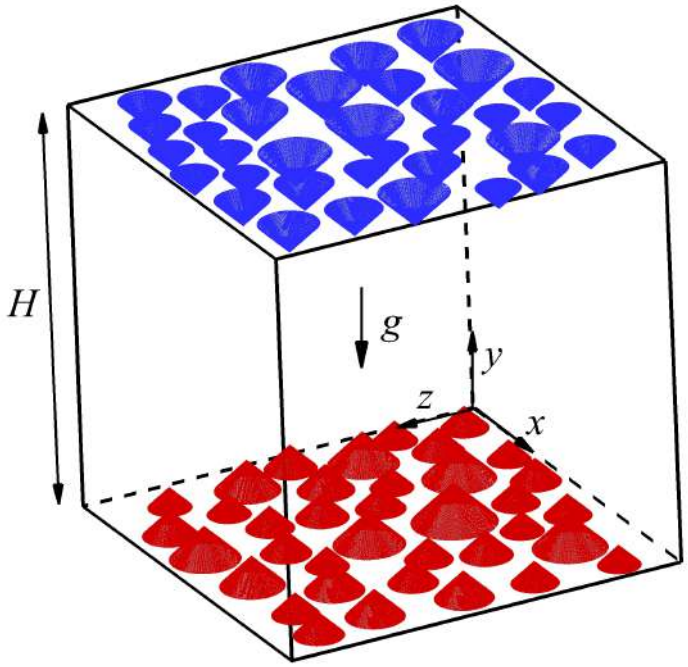

Figure 6.1: Roughness setup in the cubical convection cell is shown.

considering the effect of addition of rough surfaces. It is a general understanding that rough surfaces, whether linked to 2D or 3D convection cells, promote enhancement in heat transfer when their amplitude becomes comparable to or smaller than the thermal boundary layer thickness [35, 39–42, 79, 82, 108, 109]. In both 2D and 3D roughness studies, the importance of the choice of the geometrical attributes of roughness elements is clearly established. Plume contributions from taller roughness elements are perceived early at a lower Ra, while it takes a larger thermal forcing to expose smaller roughness elements to the edge of the TBL and effect perturbations into the system. The width of the roughness elements or the spacing between them is also an important parameter that decides whether the roughness facilitated cavity regions are washed by the bulk fluid. When the elements are crowded too closely, fluid gets trapped in the cavity regions and thus, hinders heat transport. On the other hand, when elements are too sparsely populated, the flow mechanism resembles that of a smooth cell, and no significant enhancement in heat transfer rate is achieved. It takes an optimum spacing/width of roughness elements to maximize plume emission. Note that in 2D configuration, fluid gets severely trapped inside the roughness cavities at a lower Ra. However, in the case of 3D, the availability of an extra direction promotes relatively better fluid mobility inside the cavities [108]. This is the reason that in a 3D roughness configuration, modest or no reduction in heat transfer rate is observed at a lower thermal forcing, whereas in the 2D rough cells, reduction in *Nu* is more pronounced.

The choice of fluid, marked by Pr, plays a pivot role in the evolution of dominant flow structures in the system [19, 46, 47]. Low Pr fluids exhibit disposition for large-scale structures, whereas high Pr flows are accompanied by fine thermal structures. It is quite interesting that in spite of varying prevalent flow structures at different Pr, the heat transfer rate in the moderate to high Pr range is nearly the same [48]. In other words, *Nu* is invariant of Pr. However, in recent studies [35, 60], it has been shown that Pr may assume an active role in controlling *Nu* when roughness is introduced in the system. Xie and Xia [35] conducted their study inside a cylindrical cell with periodically distributed pyramid elements for $7.5 \times 10^7 \leq Ra \leq 1.31 \times 10^{11}$ and $3.57 \leq Pr \leq 23.34$. They considered different aspect ratio ($\lambda_{ar} = h/\lambda = 0.5, 1, 1.9, 4$) of the roughness elements. They observed an interesting result where *Nu* corresponding to $Pr = 23.34$ is observed to be significantly higher than that at $Pr = 3.57$. The result is quite remarkable and unexpected, as in case of a smooth cell, *Nu* peaks around $Pr \sim 3$ to 4, and beyond that *Nu* becomes invariant of Pr. However, the increment in *Nu* at the highest $Pr = 23.34$ showed a stronger dependence on λ_{ar}. The increment in *Nu* at $\lambda_{ar} = 4, 1.9, 1$ and 0.5 is recorded as $50\%, 34\%, 4\%$ and -8%, respectively. In other words, a higher aspect ratio of the roughness

elements yielded a greater heat transfer rate, whereas a lower λ_{ar} did not confer a greater enhancement in *Nu*. The study showed evidence of Pr assuming an active role in deciding the global heat transfer rate. Recently, Yang *et al.* [60] performed 2D simulations in a rough square cell, where they highlighted the role of Pr in deciding the critical height (h_c) of the roughness elements above which *Nu* increases with respect to a smooth cell. For $10^7 \leq Ra \leq 10^9$ and $0.01 \leq Pr \leq 100$, they observed three distinct regimes for $h_c(Pr)$. The regime at low Pr, which is dominated by LSC, exhibits a decreasing h_c trend with increasing Pr. The moderate Pr regime sees an advent of thermal plumes and thus, creating strong competition between corner rolls and LSC. This regime experiences an increase of h_c with increasing Pr. The high Pr regime is characterized by very fine plumes such that the strength of large-scale flows is largely diminished. Here, h_c decreases with the increment of Pr. The above-mentioned study again brought about the nuances that decide the effectiveness of Pr in enhancing *Nu* in a roughness facilitate cell. Bhattacharya *et al.* [110] carried out 3D simulations inside a cubical box, where they investigated the effect of Prandtl number ($0.02 \leq Pr \leq 100$) on the small-scale properties at the fixed $Ra = 10^7$. It was observed that kinetic energy spectra obey the Kolmogorov scaling of $\sim k^{-5/3}$ for low Pr (≤ 1), while for high Pr ($\gg 1$), a steeper scaling ($\sim k^{-2.5}$) was noticed. The increase of Pr was linked to damping of amplitudes of kinetic energy spectra and those of the velocity structure functions. Through PDFs of local convective heat flux, they observed that the strength of heat flux fluctuations augments with increasing Pr. The reason for the same was attributed to different plume morphology at low and high Pr flows.

Note that though computationally favorable 2D roughness studies are quite lucrative, especially in exploring the prevalent heat transfer scaling laws in the high Ra range, the underlying flow mechanism in various real-life flows is quite different than revealed in 2D. To imitate 3D real-life flows occurring in nature, we introduce irregular conical-shaped roughness structures on both the top and bottom isothermal plates with random locations in a cubical cell. The idea of a random selection of the roughness elements is consistent with the rough surfaces encountered in nature. So far, majority of the studies in literature involved mono-scale or other simple roughness structures, which is a rather simplified/unrealistic version of thermal convection taking place in real-life flows. Thus, with the present 3D-roughness setup, we aim to gain an in-depth knowledge of the role of Pr in altering flow structures and global heat transport in a highly complex and realistic roughness texture.

6.2 Numerical details

The simulations inside a cubic box provided with irregular conical roughness elements on the isothermal plates are solved for a fixed $Ra = 10^8$ with Pr varying from 1 to 50. All the walls admit no-slip velocity boundary condition. While the top and bottom roughened plates are maintained at constant temperatures, lateral walls are kept adiabatic. Using a standard random number generator, the amplitude and location of the centroid of the base of cone is assigned. The aspect ratio of a conical element, defined as the ratio of its height to radius, is kept unity. The amplitude of the conical elements vary within 5% to 10% of H. The cones are populated in such a way that a minimum clearance of $0.01H$ is maintained between them. Further, the maximum change in heat transfer area due to the addition of conical elements is restricted to 20% of the base area of the isothermal plates. Note that for a direct comparison with the rough case, we have also performed sufficiently resolved simulations in a cubic box with smooth surfaces.

Table 6.1: Details of the grid independence study performed at $Ra = 10^8$ for $Pr = 1$ and 50 are listed. Here, M_3 is the adopted mesh, N^3 is the grid resolution, $\langle Nu \rangle_{V,t}$ is the calculated mean Nusselt number, and $\langle \sigma_\theta^2 \rangle_V$ is the global variance of temperature fluctuations. Note that alongside $\langle Nu \rangle_{V,t}$ and $\langle \sigma_\theta^2 \rangle_V$, their absolute relative changes (in parenthesis) with respect to the preceding coarse mesh are also listed.

		$Pr = 1$		$Pr = 50$	
Mesh (M_i)	N^3	$\langle Nu \rangle_{V,t}$	$\langle \sigma_\theta^2 \rangle_V$ ($\times 10^{-3}$)	$\langle Nu \rangle_{V,t}$	$\langle \sigma_\theta^2 \rangle_V$ ($\times 10^{-3}$)
M_1	240^3	48.9	5.007	51.3	2.77
M_2	260^3	48.83(0.143%)	5.001(0.12%)	51.3(0%)	2.739(1.2%)
M_3	300^3	48.23(1.23%)	4.815(3.72%)	50.96(0.66%)	2.68(2.15%)
M_4	320^3	48.39(0.33%)	4.832(0.35%)	51.1(0.27%)	2.677(0.11%)

A grid that is uniform in the horizontal directions and non-uniform in the vertical direction is used to sufficiently resolve the boundary layer regions. A Mesh refinement study, the details of which are presented in Table 6.1, is conducted to ensure the results are independent of the adopted grid resolution. It can be observed that both the global *Nu* and variance of temperature fluctuations $\langle \sigma_\theta^2 \rangle_V$ converge quite well for the four progressively refined meshes (M_i, i = 1 − 4)

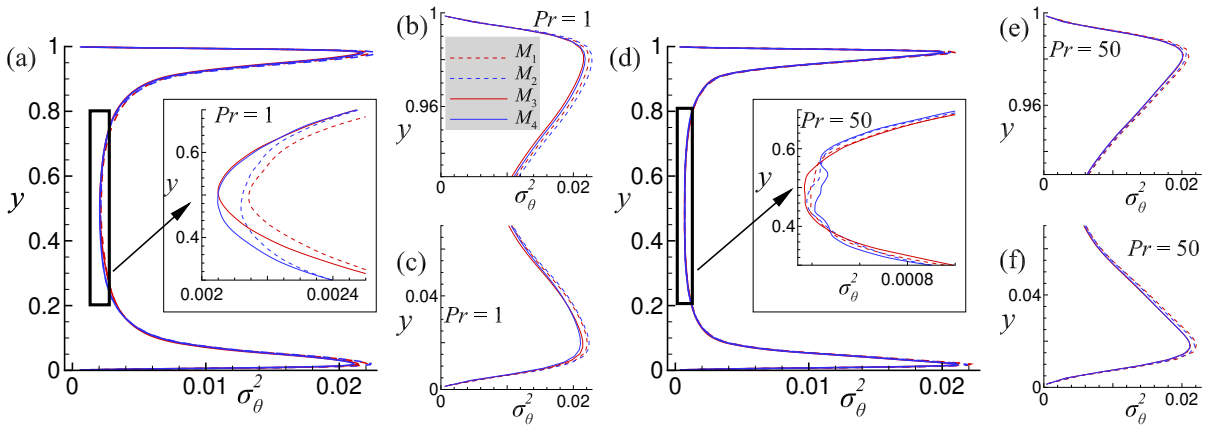

Figure 6.2: Vertical profiles of variance of temperature (σ_θ^2) obtained at different mesh resolutions are shown for (a-c) $Pr = 1$ and (d-f) $Pr = 50$. The insets in (a) and (d) show blown-up view in the bulk region, while (b,c,e,f) show the same close to the walls.

used for $Pr = 1$ and 50 cases. For $Pr = 1$ case, the maximum variation in $\langle Nu \rangle_{V,t}$ and $\langle \sigma_\theta^2 \rangle_V$ between any two successive grids does not exceed 1.4 and 3.8%, respectively. For $Pr = 50$, the maximum variation is 0.7 and 3.3% in $\langle Nu \rangle_{V,t}$ and $\langle \sigma_\theta^2 \rangle_V$, respectively. Further, we compare vertical profiles of horizontally-averaged variance of temperature for the selected mesh resolutions in Fig. 6.2. The profiles match quite well with maximum deviations of 5.29% and 4.285% for $Pr = 1$ and $Pr = 50$ cases, respectively. The adopted grid (M_3) of $300 \times 300 \times 300$ ensures adequate spatial resolution such that the maximum grid spacing in the vertical direction is smaller than the Kolmogorov length scale.

To ensure adequate time resolution, time increment is kept lower than the Kolmogorov time

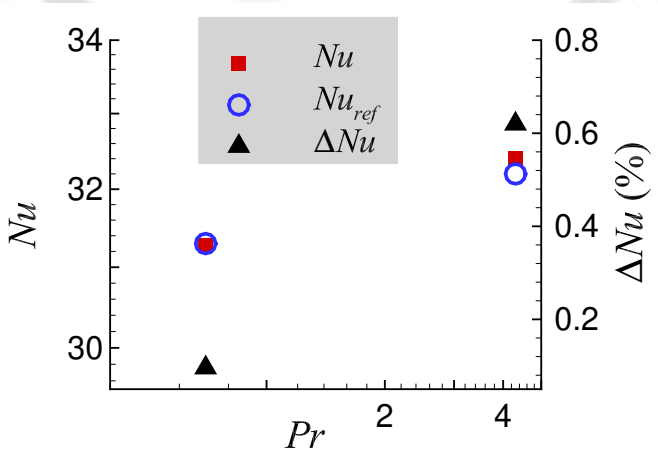

Figure 6.3: Comparison of global *Nu* with that reported by Kaczorowski and Xia [70] for the smooth cubical box. Also, deviation in the Nusselt number, $\Delta Nu = \left|(Nu/Nu_{ref}) - 1)\right|$, from the reference case is reported.

scale with the maximum Courant never exceeding 0.2. Turbulent statistics are collected for at least 250 free-fall time units once the statistically stationary state is realized. To confirm the convergence of the statistics, we compare the mean global *Nu* obtained from the complete sampling range and from the last half of it. We observe a maximum deviation of 1% in *Nu* among the Pr cases, refer Table 6.2, which confirms the statistical convergence of the simulations. The present numerical setup has been validated in the past for smooth cells in both cubic and cylindrical geometries. The comparison of the global heat fluxes with that reported by Kaczorowski and Xia [70] (numerical work) for a smooth cubic cell at $Ra = 10^8$ for $Pr = 0.7$ and 4.3 match quite well with a maximum deviation of 0.62%, refer Fig. 6.3.

Table 6.2: Global Nusselt number *Nu* averaged over the entire sampling duration is compared with Nu_{II} obtained from the last half of the sampling.

Pr	Nu	Nu_{II}	$\Delta Nu = \lvert 1 - (Nu_{II}/Nu) \rvert$
1	48.22	47.74	1.00%
4.3	51.47	51.39	0.15%
10	51.55	51.37	0.35%
20	50.91	50.93	0.03%
50	50.90	51.00	0.20%

6.3 Heat transport mechanism

Nusselt number and its scaling lie at the heart of thermal convection. In smooth cells *Nu* asymptotically reaches the exponent $5/12$ for 2D and $1/2$ for 3D [41]. However, the addition of roughness imparts the same asymptotic scaling of $1/2$ in both 2D and 3D [35, 39, 41, 42, 82, 109]. In addition to 3D simulations being computationally expensive to unravel flow physics at high Ra, the above observation led to extensive 2D simulations with rough surfaces. The effect of flow dimensionality is that a 2D flow manifests a stronger large-scale circulation driven by the ordered motion of the thermal plumes. It contrasts with a 3D flow, where plumes have the luxury of escaping through the extra lateral direction. As most flows in nature are 3D, a thorough understanding of their dominant heat transfer mechanism is needed.

In Fig. 6.4(a), the variation of *Nu* with Pr is shown for both 2D and 3D rough cells at $Ra = 10^8$, while Fig. 6.4(b) represents the relative change in *Nu* with respect to the smooth cell,

defined as $\Delta Nu = Nu/Nu_s - 1$. It can be observed that the trends followed by *Nu* in 2D and 3D configurations are different. Nusselt number is nearly invariant of Pr ($Nu \sim Pr^{0.012}$) in case of the 3D cell, while in the 2D rough case, *Nu* obeys an increasing scaling law, $Nu \sim Pr^{0.127}$. It is interesting to note that there is only a difference of about 2% between 2D and 3D data for *Nu* at $Pr = 50$. The result bears a strong resemblance to the observation in smooth cells [50] where *Nu* in 2D and 3D tend to converge at a high Pr. The relative increase in *Nu* with respect to the smooth case for 3D rough configuration is about 50% for all Pr, while for the 2D case, it is 86% for $Pr = 50$ and 1.4% for $Pr = 1$. The reason for the reduced effectiveness of the roughness in 2D flows at lower Pr can be attributed to the greater confinement of fluid inside the cavities. In the case of 3D, roughness cavities are not covered from all directions, allowing fluid to escape them. Hence, greater mobility inside the roughness cavities for 3D allows achieving an augmented *Nu* even at a low Pr.

Reynolds number is used to quantify flow intensity developed in the system in response to the applied temperature gradient between the horizontal isothermal plates. Mathematically, it is defined in terms of dimensional variables as

$$Re = \frac{UH}{\nu}$$

The non-dimensional variable version of the Reynolds number obtained using the free-fall velocity ($\sqrt{\beta g \Delta T H}$) and height of the cell (H) as the reference scales is obtained as

$$Re = U^* \frac{\sqrt{\beta g \Delta T H}\ H}{\nu} \implies Re = U^* \sqrt{\frac{\beta g \Delta T H^3}{\nu \alpha}} \sqrt{\frac{\alpha}{\nu}}$$
$$\implies Re = \sqrt{\frac{Ra}{Pr}}\, U^*$$

Here, U^* signifies the suitable velocity for calculating Re. In our calculations, the velocity is chosen such that it represents the maximum of rms (horizontally averaged) of fluctuations [84]. The Reynolds number based on maximum values of rms of u' and v' and w' is termed as Re_{urms}, Re_{vrms}, and Re_{wrms}, respectively. In Fig. 6.5, variation of Re with Pr is shown. For a better comparison, data for the 3D smooth case and 2D rough cell is also shown. It can be observed that irrespective of the choice of the velocity scale, flow intensity drops with the increase in Pr. Among the compared cell configurations, Re at a fixed Pr is highest for the 2D rough cell, followed by the 3D rough and smooth cases. The reason for the higher flow intensity in 2D configuration can be attributed to a more coherent and constrained flow of plumes. Further, it can be observed that for a fixed Pr, the maximum deviation in flow strength between the 2D and 3D

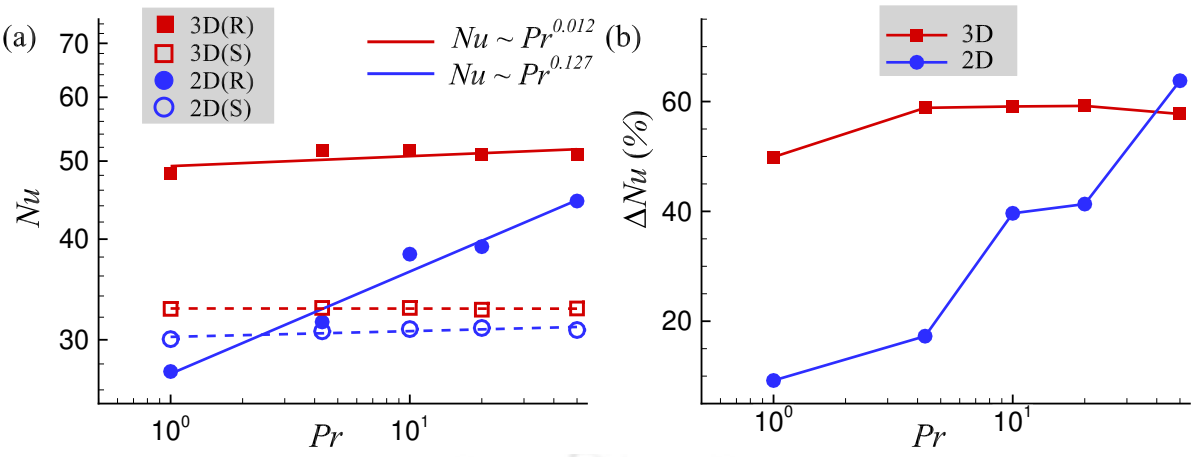

Figure 6.4: Nusselt number (Nu) and its relative change with respect to the smooth cell, $\Delta Nu = (Nu/Nu_s) - 1$, as a function of Pr are shown at $Ra = 10^8$. Here, R and S signify rough and smooth cases, respectively. The solid lines in (a) show least-squares fitting for the rough cells, while dashed ones correspond to the smooth cases.

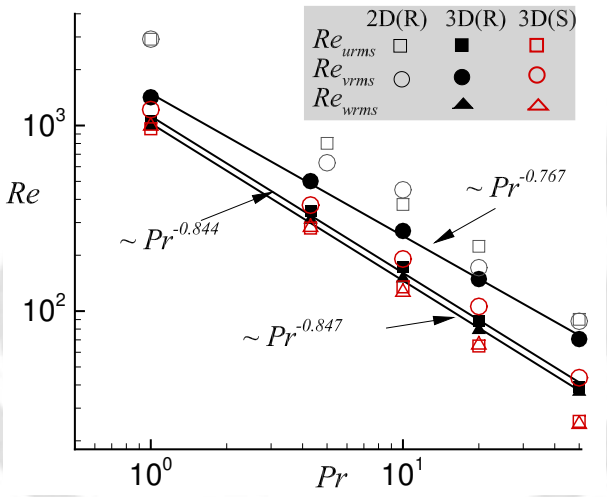

Figure 6.5: Variation of different measures of Re as a function of Pr. Note solid lines represent power law fittings to the 3D roughness data.

rough cases is observed from Re_{urms} estimate. For the 3D configurations, it can be observed that Re_{urms} and Re_{wrms} are comparable, while Re_{vrms} is slightly on the higher side. Least-squares fit to the data reveals a $Re(Pr) = APr^m$ relation. The details of the fitting parameters for different cell configurations are listed in Table 6.3. Comparison of m between the 3D rough and smooth cases clearly illustrates that Re for the former decays slowly with increasing Pr.

In Fig. 6.6, isosurfaces of temperature are shown for instantaneous data close to the bottom heated plate for different Pr. The change in flow dynamics with increasing Pr can be readily observed. At $Pr = 1$, flow structures emitted from the roughness elements are thicker with a

Table 6.3: Prefactor and exponent of least-squares fit $Re(Pr) = APr^m$ are listed for the different cell configurations.

Study	U^*	A ($\times 10^3$)	m
Rough (3D)	u_{rms}	1.122	-0.844
	v_{rms}	1.486	-0.767
	w_{rms}	1.025	-0.847
Smooth (3D)	u_{rms}	1.030	-0.926
	v_{rms}	1.261	-0.842
	w_{rms}	1.058	-0.942
Rough (2D)	u_{rms}	3.050	-0.888
	v_{rms}	2.922	-0.901

stronger mixing among them. However, with the increase in Pr, they emerge finer and columnar. It is generally perceived that large-scale circulation is dominant in low Pr flows [48, 51–53] and with increasing Pr, its strength diminishes with the emergence of finer and distinctive plumes. To observe dominating flow structures and their orientation in the present roughness setup, we chose four different planes represented as HP, VP, D1, and D2 to analyze isosurfaces of temperature, as shown in Fig. 6.7. Here, HP represents the horizontal plane taken at mid-height of the cell, VP is the vertical plane at $z = 0.5$, and D1 and D2 are the diagonal planes. In Fig. 6.8, instantaneous temperature fields for the selected planes are shown, where transformation of large flow structures into finer ones on increasing Pr is readily evident. At $Pr = 1$, see frames (a-d), we can observe a large-scale mean flow in VP, D1, and D2 planes. However, with the increase in Pr, there is an emergence of isolated fine plumes with weakened mean flow. The result is in agreement with the previous observations where the weakening of large-scale circulation is reported for higher Pr flows.

Further in Fig. 6.9, we project the strength of angular rotation (ω) of fluid flow, calculated about the geometric center of the cubic cell, onto the chosen directions (x, y, z and normals to diagonal planes $D1$ and $D2$) to identify the preferred orientation of the large-scale mean flow in both rough and smooth configurations. Large-scale circulation is one of the fascinating features of turbulent Rayleigh-Bénard convection, where a nearly coherent roll structure of large length

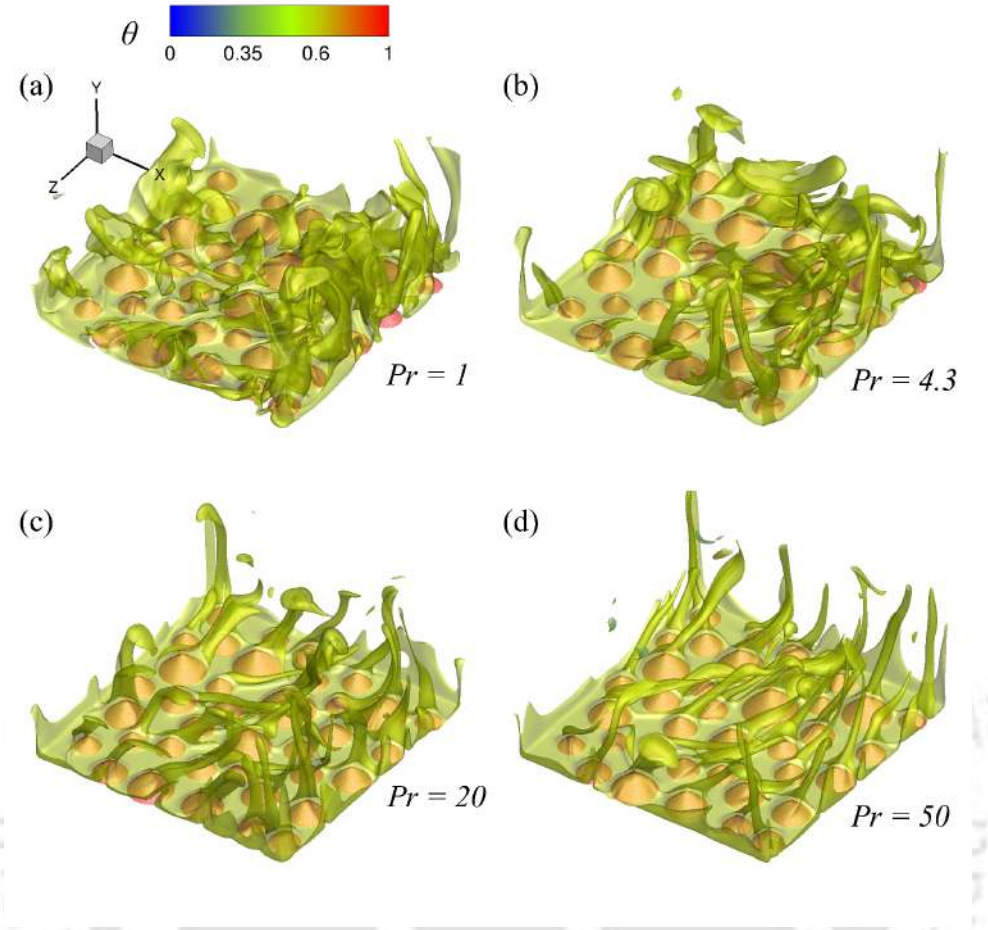

Figure 6.6: Isosurfaces of temperature at Pr = (a) 1, (b) 4.3, (c) 20, and (d) 50 are shown for the bottom plate with $\theta = 0.6$ and 1. Flow structures transform from thicker at low Pr to finer and columnar with increasing Pr.

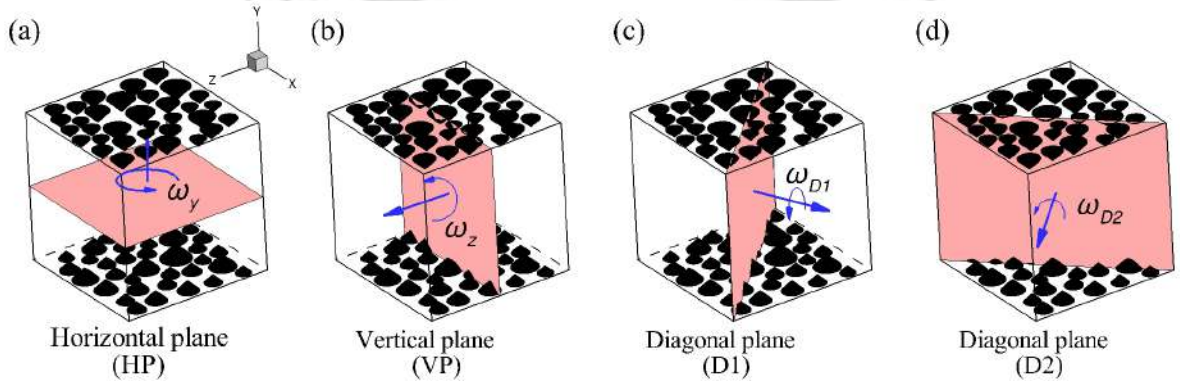

Figure 6.7: Schematic showing chosen planes to observe flow orientation and structures.

scale exists in the system with warm fluid rising and cold fluid sinking in a circular or elliptic path. This large-scale circulation (LSC) is also known as the “wind of turbulence”. The genesis

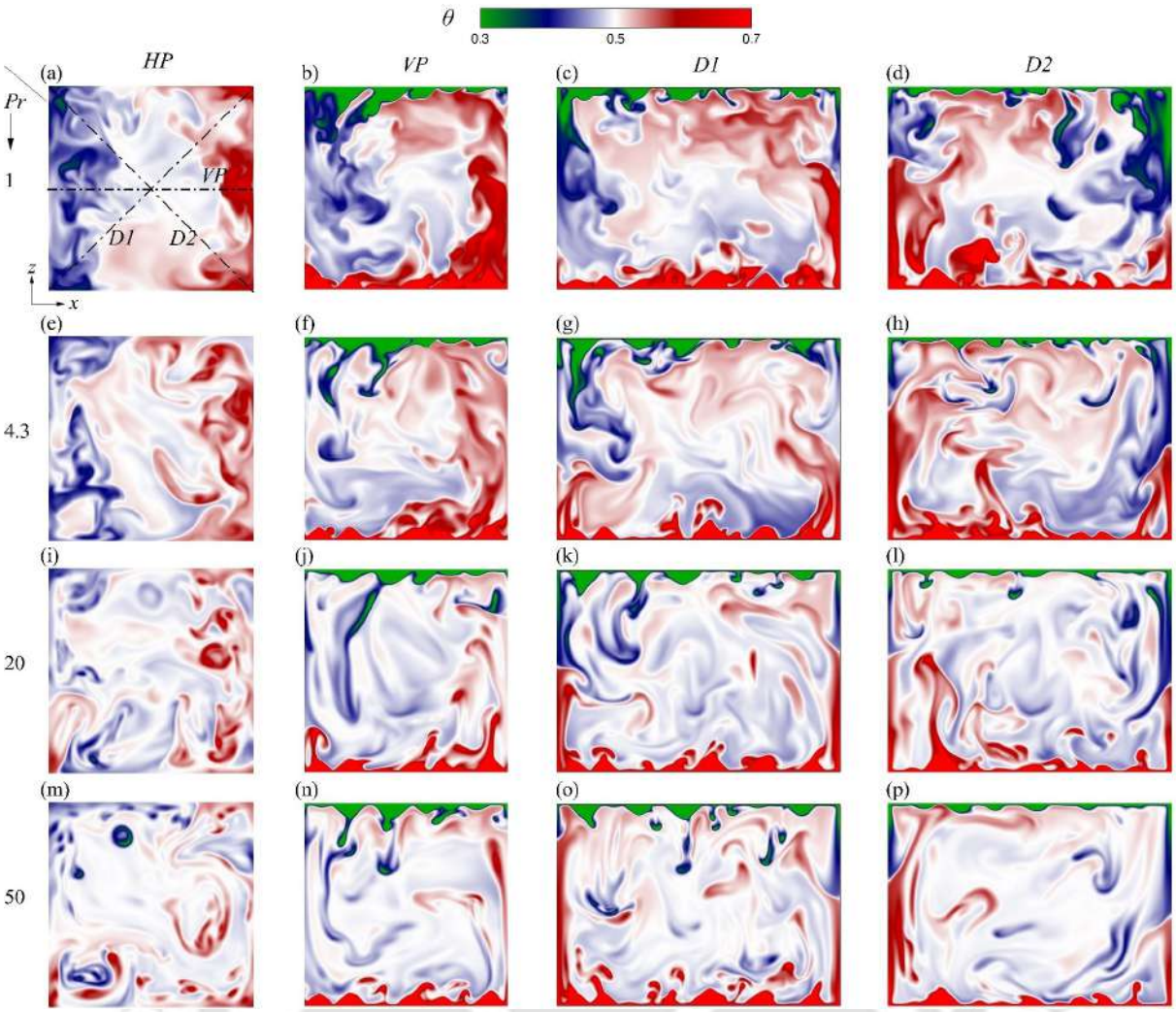

Figure 6.8: Temperature fields at different planes HP, VP, D1, and D2 are shown for (a-d) $Pr = 1$, (e-h) $Pr = 4.3$, (i-l) $Pr = 20$, and (m-p) $Pr = 50$. Note that HP is a horizontal plane taken at mid-height of the cell, while the positions of vertical (VP) and diagonal planes (D1 and D2) are shown in frame (a).

and sustenance of LSC are quite intriguing to the research community. In the literature [111], thermal plumes are believed to be the ones that initiate and sustain LSC. It is observed that during the course of motion of LSC, its plane can undergo significant angular shifts. This phenomenon is called "reorientation". It can occur in two ways. The first is rotation led, where reorientation takes place without a change of amplitude of LSC, and the second is cessation led [112, 113], where the amplitude of LSC vanishes during the reorientation. Reorientation of LSC is typically known to cause flow reversals, which are of major interest to the scientific community.

In the case of a smooth cubic cell, it is observed that LSC is locked in one of the diagonal planes [114] and has strong implications on the heat flux. In the following, we attempt to observe the relative rotational strength of large-scale flow structures in the chosen directions

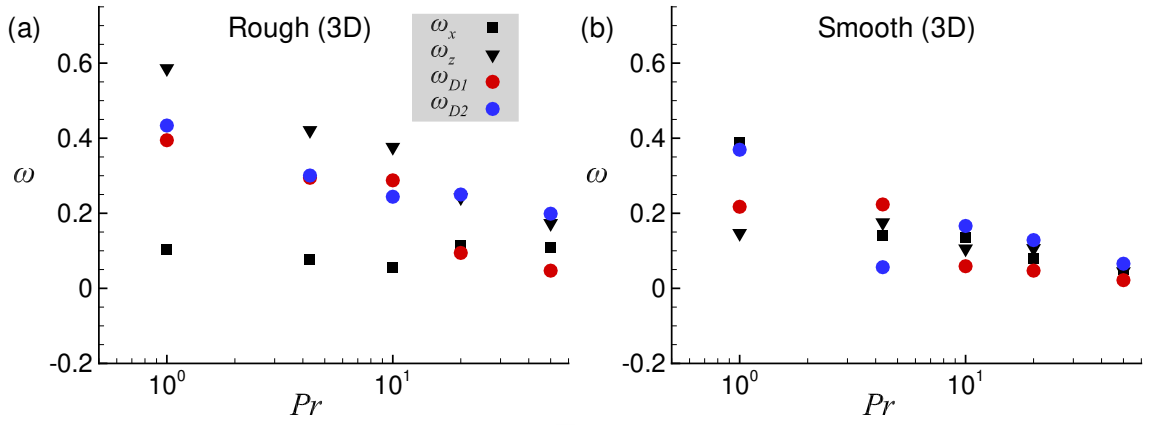

Figure 6.9: Mean Angular velocities along different axes passing through the center of the (a) rough and (b) smooth cells are shown as a function of Pr. Note that ω_{D1} and ω_{D2} (refer Fig. 6.7) are along the axes perpendicular to D_1 and D_2 planes, respectively.

for the rough and smooth cubical cells. Time series data of mean angular velocity $\langle\omega\rangle_V$ about geometric centre of the cube is recorded at fixed intervals of 0.01 non-dimensional time units. The measure of angular rotation about the Cartesian directions x, y, and z is termed as ω_x, ω_y, and ω_z, respectively, while about the diagonal planes, D1 and D2, it is defined as ω_{D1} and ω_{D2}, respectively. To obtain rotational strength in a given direction, we project $\langle\omega\rangle_V$ onto it. In the following, the procedure employed for quantification of ω in the chosen directions is described

$$\boldsymbol{\omega}(\boldsymbol{x},t) = \omega_1(\boldsymbol{x},t)\hat{i} + \omega_2(\boldsymbol{x},t)\hat{j} + \omega_3(\boldsymbol{x},t)\hat{k} \tag{6.1}$$

$$\omega_x = \langle|\langle\omega_1\rangle_V|\rangle_t = \left\langle\left|\left\langle\frac{w(\boldsymbol{x},t)}{y-0.5} - \frac{v(\boldsymbol{x},t)}{z-0.5}\right\rangle_V\right|\right\rangle_t \tag{6.2}$$

$$\omega_y = \langle|\langle\omega_2\rangle_V|\rangle_t = \left\langle\left|\left\langle\frac{u(\boldsymbol{x},t)}{z-0.5} - \frac{w(\boldsymbol{x},t)}{x-0.5}\right\rangle_V\right|\right\rangle_t \tag{6.3}$$

$$\omega_z = \langle|\langle\omega_3\rangle_V|\rangle_t = \left\langle\left|\left\langle\frac{v(\boldsymbol{x},t)}{x-0.5} - \frac{u(\boldsymbol{x},t)}{y-0.5}\right\rangle_V\right|\right\rangle_t \tag{6.4}$$

$$\omega_{D1} = \langle|\langle\boldsymbol{\omega}\cdot\hat{n}_{D1}\rangle_V|\rangle_t \tag{6.5}$$

$$\omega_{D2} = \langle|\langle\boldsymbol{\omega}\cdot\hat{n}_{D2}\rangle_V|\rangle_t \tag{6.6}$$

where, $\hat{n}_{D1}$ and $\hat{n}_{D2}$ are the unit normal vectors to the D1 and D2 planes, respectively. It can be observed from Fig. 6.9 that, in general, large-scale rotational tendency drops with an increase in Pr for both rough and smooth configurations. Compared to the smooth case, ω is augmented for the roughened cell. The general drop in ω with increasing Pr signifies attenuation of turbulent mixing of the fluid, which is in agreement with our previous observations made from isosurfaces of temperature in Fig. 6.8. From Fig. 6.9(a), it can be observed that for the roughened cubic cell, ω_z is relatively higher than both ω_{D1} and ω_{D2} for $Pr \leq 10$. It hints that the preferential

direction of rotation of large-scale structures is altered with the addition of rough surfaces. From Fig. 6.9(b), it is readily evident for the smooth configuration that, in general, either of ω_{D1} or ω_{D2} dominates. The result follows the general agreement, where a higher rotational tendency is expected along the diagonal planes because of LSC residing in them. In the higher Pr regime, the advent of the isolated and columnar flow structures weakens the strength of the large-scale circulation. As a result of which, we observe that deviations among ω in the chosen directions diminish significantly, which is more apparent for the smooth case. It suggests that the bias of large-scale structures towards any particular direction is diminished with the amplification of Pr. In a nutshell, it can be summarized that at low Pr, flow orientation is largely influenced by roughness such that the natural bias of LSC towards diagonal planes is interrupted. However, at higher Pr, the emergence of finer isolated plumes moving randomly into the bulk suppresses the bias of flow towards any particular direction.

6.4 Plume statistics

In this section, we attempt to explore the role of plume and background regions in controlling heat transfer rate as a function of Pr. The identification of plume and background regions involves choosing a suitable threshold that demarcates them based on the strength of correlation of v' and θ'. The fluctuations are computed as

$$\theta'(\boldsymbol{x},t) = \theta(\boldsymbol{x},t) - \langle\theta(\boldsymbol{x})\rangle_{A,t} \tag{6.7}$$

$$v'(\boldsymbol{x},t) = v(\boldsymbol{x},t) \text{ as } \langle v\rangle_{A,t} = 0 \tag{6.8}$$

Also, we have distinguished the contributions coming from hot and cold plumes such that positive temperature fluctuations are linked with the former, while negative ones are the hallmark of the latter. It has enabled us to further decompose plumes into hot and cold ones. The criterion employed for the detection of plume and background regions is described below

$$\Omega_{pl} = \boldsymbol{x} \in V : |v'\theta'|/\Gamma' > \delta \tag{6.9}$$

$$\Omega_{plc} = \boldsymbol{x} \in V : |v'\theta'|/\Gamma' > \delta \quad \text{and} \quad \theta' < 0 \tag{6.10}$$

$$\Omega_{plh} = \boldsymbol{x} \in V : |v'\theta'|/\Gamma' > \delta \quad \text{and} \quad \theta' > 0 \tag{6.11}$$

$$\Omega_{bg} = \boldsymbol{x} \in V : |v'\theta'|/\Gamma' \leq \delta. \tag{6.12}$$

Here, Ω_{pl} and Ω_{bg} signify volume occupied by plume and background regions, respectively. Decomposition of Ω_{pl} into hot and cold plume regions provide their volume coverage as Ω_{plh} and

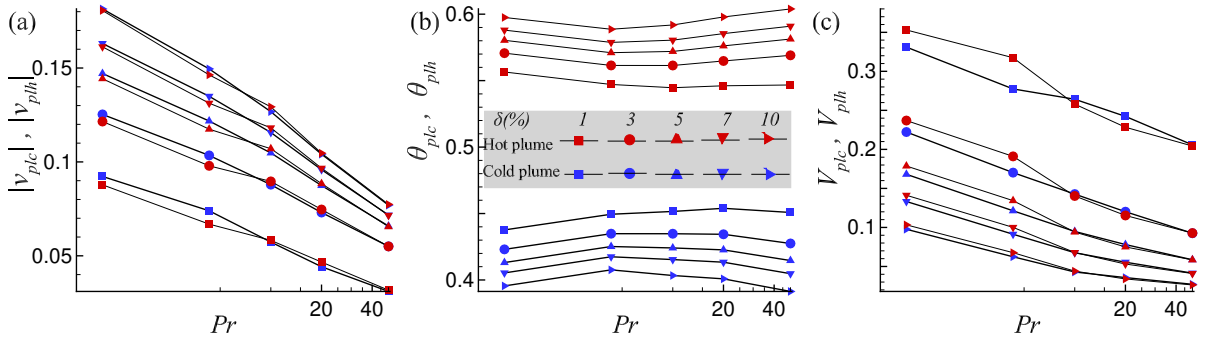

Figure 6.10: Threshold dependence of (a) absolute mean vertical velocities, (b) mean temperatures, and (c) volume fractions of hot and cold plumes are shown as a function of Pr.

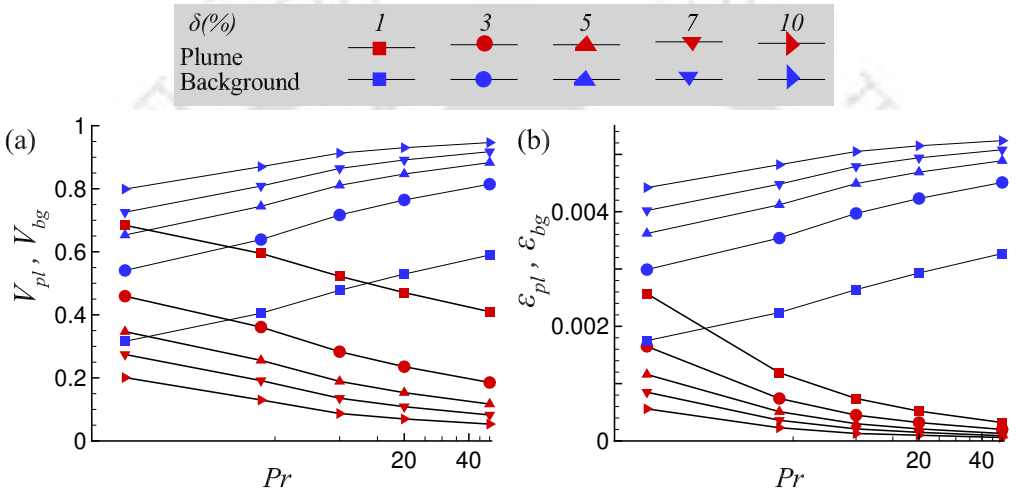

Figure 6.11: Variation of (a) V_{pl} and V_{bg} along with their (b) contributions in thermal dissipation rate, ϵ_{pl} and ϵ_{bg}, respectively, is shown as a function of Pr at different thresholds.

Ω_{plc}, respectively, Γ' denotes instantaneous global maximum of $|v'\theta'|$, and δ is a free parameter that is used to define the threshold limit for plume identification. The threshold limits used in this study are $\delta = 1, 3, 5, 7$ and 10%. For the calculation of volume fractions, the volumes of different regions are normalized by the effective net volume of the cell. The volume fractions of hot, cold, and entire plume regions are represented as V_{plh}, V_{plc} and V_{pl}, respectively, while for the background region, it is V_{bg}.

The intensity of hot and cold plumes can be revealed by analyzing their vertical velocity and mean temperature. Hot plumes are expected to have a higher mean temperature than the mean bulk temperature ($\theta = 0.5$) of the fluid, while cold ones have a lower mean temperature. Thermal plumes being energetic fluid parcels possess high vertical velocity during their movement into the bulk. It is natural for cold plumes to follow the downward motion and for hot plumes to ascend. Thus, in the following discussion, to compare the strength of vertical velocity associated with hot

and cold plumes, we only consider v in the absolute sense. In Fig. 6.10, the variations of absolute mean vertical velocity (v_{plh}/v_{plc}), mean temperature ($\theta_{plh}/\theta_{plc}$) and volume fraction ($V_{plh}/V_{plc}$) associated with hot and cold plumes are shown as a function of Pr at different thresholds. The quantities are calculated in the following manner

$$v_{plc} = \left\langle \frac{1}{\Omega_{plc}} \int_{\Omega_{plc}} v(\boldsymbol{x}, t) dV \right\rangle_t \tag{6.13}$$

$$v_{plh} = \left\langle \frac{1}{\Omega_{plh}} \int_{\Omega_{plh}} v(\boldsymbol{x}, t) dV \right\rangle_t \tag{6.14}$$

$$\theta_{plc} = \left\langle \frac{1}{\Omega_{plc}} \int_{\Omega_{plc}} \theta(\boldsymbol{x}, t) dV \right\rangle_t \tag{6.15}$$

$$\theta_{plh} = \left\langle \frac{1}{\Omega_{plh}} \int_{\Omega_{plh}} \theta(\boldsymbol{x}, t) dV \right\rangle_t \tag{6.16}$$

From Fig. 6.10(a), it is evident that the absolute mean vertical velocity of both hot (v_{plh}) and cold (v_{plc}) plumes diminish with increasing Pr. It is in agreement with flow becoming quiescent at an augmented Pr. Further, it can be observed that both v_{plc} and v_{plh} are comparable irrespective of the choice of δ. From Fig. 6.10(b), we can observe that for $\delta > 1\%$, mean temperature of hot/cold plumes ($\theta_{plh}/\theta_{plc}$) increases/decreases with the increase in Pr. It substantiates that the plumes emerge brighter and more intense (temperature sense) such that they do not diffuse quickly for a large Pr. From Fig. 6.10(c), it can be observed that the volume fraction of hot (V_{plh}) and cold (V_{plc}) plumes are comparable for $\delta > 1\%$. It is in agreement with general expectation of equal volume coverage by hot and cold plumes.

In Fig. 6.11, variation of volume fractions of plume (V_{pl}) and background regions along with their contributions, ϵ_{pl} and ϵ_{bg}, respectively, in thermal dissipation rate is shown with Pr. Note that in the following discussion, when we refer to plume regions, we collectively consider contributions from hot and cold plumes. The calculations for ϵ_{pl} and ϵ_{bg} are described below

$$\epsilon_{pl} = \left\langle \int_{\Omega_{pl}} \epsilon_\theta(\boldsymbol{x}, t) dV \right\rangle_t \text{ and } \epsilon_{bg} = \left\langle \int_{\Omega_{bg}} \epsilon_\theta(\boldsymbol{x}, t) dV \right\rangle_t,$$

From Fig. 6.11(a), it can be observed that as Pr is increased the effective net volume occupied by the plumes (V_{pl}) drops with the increasing Pr, whereas for the background-dominated regions (V_{bg}) rises. The diminishing coverage of plumes in the domain results from their emergence as finer and distinct flow structures with increasing Pr. As evident from Fig. 6.11(b), the trends followed by ϵ_{pl} and ϵ_{bg} are similar to that followed by V_{pl} and V_{bg}, respectively. Plumes are known to be associated with higher thermal dissipation rates [86]. Since plumes cover a relatively smaller portion of the domain as Pr increases, their net contribution to the net thermal dissipation rate also diminishes, while for the background, it is the other way around. As

a consequence of which, it can be observed that at the highest explored $Pr = 50$, the difference between ϵ_{pl} and ϵ_{bg} is maximum. An interesting observation is that ϵ_{pl} becomes so small at $Pr = 50$ that it appears to converge for the different thresholds.

In Fig. 6.12, a direct comparison between plume statistics of the 3D rough and smooth cells is made for the explored Pr cases at $\delta = 5\%$ and 10%. It can be observed that for $Pr > 1$, both v_{plc} and v_{plh} are higher for the rough case. It signifies that plumes are energized in the presence of rough surfaces. Further, a higher θ_{plh} or a lower θ_{plc}, in comparison to the smooth case, highlights that plumes emerge brighter in the roughened cell. Interestingly, θ_{plc} is lower than that observed for the smooth cell at all the explored Pr, while θ_{plh} assumes higher values for $Pr \geq 1$. From frames (c) and (f), it is evident that volume fractions of hot and cold plumes are higher than that for the smooth counterparts for all Pr. It substantiates the emission of extra plumes in the roughness configuration.

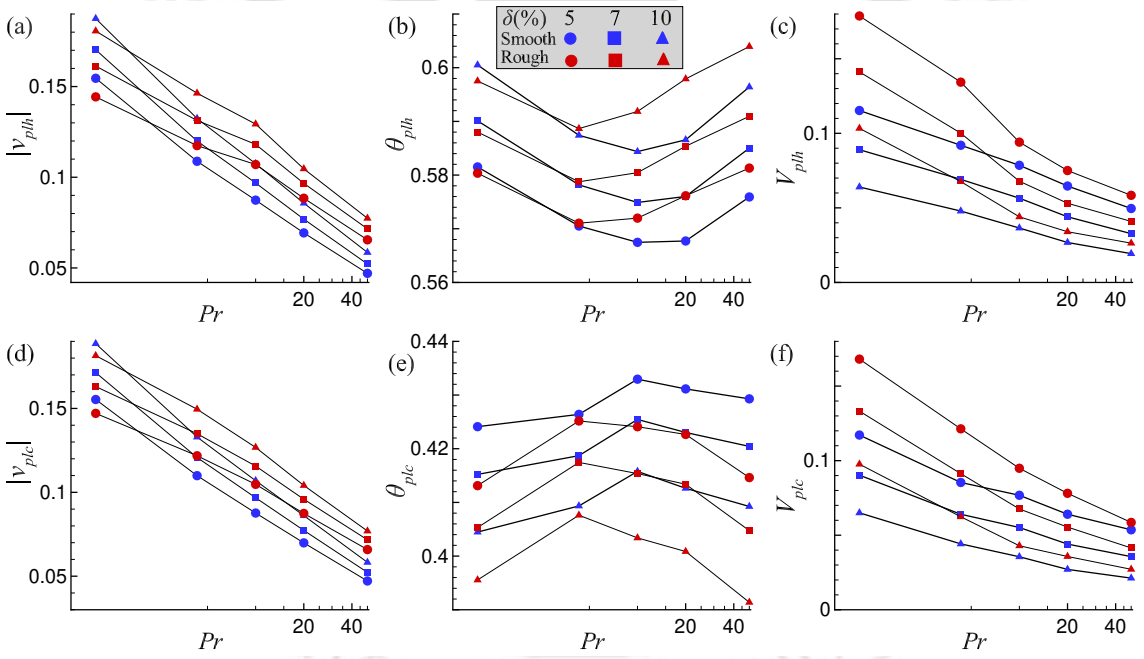

Figure 6.12: Comparison between 3D rough and smooth cells for mean vertical velocity (left column), temperature (middle column) and volume fraction (right column) associated with hot and cold plumes.

6.5 Statistics of fluctuations

The study of the behavior of fluctuations promises to reveal insightful information about the dominating heat transport mechanism in the system. The transformation of larger flow structures

to finer ones with increasing Pr or Ra can be observed from PDFs of temperature and vertical velocity. Yakhot [51], Solomon and Gollub [52, 53] observed that dominance of large-scale structures imparts Gaussian shape to temperature PDFs. However, the prevalence of small-scale structures over larger ones yields an exponential shaped θ-PDF. The same can also be observed from Fig. 6.13, where $\theta-$PDFs at higher Pr show a clear, distinct peak with exponential shape, and at lower Pr, PDFs obey Gaussian-like distribution. The appearance of sharp peaks of the PDFs with a large amplitude around $\theta \approx 0.5$ signifies the robustness of the mean flow temperature state. In general, we can observe that as Pr increases, tails of the PDFs get shortened. Further, due to squeezing of the skirts at higher Pr, amplitude of the PDFs rises around the peak, while around the tails it subsides. It also hints at the diminishing strength of θ fluctuations at higher Pr. In the case of vertical velocity PDFs, events with zero-vertical velocity become more pronounced with increasing Pr. Also, it can be observed that the probability of high amplitude velocity events drops substantially with the increase of Pr. Information regarding the variations of symmetry and shape of the PDFs of θ and v observed at different vertical locations is revealed from the skewness and flatness of the distributions. In Figs. 6.14(a-b), vertical variations of skewness of temperature (S_θ) and vertical velocity (S_v), respectively, are shown for different Pr. In Figs. 6.14(c-d), the variation is shown for flatness of θ (F_θ) and v (F_v), respectively. The calculations for skewness and flatness are performed in the following manner

$$S_\theta = \frac{\langle \theta'^3 \rangle_{A,t}}{\langle \theta'^2 \rangle_{A,t}^{3/2}}, \qquad S_v = \frac{\langle v'^3 \rangle_{A,t}}{\langle v'^2 \rangle_{A,t}^{3/2}}$$
$$F_\theta = \frac{\langle \theta'^4 \rangle_{A,t}}{\langle \theta'^2 \rangle_{A,t}^{2}}, \qquad F_v = \frac{\langle v'^4 \rangle_{A,t}}{\langle v'^2 \rangle_{A,t}^{2}} \tag{6.17}$$

Recall that skewness, the third-order moment, is a measure of the asymmetry of a distribution around its mean value. Flatness, the fourth-order moment, indicates the peakedness of a distribution that is the degree to which data is concentrated about the mean. A higher value of flatness of distribution is associated with a distinct peak around the mean, while a lower value of flatness indicates a flat top near the mean with no clear or distinct peak. Note that for a perfectly symmetric distribution, skewness is zero, and flatness for the normal distribution is three. It can be observed that values of both S_θ and S_v are nearly zero in the center of the cell, which is in agreement with the symmetry of the temporal PDFs of θ and v observed above. Significantly higher values of S_θ and S_v close to the isothermal plates are an indicator of anisotropic behavior, which is expected because of the emergence of thermal plumes. The emergence of sharper peaks with increasing Pr in the distribution of temperature and vertical velocity in the bulk, as

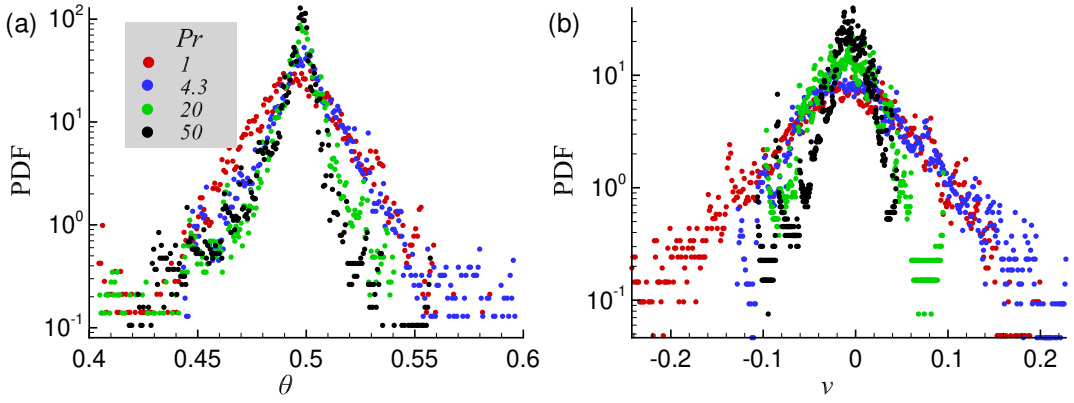

Figure 6.13: Temporal PDFs of (a) temperature and (b) vertical velocity are shown for the probe placed at the geometric center of the cubic cell as a function of Pr.

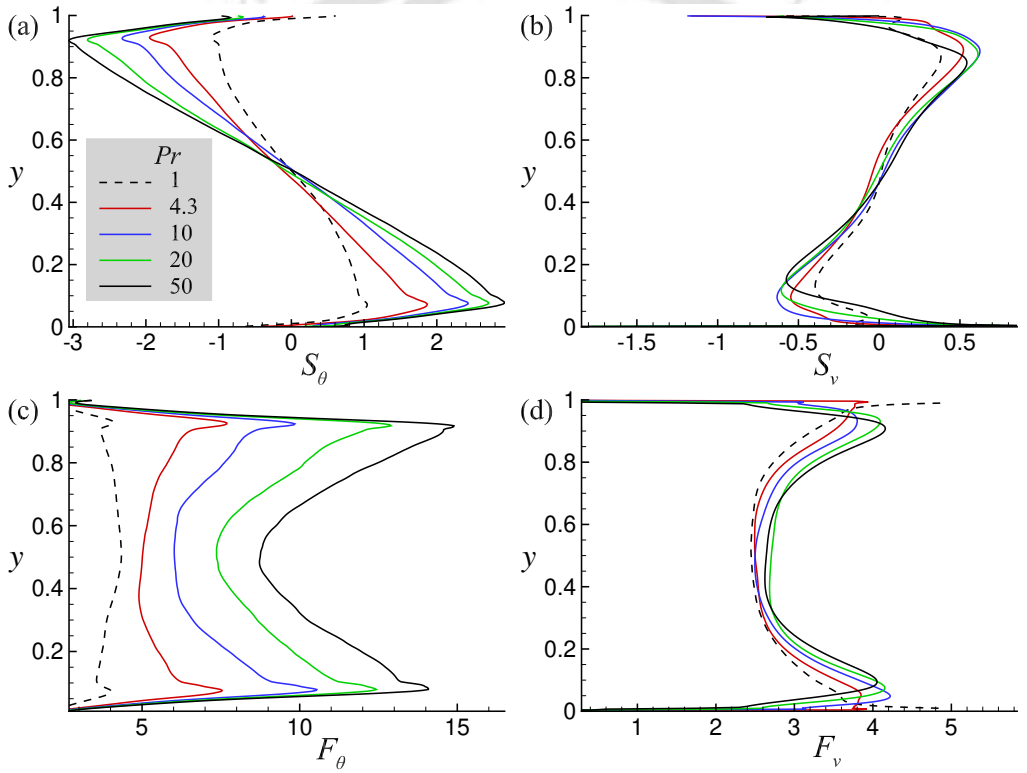

Figure 6.14: Vertical variations of (a-b) skewness of θ (S_θ) and v (S_v), respectively, are shown as a function of Pr, whereas in panels (c-d), the variation is shown for flatness of θ (F_θ) and v (F_v), respectively.

observed above, can also be verified by observing flatness [115]. Note, at $Pr = 1$, F_θ has the lowest value, while at $Pr = 50$, F_θ is the highest. Amplification of F_θ supports the emergence of sharp peaks in θ distribution. Also, it can be noted that the flatness of temperature distribution ($F_\theta > 3$) deviates significantly from that observed for the Gaussian distribution ($F_\theta = 3$) as Pr is increased. In the case of vertical velocity, F_v follows a general increasing trend in the bulk.

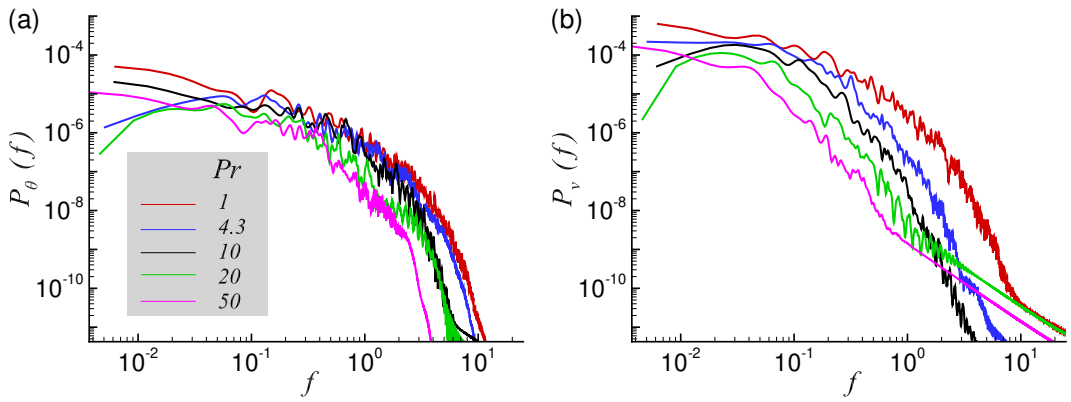

Figure 6.15: Power spectra of (a) temperature and (b) vertical velocity are shown for the probe chosen at the geometric center of the cell at different Pr.

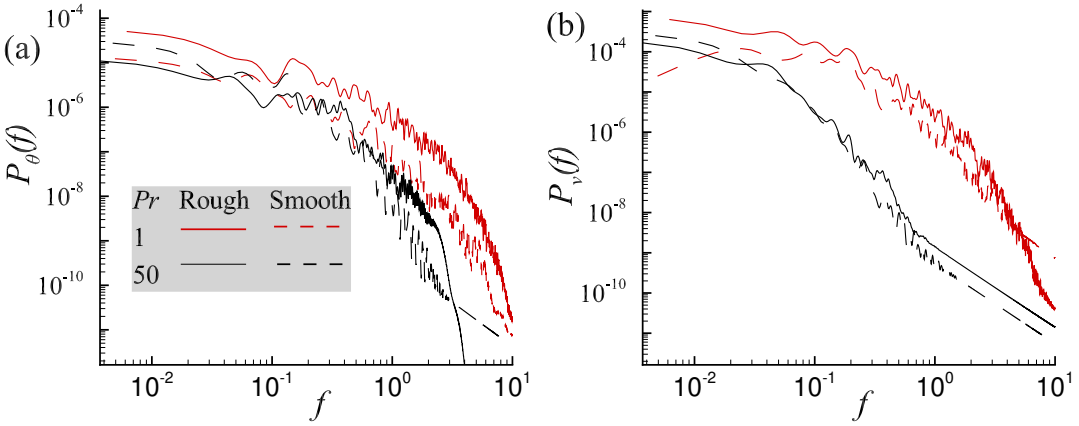

Figure 6.16: Power spectra of (a) temperature and (b) vertical velocity are compared between 3D rough and smooth cells for the probe chosen at the geometric center of the cell at different Pr.

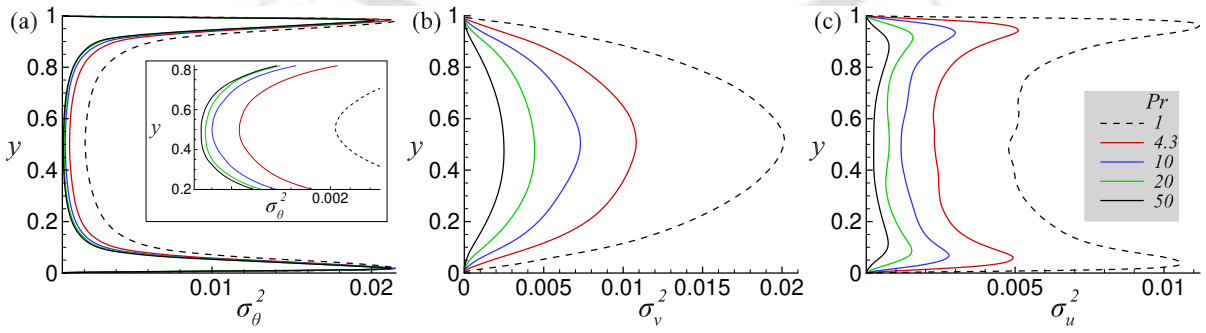

Figure 6.17: Vertical variation of variance of (a) temperature, (b) vertical velocity, and (c) horizontal velocity are shown as a function of Pr.

However, the values of F_v are lower, such that $F_v \approx 2.4$ at $Pr = 1$ and $F_v \approx 2.62$ at $Pr = 50$. It indicates that with increasing Pr, Gaussian-like distribution is approached for vertical velocity

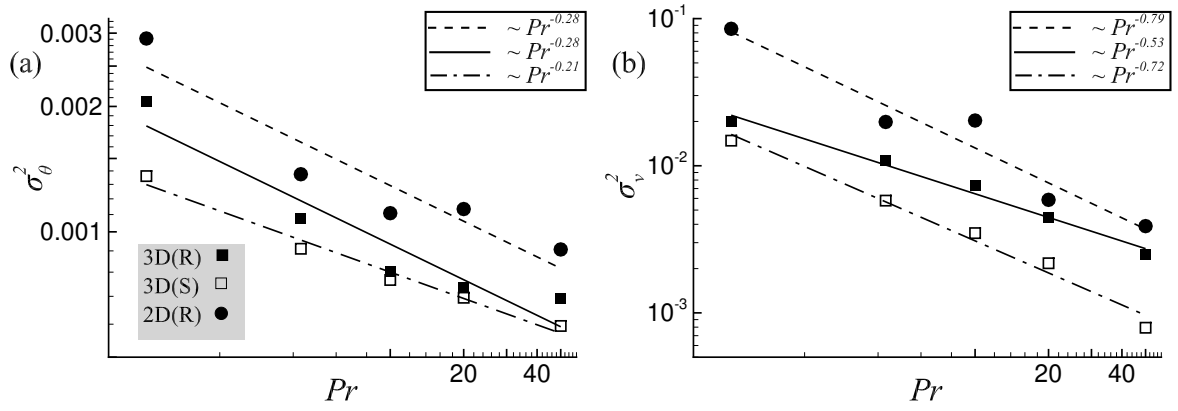

Figure 6.18: Horizontally area-time averaged variance of vertical velocity and temperature at mid-height of the cell are shown as a function of Pr. For better comparison, 2D multi-scale roughness and 3D smooth data are also included. The least-squares fitted lines corresponding to 3D rough (solid), 3D smooth (dash-dot), and 2D rough (dash) configurations reveal the decay law followed by σ_θ^2 and σ_v^2 as a function of Pr.

in the bulk region, while for temperature, the PDF deviates significantly from the Gaussian.

In Fig. 6.15, temporal spectra of temperature and vertical velocity are shown for a probe placed at the geometric center of the cell. It is clearly evident that temporal energy content is highest for the lowest $Pr = 1$. As Pr is increased, the energy content for both vertical velocity and temperature fluctuations diminishes. It again highlights the quiescent nature of flow at higher Pr, where fluctuations relatively subside. The effect of addition of conical roughness elements on the spectral energy content in the bulk can be observed from Fig. 6.16, where a direct comparison is made with the smooth case for $Pr = 1$ and 50. It is clearly evident that spectra of both v and θ corresponding to the 3D rough case show increased energy levels, especially for the small-scale frequencies, at both $Pr = 1$ and $Pr = 50$. Thus, it confirms the ability of rough surfaces to elevate the strength of fluctuations.

The waning strength of fluctuations with increasing Pr can also be observed from the vertical variation of the variance of u (σ_u^2), v (σ_v^2) and θ (σ_θ^2), as shown in Fig. 6.17. The amplitude of σ_θ^2, σ_v^2, and σ_u^2 is maximum at the lowest $Pr = 1$, and with the increase in Pr, it is seen to attenuate. It is in agreement with our previous observation, where we linked higher fluctuations with lower Pr. Further, it can be observed that both velocity and temperature fluctuations exhibit different behavior close to the walls and in the bulk region. From Fig. 6.17(a), it is evident that θ fluctuation has a higher value close to the walls, which is mainly because of the emission of thermal structures carrying large gradient from the TBL. As these thermals move into the bulk, they are diffused, rendering them ineffective in producing large fluctuations. This is the reason

as one moves away from the walls, θ fluctuation is attenuated. For vertical velocity, it is the other way around, i.e., the maximum of v fluctuation is observed in the bulk region, while near-wall regions exhibit a lower magnitude of the fluctuation. Large-amplitude vertical velocity fluctuations in the bulk are a result of the interaction of high-intensity rolls with the background. The same is responsible for the vigorous mixing of fluid that damps out temperature fluctuations.

To observe variation of θ (σ_θ^2) in the bulk region for different Pr, we refer to the inset in Fig. 6.17(a). It is readily seen that θ fluctuation is highest for the lowest $Pr = 1$, while for the highest $Pr = 50$, it is least. The profiles of σ_v^2 shown in Fig. 6.17(b) also depict the same trend. It, therefore, corroborates the observation that θ and v are attenuated with increasing Pr. Further, in Fig. 6.17(c), we explore how u fluctuation varies as a function of Pr. Similar to v and θ fluctuations, the magnitude of u fluctuation diminishes with increasing Pr. Comparing bulk and near-wall regions reveal that u fluctuation has a higher value close to the walls, and in the bulk it drops. The reason for a higher value of u fluctuation is because of the strong horizontal motion of fluid close to the isothermal plates.

In Fig. 6.18, variation of σ_θ^2 and σ_v^2 calculated at mid-height of the cell is observed as a function of Pr. For comparison, the data for the 3D smooth case and 2D rough cell is also plotted. It can be observed that at a fixed Pr, the order of magnitude of σ_θ^2 and σ_v^2 differs significantly, with the latter being higher. Both σ_θ^2 and σ_v^2 for the 3D rough case are augmented in comparison to their smooth counterparts. However, in comparison to the 2D rough case, the intensity of fluctuations is lower for the present 3D rough case. As discussed previously, the lack of an extra direction promotes a stronger mean flow in a 2D cell, and hence, stronger fluctuations are recorded. Further, we observe power scaling laws for σ_v^2 and σ_θ^2 for the rough 3D case as a function of Pr, where $\sigma_v^2 \sim Pr^{-0.5338}$ and $\sigma_\theta^2 \sim Pr^{-0.2839}$. It implies that vertical velocity fluctuations decay significantly faster than temperature fluctuations. At the highest $Pr = 50$, we observe that the difference between the intensity of θ and v fluctuations is significantly reduced.

Next, in Fig. 6.19 we observe vertical variation of horizontally averaged thermal (ϵ_θ) and viscous dissipation (ϵ_u) rates as a function of Pr. The dissipation rates are calculated as

$$\langle \epsilon_u \rangle_{A,t} = \sqrt{\frac{Pr}{Ra}}\ \langle |\nabla \boldsymbol{u}|^2 \rangle_{A,t}, \qquad \langle \epsilon_\theta \rangle_{A,t} = \sqrt{\frac{1}{RaPr}}\ \langle |\nabla \theta|^2 \rangle_{A,t} \tag{6.18}$$

It is clearly evident that both ϵ_θ and ϵ_u diminish with the increase in Pr. Based on the order of magnitudes of the dissipation rates, flow dynamics in the near-wall and bulk regions can be easily distinguished. The insets in Fig. 6.19(a), showing a magnified view of ϵ_θ in the bulk and near-wall region of the hot plate, confirm the same. The profiles of ϵ_u, shown in Fig. 6.19(b), also depict the same observation. In close proximity to the isothermal walls, high dissipation rates

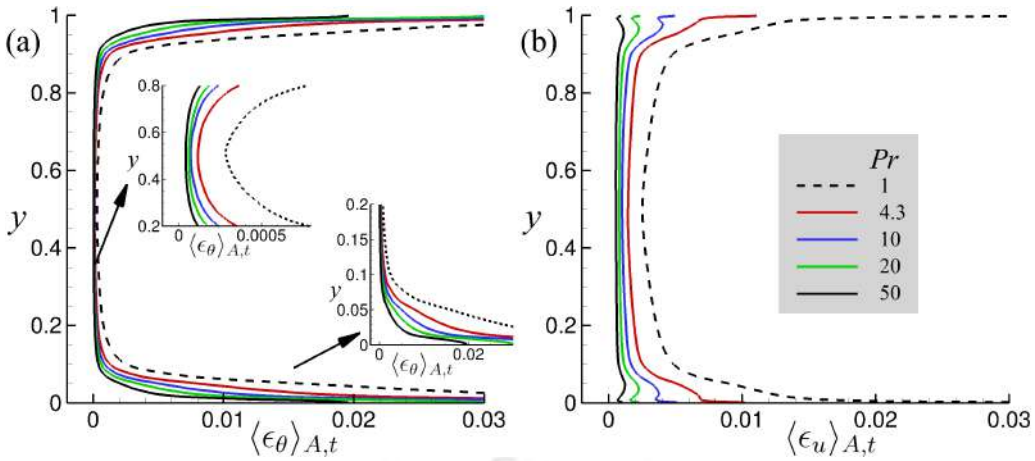

Figure 6.19: Vertical variation of horizontally area-time averaged (a) thermal (ϵ_θ) and (b) viscous dissipation rates are shown for different Pr. The insets in frame (a) show the magnified view for the regions in bulk and close to the bottom heated plate.

can be observed. The promotion of diffusive structures like thermal plumes from the boundary layer regions is responsible for the same. However, in the bulk, where the dominant mode of heat transfer is convection, fluid is well mixed, and thus, relatively lower dissipation rates are seen. An important observation is that viscous dissipation dominates thermal dissipation in nearly all parts of the cell, especially in the bulk. The only region where ϵ_θ dominates ϵ_u is close to the isothermal plates. In the bulk, ϵ_u is approximately ten times greater than ϵ_θ.

To further investigate flow behavior at different Pr, we calculate cross-correlation $C_{v\theta}(\tau)$

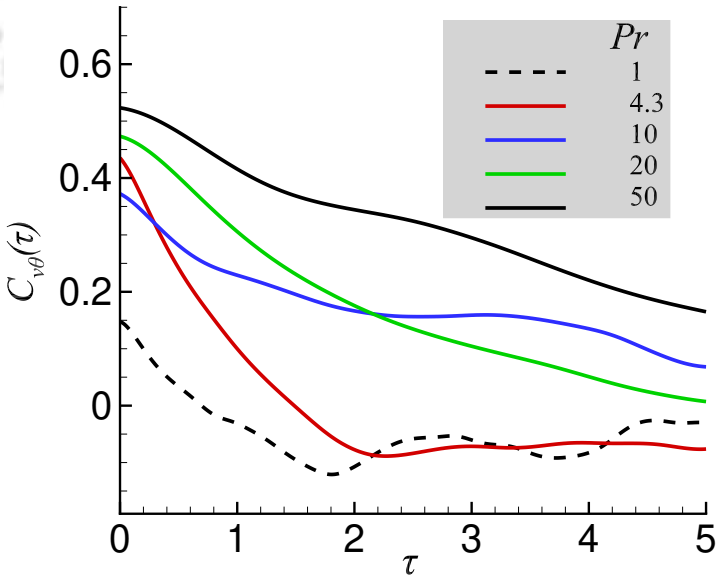

Figure 6.20: Cross-correlation of vertical velocity and temperature fluctuations for different Pr is shown for the probe located at the geometric center of the cell.

of vertical velocity and temperature fluctuations at the geometric center of the cell, as shown in Fig. 6.20. The calculations are performed as

$$C_{v\theta}(\tau) = \frac{\overline{v'(t)\ \theta'(t+\tau)}}{\sigma_v\ \sigma_\theta} \tag{6.19}$$

, where overbar denotes temporal average, τ is the delay time, and σ_v and σ_θ denote standard deviation of vertical velocity and temperature, respectively. From Fig. 6.20, it can be readily observed that $C_{v\theta}$ is least correlated for $Pr = 1$, while for the highest $Pr = 50$, the correlation is highest with the slowest decay rate. Lower Pr flows being more turbulent are responsible for a lower cross-correlation coefficient. High Pr flows, on the other hand, are comparatively quiescent and exhibit lower thermal diffusivity, as a result of which we observe a long-time correlation between vertical velocity and temperature fluctuations. Another way of looking at the result is from the point of view of thermal plumes. As already discussed, high Pr fluids have lower thermal diffusivity because of which thermal plumes are able to traverse the bulk region without losing their energy. Now, because of the relatively quiescent nature of high Pr flows, when a thermal plume passes through a point in the bulk region, a higher $v'\theta'$ correlation is sustained for a longer time. However, for the low Pr flows, both high thermal diffusivity and turbulent intensity are responsible for the weakened correlation. Because of high thermal diffusivity, thermal plumes relatively lose their energy as they enter the bulk region, and thus, they do not confer stronger $v'\theta'$. The swift and speedy motion of plumes while traversing the bulk region further shortens the duration of high $v'\theta'$ correlation. Thus, varying decay rates of the cross-correlation coefficient of $v'\theta'$ with Pr essentially highlight different flow dynamics.

6.6 Summary

In this work, we have focussed on the role played by Pr in deciding the heat transport and flow mechanism in a rough 3D cubic box. Thermal forcing is kept fixed at $Ra = 10^8$ while Pr is varied as $1 \leq Pr \leq 50$. The addition of irregular conical roughness elements enhances the heat transfer rate by about 50% compared to the smooth cell case. Contrary to the monotonic increasing trend of $Nu(Pr)$ observed in 2D irregular roughness, *Nu* becomes nearly invariant in the 3D roughened cell. Flow intensity, measured in terms of the Reynolds number, shows comparatively lower values for the 3D configuration with a general decreasing trend with Pr. The availability of an extra direction in the 3D configuration does not allow plumes to be contained in a particular vertical plane, leading to a comparatively less coherent and organized flow of plumes.

The analysis of flow structures through isosurfaces of temperature in two lateral and diagonal planes reveal the presence of large-scale mean flow at $Pr = 1$, whereas, for higher Pr, isolated plumes emerge with the debilitated mean flow. Further, we project the strength of angular rotation of fluid flow, calculated about the geometric center of the cell, onto the chosen directions. It is observed that roughness alters the preferred orientation of the large-scale mean flow. For $Pr \leq 10$, large-scale rotational tendency is found to be highest in the horizontal direction z. The result is in contrast to the observation made for the smooth cubic cell where large-scale flow has a strong inclination to reside in one of the two diagonal planes. For $Pr = 50$, as the flow structures become finer, they do not follow a particular direction, which is reflected in nearly comparable strength of angular rotation in the chosen directions.

The investigation of plume statistics reveals that though the volume fraction of plumes decreases with increasing Pr, the brightest plumes are associated with high Pr. Temporal PDFs of temperature in the geometric center of the box reveal a distinct peak with the exponential shape at a higher Pr, while for a lower Pr, Gaussian-like distribution is followed. From temporal power spectra and variance of temperature and vertical velocity, decreasing strength of the fluctuations with increasing Pr is observed. The quiescent and homogeneous nature of high Pr fluids is substantiated by lower values of horizontally averaged thermal and viscous dissipation rates. Another manifestation of the quiescent nature of the flow at higher Pr, exhibiting lower thermal diffusivity, is realized through a stronger cross-correlation between fluctuations of vertical velocity and temperature. For low Pr, thermal plumes being swift and highly diffusive do not retain the strong correlation.

7

CONCLUSIONS AND FUTURE SCOPE

The present thesis contains results of the direct numerical simulations, where different aspects of turbulent Rayleigh-Bénard convection in the presence of roughened surfaces are explored for both 2D and 3D configurations. For 2D studies, irregular triangular elements are used, while for 3D simulations, conical elements are introduced. We have tested the efficacy of novel irregular multi-scale roughness used in 2D in sustaining enhanced heat transport scaling for higher $10^8 \leq Ra \leq 10^{11}$ *range. Further, the effect of* Pr *in conjunction with roughness on heat transfer mechanism and flow structures is taken up in both 2D and 3D configurations. In this chapter, we briefly summarize the main findings of the work and discuss the prospects for future work on turbulent Rayleigh-Bénard convection with rough surfaces.*

7.1 Conclusions

Roughness-facilitated Rayleigh-Bénard convection has been identified as a means to augment heat flux and introduce turbulence in the boundary layer regions. In the present work, we have employed multi-scale irregular rough isothermal plates to obtain a greater global heat flux rate. It is in contrast to the previous roughness studies, where only a limited number of roughness length scales were incorporated. We have attempted to include a wider range of length scales with no bias towards any particular length scale. This rough texture is motivated by the real-life rough surfaces seen in nature and various industrial applications. In a 2D rectangular box of aspect ratio 2 with air as working fluid, we establish the efficacy of the irregular triangular roughness in sustaining enhanced heat transport scaling exponent for a wider Rayleigh range ($10^8 \leq Ra \leq 10^{11}$). The 2D roughness setup is further used to study the effect of Pr on flow mechanism and structures, though for a relatively lower range, $10^7 \leq Ra \leq 5 \times 10^9$. Also, we have conducted 3D simulations with rough surfaces containing conical elements to observe the

Pr effect at a fixed thermal forcing of $Ra = 10^8$. In the following, main findings of the work are summarized.

Considering air as a working fluid, we have explored the effect of irregular triangular roughness on the flow dynamics and heat transport properties in a two-dimensional rectangular cell for $10^8 \leq Ra \leq 10^{11}$. The inclusion of roughness elements with multiple scales has enabled sustenance of the enhanced heat transfer scaling throughout the explored three decades of Ra. At lower Ra, only taller elements are active in enhancing plume emission from their tips, while at higher Ra, substantial contributions from the smaller elements are received, which play a pivotal role in casting aside the saturation of the enhanced heat transport scaling. Detailed analysis of the near-wall dynamics reveals the complex role of the roughness elements and the associated throat, cavity, and tip regions. Throat regions are inaccessible to the bulk flow at lower Ra. However, with increasing thermal forcing, penetration of the bulk fluid improves, which is also reflected through increased velocity fluctuations. Similarly, tip regions associated with smaller roughness elements get activated at higher Ra such that they start to protrude the TBL and incite plume emissions which are recorded from temperature fluctuations.

Vertical profiles of mean temperature passing through different valley regions also reveal distinct flow dynamics. The transformation of flat linear profiles into steeper ones with increasing Ra marks the washing away of the cavities. The transitional phase of the profiles, where the cavities are partially washed, confers the augmented heat transfer rate. As the profiles complete the transformation to steeper ones, rough surfaces lose their effectiveness in influencing heat transport. Depending on whether throat regions are spacious or confined, transition to the enhanced local heat flux regime occurs at different thermal forcings. Thus, the addition of a variety of roughness elements ensures that there are enough active spots in higher Ra that can sustain the augmented heat transfer rate. In other words, activation of small-scale roughness elements and ventilation in the highly confined regions at higher Ra promotes sustenance of the enhanced heat transfer scaling.

The role of Pr in influencing flow structures and the prevalent heat transport mechanism in 2D roughness configuration is observed for $10^7 \leq Ra \leq 5 \times 10^9$ and $0.1 \leq Pr \leq 100$. The distinct role played by Pr in the presence of roughness is evident in the form of a monotonic increase of *Nu* with increasing Pr. The result is a significant improvement to the nearly invariant *Nu* observed in the smooth cell. At a lower Pr, a thick layer of hot/cold fluid is observed above the top/bottom plate, while a higher Pr is associated with a thinner thermal boundary layer (TBL). For the former, large-scale diffuse structures are prevalent, while for the latter, fine

mushroom-shaped structures are discharged from the near-wall regions. At a lower Ra, since roughness elements are embedded beneath the TBL, plume emission is thwarted. The creation of numerous nucleation sites and subsequent frequent plume emission is observed at higher Pr as roughness elements penetrate the TBL. At a given Ra, since a high Pr flow boasts of a thinner TBL, roughness elements become thermally active quickly. This results in augmented *Nu* at higher Pr. A direct comparison of flow intensity measured in terms of the global Reynolds number between rough and smooth cells reveal that Re is superior for the rough cell for a larger Ra or Pr. Further, the comparison of variance of temperature and vertical velocity between the smooth and roughened cells shows that the fluctuations are strengthened in the bulk in the presence of roughness. The increased energy of fluctuations in the rough case is also substantiated by their power spectra.

We have also investigated the effect of Pr on the flow structures and dominant heat transfer mechanism in a rough cubical box at $Ra = 10^8$ and $1 \leq Pr \leq 50$. The addition of irregular conical roughness elements is seen to augment the heat transfer rate by about 50% compared to the smooth case. Contrary to the monotonic increasing trend of $Nu(Pr)$ observed in 2D irregular roughness, *Nu* becomes nearly invariant in the 3D roughened cell. The analysis of flow structures through isosurfaces of temperature in two lateral and diagonal planes reveals the presence of large-scale mean flow at $Pr = 1$, whereas for higher Pr, isolated plumes emerge with the debilitated mean flow. The rough surfaces are seen to alter the preferred orientation of the large-scale mean flow. For $Pr \leq 10$, we have observed a higher rotational tendency of the flow in a Cartesian direction. The result is in contrast to the smooth cubic cell, where the large-scale flow has a strong inclination to reside in one of the two diagonal planes.

The investigation of plume statistics reveals that though volume fraction of plumes diminishes with increasing Pr, the brightest plumes are associated with high Pr. Temporal PDFs of temperature in the geometric center of the box reveal a distinct peak with the exponential shape at a higher Pr, while for a lower Pr, Gaussian-like distribution is observed. From temporal power spectra and variance of temperature and vertical velocity, decreasing strength of fluctuations with increasing Pr is observed. The quiescent and homogeneous nature of high Pr fluids is substantiated by lower values of horizontally averaged thermal and viscous dissipation rates. Another manifestation of the quiescent nature of the flow with higher Pr, exhibiting lower thermal diffusivity, is realized through a stronger cross-correlation between fluctuations of vertical velocity and temperature. For low Pr, thermal plumes being swift and highly diffusive do not retain the strong correlation.

7.2 Future scope

In addition to the roughness-facilitated variant of Rayleigh-Bénard convection, we list some avenues for future research which are other possible variants of standard RBC. Thermal convection in nature is subjected to various factors, such as rotation, magnetic field, tilt, rough surfaces, etc., which are responsible for highly complex flow dynamics. Incorporating these factors in standard RBC is essential to enhance understanding of various flows occurring in nature. Some of the possible and meaningful issues that can be looked at in future are discussed below.

- Combined effect of rotation and roughness: In various geo- and astrophysical flows, the effect of rotation [116, 117] plays an important role in deciding the dominating flow structures and heat transport mechanism. Also, the surfaces in natural flows are rough, so it becomes a natural choice to consider the effect of both rotation and roughness when analyzing such a system. It will be interesting to explore how irregular roughness and rotation rates influence the heat transport mechanism and which combination of the input parameters yields an augmented heat transfer rate.

- Effect of Pr on global heat transfer rate for a roughened RBC cell with inclination: In the present work, we have explored the effect of Pr in 2D and 3D roughened cells. The study can be further extended to incorporate tilt [118, 119], which has the potential to alter the flow features, LSC dynamics, and heat transport mechanism. The choice of the Pr is expected to influence the rate at which flow makes a transition to laminar with increasing inclination. Varying plume dynamics as a function of Pr might play an essential role in deciding the dominant flow structures in the tilted cell and, thus, the heat transfer mechanism.

- Vibration-induced thermal convection in a roughened cell: Introducing instability via vibrations [120, 121] of suitable frequency is expected to alter the flow dynamics inside the roughness cavity regions. At lower Ra, as the fluid gets stuck inside the cavity regions, vibration-induced instability would extract out the otherwise immobile fluid and promote a stronger interaction with the bulk. It also promises a greater plume emission from the roughened surfaces. Thus, an augmented heat transfer rate, even at a lower thermal forcing, can be realized by facilitating vibration-induced instability in the RBC setup.

REFERENCES

[1] Goluskin D. and Doering C.R. Bounds for convection between rough boundaries. *J. Fluid Mech.*, **804**:370–386, 2016.

[2] Kandanoff L. P. Turbulent heat flow: Structures and scaling. *Phys. Today*, **54**:34–39, 2001.

[3] Wettlaufer J.S. The universe in a cup of coffee. *Phys. Today*, **64**:66–67, 2011.

[4] Thermal convection in the mantle of the earth. URL https://sciencestruck.com/what-are-convection-cells-how-do-they-work.

[5] Sea and land breeze. URL https://byjus.com/physics/land-and-sea-breeze/.

[6] Convection in boiling of water. URL https://studiousguy.com/examples-convection-everyday-life/.

[7] Venugopal V. T. *Statistical Coherence of Large-Scale Circulation in Turbulent Rayleigh-Bénard convection*. PhD thesis, Guwahati, Assam, India, 2021.

[8] Chandrasekhar S. *Hydrodynamic and Hydromagnetic Stability*. Dover Publications, New York, 2013.

[9] Bodenschatz E., Pesch W., and Ahlers G. Recent developments in Rayleigh-Bénard convection. *Annu. Rev. Fluid Mech.*, **32**:709–778, November 2000.

[10] Ahlers G., Grossmann S., and Lohse D. Heat transfer and large scale dynamics in turbulent Rayleigh-Bénard convection. *Rev. Mod. Phys*, **81**:503–537, June 2009.

[11] Chilla F. and Schumacher J. New perspectives in turbulent Rayleigh-Bénard convection. *Eur. Phys. J. E*, **35**:58, July 2012.

[12] Krishnamurti R. and Howard L. Large-scale flow generation in turbulent convection. *Proc. Natl. Acad. Sci. U.S.A*, **78**:1981–1985, 1981.

[13] Malkus W. V. R. The heat transport and spectrum of thermal turbulence. *Proc. R. Soc. Lond.*, **225**:196–212, August 1954.

[14] Priestley C. H. B. Convection from a large horizontal surface. *Australian Journal of Physics*, **7**:176, 1954.

[15] Kraichnan R. H. Turbulent thermal convection at arbitrary Prandtl number. *Phys. Fluids*, **5**:1374, November 1962.

[16] Speigel E. A. Convection in stars I. Basic Boussinesq convection. *Annu. Rev. Astron. Astrophys.*, **9**:323–352, 1971.

[17] Castaing B., Gunaratne G., Heslot F., Kadanoff L., Libchaber A., Thomae S., Wu X., and Zanetti S. Scaling of hard thermal turbulence in Rayleigh-Bénard convection. *J. Fluid Mech.*, **204**:1–30, August 1989.

[18] Shraiman B. I. and Siggia E. D. Heat transport in high-Rayleigh-number convection. *Phys. Rev. A*, **42**:3650–3653, 1990.

[19] Grossmann S. and Lohse D. Scaling in thermal convection: a unifing theory. *J. Fluid Mech.*, **407**:27–56, November 2000.

[20] He X., Funfshilling D., Bodenschatz E., and Ahlers G. Heat transport by turbulent Rayleigh-Bénard convection for $Pr \simeq 0.8$ and $4 \times 10^{11} \lesssim Ra \lesssim 2 \times 10^{14}$: Ultimate-state transition for aspect ratio Γ = 1.00. *New J. Phys.*, **14**:063030, Jun 2012.

[21] He X., Funfshilling D., Nobach H., Bodenschatz E., and Ahlers G. Transition to the ultimate state of turbulent Rayleigh-Bénard convection. *Phys. Rev. Lett.*, **108**:024502, Jan 2012.

[22] Ahlers G., Bodenschatz E., and He X. Logarithmic temperature profiles of turbulent Rayleigh-Bénard convection in the classical and ultimate state for a Prandtl number of 0.8. *J. Fluid Mech.*, **758**:436–467, 2014.

[23] Niemela J. J., Skrbek L., Sreenivasan K. R., and Donnelly R. J. Turbulent convection at very high Rayleigh numbers. *Nature*, **404**:837, 2000.

[24] Niemela J. J. and Sreenivasan K. R. Does confined turbulent convection ever attain the 'asymptotic scaling' with 1/2 power? *New J. Phys.*, **12**:115002, nov 2010.

[25] Urban P., Hanzelka P., Musilová V., Králík T., Mantia M.L., Srnka A., and Skrbek L. Heat transfer in cryogenic helium gas by turbulent Rayleigh-Bénard convection in a cylindrical cell of aspect ratio 1. *New J. Phys.*, **16**:053042, 2014.

[26] Zhu X., Mathai V., Stevens R. J. A. M., Verzicco R., and Lohse D. Transition to the ultimate regime in two-dimensional Rayleigh-Bénard convection. *Phys. Rev. Lett.*, **120**: 144502, April 2018.

[27] Lohse D. and Toschi F. Ultimate state of thermal convection. *Phys. Rev. Lett.*, **90**:034502, Jan 2003.

[28] Lepot S., Aumaître S., and Gallet B. Radiative heating achieves the ultimate regime of thermal convection. *Proc. Natl Acad. Sci. USA*, **115**:8937 – 8941, Sep 2018.

[29] Shen Y., Tong P., and Xia K.-Q. Turbulent convection over rough surfaces. *Phys. Rev. Lett.*, **76**:908–911, Feb 1996.

[30] Du Y.-B. and Tong P. Enhanced heat transport in turbulent convection over a rough surface. *Phys. Rev. Lett.*, **81**:987–990, Aug 1998.

[31] Villermaux E. Transfer at rough sheared interfaces. *J. Fluid Mech.*, **81**:4859–4862, Nov 1998.

[32] Zhang Y., Sun C., Bao Y., and Zhou Q. How surface roughness reduces heat transport for small roughness heights in turbulent Rayleigh-Bénard convection. *J. Fluid Mech.*, **836**: R2, December 2018.

[33] Roche P.-E., Castaing B., Chabaud B., and Hébral B. Observation of the $\frac{1}{2}$ power law in Rayleigh-Bénard convection. *Phys. Rev. E*, **63**:045303, Mar 2001.

[34] Qiu X.-L., Xia K.-Q., and Tong P. Experimental study of velocity boundary layer near a rough conducting surface in turbulent natural convection. *J. Turbul.*, **6**:N30, 2005.

[35] Xie Y.-C. and Xia K.-Q. Turbulent thermal convection over rough plates with varying roughness geometries. *J. Fluid Mech.*, **825**:573–599, June 2017.

[36] Wei P., Chan T.-S., Ni R., Zhao X.-Z., and Xia K.-Q. Heat transport properties of plates with smooth and rough surfaces in turbulent thermal convection. *J. Fluid Mech.*, **740**: 28–46, 2014.

[37] Tisserand J.-C., Creyssels M., Gasteuil Y., Pabiou H., Gibert M., Castaing B., and Chillá F. Comparison between rough and smooth plates within the same Rayleigh-Bénard cell. *Phys. Fluids*, **23**:015105, 2011.

[38] Du Y.-B. and Tong P. Turbulent thermal convection in a cell with ordered rough boundaries. *J. Fluid Mech.*, **407**:57–84, 2000.

[39] Toppaladoddi S., Succi S., and Wettlaufer J. S. Roughness as a Route to the Ultimate Regime of Thermal Convection. *Phys. Rev. Lett.*, **118**:074503, February 2017.

[40] Stringano G., Pascazio G., and Verzicco R. Turbulent thermal convection over grooved plates. *J. Fluid Mech.*, **557**:307–336, November 2006.

[41] Zhu X., Stevens R. J. A. M., Verzicco R., and Lohse D. Roughness-Facilitated local 1/2 Scaling Does Not Imply the Onset of the Ultimate Regime of Thermal Convection. *Phys. Rev. Lett.*, **119**:154501, October 2017.

[42] Zhu X., Stevens R. J. A. M., Shishkina O., Verzicco R., and Lohse D. $Nu \sim Ra^{1/2}$ scaling enabled by multiscale wall roughness in Rayleigh-Bénard turbulence. *J. Fluid Mech.*, **869**:R4, 2019.

[43] Shishkina O. and Wagner C. Modelling the influence of wall roughness on heat transfer in thermal convection. *J. Fluid Mech.*, **686**:568–582, September 2011.

[44] Xu B.-L., Wang Q., Wan Z.-H., Yan R., and Sun D.-J. Heat transport enhancement and scaling law transition in two-dimensional Rayleigh-Bénard convection with rectangular-type roughness. *Int. J. Heat Mass Transf.*, **121**:872–883, 2018.

[45] Jiang H., Zhu X., Mathai V., Verzicco R., Lohse D., and Sun C. Controlling heat transport and flow structures in thermal turbulence using ratchet surfaces. *Phys. Rev. Lett.*, **120**: 044501, Jan 2018.

[46] Grossmann S. and Lohse D. Thermal convection for Large Prandtl Numbers. *Phys. Rev. Lett.*, **86**:3316–3319, Apr 2001.

[47] Silano G., Sreenivasan K. R., and Verzicco R. Numerical simulations of Rayleigh-Bénard convection for Prandtl numbers between 10^{-1} and 10^{4} and Rayleigh numbers between 10^{5} and 10^{9}. *J. Fluid Mech.*, **662**:409–446, 2010.

[48] Verzicco R. and Camussi R. Prandtl number effects in convective turbulence. *J. Fluid Mech.*, **383**:55–73, 1999.

[49] Malevsky A. V. Patterns of convective turbulence: an effect of Prandtl number. *Physics of the Earth and Planetary Interiors*, **88**:31–41, 1995.

[50] van der Poel E. P., Stevens R. J. A. M., and Lohse D. Comparison between two-and three-dimensional Rayleigh-Bénard convection. *J. Fluid Mech.*, **736**:177–194, 2013.

[51] Yakhot V. Probability distributions in high-Rayleigh-number Bénard convection. *Phys. Rev. Lett.*, **63**:1965, 1989.

[52] Solomon T. H. and Gollub J. P. Sheared boundary layers in turbulent Rayleigh-Bénard convection. *Phys. Rev. Lett.*, **64**:2382, 1990.

[53] Solomon T. H. and Gollub J. P. Thermal boundary layers and heat flux in turbulent convection: The role of recirculating flows. *Phys. Rev. A*, **43**:6683, 1991.

[54] Obukhov A. M. On the influence of Archimedean forces on the structure of the temperature field in a turbulent flow. *Dokl. Akad. Nauk. SSR*, **125**:1246–1248, 1959.

[55] Bolgiano R. Turbulent spectra in a stably stratified atmosphere. *J. Geophys. Res.*, **64**: 2226–2229, 1959.

[56] Brandenburg A. Energy spectra in a model for convective turbulence. *Phys. Rev. Lett.*, **69**:605–608, 1992.

[57] Lesieur M. *Turbulence in Fluids*. Martinus Nijhoff, Dordrecht, 1987.

[58] Huang Y.-X. and Zhou Q. Counter-gradient heat transport in two-dimensional turbulent Rayleigh-Bénard convection. *J. Fluid Mech.*, **737**:R3, 2013.

[59] Pandey A., Verma M. K., Chatterjee A. G., and Dutta B. Similarities between 2D and 3D convection for large Prandtl number. *J. Phys.*, **87**:13, 2016.

[60] Yang J.-L., Zhang Y.-Z., Jin T.-C., Dong Y.-H., Wang B.-F., and Zhou Q. The Pr-dependence of the critical roughness height in two-dimensional turbulent Rayleigh-Bénard convection. *J. Fluid Mech.*, **911**:A52, 2021.

[61] Stevens R., Verzicco R., and Lohse D. Radial boundary layer structure and nusselt number in Rayleigh-Bénard convection. *J. Fluid Mech.*, **643**:495–507, Jan 2010.

[62] Kolmogorov A. N. Dissipation of energy in locally isotropic turbulence. *Dokl. Akad. Nauk SSSR*, **32**:16, Apr 1941.

[63] Lohse D. and Xia K.-Q. Small-scale properties of turbulent Rayleigh-Bénard convection. *Annu. Rev. Fluid Mech.*, **42**:335–364, 2010.

[64] Yakhot V. 4/5 Kolmogorov law for statistically stationary turbulence: Application to high-Rayleigh-number Bénard convection. *Phys. Rev. Lett.*, **69**:769–771, Aug 1992.

[65] Kunnen R. P. J., Clercx H. J. H., Geurts B. J., Bokhoven L. J. A., Akkermans R. A. D., and Verzicco R. A numerical and experimental investigation of structure function scaling in turbulent Rayleigh-Bénard convection. *Phys. Rev. E*, **77**:016302, 2008.

[66] Kunnen R. P. J. and Clercx H. J. H. Probing the energy cascade of convective turbulence. *Phys. Rev. E*, **90**:063018, 2014.

[67] Corrsin S. On the spectrum of isotropic temperature fluctuations in an isotropic turbulence. *J. Appl. Phys.*, **22**:469–473, 1951.

[68] Obukhov A. M. Structure of the temperature field in a turbulent flow. *Izv. Akad. Nauk SSSR*, **13**:58–69, 1949.

[69] Camussi R. and Verzicco R. Temporal statistics in high Rayleigh number convective turbulence. *Eur. J. Mech. B Fluids*, **23**:427–442, 2004.

[70] Kaczorowski M. and Xia K.-Q. Turbulent flow in the bulk of Rayleigh-Bénard convection: small-scale properties in a cubic cell. *J. Fluid Mech.*, **722**:596–617, 2013.

[71] De A. K. A diffuse interface immersed boundary method for complex moving boundary problems. *J. Comput. Phys.*, **366**:226–251, 2018.

[72] Peter S. and De A. K. Wake instability modes for forced transverse oscillation of a sphere. *Ocean Eng.*, **115**:48–59, January 2016.

[73] De A. K., Eswaran V., and Mishra P. K. Dynamics of plumes in turbulent Rayleigh-Bénard convection. *Eur. J. Mech. B/Fluids*, **72**:164–178, May 2018.

[74] Anderson A. D., Tannehill J. C., and Pletcher R. H. *Computational Fluid Mechanics and Heat Transfer*. Taylor and Francis, 1997.

[75] De A. K. and Sarkar S. Three-dimensional wake dynamics behind a tapered cylinder with large taper ratio. *Phys. Fluids*, **32**:063604, 2020.

[76] Chand K., Sharma M., and De A. K. Significance of near-wall dynamics in enhancement of heat flux for roughness aided turbulent Rayleigh-Bénard convection. *Phys. Fluids*, **33**: 065114, 2021.

[77] De A. K. and Sarkar S. Dependence of wake structure on pitching frequency behind a thin panel at $Re = 1000$. *J. Fluid Mech.*, **924**:A33, 2021.

[78] De A. K. and Sarkar S. Spatial wake transition past a thin pitching plate. *Phys. Rev. E*, **104**:025106, 2021.

[79] Toppaladoddi S., Wells A. J., Doering C. R., and Wettlaufer J. S. Thermal convection over fractal surfaces. *J. Fluid Mech.*, **907**:A12, 2021.

[80] Spiegel E. A. A generalization of the mixing-length theory of turbulent convection. *Astrophys. J.*, **138**:216–225, Jul 1963.

[81] Ciliberto S. and Laroche C. Random roughness of boundary increases the turbulent convection scaling exponent. *Phys. Rev. Lett.*, **82**:3998–4001, 1999.

[82] Emran M. S. and Shishkina O. Natural convection in cylindrical containers with isothermal ring-shaped obstacles. *J. Fluid Mech.*, **882**:A3, 2020.

[83] Chand K., Sharma M., Sharma V. T., and De A. K. Statistics of coherent structures in two-dimensional turbulent Rayleigh-Bénard convection. *Phys. Fluids*, **31**:115112, 2019.

[84] Zhang Y., Huang Y.-X., Jiang N., Liu Y.-L., Lu Z.-M., Qiu X., and Zhou Q. Statistics of velocity and temperature fluctuations in two-dimensional Rayleigh-Bénard convection. *Phys. Rev. E*, **96**:023105, 2017.

[85] Zhou Q., Sun C., and Xia K.-Q. Morphological evolution of thermal plumes in turbulent Rayleigh-Bénard convection. *Phys. Rev. Lett.*, **98**:074501, 2007.

[86] Shishkina O. and Wagner C. Analysis of sheet-like thermal plumes in turbulent Rayleigh-Bénard convection. *J. Fluid Mech.*, **599**:383–404, 2008.

[87] Zhou Q. and Xia K.-Q. Physical and geometrical properties of thermal plumes in turbulent Rayleigh-Bénard convection. *New J. Phys.*, **12**:075006, July 2010.

[88] Emran M. S. and Schumacher J. Conditional statistics of thermal dissipation rate in turbulent Rayleigh-Bénard convection. *Eur. Phys. J. E*, **35**:108, October 2012.

[89] Tilgner A., Belmonte A., and Libchaber A. Temperature and velocity profiles of turbulent convection in water. *Phys. Rev. E*, **47**:R2253–R2256, Apr 1993.

[90] Du Y.-B. and Tong P. Temperature fluctuations in a convection cell with rough upper and lower surfaces. *Phys. Rev. E*, **63**:046303, 2001.

[91] Castaing B., Gunaratne G., Heslot F., Kadanoff L., Libchaber A., Thomae S., Wu X.-Z., Zaleski S., and Zanetti G. Scaling of hard thermal turbulence in Rayleigh-Bénard convection. *J. Fluid Mech.*, **204**:1–30, 1988.

[92] Wang Y., He X., and Tong P. Turbulent temperature fluctuations in a closed Rayleigh-Bénard convection cell. *J. Fluid Mech.*, **874**:263–284, 2019.

[93] Pope S. B. *Turbulent Flows*. Cambridge University Press, 2000.

[94] Richardson L. F. *Weather Prediction by Numerical process*. Cambridge University Press, 1922.

[95] Boffetta G. and Ecke R. E. Two-dimensional turbulence. *Annu. Rev. Fluid Mech.*, **44**: 427–451, 2012.

[96] Berkooz G., Holmes P., and Lumley J. L. The proper orthogonal decomposition in the analysis of turbulent flows. *Annu. Rev. Fluid Mech.*, **25**:539–575, 1993.

[97] Lumley J. L. and Poje A. Low-dimensional models for flows with density fluctuations. *Phys. Fluids*, **9**(7):2023–2031, 1997.

[98] Podvin B. and Sergent A. Precursor for wind reversal in a square Rayleigh-Bénard cell. *Phys. Rev. E*, **95**:013112, 2017.

[99] Soucasse L., Podvin B., Riviére P., and Soufiani A. Proper orthogonal decomposition analysis and modelling of large-scale flow reorientations in a cubic Rayleigh-Bénard cell. *J. Fluid Mech.*, **881**:23–50, 2019.

[100] Verdoold J., Tummers M. J., and Hanjalić K. Prime modes of fluid circulation in large-aspect-ratio turbulent Rayleigh-Bénard convection. *Phys. Rev. E*, **80**:037301, 2009.

[101] Podvin B. and Sergent A. Proper orthogonal decomposition investigation of turbulent Rayleigh-Bénard convection in a rectangular cavity. *Phys. Fluids*, **24**:105106, 2012.

[102] Podvin B. and Sergent A. A large scale investigation of wind reversal in a square Rayleigh-Bénard cell. *J. Fluid Mech.*, **766**:172–201, 2015.

[103] Sirovich L. Turbulence and the dynamic of coherent structures. Part I: coherent structures. *Q. Appl. Maths*, **45**(3):561–571, 1987.

[104] Yang Y.-H., Zhu X., Wang B.-F., Liu Y.-L., and Zhou Q. Experimental investigation of turbulent Rayleigh-Bénard convection of water in a cylindrical cell: The Prandtl number effects for $Pr > 1$. *Phys. Fluids*, **32**:015101, 2020.

[105] Li X.-M., He J.-D, Tian Y., Hao P., and Huang S.-D. Effects of Prandtl number in quasi-two-dimensional Rayleigh-Bénard convection. *J. Fluid Mech.*, **915**:A60, 2021.

[106] Zhang Y., Zhou Q., and Sun C. Statistics of kinetic and thermal energy dissipation rates in two-dimensional turbulent Rayleigh-Bénard convection. *J. Fluid Mech.*, **814**:165–184, February 2017.

[107] Dong D.-L., Wang B.-F., Dong Y.-H., Huang Y.-X., Jiang N., Liu Y.-L., Lu Z.-M., Qiu X., Tang Z.-Q., and Zhou Q. Influence of spatial arrangements of roughness elements on turbulent Rayleigh-Bénard convection. *Phys. Fluids*, **32**:045114, 2020.

[108] Foroozani N., Niemela J. J., Armenio V., and Sreenivasan K. R. Turbulent convection and large scale circulation in a cube with rough horizontal surfaces. *Phys. Rev. E*, **99**: 033116, Mar 2019.

[109] Belkadi M., Sergent A., Fraigneau Y., and Podvin B. On the role of roughness valleys in turbulent Rayleigh-Bénard convection. *J. Fluid Mech.*, **923**:A6, 2021.

[110] Bhattacharya S., Verma M. K., and Samtaney R. Prandtl number dependence of the small-scale properties in turbulent Rayleigh-Bénard convection. *Phys. Rev. Fluids*, **6**:063501, Jun 2021.

[111] Xi H.-D., Lam S., and Xia K.-Q. From laminar plumes to organized flows: the onset of large-scale circulation in turbulent thermal convection. *J. Fluid Mech.*, **503**:47–56, 2004.

[112] Brown E., Nikolaenko A., and Ahlers G. Reorientation of the large-scale circulation in turbulent Rayleigh-Bénard convection. *Phys. Rev. Lett.*, **95**:084503, August 2005.

[113] Brown E. and Ahlers G. Rotations and cessations of the large-scale circulation in turbulent Rayleigh-Bénard convection. *J. Fluid Mech.*, **568**:351–386, May 2006.

[114] Venugopal V. T., De A. K., and Mishra P. K. Dynamics of large-scale circulation and energy transfer mechanism in turbulent Rayleigh-Bénard convection in a cubic cell. *Phys. Fluids*, **32**:095115, 2020.

[115] Zhou Q. and Xia K.-Q. Thermal boundary layer structure in turbulent Rayleigh-Bénard convection in a rectangular cell. *J. Fluid Mech.*, **721**:199–224, 2013.

[116] Busse F. H. Convection driven zonal flows and vortices in the major planets. *Chaos*, **4**: 123–134, 1994.

[117] Miesch M. S. The coupling of solar convection and rotation. *Solar Phys.*, **192**:59–89, 2000.

[118] Riedinger X., Tisserand J.-C., Seychelles F., Castaing B., and Chillá F. Heat transport regimes in an inclined channel. *Phys. Fluids*, **25**:015117, 2013.

[119] Jiang L., Sun C., and Calzavarini E. Robustness of heat-transfer in confined inclined convection at high Prandtl number. *Phys. Rev. E*, **99**:013108, Jan 2019.

[120] Yang R., Chong K. L., Wang Q., Verzicco R., Shishkina O., and Lohse D. Periodically modulated thermal convection. *Phys. Rev. Lett.*, **125**:154502, 2020.

[121] Reiter P., Zhang X., Stepanov R., and Shishkina O. Generation of zonal flows in convective systems by travelling thermal waves. *J. Fluid Mech.*, **913**:A13, 2021.

PUBLICATIONS

Journals

1. Statistics of coherent structures in two-dimensional turbulent Rayleigh-Bénard convection, K. Chand, **M. Sharma**, T. Vishnu and A. K. De, *Phys. Fluids*, 2019, 31, 115112. https://doi.org/10.1063/1.5125758.

2. Significance of near-wall dynamics in enhancement of heat flux for roughness aided turbulent Rayleigh-Bénard convection, K. Chand, **M. Sharma** and A. K. De, *Phys. Fluids*, 2021, 33, 065114. https://doi.org/10.1063/5.0053522.

3. Investigation of flow dynamics and heat transfer mechanism in turbulent Rayleigh–Bénard convection over multi-scale rough surfaces, **M. Sharma**, K. Chand and A. K. De, *J. Fluid Mech.*, 2022, 941, A20. https://doi.org/10.1017/jfm.2022.274 .

4. Influence of Prandtl number in turbulent Rayleigh-Bénard convection over rough surfaces, **M. Sharma**, K.Chand and A. K. De, *Phys. Rev. Fluids* 2022, 7, 104609. https://doi.org/10.1103/PhysRevFluids.7.104609.

5. Effect of inclination angle on heat transport properties in two-dimensional Rayleigh-Bénard convection with smooth and rough boundaries, K. Chand, **M. Sharma** and A. K. De, *J. Fluid Mech.*, 2022, 950, A16. https://doi.org/10.1017/jfm.2022.815.

6. Heat transfer mechanism in a cubic box facilitated with conical roughness in turbulent Rayleigh-Bénard convection, **M. Sharma**, K. Chand and A. K. De (under preparation).

7. Understanding the enhanced heat flux through coherent structures in three-dimensional turbulent Rayleigh-Bénard convection with rough boundaries, K. Chand, **M. Sharma** and A. K. De (under preparation).

8. Effect of rough boundaries on the statistics of velocity and temperature fluctuations in 2D turbulent Rayleigh-Bénard convection, K. Chand, D. N. Laskar, **M. Sharma** and A. K. De (under preparation).

Conference proceedings

1. Role of multi-scale roughness in sustaining the enhanced heat transport regime for Rayleigh-Bénard convection, **M. Sharma** and A. K. De, *The* 8^{th} *International and* 47^{th} *National Conference on Fluid Mechanics and Fluid Power*, IIT Guwahati, 2020.

2. Effect of random roughness on heat flux in turbulent Rayleigh-Bénard convection, K. Chand, **M. Sharma**, and A. K. De, *The* 8^{th} *International and* 47^{th} *National Conference on Fluid Mechanics and Fluid Power*, IIT Guwahati, 2020.

3. Extending the range of local $1/2$ scaling regime in Rayleigh-Bénard convection using multi-scale random roughness, **M. Sharma**, K. Chand and A. K. De, *The* 26^{th} *National and* 4^{th} *International ISHMT-ASTFE Heat and Mass Transfer Conference*, IIT Madras, 2021.

4. $Pr-$effect on flow structures and heat transport in turbulent Rayleigh-Bénard convection from rough surfaces, **M. Sharma**, K. Chand and A. K. De, *The* 9^{th} *International and* 49^{th} *National Conference on Fluid Mechanics and Fluid Power*, IIT Roorkee, 2022.

5. Heat transfer mechanism in roughness aided tilted Rayleigh-Bénard convection, K. Chand, **M. Sharma**, and A. K. De, *The* 9^{th} *International and* 49^{th} *National Conference on Fluid Mechanics and Fluid Power*, IIT Roorkee, 2022.